

STUDIES OF THE CRUST - MANTLE SYSTEM

BENEATH SOUTHERN CALIFORNIA

Thesis by

Eugene Drake Humphreys

In Partial Fulfillment of the Requirements

for the Degree of

Doctor of Philosophy

California Institute of Technology

Pasadena, California

1985

(Submitted April 4, 1985)

Acknowledgments

There is no way to properly recognize those who deserve acknowledgement, yet like those who have preceded me, I feel compelled to try. My stay here at Caltech has been an enjoyable experience. This has been the result of the people I have known and worked with. In particular, my two advisors, Rob Clayton and Brad Hager, have been great. From them I have received strong support and have learned a great deal. The work on tomography has been a team effort, including Rob Comer and Tom Hearn, and under the leadership of Rob Clayton. How could such a group not benefit from one another?

Chapter III, more than any other, has developed as the result of various interactions which probably could have occurred no where else. This chapter is still alive, and seems to be growing still, and without signs of slowing. I have been strongly influenced by Brad Hager in much of my thinking on the material of this chapter. The kinematic model portion of this chapter has been the result of work done with Ray Weldon, and I feel it is to him that the majority of our accomplishments are due. This section also has benefited from conversations with Lee Silver. His skepticism and enthusiastic encouragement have left their positive influence not only on this section, but on much of the work within this thesis.

Tom Ahrens has been my "buddy" advisor over the years, and given the choice I would have had it no other way.

It will never be known to anyone who may read this thesis just how much help I have received from many of my fellow students, especially at deadline time. Luciana Astiz was particularly selfless, though a cast of Ronan LeBras, Vicki LeFevre, John Louie, Janice Regan, Richard Stead, Christof Stork, and John Vidale teamed to make timely submission possible. Other students who, as good friends, have made my stay enjoyable are Steve Grand, Chris Sanders, Mark Richards, Keith Echelmeyer and Mindy Brugman. Jim Pechmann was, before graduating, about as good an officemate as a green student could ever hope for.

I would like to thank Shawn Biehler, Tien Lee, Pete Borella and John Elliot for their roles as excellent teachers as well as friends.

Finally, my wife has endured what surely must have seemed like perpetual studentness on my part, and deserves a big hug as well as recognition for her support and patience.

Abstract

A back-projection method of tomographic reconstruction is adapted to invert seismic travel-time data. The problems encountered in inverting these data include ray set inhomogeneity and anisotropy and the three-dimensionality of the space interrogated. Jacobi iteration, deconvolution and variable ray weighting are shown to work well in augmenting the basic back-projection method to produce a well-focused image. Applications of the various focusing algorithms are shown to have a degree of success that depends on the ray geometry used. Also, the ability to reconstruct an accurate image when the data include moderate amounts of noise is shown to be good.

P- wave teleseismic travel time delays recorded by the southern California array are inverted with the tomographic method to obtain variations in the P-wave velocity structure to a depth of 750 km. Two major anomalies are imaged. A curtain-like E-W trending high velocity feature is found directly beneath the Transverse Ranges. This feature is about 50 km in thickness, extends in depth to a maximum of about 250 km on its eastern end, and attains a maximum velocity that is about 3% greater than average mantle at the same depth beneath southern California. A zone of low-velocity material is found in the uppermost 100 km beneath the region of the Salton Trough. The seismic velocities here are depressed by about 4%.

These anomalous regions are interpreted to be related to the geologic processes that have been active recently in southern California. Scaling relations are used to estimate that the Transverse Range anomaly is about 500°C colder and 1% more dense than average southern California mantle of the same depth, while the Salton Trough anomaly is about 1/2% less dense and contains about 3% melt. The density distribution drives a flow of upper mantle material from the Salton Trough region towards the Transverse Ranges, where it sinks into the mantle to form the feature seen beneath these ranges. Mantle flow results in tractions that act on the base of the lithosphere to produce stresses within the lithosphere that are tensile in the Salton Trough and compressive in the Transverse Ranges. These stresses are thought to account for the physiography seen in these provinces.

The southern California crust is modeled using late Quaternary slip rates on major faults, and a kinematic description is determined that has: 1) only local sites of convergence in the Transverse Ranges, and 2) the occurrence of significant strain rates near to the southern California coast, including the western Transverse Ranges.

TABLE OF CONTENTS

| | |
|---|---------|
| Acknowledgements | ii |
| Abstract | iii |
| | |
| I Application of the Tomographic Method of Inversion to Seismic Travel Time Problems | |
| 1.1 Introduction | 1 |
| 1.2 Introduction to Method of Inversion | 2 |
| 1.3 Ray Weighting | 5 |
| 1.4 Deblurring | 6 |
| 1.5 Iteration | 10 |
| 1.6 Comparison of Methods | 11 |
| 1.7 Application of Tomographic Schemes | 12 |
| 1.8 Resolution and Error Estimations | 27 |
| | |
| II A Tomographic Inversion of Teleseismic P Travel Times for Structure Beneath Southern California | |
| 2.1 Introduction | 33 |
| 2.2 Data Reduction | 35 |
| 2.3 Method of Inversion | 42 |
| 2.4 Details of the Specific Inversion Algorithm Used | 43 |
| 2.5 Estimations of Resolution and Error | 61 |
| 2.6 Application of Tomographic Algorithm to Test Structures | 64 |
| 2.7 Results | 66 |
| 2.8 Discussion | 101 |
| | |
| III Kinematic and Dynamic Modeling of Southern California Tectonics | |
| 3.1 Introduction | 103 |
| 3.2 The Kinematic Model of the Crust | 105 |
| 3.3 Late Cenozoic History of the San Andreas Fault | 130 |
| 3.4 Three Dimensional, Constant Viscosity Dynamic Modeling | 136 |
| 3.5 A Model for the Recent Development of Southern California | 164 |
| References | 183 |

Application of the Tomographic Method of Inversion to Seismic Travel Time Problems

1.1 Introduction

The theoretical basis of tomography was pioneered by Radon (1917), who devised the forward and inverse transforms that now bear his name. This transform can often be related to the projection of a two-dimensional scalar field, such as the projection of a slowness field along parallel ray paths to produce the travel time delays associated with the paths. One of the first significant applications of this theory to a physical problem was that of Bracewell (1956), who used the method to image the solar corona. Seismologists have also been using the principle of the Radon Transform for quite some time in the construction of "slant-stacks". But it has been the medical researchers that have had the most remarkable success, and they who coined the word tomography for the high-resolution, two-dimensional "tomo-graph" (slice-picture) through a patient. Fundamental to their success has been the discretization of the space to be imaged into cells, thus posing the problem in a manner well suited to digital computers. High resolution is achieved by dividing the space into many small cells. The key inversion algorithm employed by this method is a back-projection scheme in which each ray is back-projected, one at a time, and the signal associated with the ray is distributed in the region along the ray path. The superposition of many rays reconstructs an image. By itself, simple back-projection produces a rather blurred image. The nature of the blurring is well understood, though, and

the application of procedures specifically designed to remove the blurring results in a high-quality image.

It is the ability of tomography to produce a highly resolved image that makes it attractive for seismic application. However, we must now be able to handle ray distributions that are anisotropic and inhomogeneous, and possibly three-dimensional. These are all problems carefully avoided in the medical application of the technique. In this chapter the adaptations of the tomographic method needed to make it applicable to these more general ray geometries are discussed. Following the discussion of the method will be a section presenting the results of various algorithms acting on ray distributions that are strongly anisotropic and inhomogeneous. We also address the important topics of resolution and error.

1.2 Introduction to Method of Inversion

A common problem in seismology is the determination of the velocity transmission structure of a region that has been probed by a set of rays. The usual approach in formulating the inverse problem is to divide the region to be modeled into a set of blocks. A reference velocity structure is assumed, and deviations from the expected travel times are inverted to obtain the slowness perturbations of the blocks. In practice the assumed velocity structure is used only to guide the ray's path, thus forming an approximate formulation, but one in which the slowness distribution is not dependent upon itself. This linearizes the problem.

The discrete forward problem can be written $t_r = \sum_b l_{rb} s_b$, where t_r is the time delay associated with the r^{th} ray, s_b is the slowness perturbation of the b^{th}

block, and l_{rb} is the length of the r^{th} ray segment in the b^{th} block. This is simply the discretized version of the travel time equation, $t = \int_{ray} s \, dl$. In matrix form, the discrete representation can be compactly written $\mathbf{t} = \mathbf{L} \mathbf{s}$. The classical least-squares solution to this problem is found by solving the normal equations, $\mathbf{L}^T \mathbf{L} \mathbf{s} = \mathbf{L}^T \mathbf{t}$. At this point it is desired to invert $\mathbf{L}^T \mathbf{L}$, where this matrix has dimensions equal to the model size squared. The matrix $\mathbf{L}^T \mathbf{L}$ is sometimes referred to as the model covariance matrix or the information matrix. The $i-j^{th}$ element of this matrix gives a measure of how well "connected" the information is between the i^{th} block and the j^{th} block of the model.

The construction, storage and direct inversion of $\mathbf{L}^T \mathbf{L}$ can be formidable, but is avoided with the back-projection method. The simplest approach one can take is to approximate the inversion by initially using only the diagonal of $\mathbf{L}^T \mathbf{L}$, which gives an estimation for slowness of

$$s_b = \sum_r t_r l_{rb} / \sum_r l_{rb}^2 . \quad (\text{I.1})$$

An efficient procedure can be used to accomplish this. Each ray is back-projected one at a time, and for each block encountered, the contributions to the sums $\sum_r t_r l_{rb}$ and $\sum_r l_{rb}^2$ are accumulated in separate computer storage spaces. After all rays have been back-projected, each block's slowness is estimated by taking the ratio of that block's two accumulated sums. This simple scheme, called the basic back-projection reconstruction, is fast and requires comparatively little storage space. The resulting inversion, however, has a tendency to be strongly blurred, especially along the paths of high-ray density. Two general classes of methods have been developed to correct

this problem which, in effect, take into account the entire information matrix instead of only the diagonal. These methods often go under the names of deblurring and reconstruction techniques (Herman et al, 1973) in the medical literature.

In principle, deblurring is a deconvolutional scheme accomplished in either the space or wavenumber domain. Any particular row of $\mathbf{L}^T\mathbf{L}$ can be identified with the basic back-projection reconstruction of the particular block associated with that row. This reconstruction, often called the block's spread function, is the Green's function of that block to the basic back-projection. The effect of deconvolution is to transform the information matrix into the identity matrix. This identifies the operation of deconvolution, in some sense, with the inverse of $\mathbf{L}^T\mathbf{L}$.

The other approach to solving the blurring problem is iteration, such as ART (algebraic reconstruction technique, Herman et al, 1973) or SIRT (simultaneous iterative reconstruction technique, Gilbert, 1972). One possible algorithm is to iterate on the difference between the observed delays and those predicted by the latest inverse, back-projecting this difference, and then adding this correction to the existing inverse in order to obtain an updated version.

These topics will be discussed in some detail. But before these methods are addressed, the procedure of selectively weighting rays is discussed. This procedure improves the effectiveness of deblurring and iterating when anisotropic and inhomogeneous ray geometries are used.

1.3 Ray Weighting

In the medical application of tomography, the experimental geometry is designed to produce ray coverage that is both isotropic and homogeneous. In seismic application usually one or both of these properties do not hold. The spread function of a block, simply the reciprocal distance from the block in the medical case (i.e., $1/r$), is then distorted. The effects of the non-uniform ray distribution often produce prominent streaks emanating from any anomalous block along the directions most commonly taken by the rays that traverse the block. By varying the amount of weight given each ray, the character of the spread function can be improved. To accomplish this, each ray is weighted in inverse proportion to the ray density in that particular ray's direction. This modification can easily be accommodated by equation (I.1) with the inclusion of a weighting parameter, w_{rb} , in both the numerator and denominator. In application, two methods of determining w have been tried: 1) weighting each ray hitting a block by the inverse ray density in the slowness-azimuth neighborhood of the ray in question, as determined by the distribution of the entire set of rays, and 2) determining a weight resulting from a more approximate ray density estimation scheme, but based on the distribution of rays investigating only the single block. In the first case each ray has the same weight along its entire length, and w_{rb} can be replaced by w_r . This is straightforward and can be rapidly employed, but it depends on the distribution of the complete ray set being a fairly faithful representation of the ray set investigating each block; that is, that the ray set is nearly homogeneous. When this is the case, the method can significantly improve the spread function, even for strongly anisotropic ray geometries.

The second approach to weighting is very similar. In this approach, the delays for each block are divided into several slowness-azimuth regions, the average for each region is found, and then these regional determinations are averaged to arrive at a whole block estimate. With this scheme, the homogeneity of the ray set is much less critical. However, a ray may possess a weight that varies along its length.

1.4 Deblurring

When one is dealing with a two-dimensional situation having homogeneous and isotropic ray coverage, the reconstruction of a single anomalous block resulting from equation (I.1) will produce a $1/r$ spread function centered on the anomalous block, where r is the distance from the anomalous block. It has been shown that the functions $1/r$ (in space) and $1/|k_r|$ (in the wavenumber domain, where $|k_r|$ is the wavenumber) are space-wavenumber counterparts (Rowland, 1979). For the two-dimensional case, then, multiplying the Fourier transformed slowness inversion by $|k_r|$ and then transforming back to the space domain will properly compensate for the $1/r$ blurring. Of course, when taking this product, the function $|k_r|$ must be truncated or otherwise terminated for wavenumbers higher than are of interest since this function is not bounded far from the origin.

In three dimensions, the spread function of a single anomalous block is $1/r^2$. It is still true, however, that multiplication by $|k_r|$ corrects for the radial blurring. This can be seen by Fourier transforming r^{-2} , which when spherical symmetry applies and r is the absolute distance from the origin, reduces to (Bracewell, 1965)

$$f(k_r) = 4\pi \int_0^{\infty} r^{-2} \operatorname{sinc}\left(\frac{k_r r}{\pi}\right) r^2 dr \quad . \quad (\text{I.2})$$

This gives $f(k_r) = (2\pi^3 k_r)^{-1}$. But since equation (I.2) assumes r to be always positive away from the origin, $f(k_r) = (2\pi^3 |k_r|)^{-1}$ is the desired relation if one is considering negative values of k_r .

The space domain offers an alternate approach to deblurring, which is convenient since operations in space avoid the direct use of Fourier transforms. The space domain filter which is the Fourier inverse of $|k_r|$ weighting in the wavenumber domain can be found by rewriting $|k_r|$ as $-i |k_r| / k_r = ik_r$. It is seen that this is equivalent to the application of the Hilbert transform and the radial derivative (for brevity HD). In space, the convolution of these two operators gives a filter with a central peak, and negative, diminishing side lobes (Figure I.1). This spatial representation of $|k_r|$ can be viewed as a high wavenumber enhancer, like the first derivative, though the response is kept phaseless by the application of the Hilbert transform.

To relate deblurring to the matrix formulation of the problem, we pre-multiply the normal equations by \mathbf{D}^{-1} to get $\mathbf{D}^{-1}[\mathbf{L}^T \mathbf{L}] \mathbf{s} = \mathbf{D}^{-1} \mathbf{L}^T \mathbf{t}$, where \mathbf{D} is the diagonal of $\mathbf{L}^T \mathbf{L}$. This equation is the same as equation (I.1) except that in equation (I.1) $\mathbf{D}^{-1}[\mathbf{L}^T \mathbf{L}]$ has been approximated with \mathbf{I} . The j^{th} column of $\mathbf{D}^{-1}[\mathbf{L}^T \mathbf{L}]$ is the j^{th} spread function. (This can easily be seen by setting all model slowness values to zero except for the j^{th} , which is set to unity. The left side is then the j^{th} row of $\mathbf{D}^{-1} \mathbf{L}^T \mathbf{L}$ while the right side is the basic back-projection inverse (i.e., equation I.1) of this slowness distribution.) Applying deconvolution to the left-hand side, therefore, leaves one simply with \mathbf{s} . To deconvolve the right-hand side is to deconvolve the basic back-projection inverse given by equation (I.1). Deconvolution is seen to

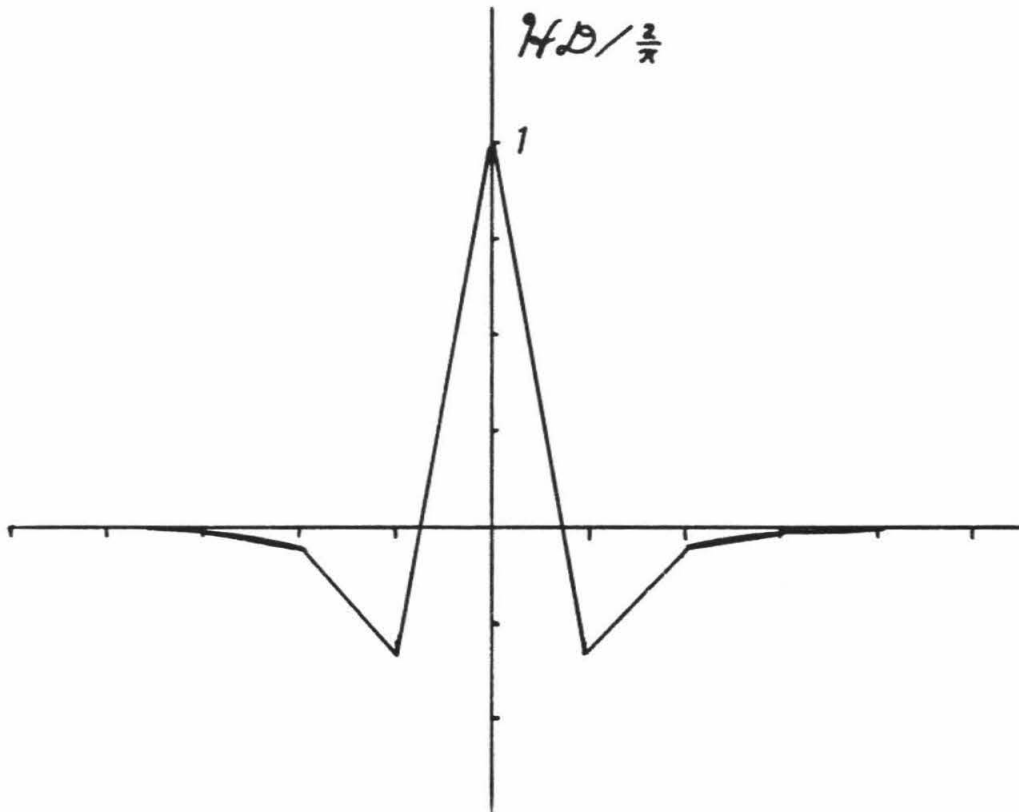


Figure I.1. The convolution of the Hilbert Transform operator and the first derivative operator, HD . This is the space domain "deblurring" operator for isotropic ray geometries.

account for the entire information matrix and to give the solution to the complete normal equations.

So far, deblurring has been discussed only for the case of isotropic and homogeneous ray coverage, and the approaches have been exact. When the ray coverage is not isotropic and homogeneous, the general approaches just described can be made to work, but they must be modified and in so doing may lose their exactness. Because of this, the seismic applications of these methods are usually used in conjunction with iteration, and in this role deblurring can be viewed as a means of accelerating the rate of convergence so that iteration need not be applied as many times. When the ray set is anisotropic yet homogeneous, wavenumber deconvolution will perform properly, so long as the spread function can be determined. But if the ray coverage varies from location to location, the spread function will be different for each block, and wavenumber deconvolution may become impractical. If, however, the ray coverage is only slightly heterogeneous, it has been found that an average spread function can be constructed that works reasonably well. When using this approach, stabilizing procedures are usually applied to keep the deblurring from becoming erratic. Two stabilizing procedures that have proven successful are discussed below.

When the ray coverage is moderately heterogeneous, space domain filtering has proven to be more useful. Since only an incomplete focusing can be accomplished, the space domain filter is approximated and, for convenience, made more compact. This is to enable easier application and to minimize interference with the inversion domain boundaries. Towards this end, a filter, F , of some arbitrary length can be constructed to have as similar an effect as HD (in an L_2 sense) as possible when applied to some slowness distribution, \mathbf{s} (i.e., minimize the energy of $((F - HD) * \mathbf{s})$ for a

given \mathbf{s}). The three-point filter has proven quite useful. In the practical use of this filter, a damping has been applied by linearly combining the filtered inversion for slowness with the prefiltered inversion, symbolically,

$$\mathbf{s}_{new} \leftarrow a(\mathbf{s}_{old}) + b(F*\mathbf{s}_{old}) \quad (I.3)$$

where a and b are constants determined by a least-squares procedure which minimizes the difference between the actual delays and those predicted by the inverse. Of course, the determination of F is dependent upon the slowness distribution in s_{old} . But it can be stated, since HD is symmetrical, that F is also symmetrical. Notice, however, that if F were altered to any other three point symmetrical filter, $(-C, 1, -C)$ for any constant C , a and b can be adjusted so that equation (I.3) is unchanged. This implies that with the use of equation (I.3) and the three-point representation of HD , \mathbf{s} has no bearing on the determination of F . Furthermore, taking $C = 1/2$, the operation represented by equation (I.3) can be rewritten as a linear combination of the second derivative operator and the identity operator,

$$\mathbf{s}_{new} \leftarrow c_1(c_2 I + D^2)*\mathbf{s}_{old} \quad (I.4)$$

for least-squares determined constants c_1 and c_2 .

1.5 Iteration

The final image enhancement is the application of an iteration scheme. Several approaches are possible, the particular example described below being perhaps the simplest of the set. With this scheme, the difference between the actual delays and those predicted by the existing inverse are inverted by the same algorithm that was used to create the existing inverse. The inversion of the differences is then added to

the existing inverse to get an updated inverse, and the process is repeated. Each iteration can be shown to be equivalent to a single Jacobi iteration. If the normal equations are written $[\mathbf{D} - (\mathbf{D} - \mathbf{L}^T \mathbf{L})] \mathbf{s} = \mathbf{L}^T \mathbf{t}$, where \mathbf{D} is the diagonal of $\mathbf{L}^T \mathbf{L}$, Clayton (in prep) has shown that $\mathbf{s}^{(k)} = \mathbf{s}^{(k-1)} + \mathbf{D}^{-1} \mathbf{L}^T (\mathbf{t} - \mathbf{t}^{(k-1)})$, where $^{(k)}$ refers to the k^{th} approximation to the solution and $\mathbf{t}^{(k-1)}$ are the delays predicted by the $(k-1)^{th}$ slowness distribution: $\mathbf{L} \mathbf{s}^{(k-1)}$. Assuming $\mathbf{s}^{(0)}$ to be zero, the first iteration gives $\mathbf{s}^{(1)} = \mathbf{D}^{-1} \mathbf{L}^T \mathbf{t}$, which is the simple back-projection inverse given by equation (I.1). Then each successive term of the Jacobi iteration is seen to be equivalent to each successive back-projection of the residuals. If this sequence converges, the infinite sum of all terms (i.e., the application of an infinite number of iterations) gives the generalized inverse solution to the normal equations (Comer and Clayton, in prep.). In the application of any of the tomographic schemes tested below, lack of convergent behavior has not been a problem.

1.6 Comparison of Methods

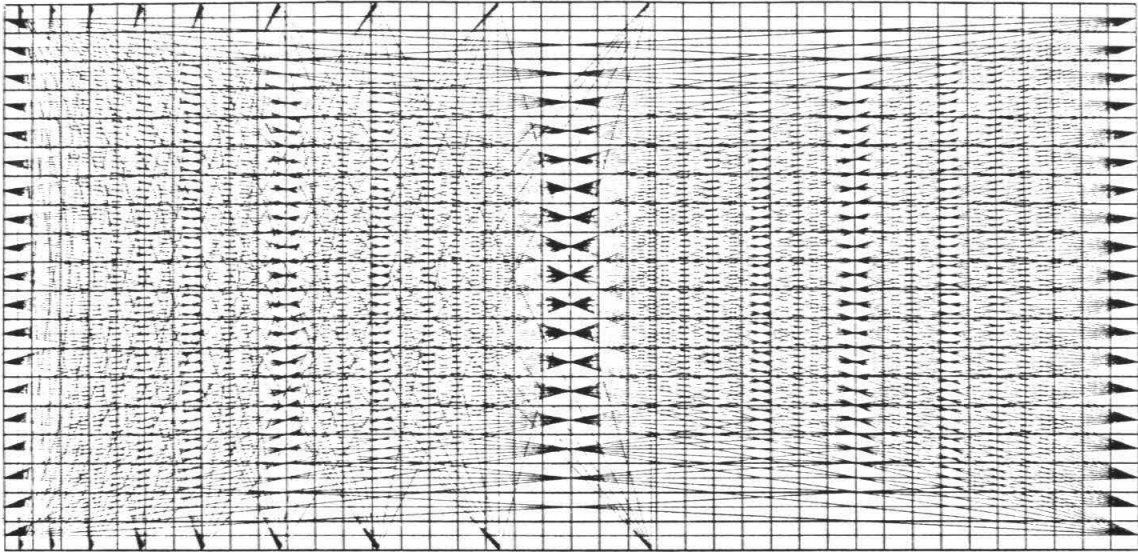
Deblurring and iteration, in principal, both give complete solutions to the normal equations. The manner in which the two methods reconstruct an image, however, is quite different. In the practical application of these methods, their differing characteristics can be taken advantage of. Iteration focuses an image through repeated application. One beneficial modification that can be incorporated is the ability to readjust the ray paths to the emerging structure. Because the reconstruction is initially very smooth, the ray path perturbations are expected to be smooth and stable (see Figure I.6). Another desirable aspect of iteration is that the iterative sequence can be terminated at the point where the structure is resolved to the degree

one feels is allowed by the data. This takes advantage of the back-projection's inherent smoothing properties, and is somewhat analogous to diminishing the influence of the small eigenvectors of $\mathbf{L}^T\mathbf{L}$ when inverting with the generalized inverse. The major problem with iteration is that the rate at which the reconstruction becomes focused can be very slow, especially along corridors where there are few crossing rays. To a degree, this is an advantage because this is just the direction in which there is the least constraint, but the slow rate of focusing can be frustrating. Deconvolution, on the other hand, does not have this problem because no iteration is involved. The major drawback to deconvolution is that it can be rather unstable; i.e., producing a rather energetic, high wavenumber rich inverse. Accentuating this problem is that with an inhomogeneous ray sampling, the spread functions are not the same for every block. When this is so, a simple deconvolution of some chosen spread function will not work well in those regions where this function is not representative. When such problems exist, space domain filtering has proven to be more successful since it does not usually suffer from the same degree of instability.

1.7 Application of Tomographic Schemes

In this section the procedures outlined above are applied to synthetic test structures. To do this, a test structure and a ray set are chosen and "observed" delays are calculated. (In these test cases, it is pointed out, the ray paths are assumed and there are therefore no ray tracing problems such as may exist when inverting real data.) These delays are then inverted using the procedures outlined above. Two ray sets have been chosen, and these are shown in Figure I.2. In both cases the rays are inhomogeneous and strongly isotropic. In the first case (Figure I.2•1), the rays are not as

(● 1)



(● 2)

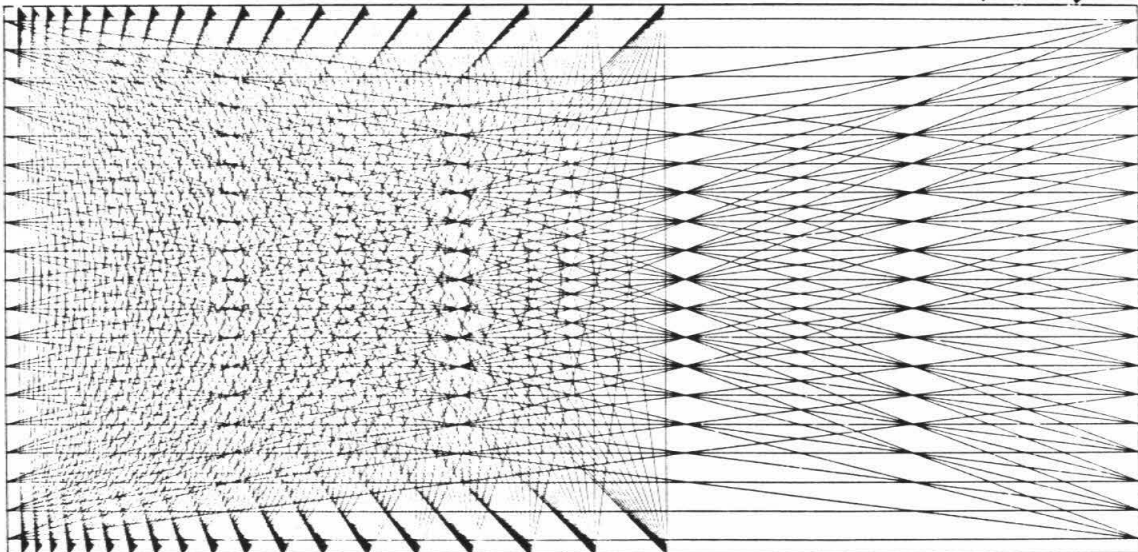


Figure I.2. Map of the ray geometries used. These geometries are strongly anisotropic and inhomogeneous, though configuration (●1) is more inhomogeneous than is (●2). Also note that the block structure is indicated on (●1).

inhomogeneous as in the second case (Figure I.2●2). Also shown in Figure I.2●1 are the blocks chosen to describe the model space. Notice that the initial structure and the ray set are symmetrical about the mid-plane, and hence the reconstructions are similarly symmetric.

Figure I.3 shows the starting model. This test structure was chosen to show the point response in each of the two basic regions represented, one with good azimuthal coverage and one with restricted coverage. Following are figures displaying the results of the various methods. These figures are grouped together according to the type of procedure being applied: weighting to compensate for anisotropy, iteration, and deblurring. In each figure, only the application of the particular procedure being investigated is shown in order to isolate the effect of the single procedure. In practice better results can be obtained by using a combined set of procedures, one from each group. One such example that uses the combined application of several procedures is shown after the individual procedures are presented.

Figure I.4 shows the basic back-projection inverse given by equation (I.1). Notice the tendency of the reconstruction to be more strongly blurred along the paths most commonly taken by the rays. Figure I.5 shows the effects of the two previously discussed weighting schemes. Deweighting rays that traverse the model in the direction most commonly taken reduce the tendency to streak in that direction. When ray directionality is fairly homogeneous, direct ray-weighting works well, as seen in Figure I.5a. The weighting function used is shown in the inset; in this case horizontal rays are given 30% as much weight as the vertical rays. In the bottom portion of Figure 5a it is seen that this weighting only works well when the weighting function is well suited to the degree of anisotropy in the region. Figure I.5b shows that the binning

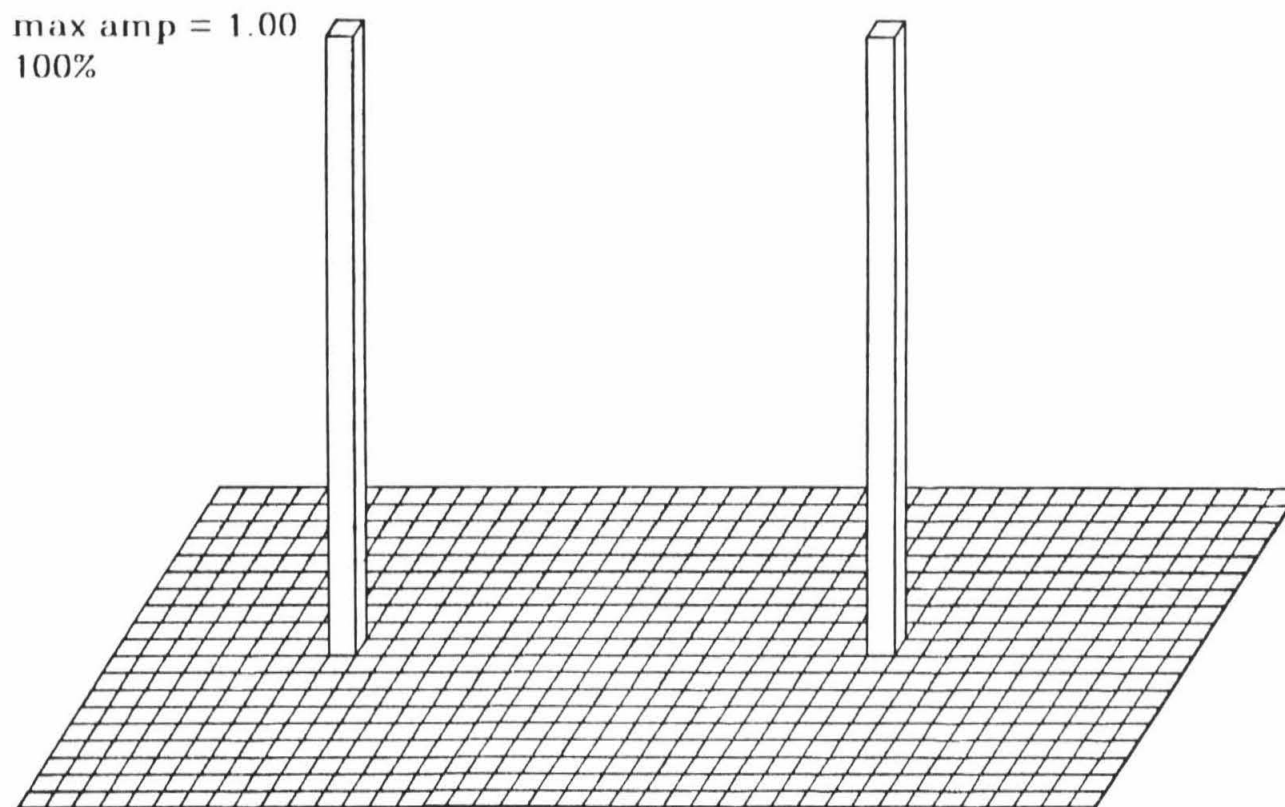


Figure I.3. Display of the input structure. On this figure and following figures the maximum amplitude of the plot is indicated since the vertical scale is adjusted to make the plot clear. Also, the fraction of the “data” (RMS) accounted for by the structure is shown in percent.

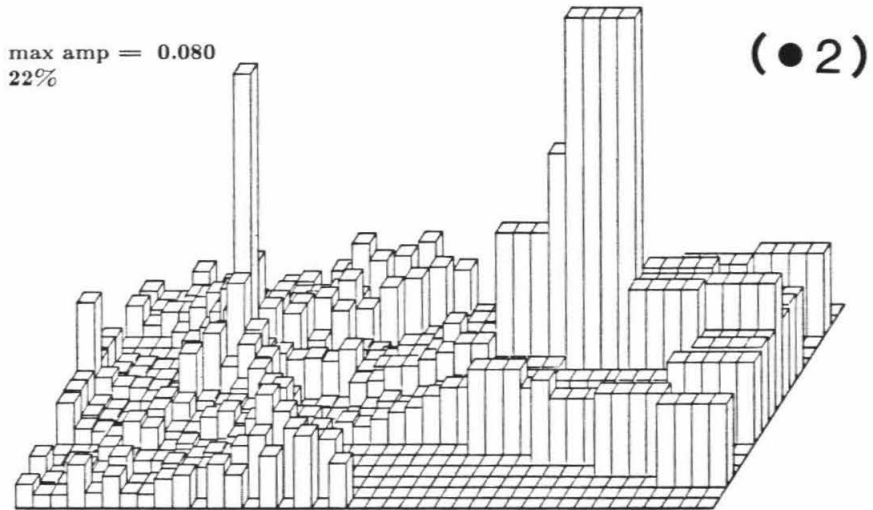
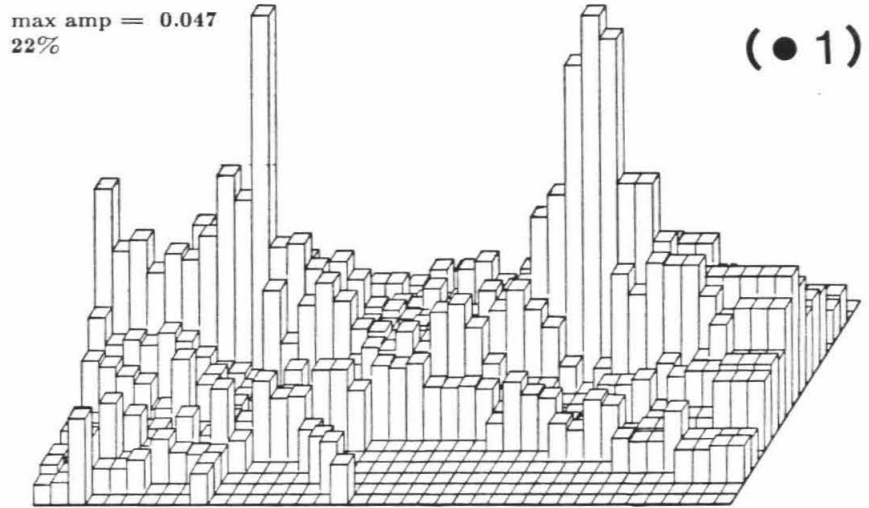


Figure I.4. The basic back-projection inverse of the travel times produced by the structure shown in Figure I.3. In (●1) the ray set is that of Figure I.2●1, while in (●2) the rays are those of Figure I.2●2.

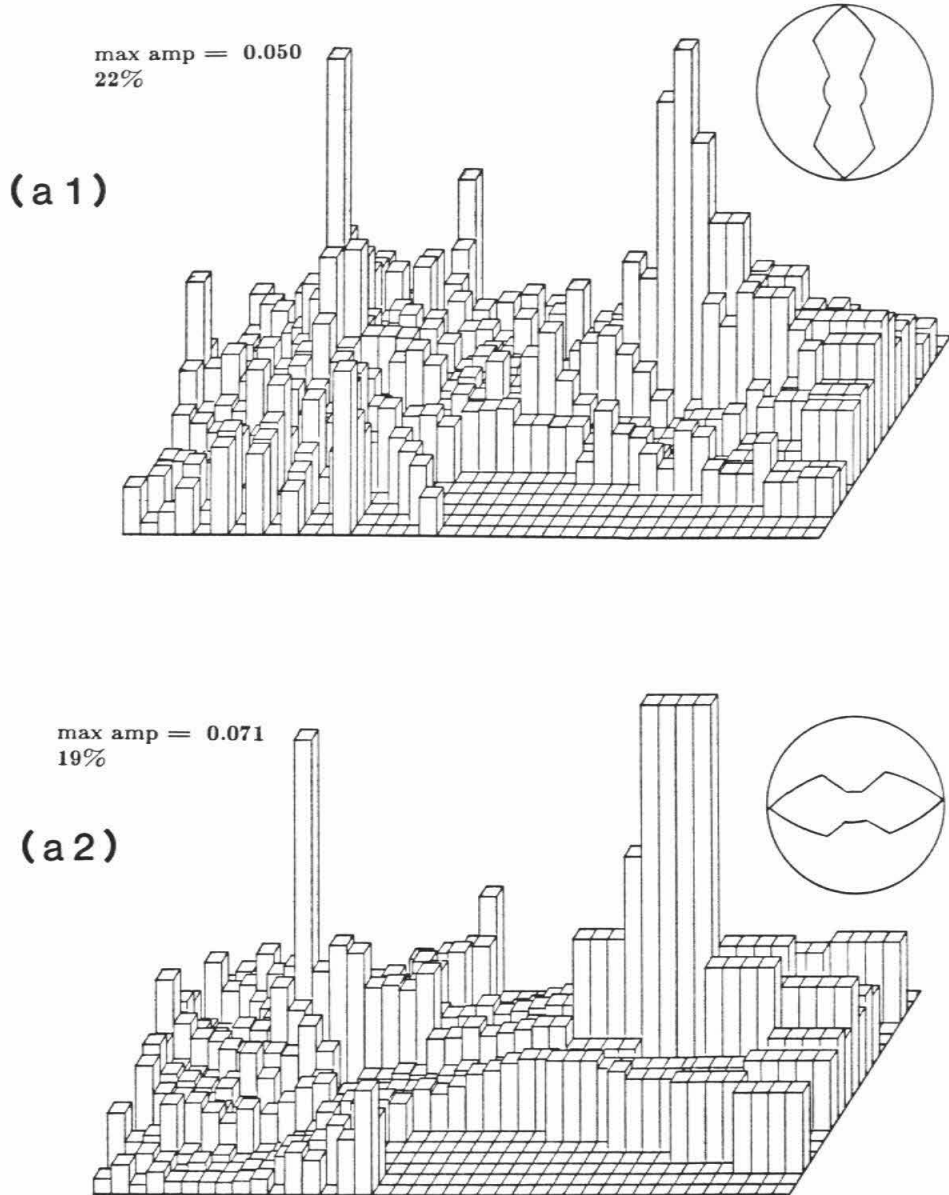


Figure I.5. The effect of the two weighting schemes used: ray weighting and azimuthal weighting. Figure I.5a is in the same format as Figure I.4, but in this figure ray weighting has been applied by an amount that is indicated by the polar plots in the upper left corners. Figure I.5b is in the same format as Figure I.4, but in this figure binning of the rays has been applied, as described in the text. The “pie-slice” diagram shows the four azimuthal bins used, where the two “slices” directly across from one another comprise a single azimuth bin.

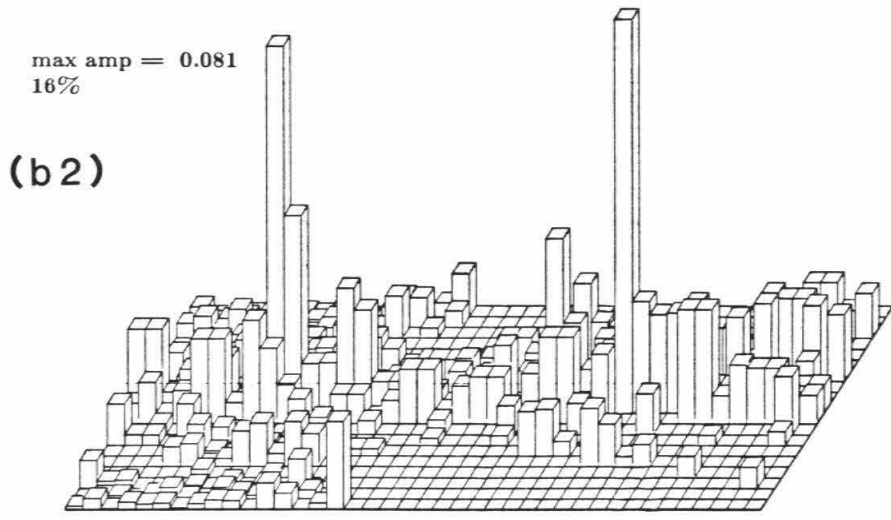
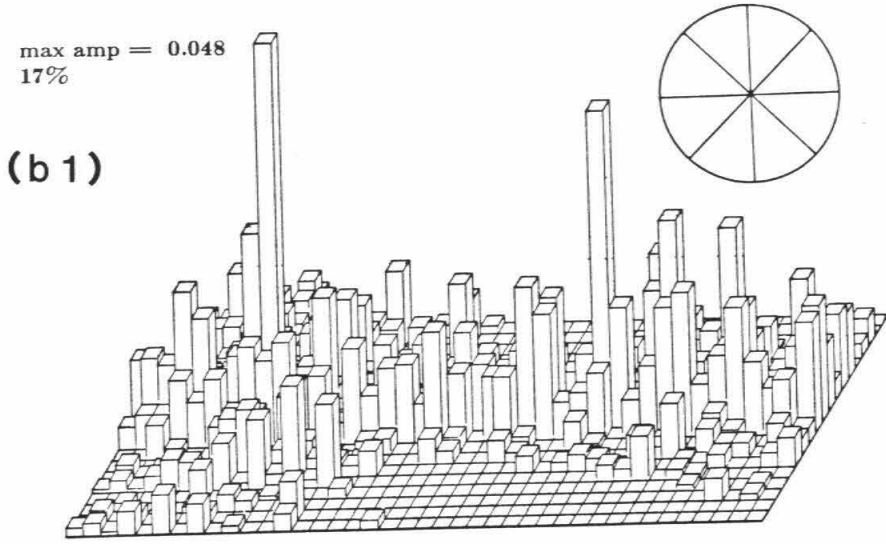
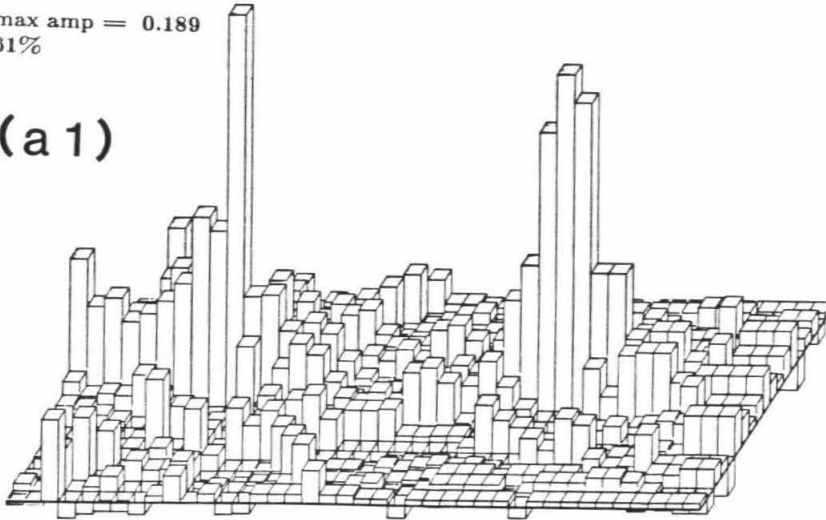


Figure 1.5 (continued)

max amp = 0.189
61%

(a1)



max amp = 0.300
62%

(a2)

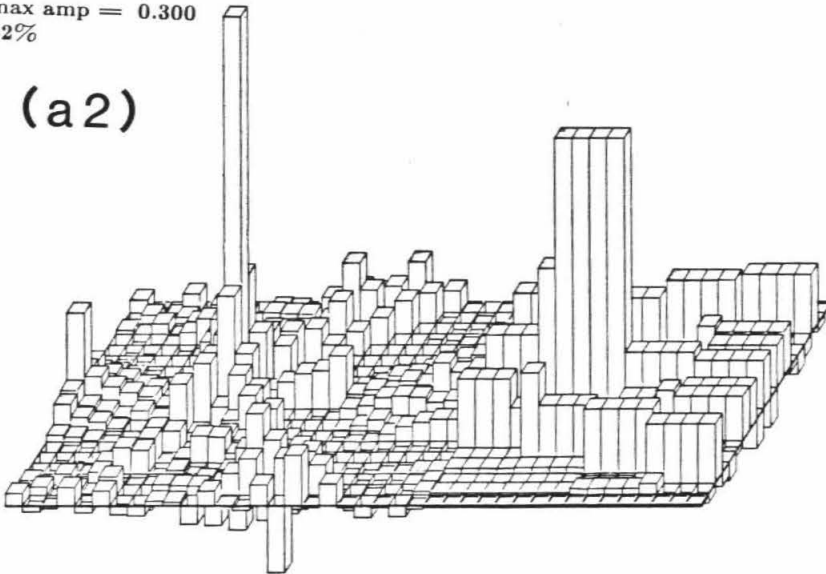


Figure I.6. The effectiveness of iteration on the travel time residuals. Figure I.6a is in the same format as Figure I.4, but with two successive iterations applied. Figure I.6b is in the same format as Figure I.4, but with five successive iterations applied.

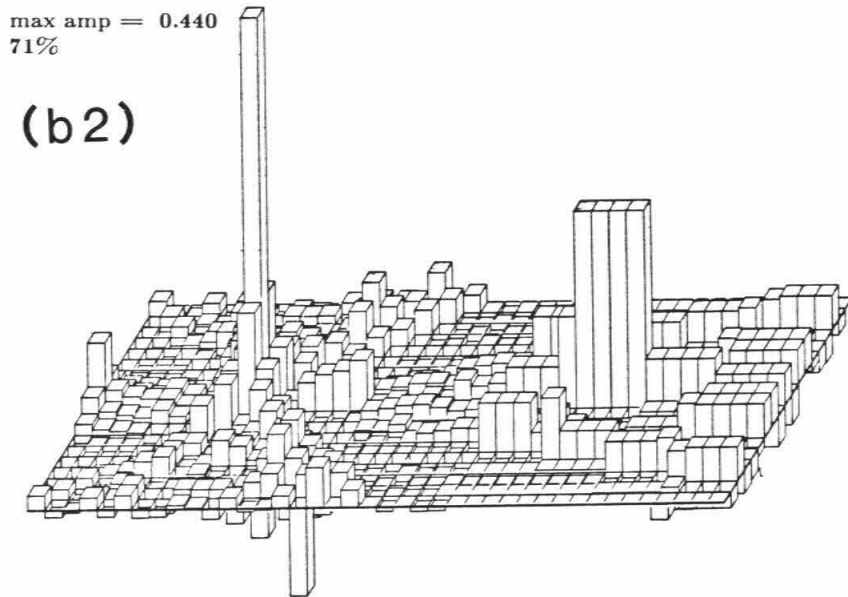
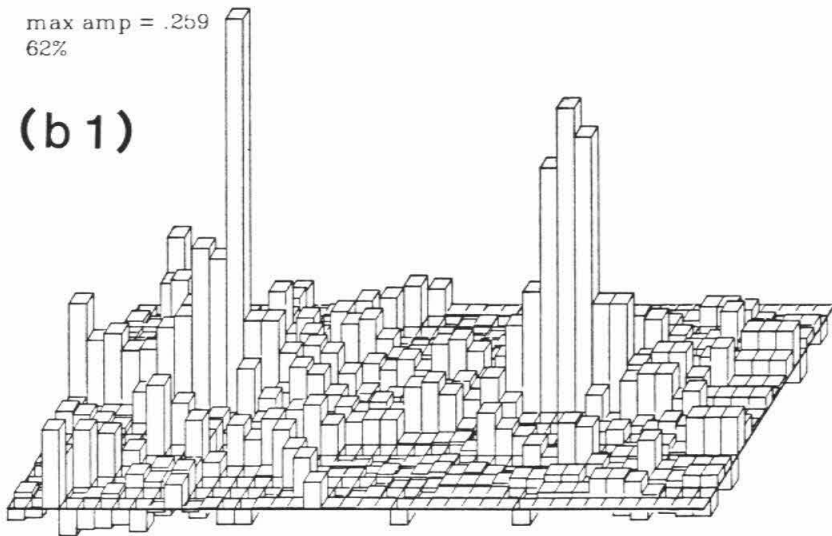


Figure I.6 (continued)

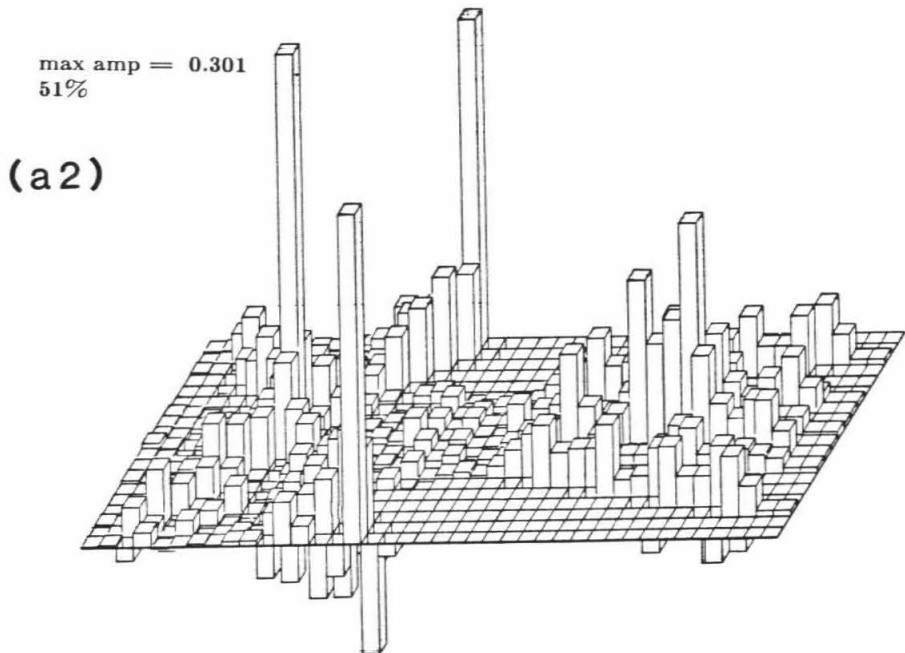
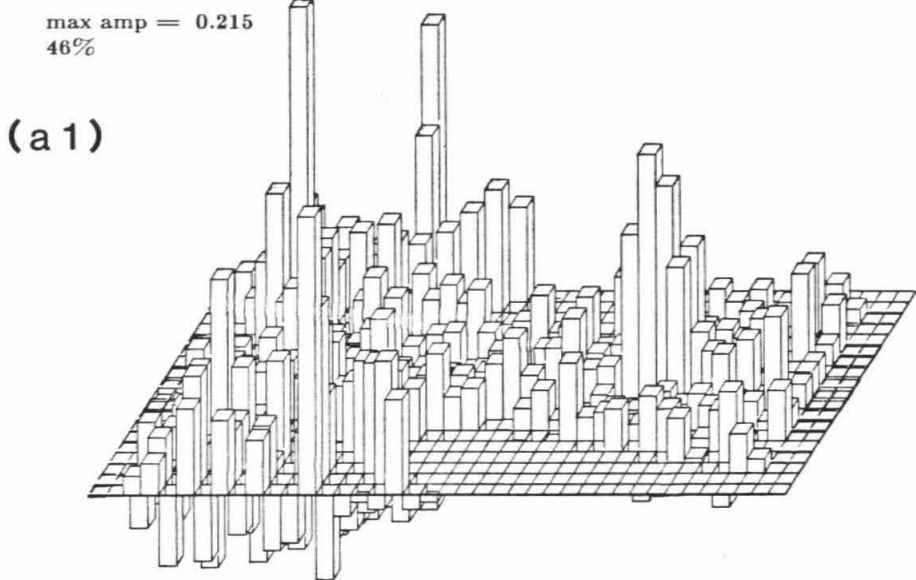


Figure I.7. The effectiveness of deconvolution. Figure I.7a is in the same format as Figure I.4, but the nearest-neighbor deblurring filter has been applied. Figure I.7b is in the same format as Figure I.4, but the broader deblurring filter has been applied. Figure I.7c shows the effect of wavenumber domain deconvolution on the ray distribution shown in Figure I.2•1. The upper plot is constructed with a lower wavenumber clamp set at the level of the RMS for the unfiltered inversion, while the lower plot has the clamp set at half the unfiltered RMS level.

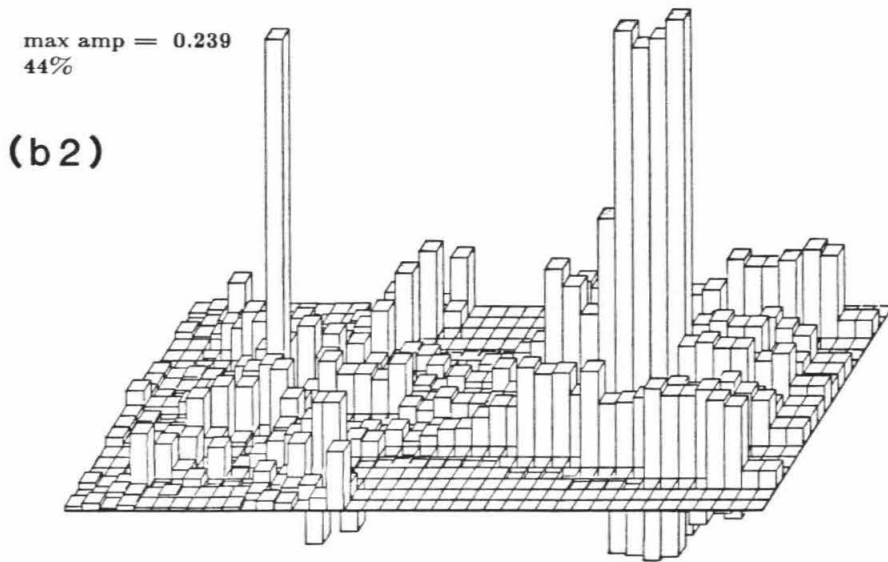
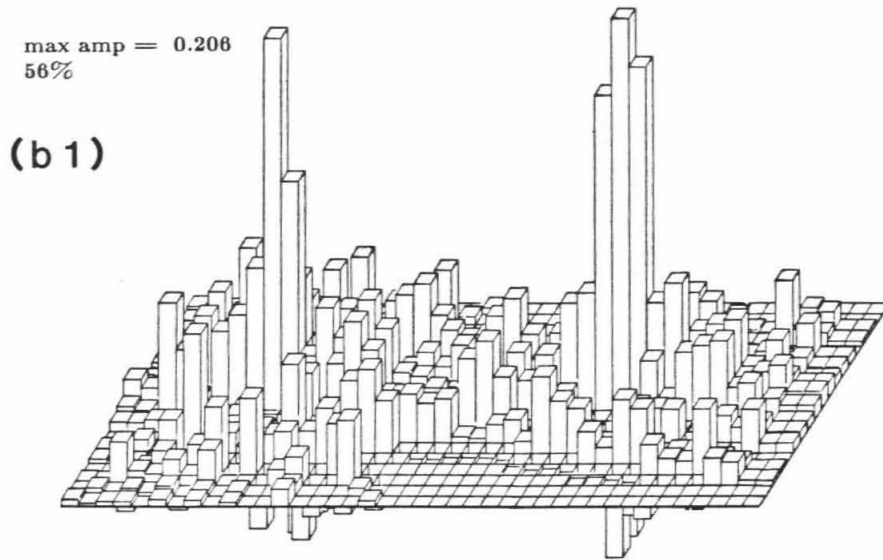


Figure I.7 (continued)

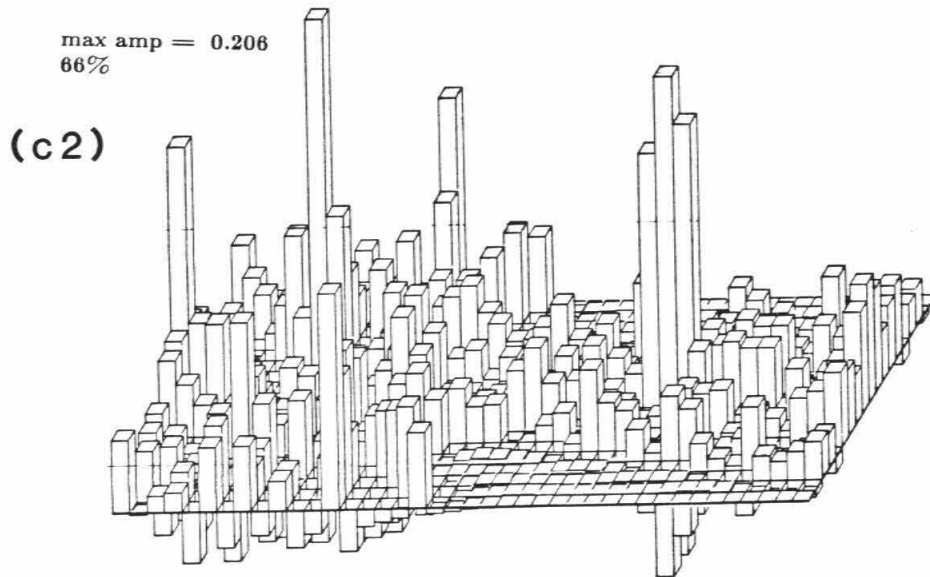
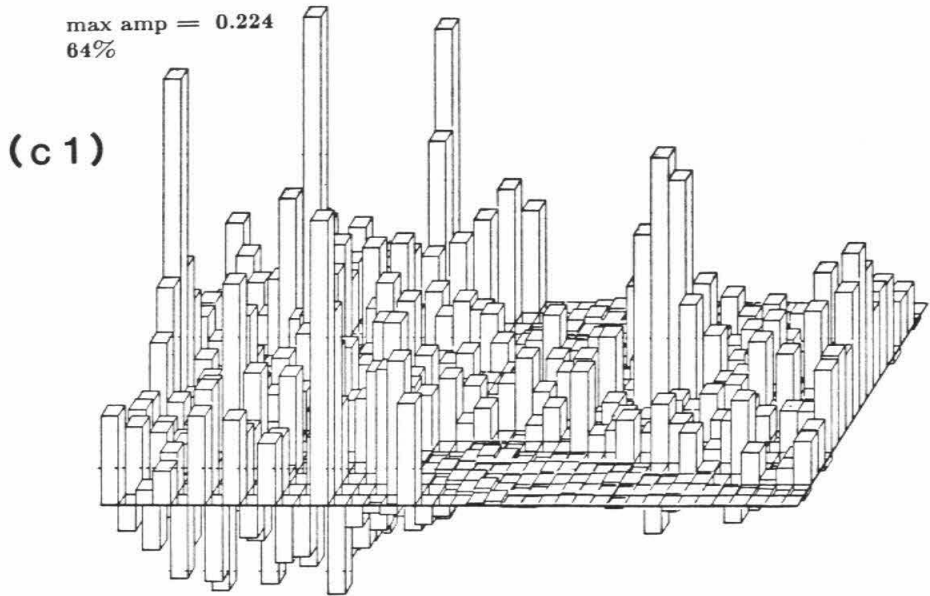


Figure 1.7 (continued)

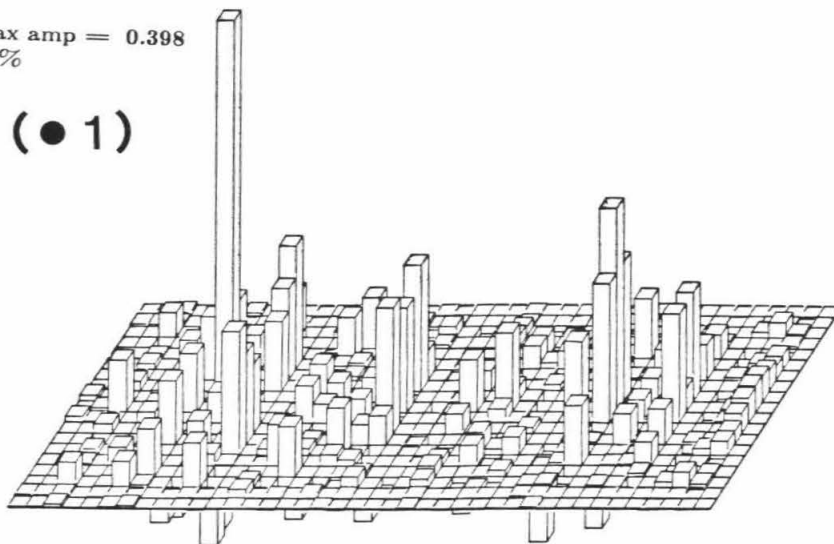
approach to weighting adapts itself fairly well to anisotropy of severity that is spatially variable. This suggests that the choice of a weighting scheme should be made with consideration to the ray geometry one is dealing with.

Next are shown the results of applying iteration. The basic back-projection inverse (Figure I.4) is the zeroth iteration. The second and fifth iterations are shown in Figure I.6. It is seen that with each iteration the reconstruction becomes more focused, but that in those areas where there are few crossing rays the rate of improvement is slow.

Two deblurring schemes are shown in Figure I.7. It is seen that different approaches work better under different conditions. Since iteration can be used in conjunction with any of these deblurring schemes, the most desirable results are those which produce an improved response (i.e., succeed in "deblurring") while producing a minimal amount of artifact. Figure I.7a gives the results of applying the second derivative filter as in equation (I.4), where the second derivative is calculated by using the four nearest-neighbor blocks to the central block. Figure I.7b shows the response when the filter is spatially broader. Extending this filter is done to simulate HD more closely, and in this case includes the 12 nearest-neighbor blocks to the central block. These blocks have been weighted in decreasing amounts as distance increases away from the central block. Figure I.7c has been produced through direct deconvolution. In this case, the distribution chosen for a Green's function was the average of the two spread functions given by the basic back-projection reconstruction for the more homogeneous ray set. This Green's function was then tapered to zero at a distance of 4 blocks away from the central block, and applied in the wavenumber domain through division. To stabilize this process, the ratio was clamped so that it

max amp = 0.398
92%

(● 1)



max amp = 0.521
94%

(● 2)

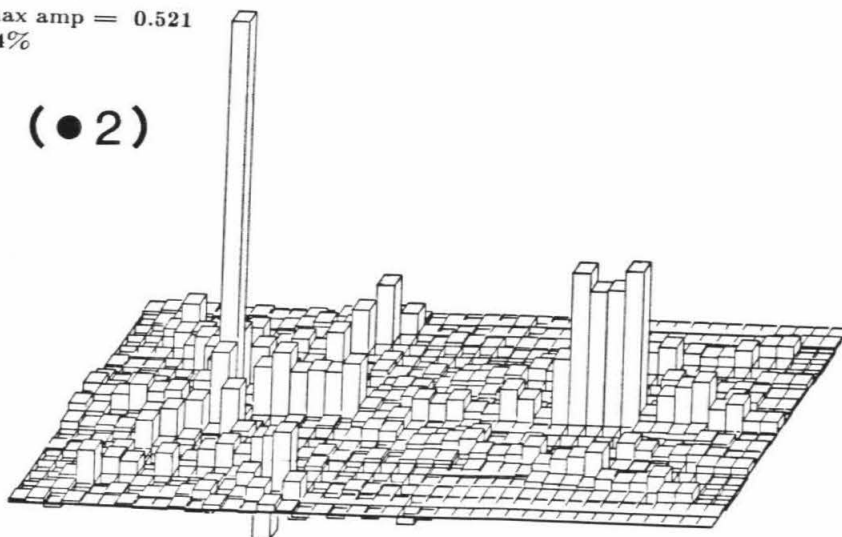


Figure I.8. Examples of the integrated application of techniques. The display format is the same as Figure I.4. Binning has been used for ray weighting, deblurring was applied through space-domain filtering with the broad filter, and five iterations were applied. Other combinations of techniques are also possible.

never dropped below a value equal to the RMS of the reconstruction. This algorithm reconstructs only the intermediate wavenumbers since the high wavenumbers have been ignored through the clamping, and the lower wavenumbers were eliminated when the Green's function was windowed so as to include only its central portion. This procedure was applied only to the more homogeneous ray set (Figure I.2•1). This is because the method depends upon the chosen Green's function being a good representation of the point response throughout the inversion domain, and the method is not expected to work for ray geometries as strongly nonhomogeneous as that shown in Figure I.2•2. In fact, the amount of nonhomogeneity in the ray set shown in Figure I.2•1 is greater than this method performs well with, and the inversions shown in Figure I.7c are rather erratic because of this.

Finally, Figure I.8 shows a reconstruction with the combined use of several of the techniques. Figure I.8a is the reconstruction using ray set from Figure I.2•1, and is produced by using the binning approach to weighting, the broad filter deblurring, and five iterations. This reconstruction is fairly good in light of the strong anisotropic and inhomogeneous character of the ray set. The strongest artificial anomaly, existing near the center of the inversion, is probably due to the combination of a sudden change in vertical ray density in this region and a high number of horizontal rays that have passed through one of the two blocks having a non-zero slowness. Figure I.8b is the reconstruction using ray set from Figure I.2•2, and is produced by using direct ray weighting, the space domain filtering, and five iterations. It is seen that the reconstruction of the right-hand-side block is distributed over four blocks. This is due to the absence of obliquely crossing rays which are necessary to constrain the position of the block successfully.

Other combinations of techniques are, of course, possible.

1.8 Resolution and Error Estimations

To this point, the discussion has not addressed the important topics of resolving ability or the effects of noise in the input data. These are now given some attention. When one has the entire information matrix ($\mathbf{L}^T\mathbf{L}$) available, such as when using the generalized inverse, these can be simply and directly estimated (Wiggins, 1972). Resolution kernels can be constructed that indicate the weighted average used to form each block's slowness estimate, and the model covariance matrix can be used to infer the sensitivity of the inverse to noise. When dealing with a detailed inverse, there is the problem that the information matrix is of very large proportions and is difficult (if not impossible) to store in a computer. Without the availability of $\mathbf{L}^T\mathbf{L}$, the question arises as to how one handles the estimations of resolution and sensitivity to noise.

Resolution is determined, when using the generalized inverse, with the resolution matrix, $\mathbf{R} = \mathbf{L}^T(\mathbf{L}\mathbf{L}^T)^{-1}\mathbf{L}$. It can be shown (Backus and Gilbert, 1968; Wiggins, 1972) that $\mathbf{s} = \mathbf{R} \hat{\mathbf{s}}$, where the j^{th} row of \mathbf{R} gives the weighting coefficients (j^{th} resolution kernel) applied to the "actual" slowness values ($\hat{\mathbf{s}}$) in producing the j^{th} element of the slowness estimate (\mathbf{s}). When using the method of tomography, resolution is addressed in a similar though less direct manner. Instead of examining the weights used in the construction of the j^{th} block, we now examine the contribution to the weights that are produced by the j^{th} block. The reason for doing this is that these are much easier to determine; the weights resulting from the j^{th} block are given by its single-block response (such as are shown in Figures I.3-I.7). If one desired

the actual resolution kernel for the j^{th} block, this could be constructed by summing the contributing weights from all other producing blocks. This is simply a problem of reordering before the summation to get the elements of $\mathbf{L}^T\mathbf{L}$. In practice this is impractical, so we must be content with using the single block response functions as indicators of resolution.

It is noted that when the single block responses are translationally invariant and also possess center symmetry, that the j^{th} response is in fact the j^{th} resolution kernel. When the responses approximately have center symmetry and are stable over the space occupied by the bulk of the j^{th} response, then the j^{th} response is very similar to the j^{th} resolution kernel. These latter conditions on the single block response are approximately true for the ray geometries examined here, and so the observation of the single block responses gives one a direct idea of the resolution kernels.

Covariance of the model parameters (i.e., covariance of the slowness estimates, $cov(\mathbf{s}) = \mathbf{ss}^T$) is commonly used to estimate the effects of noise on the model through the relation $cov(\mathbf{s}) = \sigma^2(\mathbf{L}^T\mathbf{L})^{-1}$ (Jackson, 1972). This relation holds true when all of the estimated variances in the data, σ_i^2 , are independent and equal to some constant variance estimate, σ^2 . Unfortunately, we cannot perform this test since $(\mathbf{L}^T\mathbf{L})^{-1}$ is not at our disposal. To test the sensitivity of the inverse to noise, a direct inversion is run on a Gaussian distribution of time delays which are input as though they were the data, and the output is examined. If some eigenvectors were to be exceptionally excited, this procedure lacks the ability to identify explicitly the responsible eigenvectors or to quantify accurately the degree of sensitivity these

eigenvectors have to noise (i.e., determine the eigenvalues). It is possible, however, to give the variance of the inversion, which is a general statistical description on the effects of the input noise. This procedure, then, can test to determine if the inversion is sufficiently insensitive to noise, but if failings occur it cannot be specific about this, short of an overall statistical description of the failure. Since the noise used for this test is randomly generated, it is possible that the potentially sensitive eigenvectors happen to miss getting excited. For this reason, several sets of random noise are tried, and it is unlikely that any sensitive eigenvectors will pass unexcited.

Figure I.9 shows the results of one such test run for both of the ray geometries discussed. Several noise tests were run, but they all gave statistically similar results. Table 1 gives the ratios of the output standard deviation (of the model) to the input standard deviation (of the times), where the input standard deviation is divided by the average ray length to make the ratio dimensionless (a unit of ray length being the width of a block.). For five iterations the standard deviation of the inversion is about 7% of the standard deviation of the input random time delays (i.e., a variance of .5%). The low values suggest that the inversions should be well-behaved in the presence of noisy data. To show this explicitly, test cases have been run with data created synthetically as before, but now including a component of noise having a standard deviation equal to half the amplitude of the signal produced by the coherent test structure. The results are shown in Figure I.9. Considering that all of the energy in the test structure is contained in only two blocks, the energy of the noise is many times that of the coherent signal. The ability of the procedure to locate the structure in the presence of this high level of noise, attests to the robustness of the inversion.

| it# | RMS | | |
|-------|------|------|------|
| ----- | | | |
| 0 | .029 | .034 | .041 |
| 2 | .053 | .057 | .056 |
| 5 | .067 | .074 | .067 |
| 10 | .078 | .086 | .077 |

Table I.1. Tabulated values showing the tendency of the tomographic inversion to construct a slowness structure from an input signal consisting of only random time delays. Values are $\text{RMS}(\text{inverse})$ normalized by $\text{RMS}(\text{delays})/\langle L \rangle$, where $\langle L \rangle$ is the average ray length. This ratio yields a value of about unity when the structure predicts the delays. Three different sets of randomly generated delay times comprise the three columns of the table. The implication is that random noise in the data has little effect on the reconstruction.

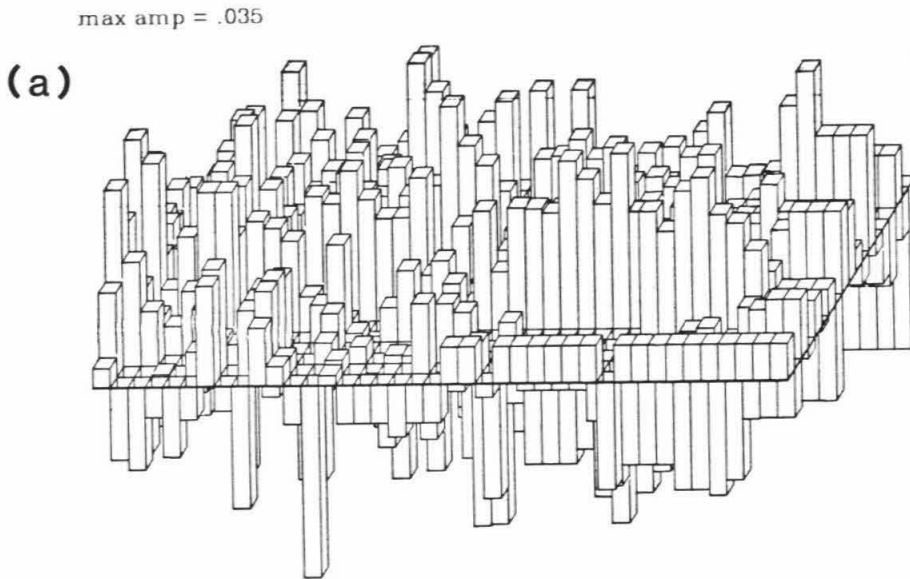


Figure I.9. The response of the inversion method to random noise using the mildly inhomogeneous ray set. Figure I.9a shows the response to random noise, while (b) and (c) show the response to this noise with the structure of Figure I.3 included. The noise has a standard deviation equal to half of the amplitude of the two anomalous blocks from Figure I.3. The lower plot (b) is the basic back-projection inverse, while the upper plot (c) has been processed with five iterations.

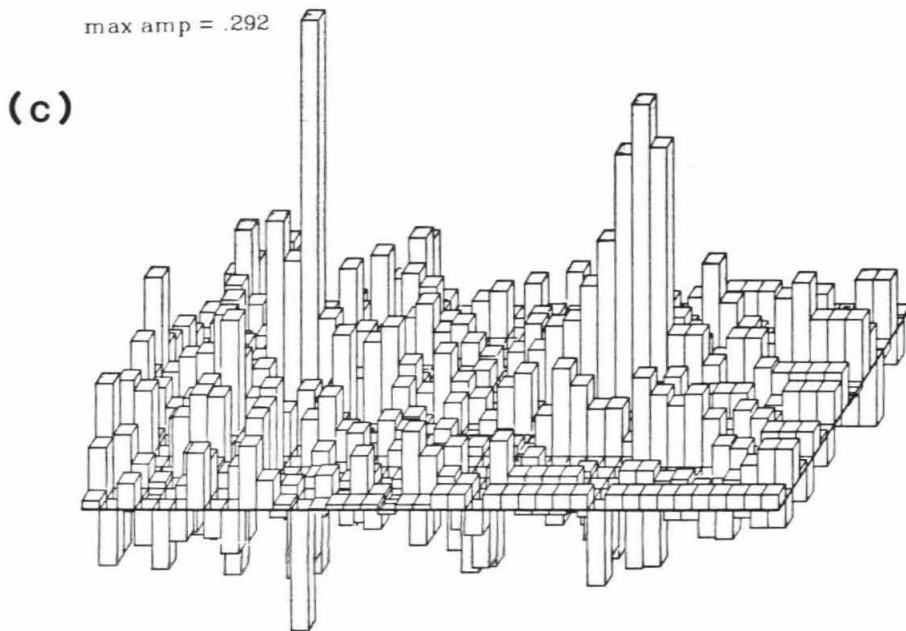
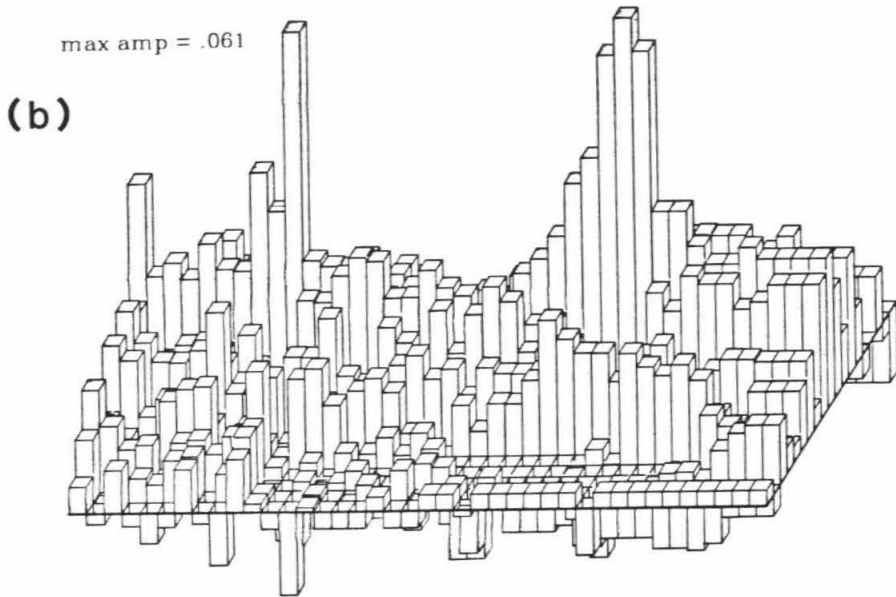


Figure I.9 (continued)

A Tomographic Inversion of Teleseismic P Travel Times for Structure Beneath Southern California

2.1 Introduction

The deployment of the Southern California Array has made possible the investigation of the local upper mantle and crustal structure with the use of teleseismic P arrivals. The first such study was that of Hadley and Kanamori (1977), who discussed the P delay map resulting from PKIKP arrivals originating from an earthquake in Sumatra ($\Delta = 120^\circ$). Rays associated with these arrivals are fairly vertical, and thus indicate the P velocity variations that exist roughly beneath the stations. The most prominent feature observed by Hadley and Kanamori (1977) is an area, coinciding approximately with the Transverse Ranges, that has arrivals about 0.5 - 1.0 second early relative to the other southern California stations. They deduced that this pattern was produced by an anomalous region of subcrustal location because the observed delay pattern extends across the surface trace of the San Andreas Fault. They observed early arrivals occurring on some refraction lines in this region, which they attributed to the top of the anomalous region at a depth of about 40 km.

In a later study, Raikes (1980) looked at teleseismic P arrivals from a variety of regions of differing azimuth. By making use of the systematic way in which the observed P delay pattern shifts with the various earthquake source directions, she was able to invert these data for P structure with depth.

The method chosen was the least-squares block approach of Aki et al. (1977), which was used to invert for structure to a depth of 150 km. Her results indicate that the anomalous fast region beneath the Transverse Ranges extends in depth to at least the bottom of her inversion space. She also determined that the uppermost mantle beneath the Salton Trough is anomalously slow.

More recently, Walck and Minster (1982) have reanalyzed Raikes' data supplemented with data from additional events. They used a method in which the anomalous zone is ascribed to a thin lens located at some depth and allowed this depth to vary while keeping track of the L_2 measure of travel time error. They found that if all wavefront refraction is to be attributed to a single depth, this depth is greater than 100 km, possibly much greater.

Bird and Rosenstock (1984) have proposed a kinematic model in which the lithosphere is converging in the Transverse Range region, and the sub-crustal portion is subducting beneath these ranges. The lower temperature of this material results in an increase of its elastic parameters and hence its seismic velocity. Another possible model is that convective downwelling in the mantle produces the anomalous region by locally depressing the temperature (Humphreys and Hager, 1984). Downwelling could also preferentially align olivine's a axis to the vertical direction. Each of these mechanisms can produce a situation capable of accounting for the entirety of the observed early teleseismic arrivals.

In this study the P delay data are inverted with a relatively high degree of resolution. In light of the interesting tectonic setting of southern California, and the remarkable spatial association of mantle features with major surface

provinces, an integrated understanding of the mantle-crust system is important. To achieve the desired degree of resolution several means have been employed. First, core phases have been added to the data set so that rays with angles more nearly vertical than the direct P arrivals can be used. These rays help constrain the structure, especially that which is deep beneath southern California. Also, a tomographic method of inversion has been used since it allows for a detailed inversion.

The first part of this chapter discusses the data and the reduction procedures that have been applied to bring the data to a set of travel time residuals. This is followed by a description of the details of the tomographic method of inversion needed in this specific application. A more general discussion of tomography is the topic of Chapter I. Included are a few examples of reconstructions performed on artificially created "data" computed from synthetic structures. Finally, the inversion of the actual P delay data is given and discussed. Chapter III deals with the interpretation, modeling, and tectonic significance of the observed features.

2.2 Data Reduction

The raw data consist of P, PKP, and PKIKP arrival times. The direct P wave data are taken from the studies of Raikes (1980) and Walck and Minster (1982), while the core phase information has been gathered for this study. The event map shown in Figure II.1a gives the source distribution. The same information is shown in Figure II.1b, though in this figure each event is displayed in ray parameter-azimuth space. The ray parameter and azimuth of

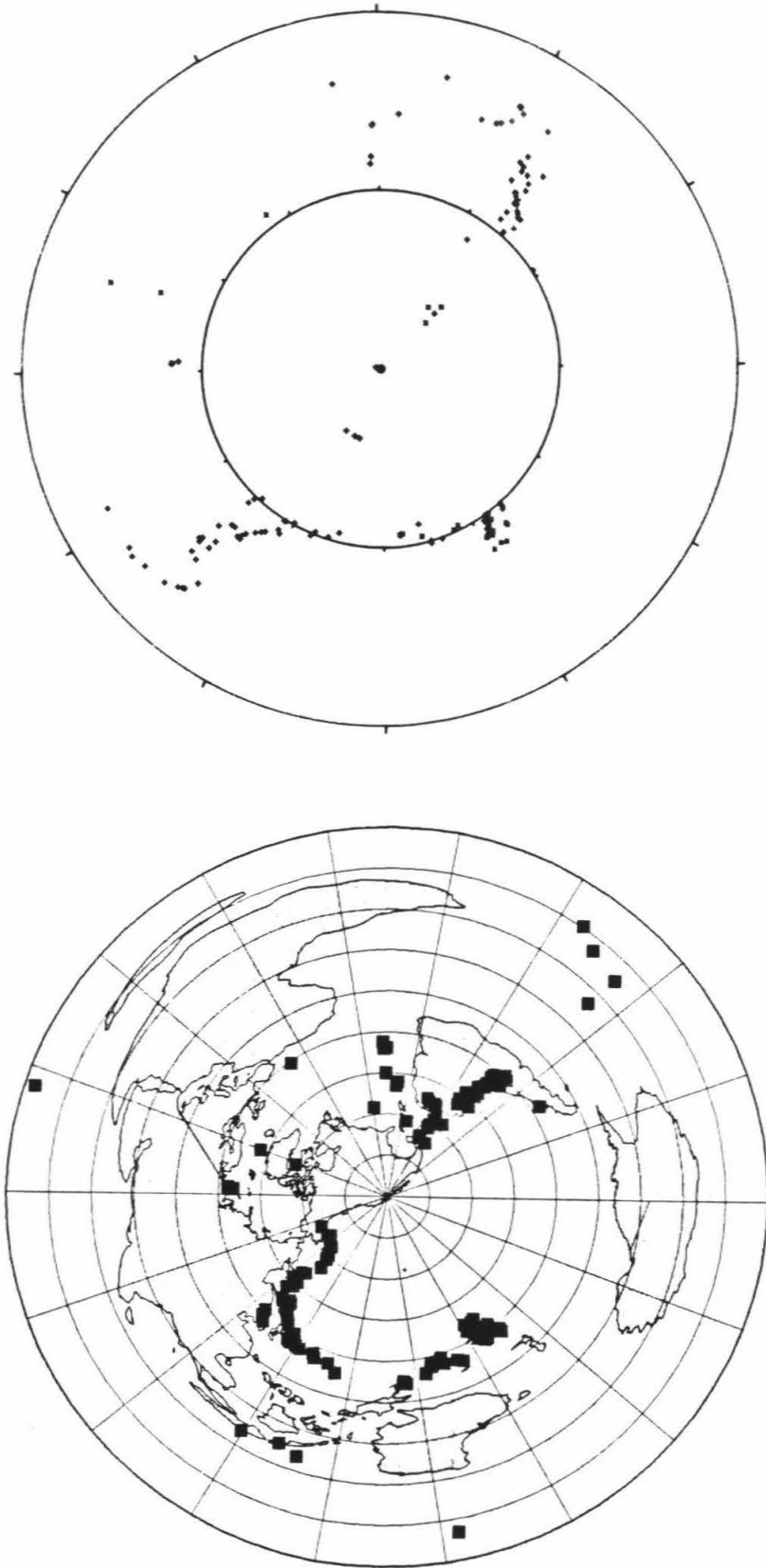


Figure II.1. Locations of the 163 events used in this study. Map (a) gives the geographical locations, while (b) displays the same events in ray parameter-azimuth space. In (b) the inner circle is 5 sec/deg and the outer circle is 10 sec/deg.

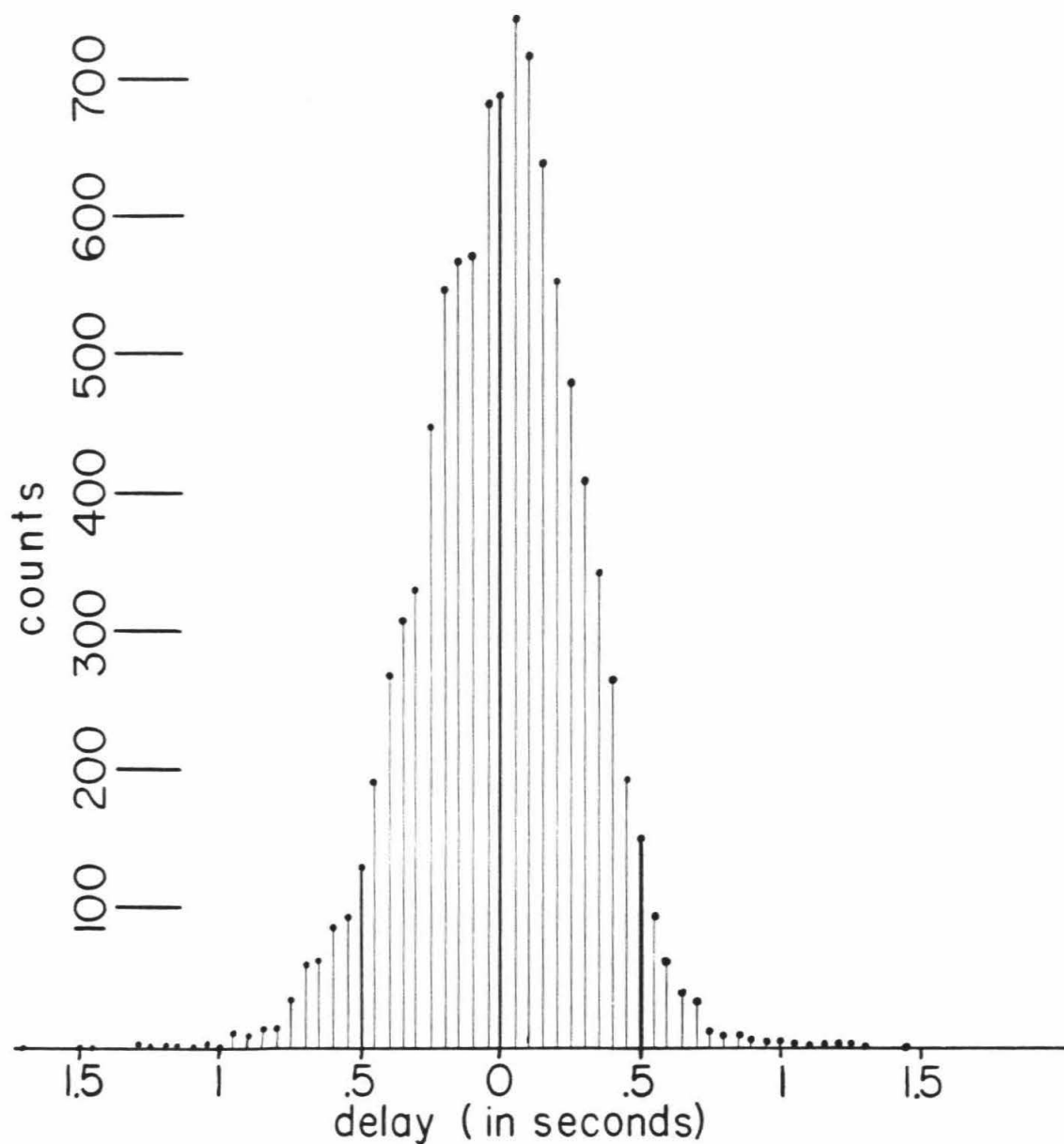


Figure II.2. Histogram of the 9888 travel time residuals used in this study. Each ray has associated with it one residual, and the residuals have been tallied for each $1/20^{th}$ second increment.

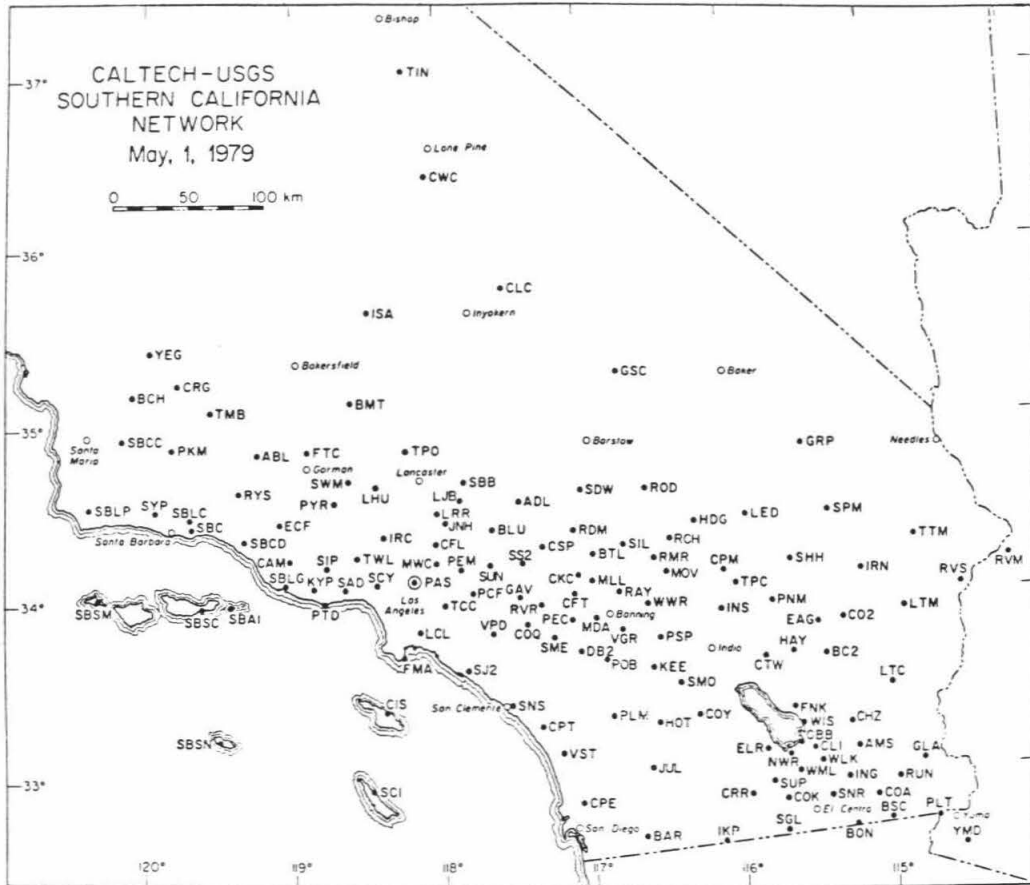


Figure II.3. Map of the seismic station locations for the Southern California Array. This particular figure shows the station distribution for May 1, 1979, which is representative of the distribution during the time interval that data used in this study were recorded .

the observations are determined by using the NEIS locations and the Herrin Tables (Herrin, 1968). The core phases are represented by the symbols with epicentral distances greater than 100° , or with slowness less than 4 sec/deg. The data are seen to cover all quadrants and range in ray parameter from 0-10 sec/deg. The south and northeast directions, however, are much more poorly represented than the northwest and southeast directions. In all, about 160 events recorded by the Southern California Array are used. The number of stations giving usable records for any particular event varies, and the resulting data set consists of nearly 10,000 rays. Figure II.2 is a histogram of the data delay values. Most of the data deviate from the mean by no more than half a second. A station location map is shown in Figure II.3 for the year 1979. There has been some change in station distribution through time, but the coverage shown in Figure II.3 is typical for the times from which the data were recorded. In total, 158 stations were used in this study. Each station recorded an average of 63 events while each event was recorded by an average of 61 stations.

To reduce the data to a set of travel time delays, several standard corrections are applied. These corrections are elevation and sediment corrections (applied in the same manner as Raikes, 1980) and travel time corrections. The travel time corrections include reductions by $dT/d\Delta$ and $d^2T/d\Delta^2$ (from the Herrin Tables). Also, the average delay for each event is removed to reduce the effect of errors in the source parameters. The core phases, PKP and PKIKP, are reduced somewhat differently since reduction by the Herrin Tables consistently underestimates $dT/d\Delta$. Fortunately, a large event ($m_b = 6.1$)

occurred near the antipode to southern California ($\Delta \approx 175^\circ$). The Herrin corrections, small for this event, were applied to produce a reference delay map. It was then a straightforward matter to adjust $dT/d\Delta$ for each of the other events in order to best match the reference P delay map in a least-squares sense. Since the antipodal travel time residuals indicate the delay accumulated directly beneath each observation site, and also because this event was exceptionally well recorded, this P delay map has been chosen as an example P wave map (Figure II.4). For comparison, the P delay map resulting from an event of similar magnitude ($m_b = 5.9$) that occurred in Korea ($\Delta = 70^\circ$) is also shown. Arrivals from this event are from the WNW, and the general pattern is seen to shift towards the ESE.

In addition to the standard reductions, a correction for variable crustal thickness has been applied. The individual station corrections are calculated from the station P_n time-terms of Hearn (1984a). These time terms may be due to variations in either crustal velocity or in Moho depth, but since the time term method is especially sensitive to variations in the Moho depth, this was assumed to be the cause. Corrections are determined by calculating a travel time slab correction with a slab thickness given by the deviation of the Moho from its average depth, as inferred from Hearn's time terms (1984a), and by using an assumed velocity contrast across the Moho of 1.2 km/sec. The travel time effect on the P delays resulting from varying crustal thickness is less than that produced by varying crustal velocity, and so this is the more conservative of the two approaches. The corrections made in this way are in the range ± 0.37 sec, with an average deviation of ± 0.06 sec.

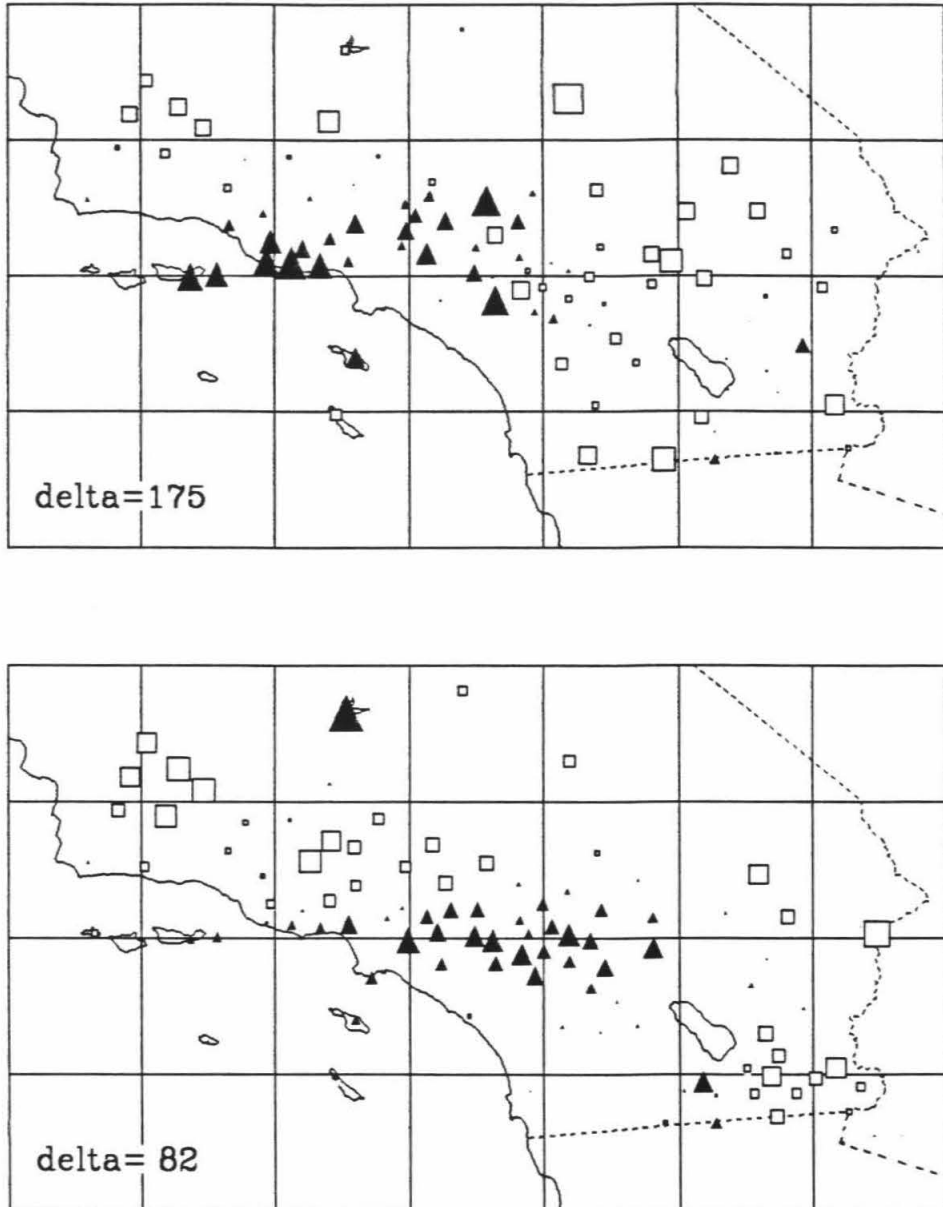


Figure II.4. Maps of travel time residuals for two events. The solid triangles represent early arrivals, and the open squares represent late arrivals. The size of the symbol is proportional to the value of the delay. The upper map is the result of a nearly antipodal event and thus shows the integrated delay directly beneath each station, while the lower map is for an event in Korea ($\Delta = 82^\circ$, to the WNW) and the delay pattern is shifted to the ESE.

2.3 Method of Inversion

The method of tomography was chosen to invert the data. The major advantage offered with this approach is the ability to handle a detailed inversion. The theory and methodology are the subjects of Chapter I, and only a few introductory comments will be given here. The statement of the problem is identical to that most commonly used in the generalized inverse problem (see, for example, Aki et al. (1977) for a discussion that is particularly relevant to the geometry of teleseismic arrivals). This involves dividing the region in which one is interested into a number of discrete blocks, and the slowness perturbations to these blocks that best produce the observations are sought.

The geometry of the near normal incidence of teleseismic rays result in a few special properties that can be taken advantage of, either for the purpose of gaining insight or to simplify the calculational formulas. An important observation can easily be made that the average slowness perturbation of each layer is the same. (Since the average delay has been removed from each events set of travel times, this value is zero.) There is no ability, therefore, to resolve the average vertical structure. This is simply a statement that all rays traverse the entire inversion domain thickness and therefore lack the ability to resolve the average vertical structure, or equivalently, that the eigenvectors of the information matrix ($\mathbf{L}^T\mathbf{L}$, Chapter I) do not span this dimension and are independent of changes in it.

Two approximations which simplify the computations have been implemented. Since all rays are fairly vertical, it is without significant loss of accuracy that one may assign the ray to one and only one block per layer. If the

ray happens to penetrate more than one block, only the block with the longest ray segment is used, and it is assumed that the ray traverses the entire layer within that single block. This greatly simplifies the geometrical considerations that have to be made. Once ray segments are associated with an entire block, all ray lengths within any block are approximately equal and equation I.1 can be simplified to $s_b = \sum_r d_r / \sum_r l_{rb}$ without perceptible alteration of the inverse. Comparison of the inverse constructed using this formulation with that produced with the use of I.1 (where in both instances the one block per layer approximation has been used) gives a difference in the most deviant blocks between the two inverses of less than 1%, and most blocks are unaltered to within the four significant places kept in the data files.

2.4 Details of the Specific Inversion Algorithm Used

The general principles of the various methods are discussed in Chapter I. The specific algorithm chosen here to invert the data includes block sub-binning, wavenumber domain deconvolution, and iteration, all used in conjunction with the basic back-projection method. Other combinations of technique are also possible, and some of these have been tried, yielding inverses very similar to those presented below.

Iteration

Iteration has been applied by taking the difference between the observed and the predicted delays and back-projecting these. Chapter I discusses the details of the method. The reconstructions shown below have been produced with five iterations. One could quite naturally incorporate a ray tracing

procedure such that the ray trajectories are recalculated between iterations. This has not been done. In this chapter all rays have been traced through the simple structure shown in Figure II.5. Some justification for use of this constant structure is that travel time variations are second-order on the ray path, and hence mislocating a ray slightly will not have a serious effect on the delay. However, the ability to properly locate and reconstruct a velocity anomaly is dependent directly upon the ability to locate the ray's positions, and this can be quite sensitive to the velocity structure. Partly for this reason the image resolution is expected to fall off somewhat away from the earth's surface (where the stations are located and the ray's positions are known). The mantle velocity variations are only of a few percent, however, and the problems associated with mantle heterogeneity are not expected to be of too much consequence.

Block sub-binning

The teleseismic ray set used in this study includes only rays that are more vertical than 45° from normal incidence. (If ever a ray is more horizontal than this it is excluded from the data set.) The result is a tendency to blur the image more strongly in the the vertical direction, and horizontal structure will therefore be the more difficult to resolve. To partly compensate for this problem a scheme has been employed that reduces the weights of those rays which traverse the structure in the directions most commonly taken. The procedure for accomplishing this is to divide the rays that hit any particular block into subsets according to ray parameter and azimuth (as indicated by the template in Figure II.6a). These individual slowness estimations are then averaged in

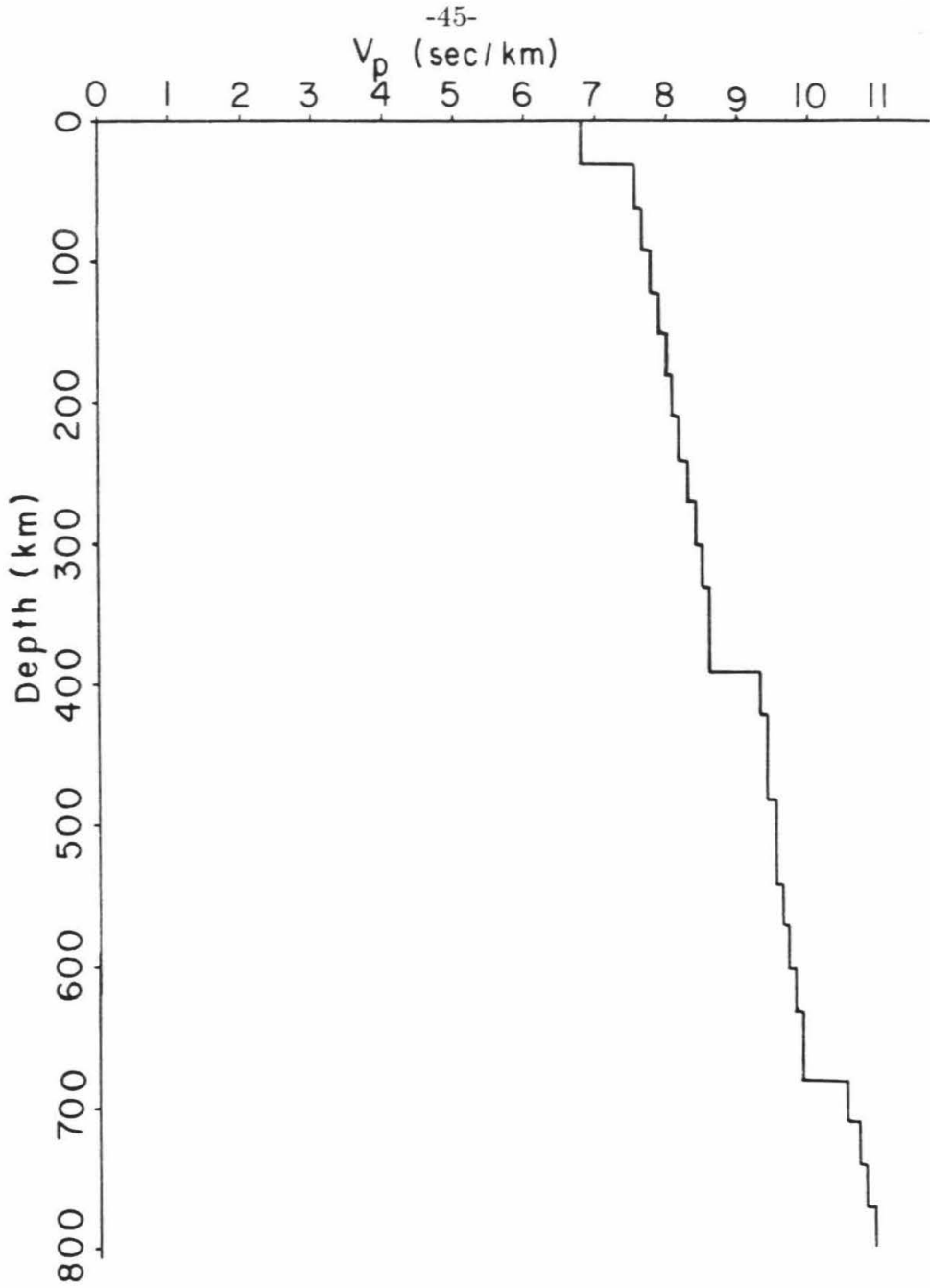


Figure II.5. One-dimensional P-velocity structure used to guide ray paths. This structure is a discretized representation of the structure determined for the Gulf of California by Walck (1984). This structure is used only in determining the ray paths, and because the ray paths are fairly vertical the exact structure is not critical.

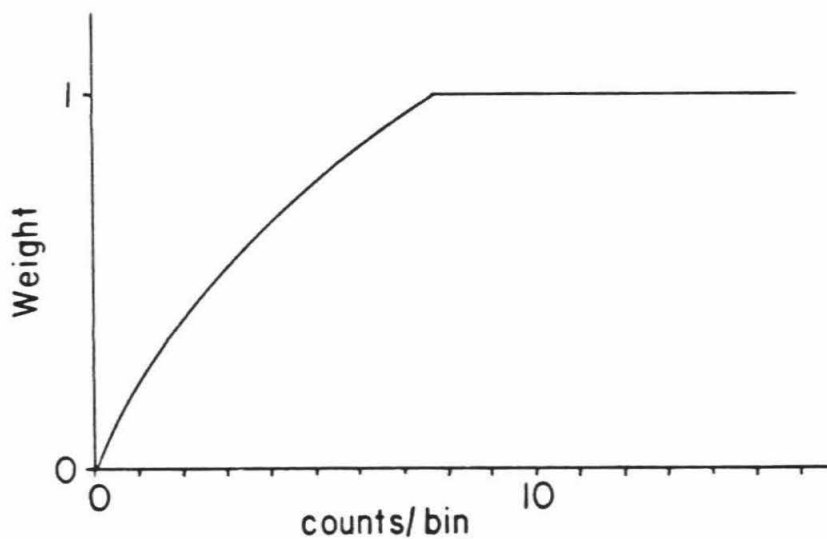
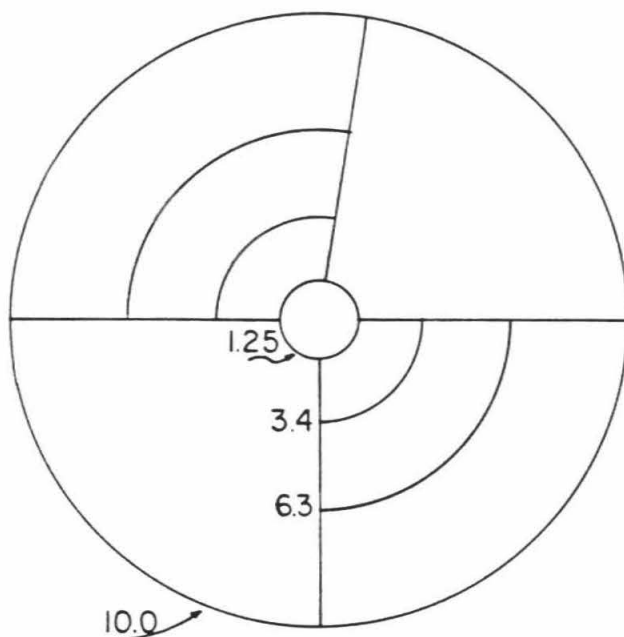


Figure II.6. Figures showing the details of the binning scheme. The nine bins are shown in (a) in ray parameter-azimuth space. North is to the top and the numbers are in units of seconds/degree. Part (b) shows the weight given each bin (as a function of hit count) prior to averaging to obtain a whole slowness estimate. For more discussion refer to the text.

order to obtain a whole-block slowness estimation. The average is performed by weighting each subset by the function shown in Figure II.6b. This function has the effect of somewhat increasing the weight of those subsets which are more frequently hit. Notice however, that this weight decreases the importance of individual rays that fall within the often hit subsets. With the block size used (15 km square in map view and 30 km deep) the number of hits per bin range in value from zero to over a hundred, with a median value for bins actually hit of three.

These weights have also been used to describe in a simple manner the quality of overall ray coverage experienced by a block. When trying to describe simply the quality of sampling, a problem exists because both the number of rays hitting a block and their distribution in azimuth and in ray parameter are important. The method we have chosen to display ray coverage quality is to show the average subset weight just discussed. This is a number that increases with hit count, but also increases with the diversity in ray coverage. The value of this number is zero if the block is not hit, and cannot exceed, for a well-hit block, a value of unity. Plots of the hit quality are shown in Figure II.7. These plots will be important to refer to later when the various inverses, of both synthetic and actual data are presented. The coverage estimator is seen to decrease towards the margin of the inversion domain in general, and below the Pacific Ocean in particular. Also, the quality of sampling is seen to decrease with depth. This property is related fundamentally to the width of the seismic array, since at depths roughly comparable to the array width angular coverage begins to rapidly diminish.

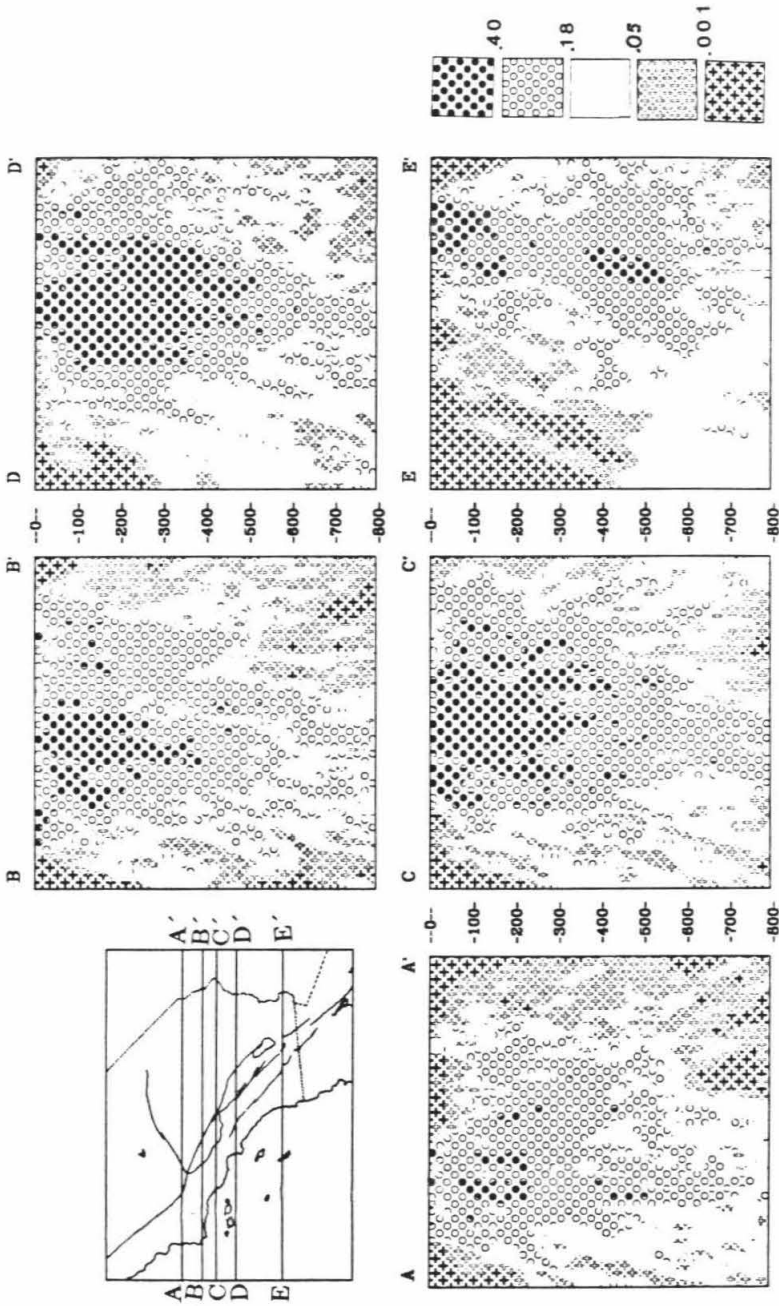


Figure II.7. Displays of the hit quality factor discussed in the text. This is a measure of the variety and number of hits a block experiences, and is determined by tracing rays back from the stations shown in Figure II.3 through the structure shown in Figure II.5 according to the ray information given in Figure II.1. An ideally hit block will have the maximal hit quality factor of one, while an unhit block will receive a value of zero. Practically speaking, a hit quality factor of over 0.18 seems to indicate sufficient ray coverage to resolve most structure.

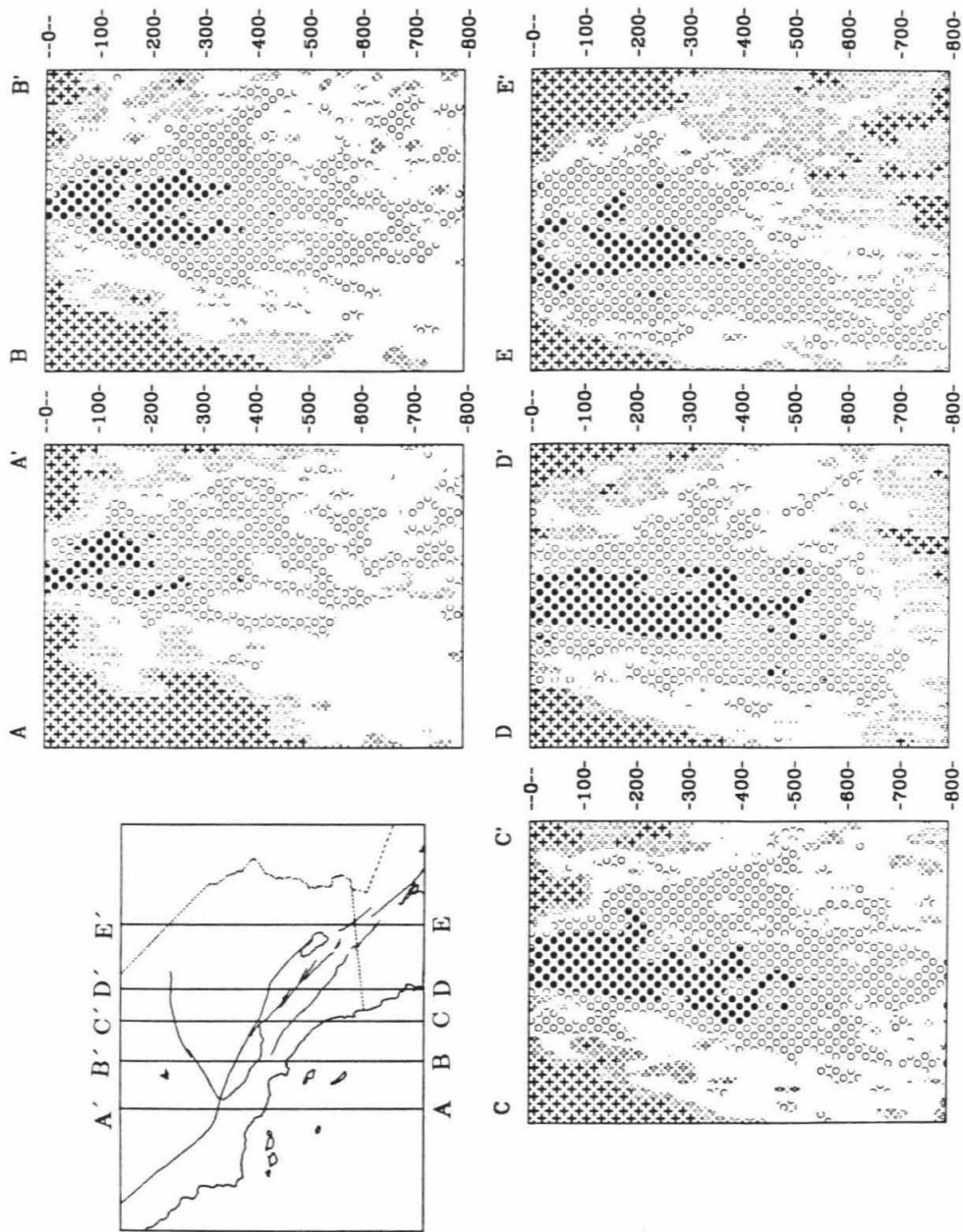
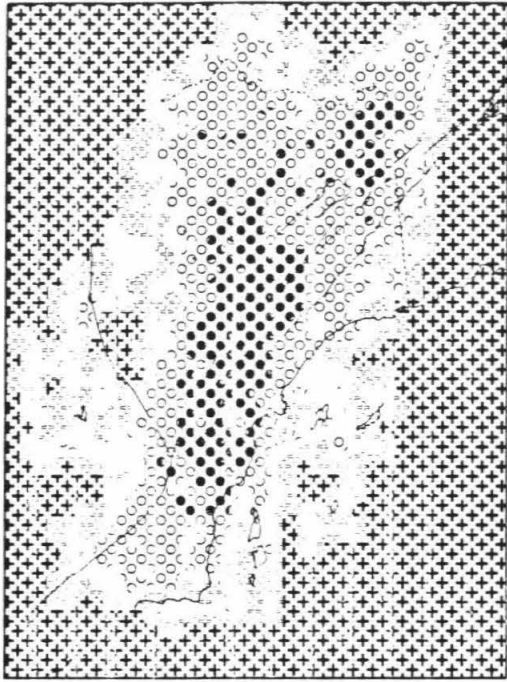
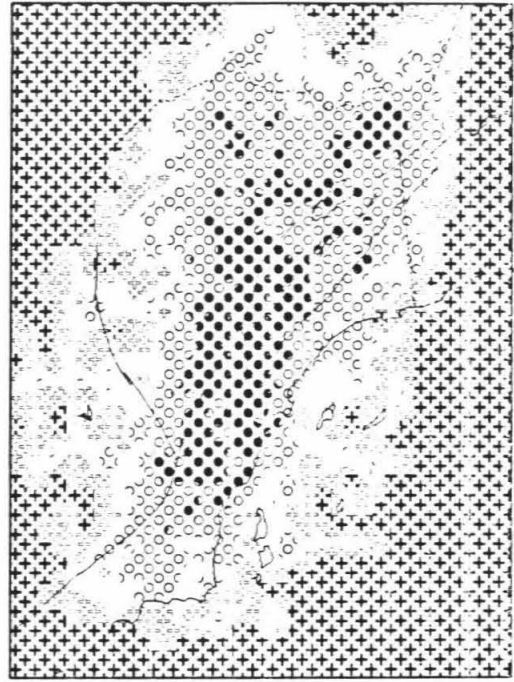


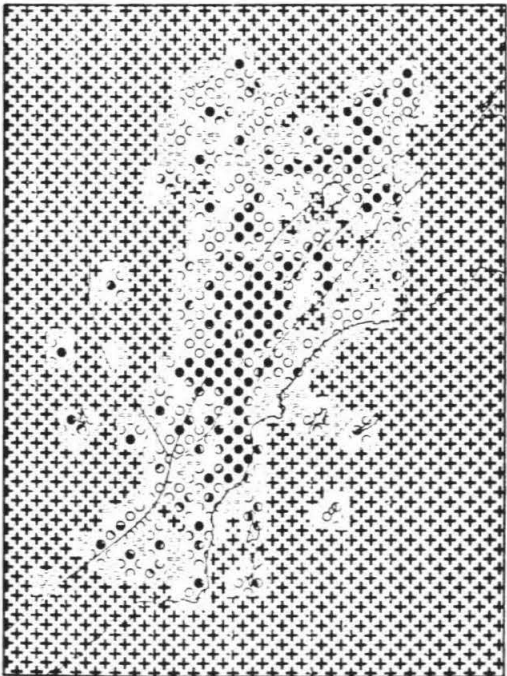
Figure II.7 (continued)



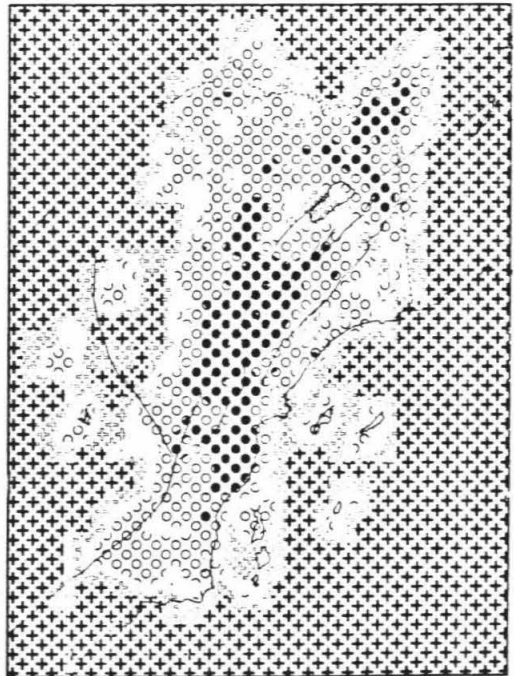
60-90 km



90-120 km

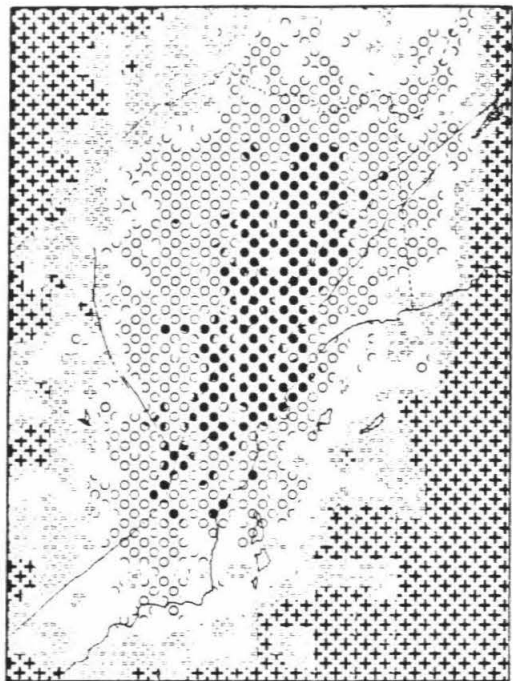


0-30 km

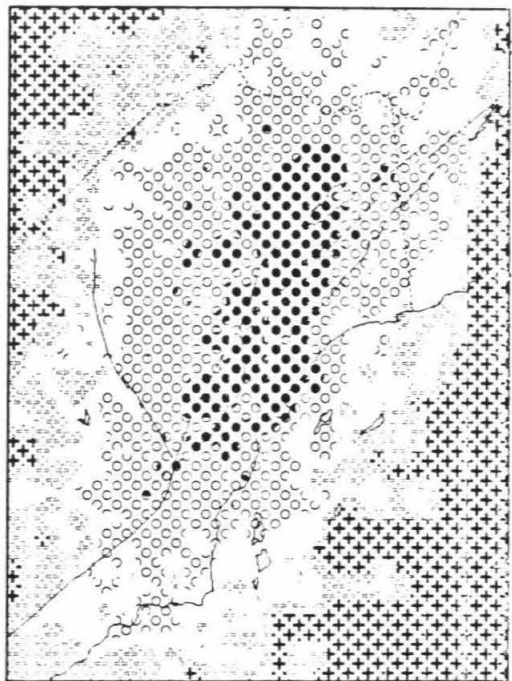


30-60 km

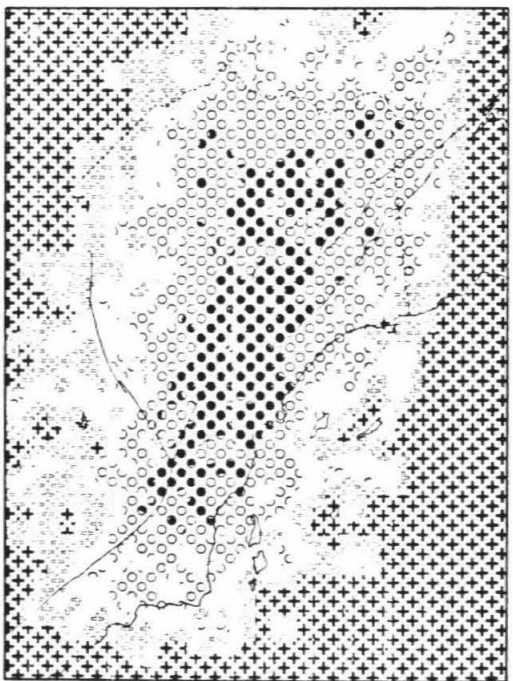
Figure II.7 (continued)



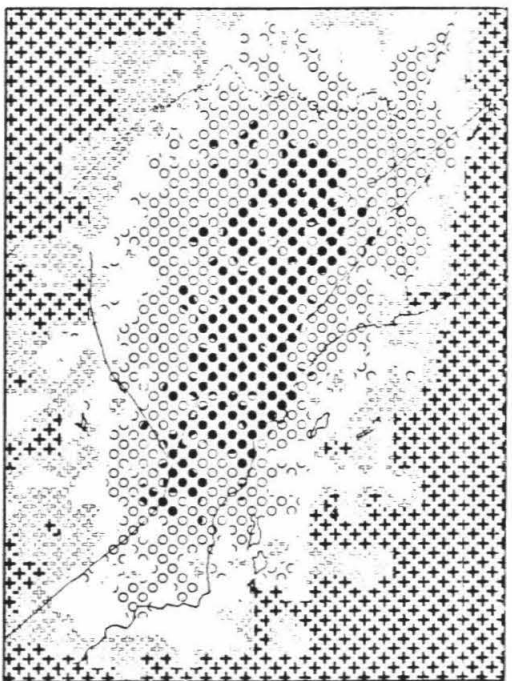
180-210 km



210-240 km



120-150 km



150-180 km

Figure II.7 (continued)

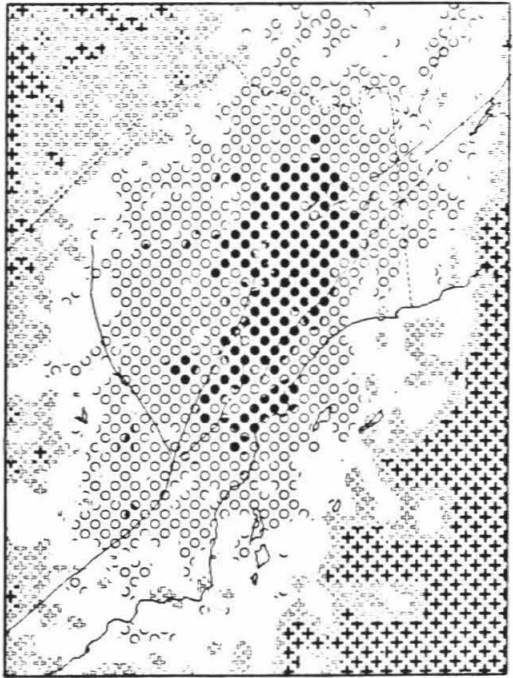
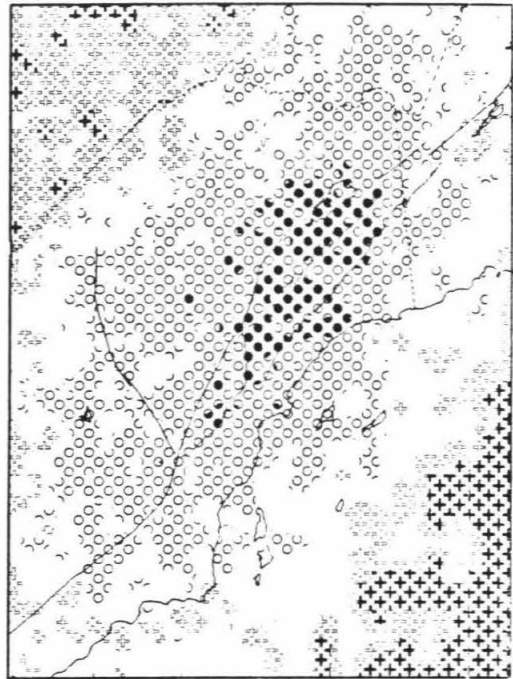


Figure II.7 (continued)

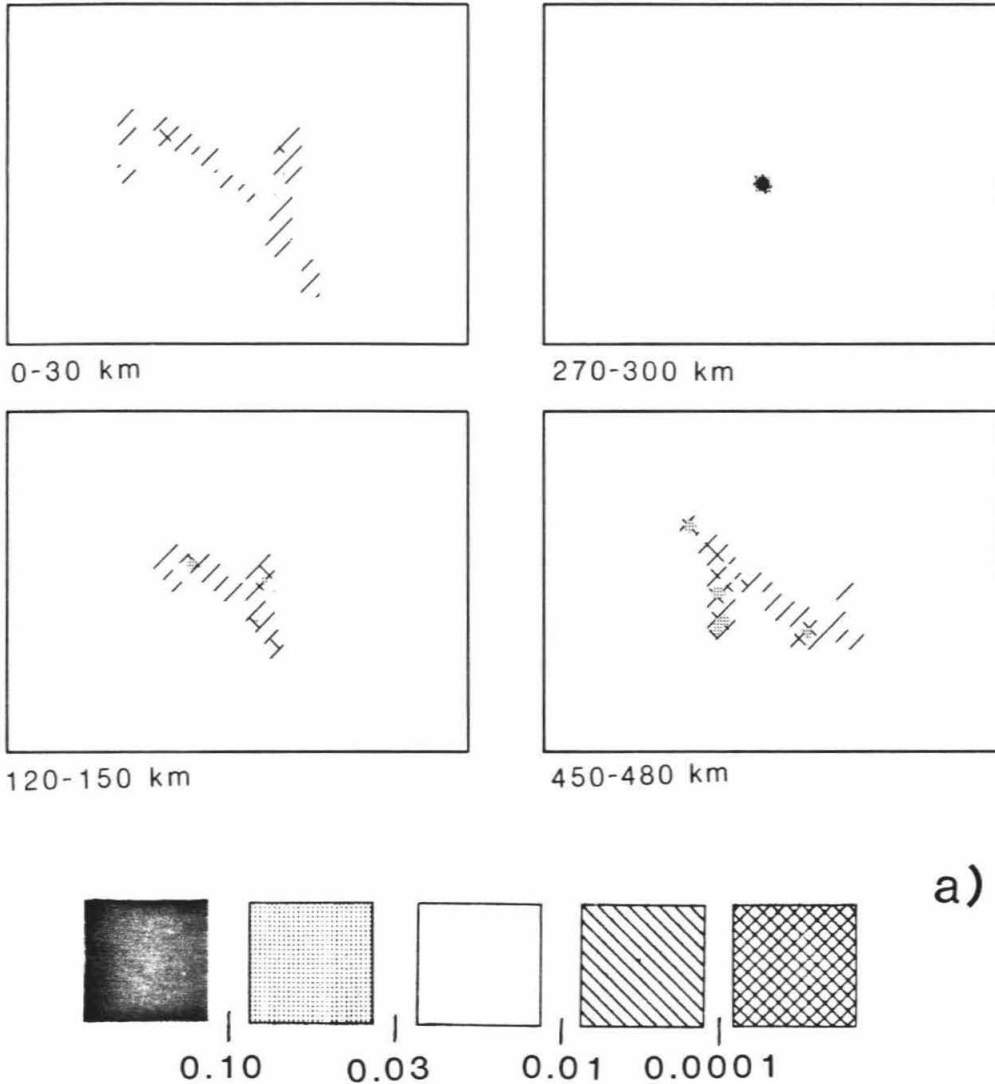


Figure II.8. An average reconstruction of an anomalous block of unit magnitude to a single back projection. A delay set has been constructed by projecting the actual ray set through the assumed structure, and nine individual responses have been determined and averaged. In (a) the reconstruction is formed by straight back projection, while in (b) the binning described in the text has been applied. Notice the improved ability to attenuate the prominent streaks with the use of binning. The response shown in panel (b) has been windowed and used as the point response in the deconvolution step. Another point to be made is that, because the single block response is similar to that block's averaging kernel, the response can be used to estimate the resolution capabilities of the back projection.

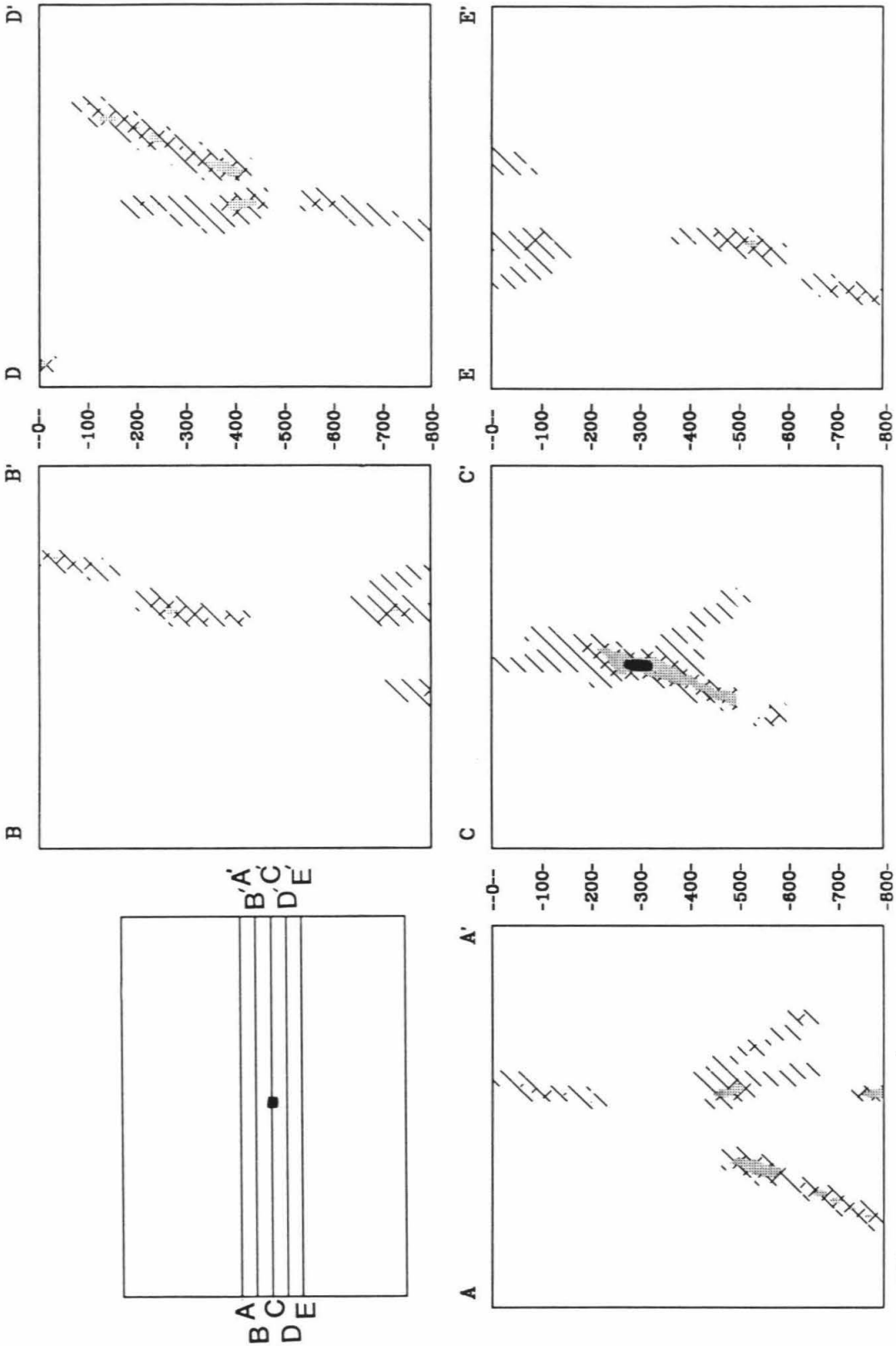


Figure II.8a (continued)

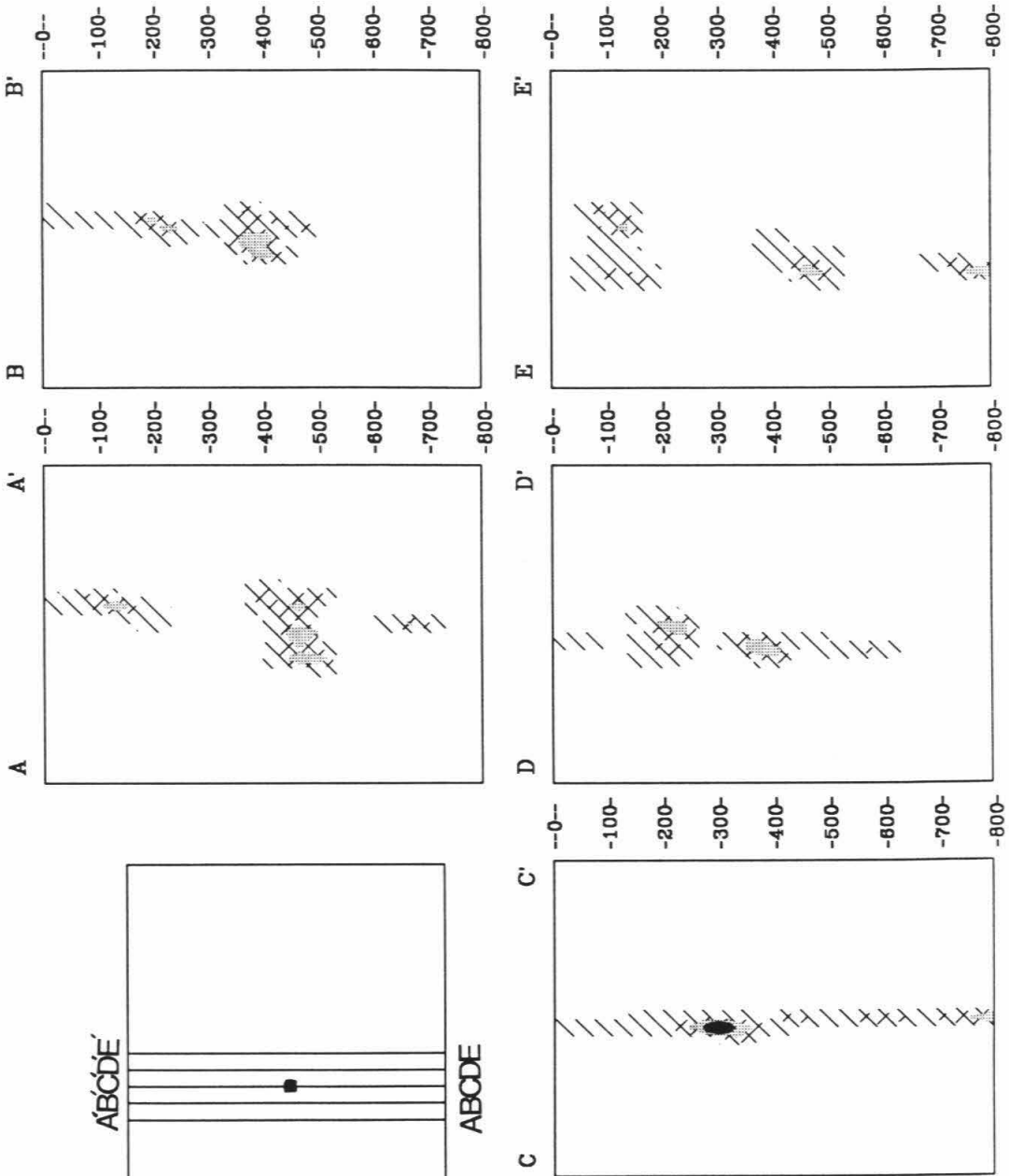
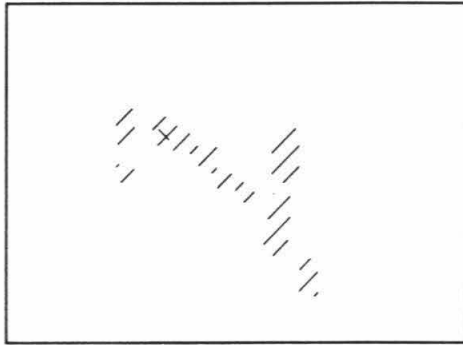
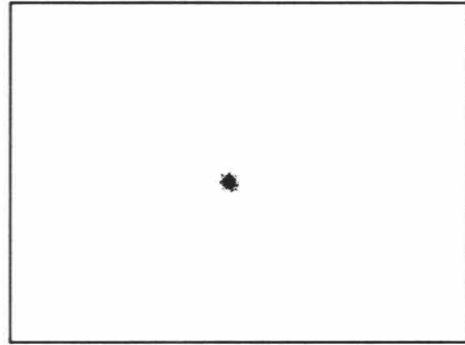


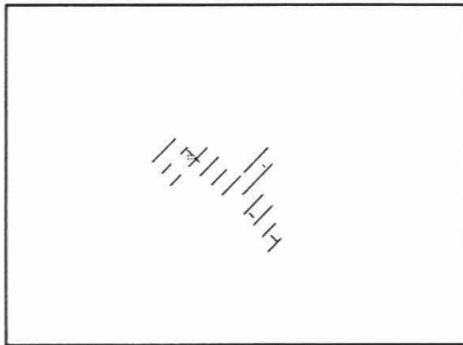
Figure II.8a (continued)



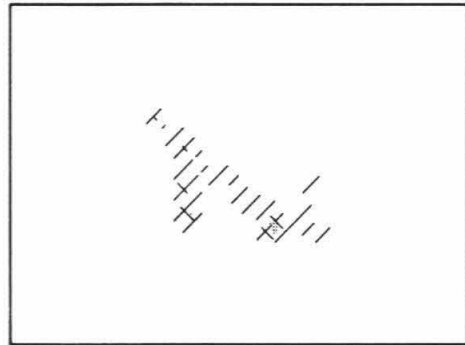
0-30 km



270-300 km



120-150 km



450-480 km

Figure II.8b

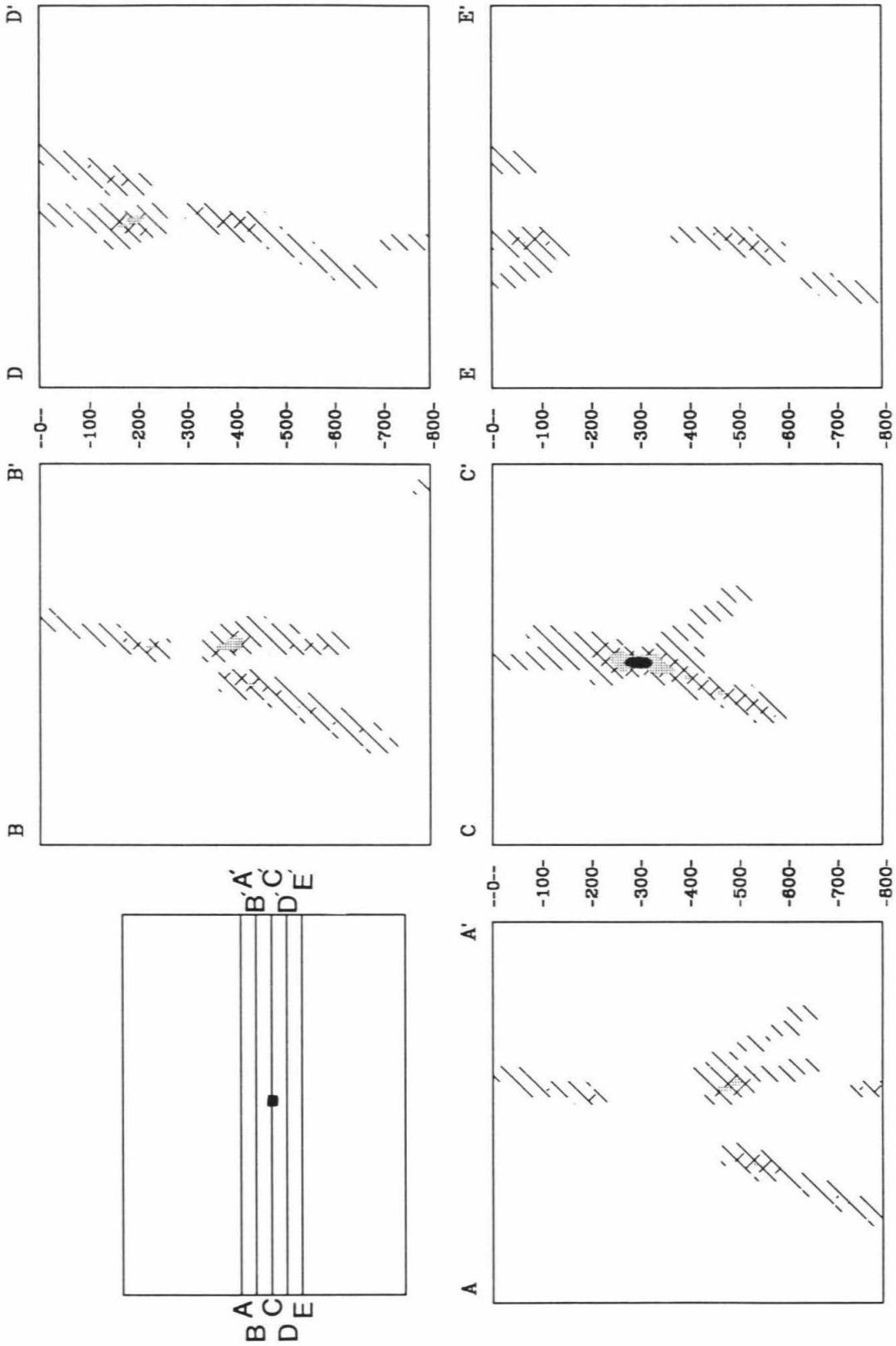


Figure II.8b (continued)

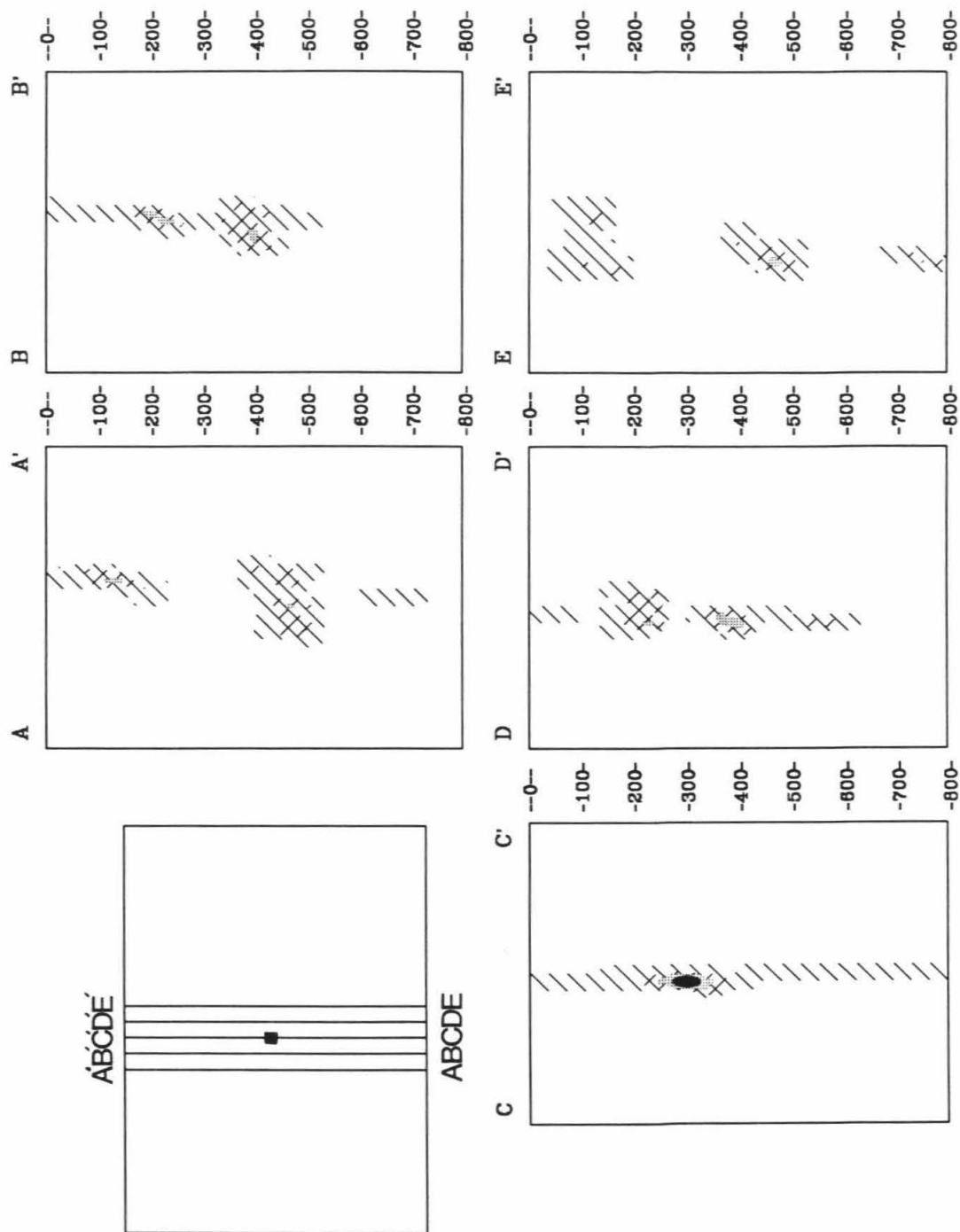


Figure II.8b (continued)

Deconvolution

Deconvolution is accomplished in the wavenumber domain through division with an empirically determined point spread function (Green's function). In practice, two steps have been taken to insure stability. First, the spread function has been windowed so as to include only 7 blocks in the vertical direction, 9 blocks in the two horizontal directions. To keep windowing from producing ringing problems the window boundaries have been tapered. Windowing effectively removes the longest wavelength components from the Green's function. The second step is to clamp the wavenumber domain representation of the spread function so that it never falls below some specified level, which in effect eliminates the the high wavenumber components from the deconvolution. This level has been chosen to be the RMS value of the response function.

When the ray set is not homogeneous, the response functions produced from differing locations are themselves different. To minimize this problem, the spread function used in deconvolution is constructed by taking the average of nine point spread functions sampled from regularly spaced locations within the inversion domain. Such averaging is justified if the response function does not vary much within the windowed region, and in fact it does not. The primary purpose of the windowing is to remove the distal portion of the spread function since this is its least constrained portion. The average response function, prior to windowing, is shown in Figure II.8. The resulting pattern is a map of the ray paths hitting the anomalous block. This is easily seen, for instance, by comparing Figure II.1b with the lower right panel of Figure II.8a

(map view). Figure II.8a shows the spread function produced without the use of binning, while Figure II.8b has binning included. Notice the degree of success binning has in attenuating the strong streaks.

Space Averaging

One final step is included, which is the application of a moving average window after each iteration. The inversion space is spanned by 51 blocks in the E-W direction, 37 blocks in the N-S direction, and 25 blocks in depth, where each block is 15 km on a side in the horizontal directions and 30 km deep. In most parts of the inversion space the ray coverage is not adequate to warrant the use of blocks this small. The averaging window is therefore designed to vary in size in inverse proportion to the hit quality estimator (Figure II.7). Well hit blocks (hit quality factor greater than 0.40) are averaged only with that block's four nearest horizontal neighbors, with the sum of these blocks given a weight equal to that of the central block. Blocks of intermediate hit quality factor (factor between 0.18 and 0.40) are further averaged with the eight next nearest horizontally located blocks, the sum of which is also given a weight equal to the central block. For poorly hit blocks (hit quality factor between 0.05 and 0.18) the eight next nearest horizontally located blocks are also included, again with an amount of weight equal to the central block. If a block is more poorly hit than hit quality factor 0.05, no inverse is determined for that block. In all cases, the averaging also takes into account the hit quality factor of each participating block by weighting that block in proportion to its particular hit quality factor. The use of such an average does not distort the inverse. In fact, with the weighting scheme used, for each

iteration the combination of several smaller blocks into a few larger blocks gives the same result as would be obtained if the inversion were run originally with the larger blocks. This point is well illustrated by comparing the inversion just discussed with that discussed in Humphreys et al, (1984), where the individual block volume is about 8 times as large. Both this and the more detailed inversion are shown below.

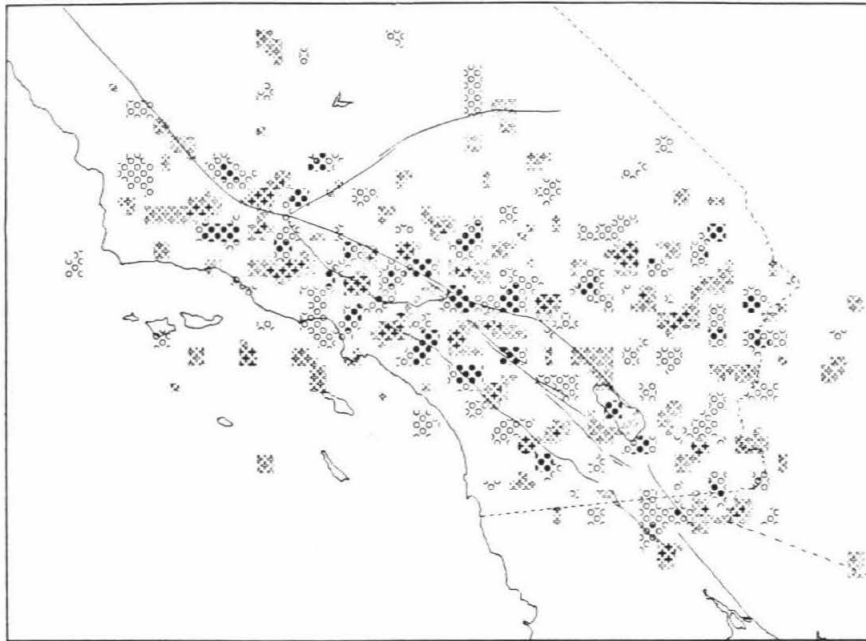
2.5 Estimations of Resolution and Error

Resolution of the inverse is estimated by examining the point spread functions. As discussed in Chapter I, when the single block responses approximately have center symmetry and are stable over the space occupied by the bulk of a particular response, then the j^{th} response is similar to the j^{th} resolution kernel. These conditions are met for the response to teleseismic rays recorded with a fairly uniform station distribution, such as is the case for the Southern California Array. Direct observation of the spread functions (e.g., Figure II.8b) can therefore be used with the southern California ray set to get an estimate of the resolution kernels.

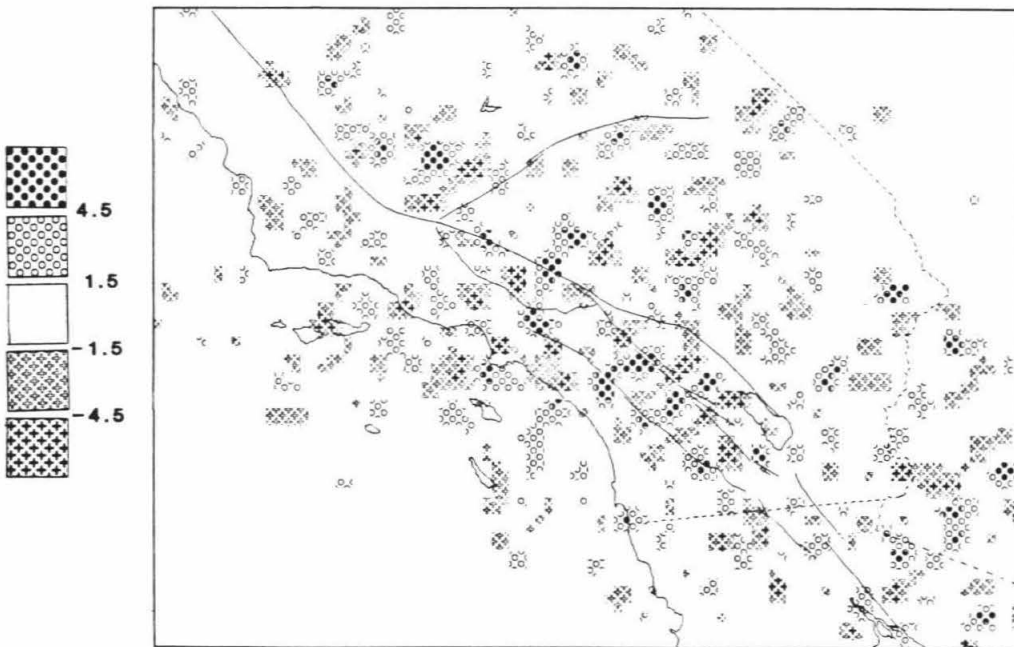
Covariance of the model parameters (i.e., covariance of the slowness estimates) is commonly used to estimate the effects of noise on the model through the relation $cov(\mathbf{s}) = \mathbf{ss}^T = \sigma^2(\mathbf{L}^T\mathbf{L})^{-1}$, which holds when all of the estimated variances in the data, σ_i^2 , are independent and equal to some constant variance estimate σ^2 . Such is expected for the southern California data. With these data, the error estimated for the picked arrival times is believed to be very small because the ability to pick the arrival times is good, usually within

± 0.05 sec. Larger sources of error are produced by approximating the structure as a spatially confined array of constant velocity blocks. Because different rays sample along different paths, travel time residuals will differ even between two rays that sample the same set of blocks. This is because the delays are influenced by structure that is of a smaller scale than the block size. Also, significant amounts of differential delay may be experienced by two rays prior to their entry into the region being imaged. It is difficult to estimate the error in the travel times due to these sources *a priori*, but the set of errors is expected to be random and each ray is as likely to be affected as any other.

Unfortunately, $(\mathbf{L}^T\mathbf{L})^{-1}$ is not at our disposal and we cannot estimate the effects of "noise" with \mathbf{ss}^T . We must therefore use a different approach. To test the sensitivity of the inverse on noise, a direct inversion is run on a random distribution of time delays which are input as though they were data, and the output is examined. A Gaussian distribution is used for the input function, though values greater than three standard deviations from the mean have not been included so that very anomalous delay values are not admitted. This simulates the actual data set, which has no delay values more than two seconds from the mean (Figure II.2). The RMS of the delays produced by this inversion are only 2.2% of the input signal. As discussed in Chapter I, the procedure used here lacks the ability to explicitly identify the eigenvectors responsible for particular instabilities. It is possible, however, to use the variance of the inversion to quantify the sensitivity of the inverse as a whole to noise. For the southern California ray geometry, the results of inverting noise are shown in Figure II.9. The inversion is produced in exactly the same way



90-120 km



300-330 km

Figure II.9. The inversion on random noise travel time residuals. The procedure includes binning, deconvolution, and five iterations. Values are in per mill of RMS of the inputted noise divided by the block height.

that the inverses for the synthetic and actual data set are constructed. It will be seen later that coherent structure is reconstructed with a degree of success that depends upon the geometry of the problem, but that at least 90% of the signal is accounted for. This attests to the robustness of the inversion even in the presence of significant amounts of noise. When it is remembered that the expected level of noise is small in the real data, it is safe to assert that noise-related artifacts in the inversion are not a major concern.

2.6 Application of Tomographic Algorithm to Test Structures

The most direct means of testing the resolving ability of the tomographic method with the ray geometry at hand is to use this ray set on synthetic test structures to produce a set of travel time delays, and to perform an inversion on these delays. This approach gives one the means of carefully testing the ability to resolve arbitrarily structure. It does not, however, indicate rather or not some other structure may produce the same or similar response. Another problem is that the testing routine is poor in simulating the inversion of the real data because it lacks the precise knowledge of the actual ray trajectories, while in the synthetic situation the ray positions are the same for both the forward and the inverse cases. As discussed earlier, ray position is sensitive to structure, but because the variations in structure are thought to be of only a few percent, it is not felt that this structure will strongly influence the ability to determine which blocks are crossed by any particular ray.

Several test structures are shown here as examples of the ability to reconstruct different forms of structure located in various regions. Other specific

structures will be introduced later when the need warrants. Both the ray set and the method of inversion employed on the test structures are the same as those used in the inversion of the real data.

SingleBlock

The first test case is the reconstruction of a single anomalous block. This is shown in Figure II.10, and should be compared to the point responses under basic back-projection, Figure II.8. The reconstruction of this simple structure is very good. This case, however, is a particularly easy one. Notice that the amount of artificial anomaly is very small, even in blocks neighboring the anomalous block, and that only the proper block has a large amount of signal. The amplitude of the reconstructed block is 66% of the amplitude of the actual anomalous block.

Cube

A much more difficult and illustrative example is the reconstruction of an anomalous cube possessing a non-anomalous interior (Figure II.11). This structure has thin slabs oriented both vertically and horizontally, and a large, non-anomalous region that is sampled only with rays that have elsewhere also sampled anomalous material. The results clearly show the capabilities and difficulties this ray geometry presents. The horizontal structures are poorly resolved. The top is diffuse and spread over several layers, and the bottom is focused even more poorly than this. This is in contrast to the good reconstruction of the vertical walls, where the amplitude attains 80% of the original value.

Horizontal Slab at Various Depths

The specific ability to detect and resolve thin horizontal structure at an arbitrary depth is tested by inverting for an anomalous horizontal slab located in the 10th and in the 17th layer of blocks. The results shown in Figure II.12 clearly indicate that this structure is difficult to constrain vertically, and that this ability decreases as the depth to the producing anomaly increases.

Surficial Check Pattern

Finally, the ability to reconstruct detail in the uppermost layer of blocks is addressed by inverting the synthetically produced delays resulting from a pattern of alternating blocks within the uppermost layer. This pattern is well reproduced by the inversion throughout the portion of southern California that is reasonably sampled (Figure II.13). Resolution is very good in both the vertical and horizontal directions, suggesting that the inversion is capable of reconstructing meaningful crustal features in areas where the ray coverage is adequate. This figure also illustrates well that in regions which are poorly sampled, the inversion does not reconstruct the anomaly to a level comparable to the reconstruction produced in heavily sampled regions.

2.7 Results

The results of the application of the tomographic method on the actual travel time delays are shown in Figure II.14. The most prominent feature seen in the inversion is the anomaly below the Transverse Ranges, which is seen to be curtain-like and trending E-W. It is located directly under the Transverse Ranges and is wedge-shaped, deepest to the east where it extends to about 250

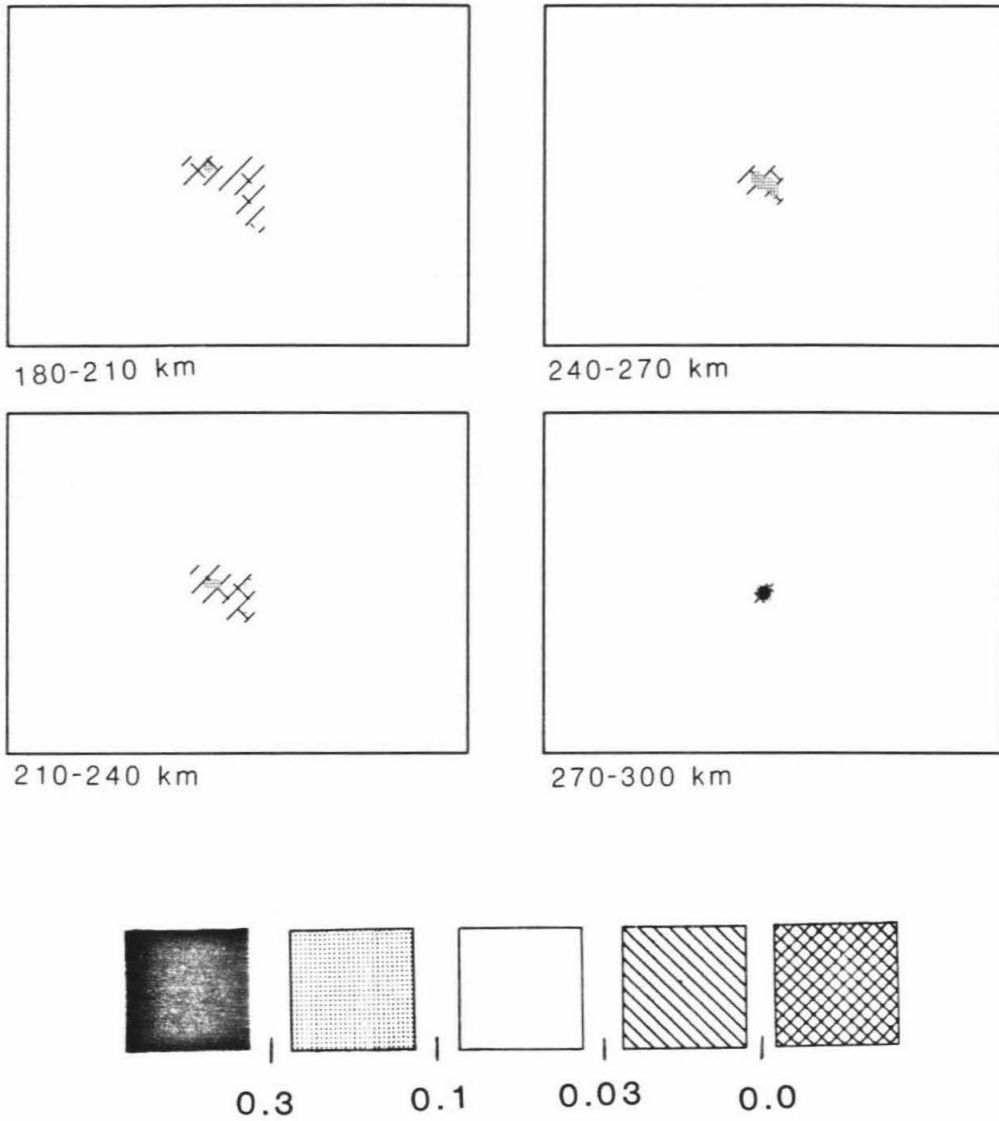


Figure II.10. The reconstruction of a single anomalous block of unit magnitude with the use of binning, deconvolution, and five iterations. The lowest horizon is through the anomalous block, and the other three horizons are those immediately above the the block.

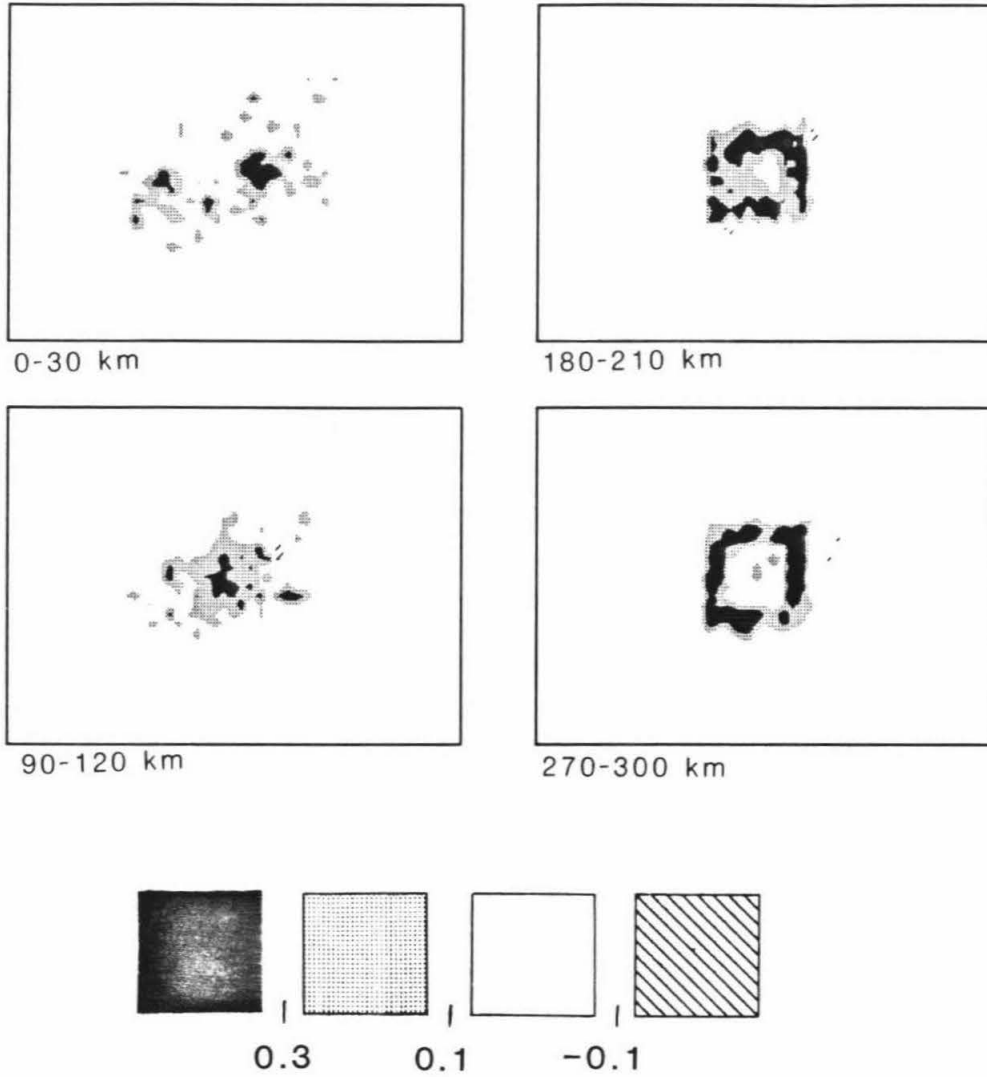


Figure II.11. The reconstruction of a cube of anomalous material that has a normal interior. Magnitude of anomaly is unity. The procedure includes binning, deconvolution, and five iterations. The four walls have been well reconstructed, but the top is very spread out in space and the bottom is nearly absent. This is a result of having only rays that traverse the structure in a near-vertical direction, making horizontal structure difficult to resolve.

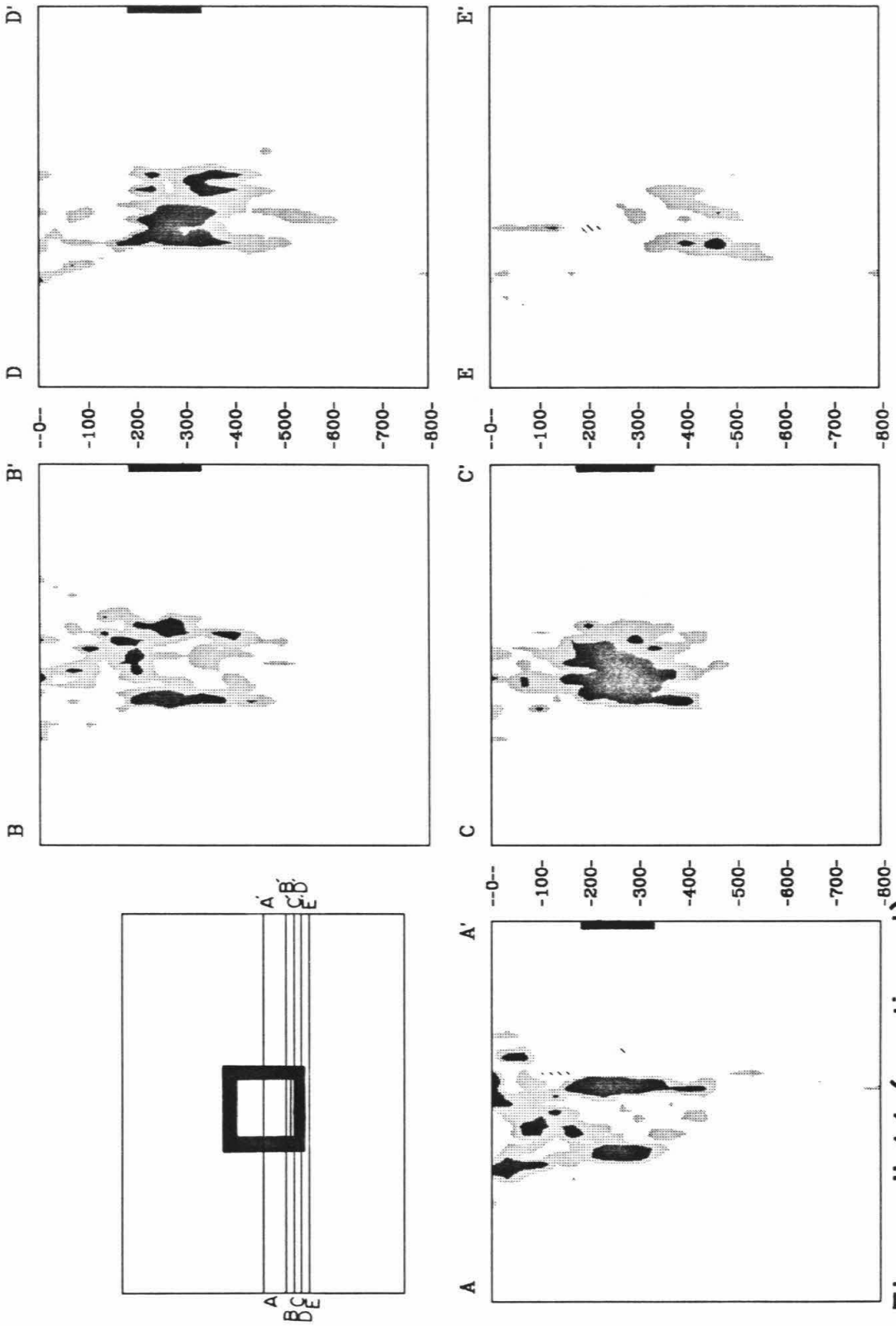


Figure II.11 (continued)

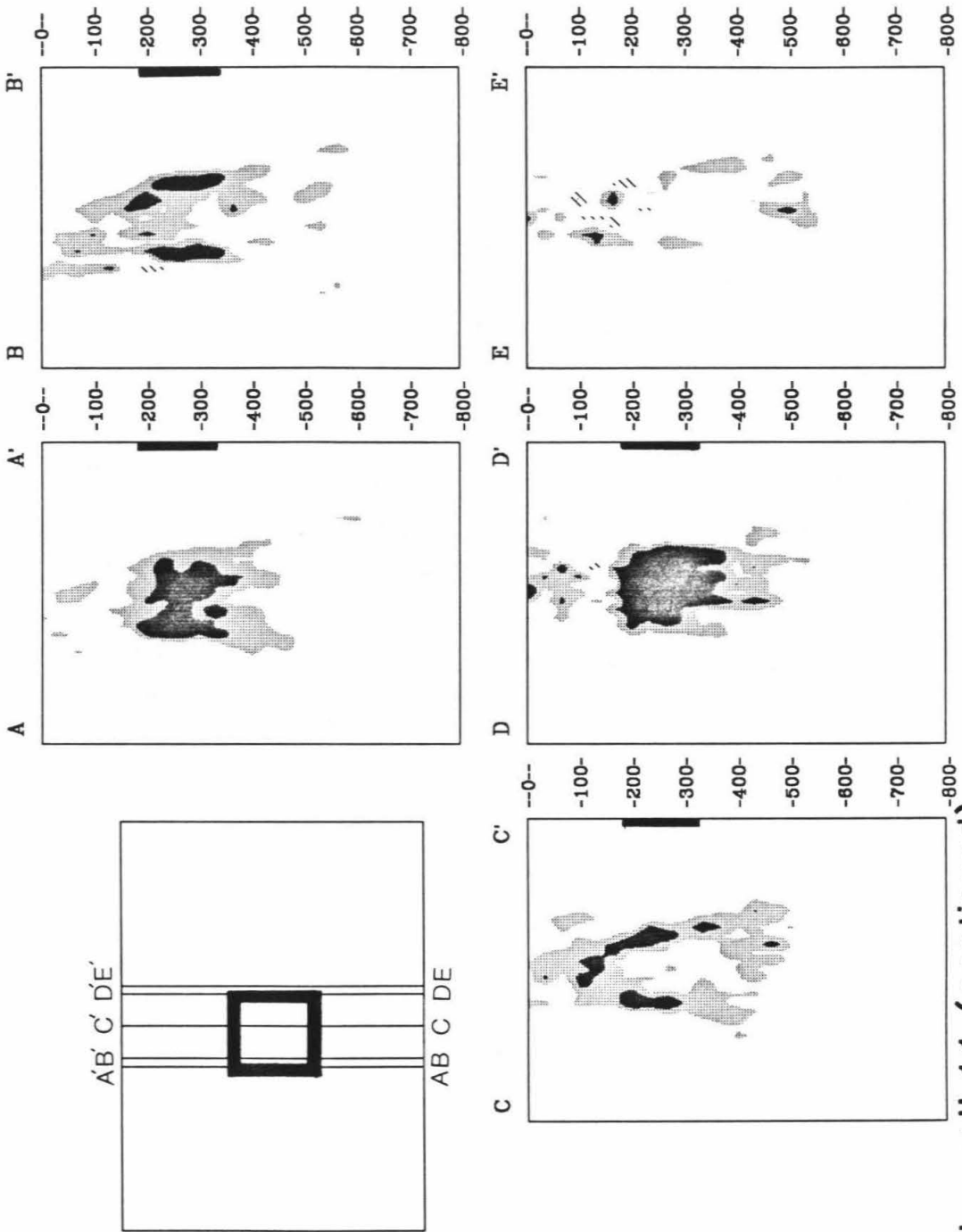


Figure II.11 (continued)

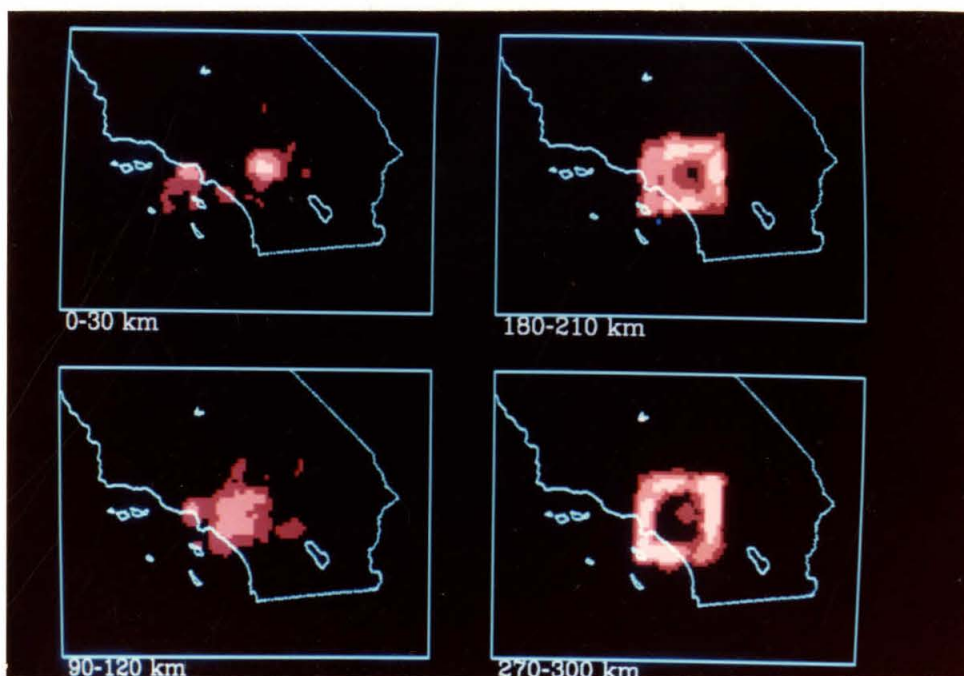


Figure II.11 (continued)

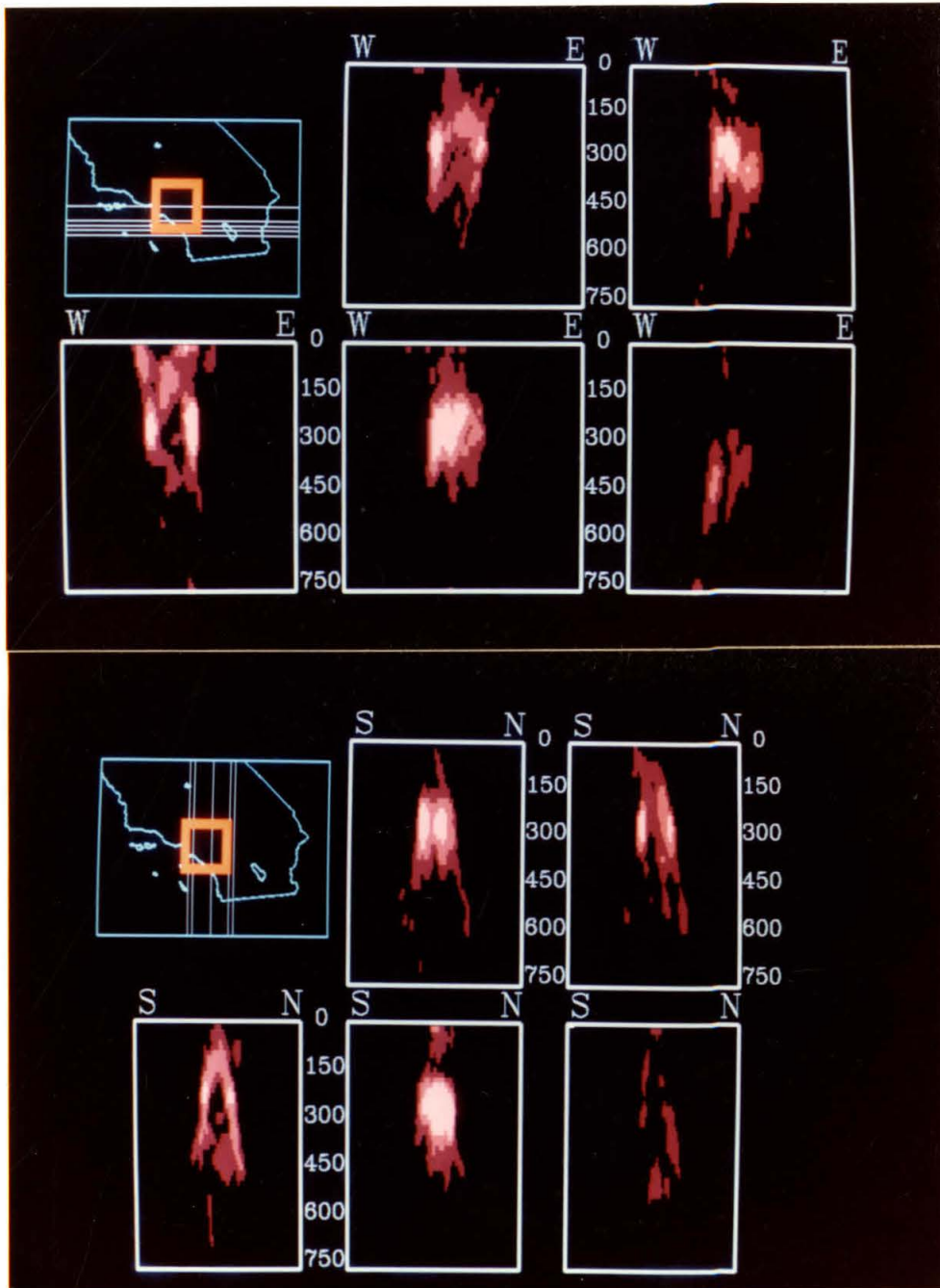


Figure II.11 (continued)

anomaly at 270-300 km

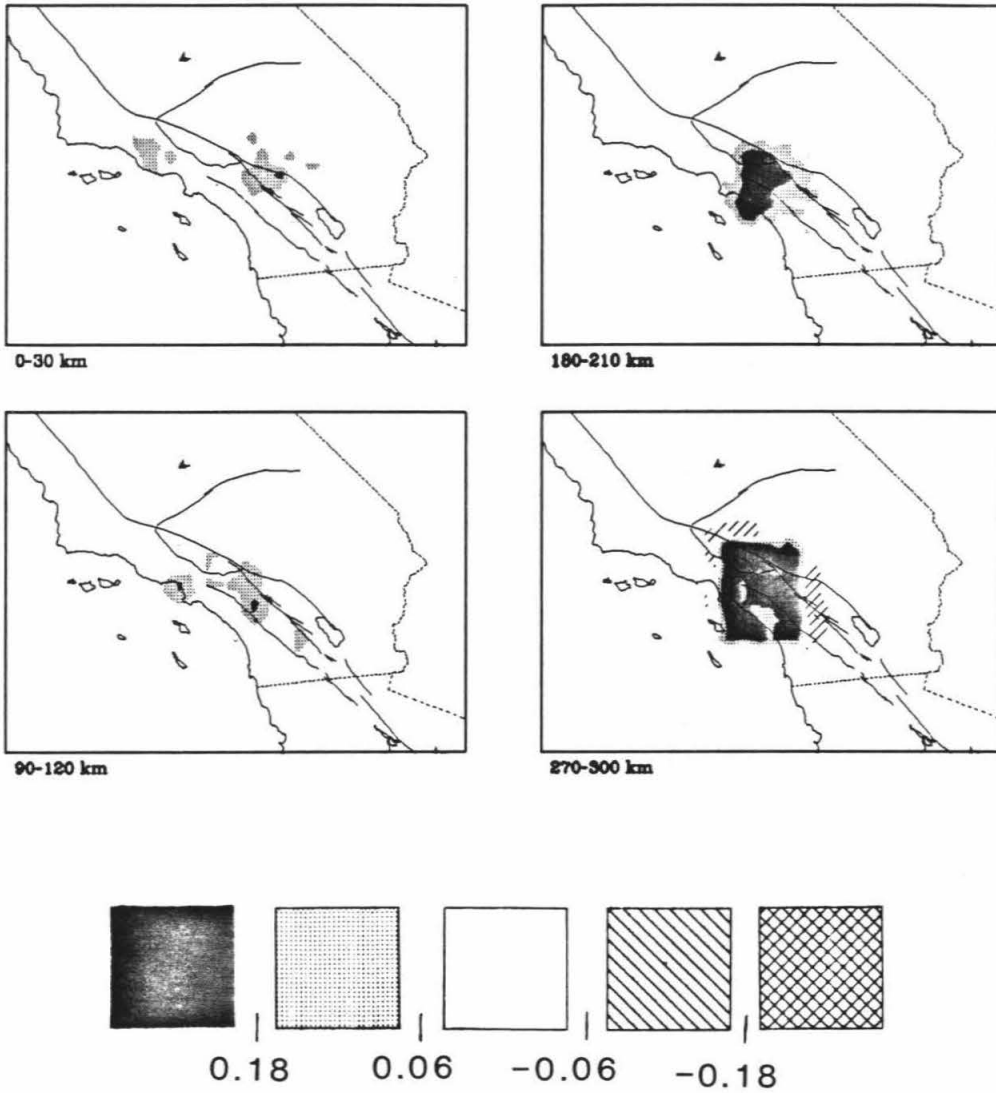


Figure II.12. Reconstructions of a horizontal slab of anomalous material located at two test depths (position shown by small mark on right hand cross sections). Magnitude of anomaly is unity. The procedure includes binning, deconvolution, and five iterations. The anomaly is not well confined vertically, but the integrated anomaly is of approximately the right magnitude.

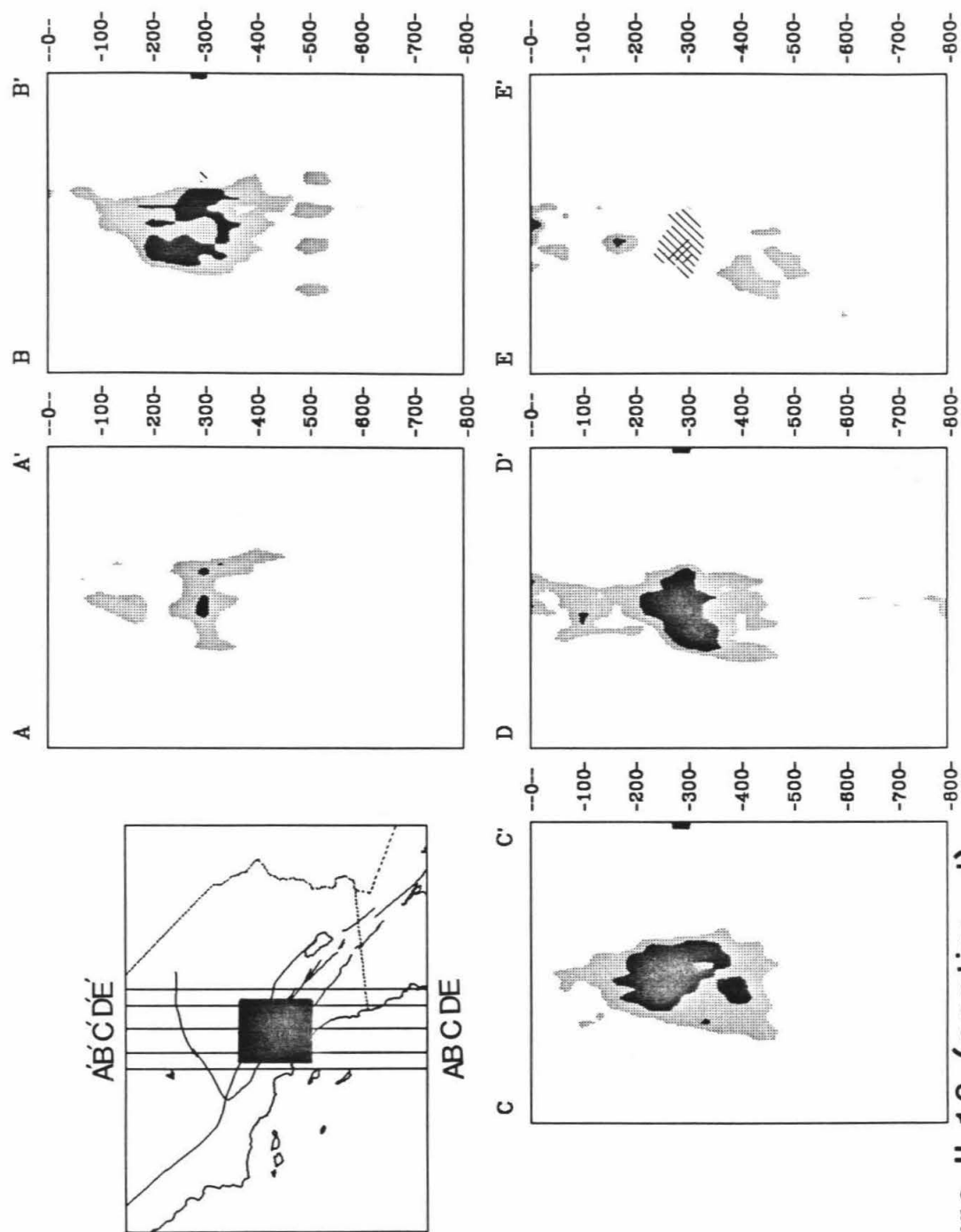


Figure II.12 (continued)

anomaly at 510-540 km

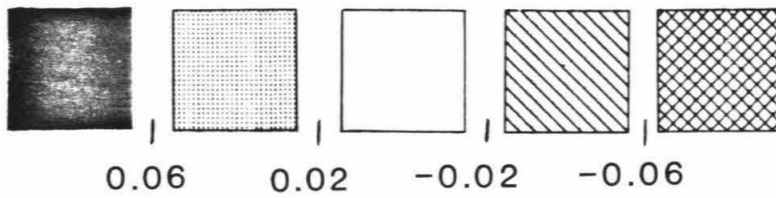
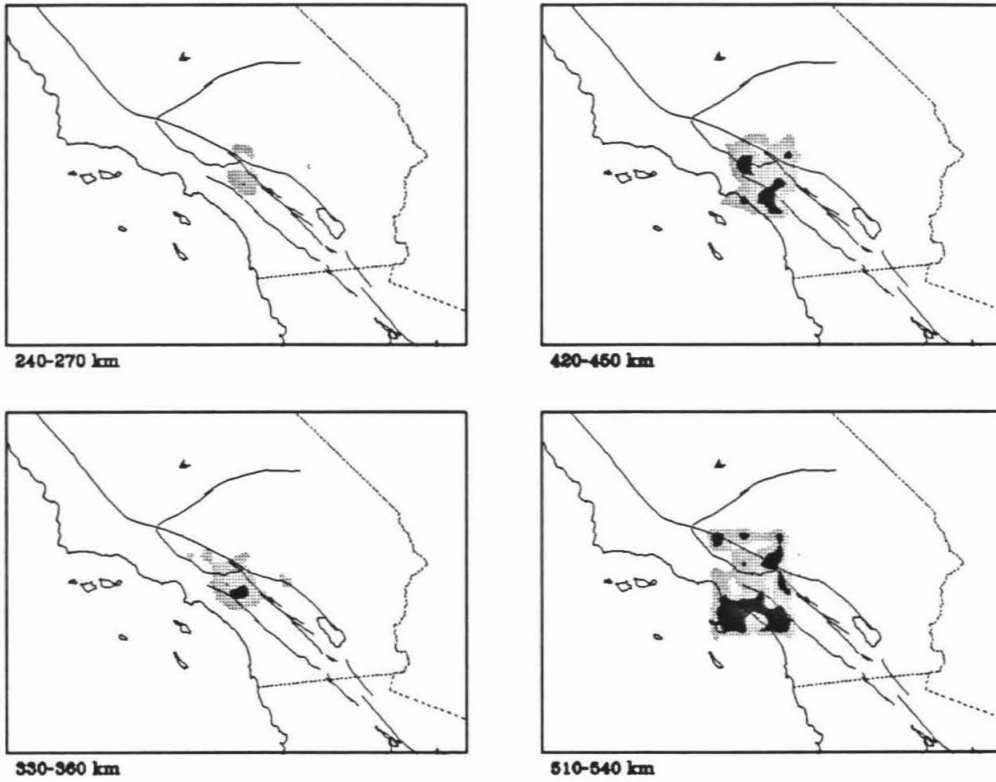


Figure II.12 (continued)

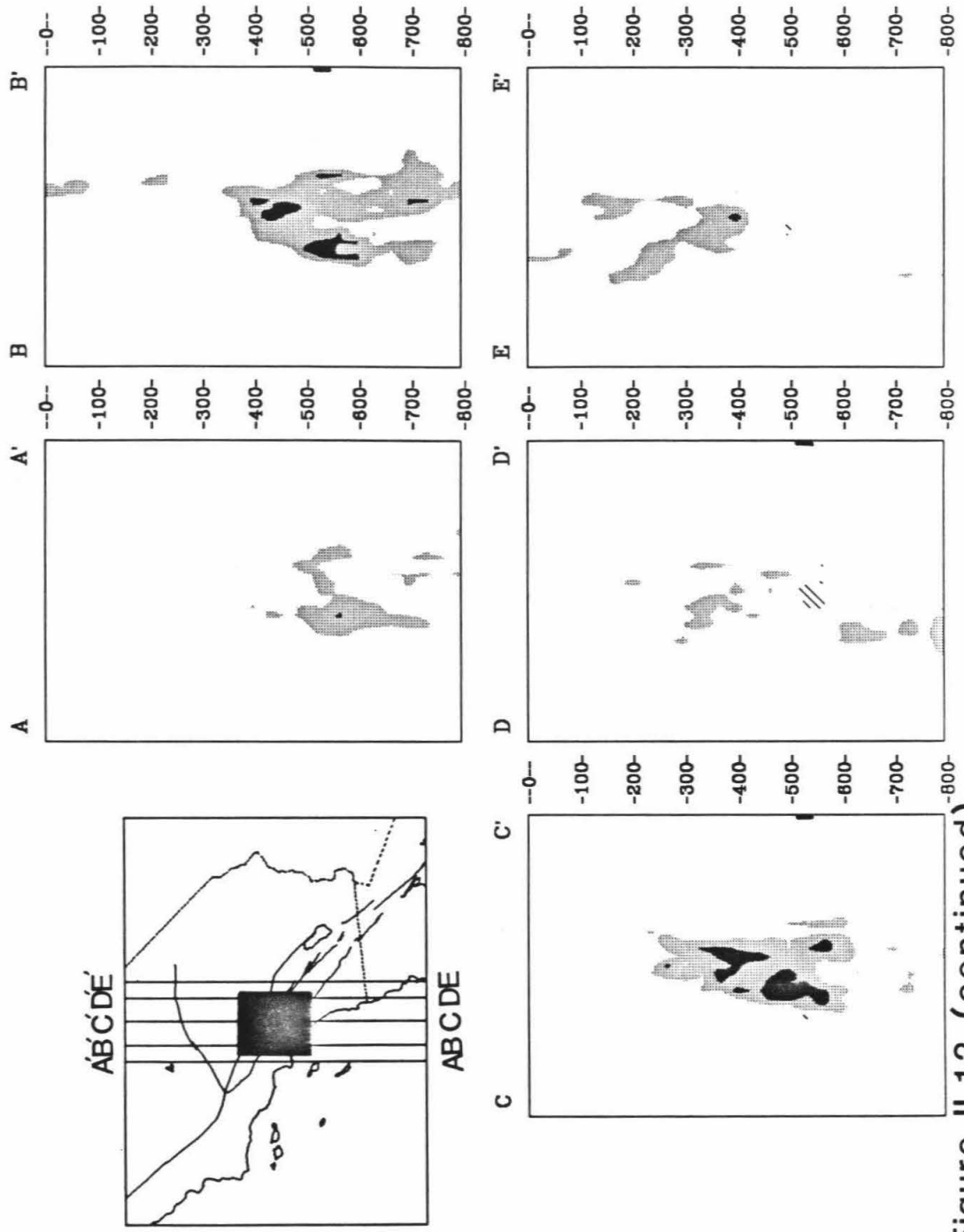


Figure II.12 (continued)

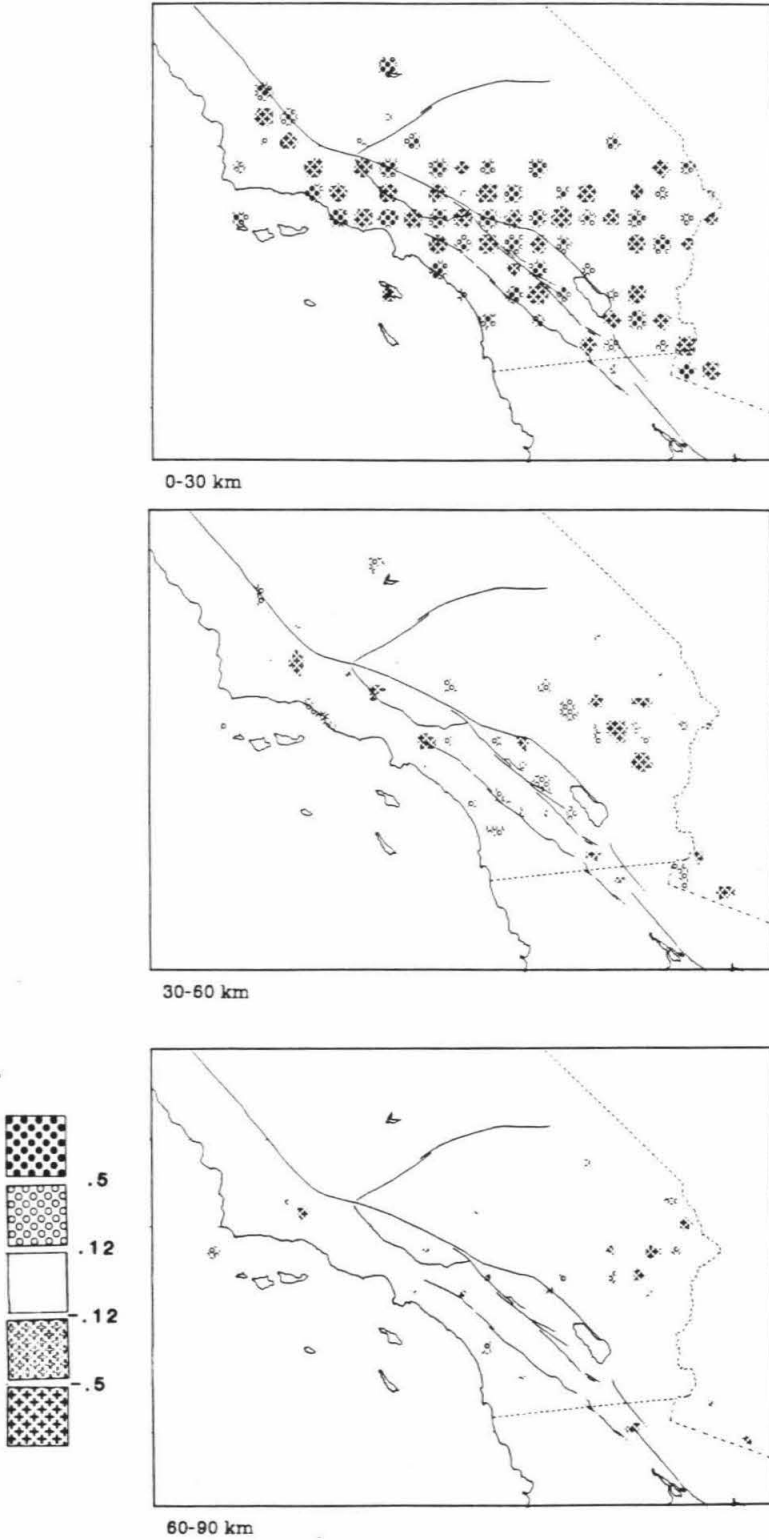


Figure II.13. The reconstruction of an anomalous surficial check pattern, where one fourth of the blocks are anomalous and nearest anomalous blocks are of opposite sign. Magnitude of anomaly is plus and minus unity. The procedure includes binning, deconvolution, and five iterations. Notice the good ability to resolve the structure when the ray coverage is good, but the weak reconstruction where ray coverage is poor. The amount of artificial anomaly below the top layer is very small, and hence it is thought that surficial structure can be well resolved without significant artifact when the ray coverage is good.

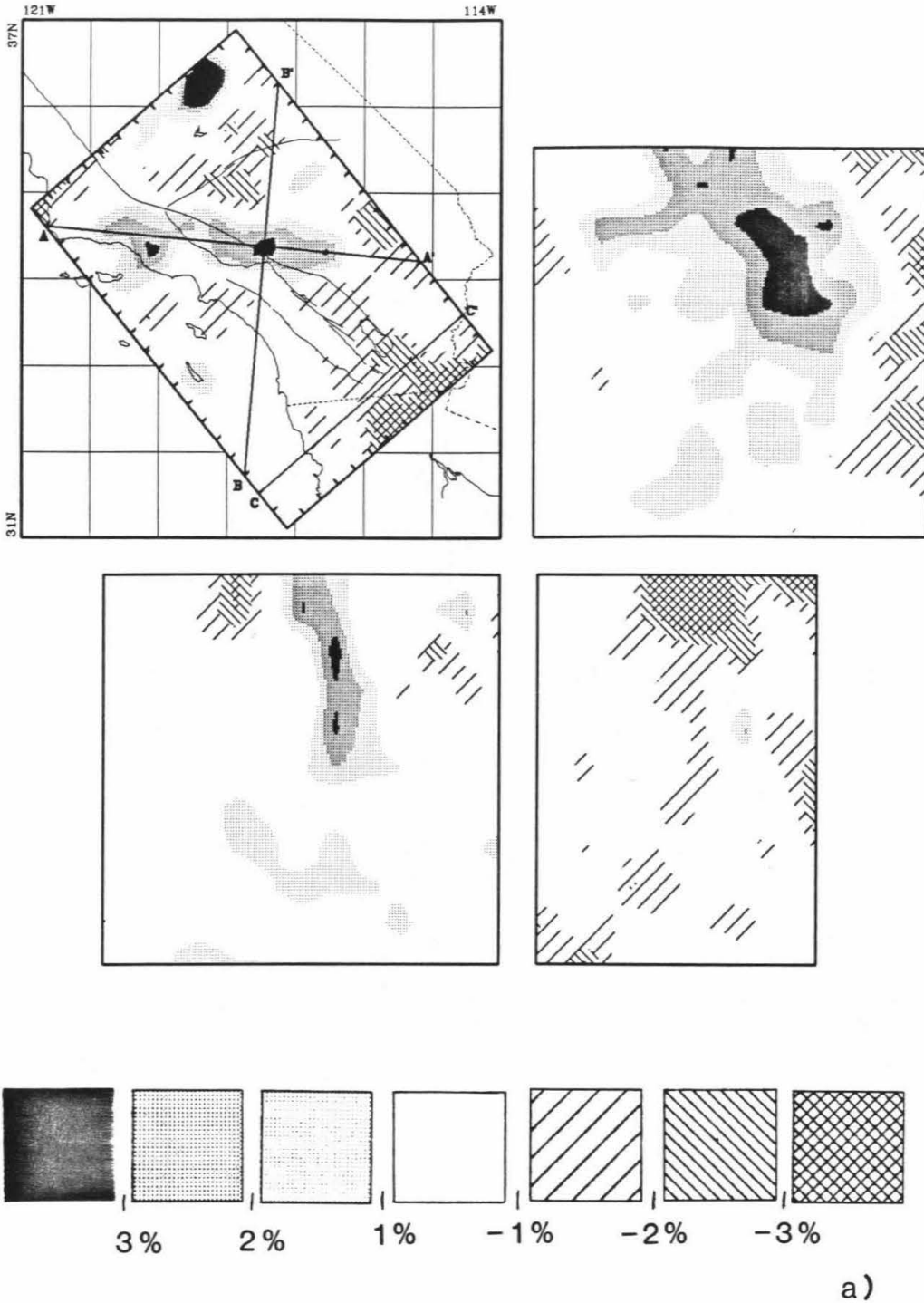


Figure II.14. The reconstruction of the actual travel time delays with the use of binning, deconvolution, and five iterations. The major anomalies seen are the zone of high velocity material beneath the Transverse Ranges and the region of slow material beneath the Salton Trough. Part a) shows the inversion using the large blocks, and part b) shows the inversion with the small blocks. See text for more discussion.

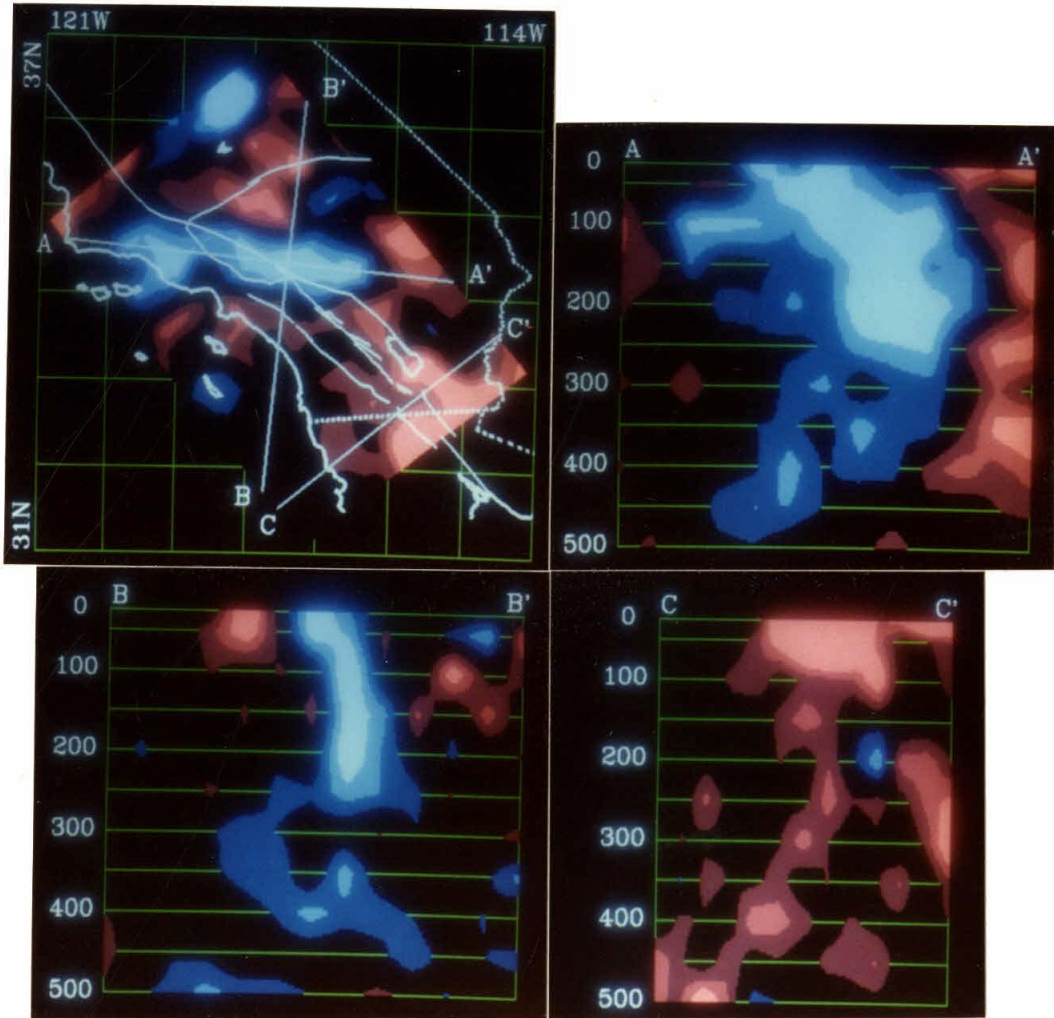


Figure II.14a (continued)

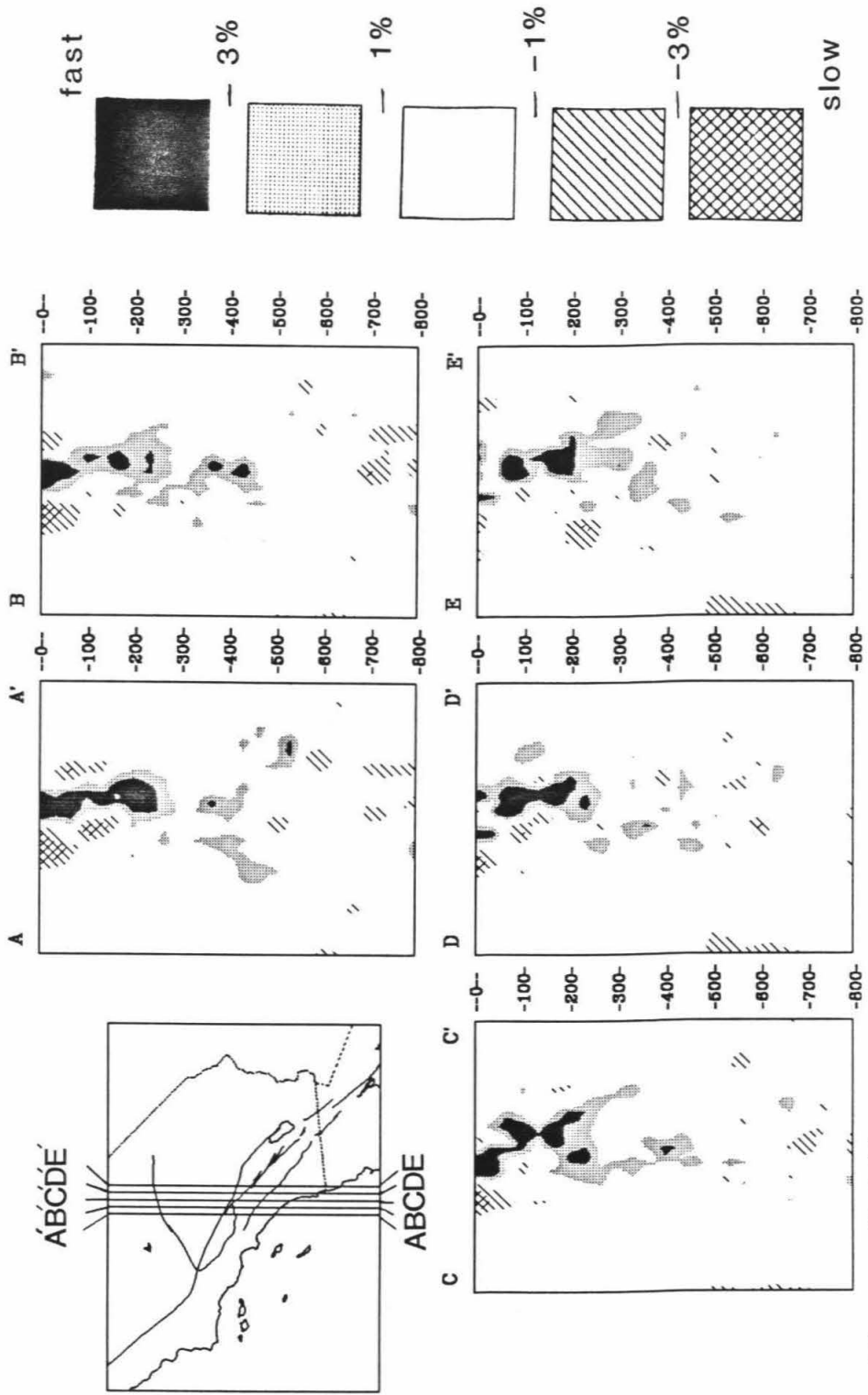


Figure II.14b

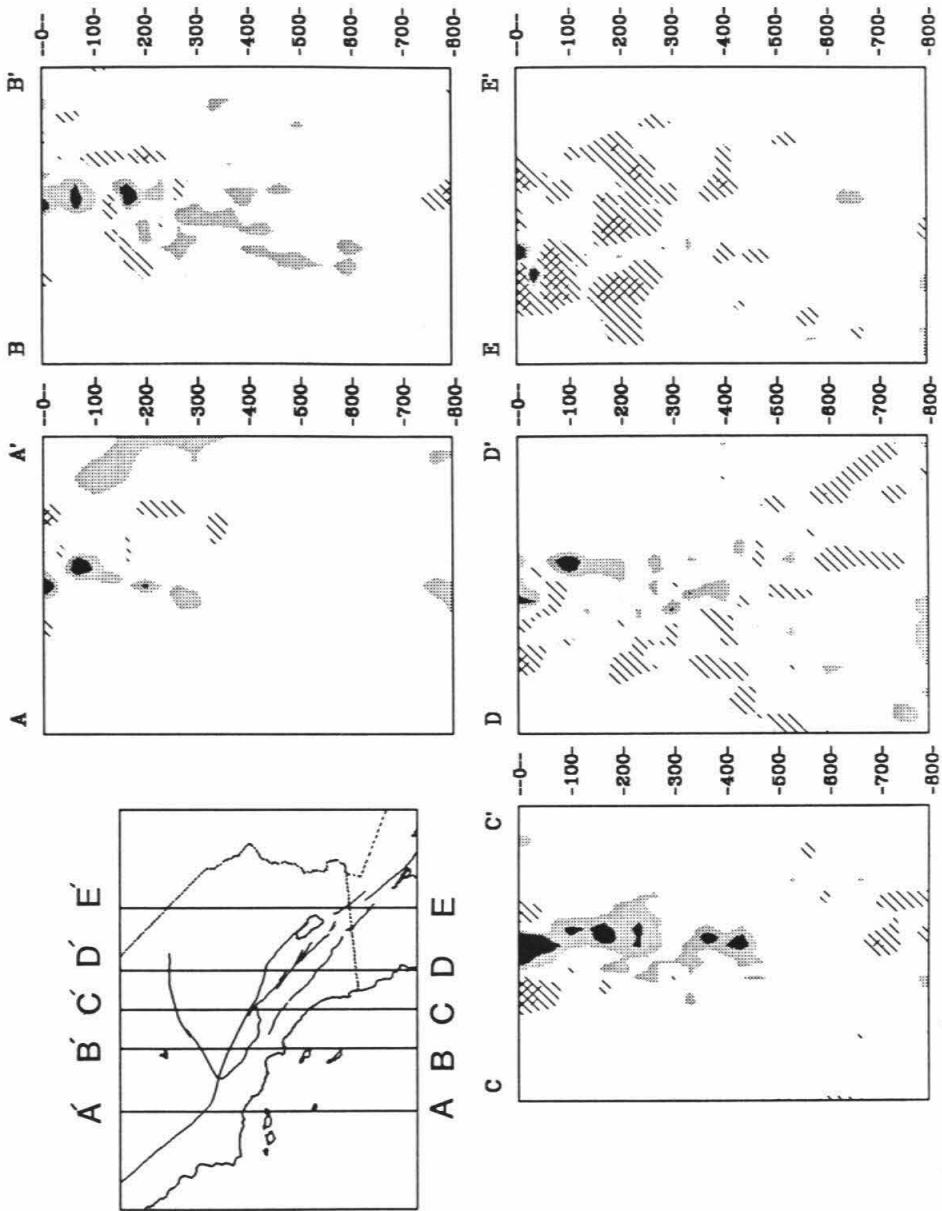


Figure II.14b (continued)

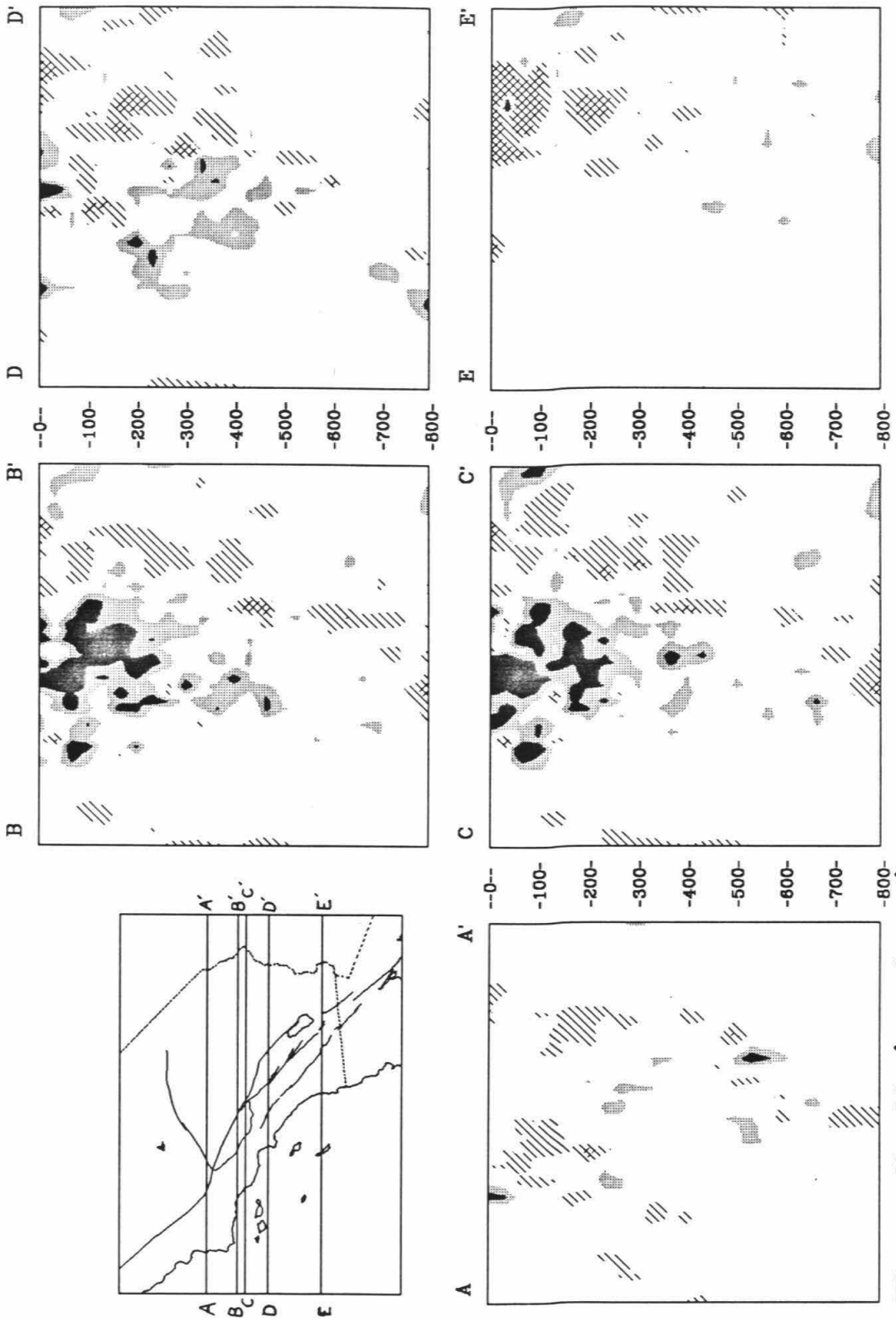
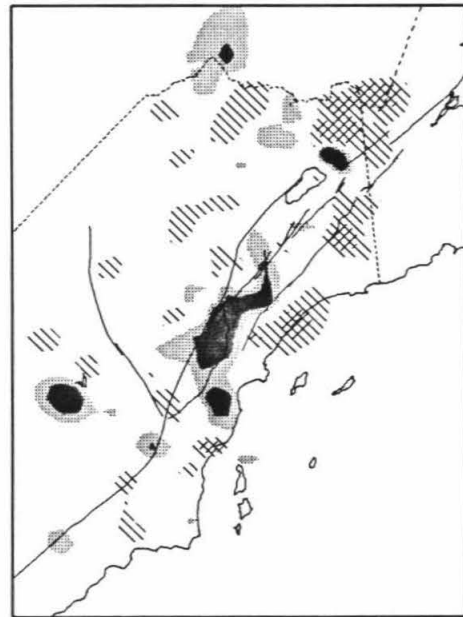
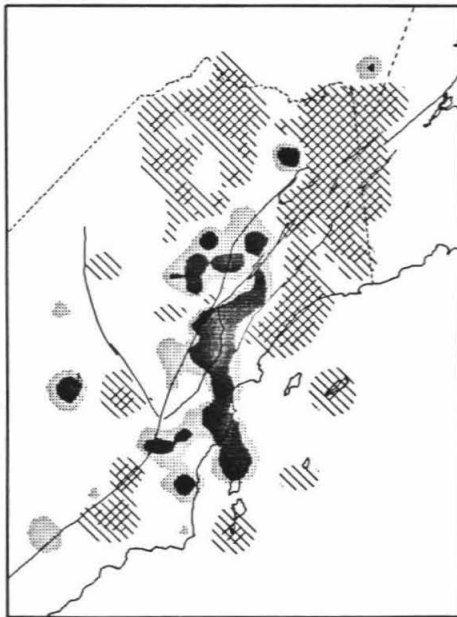
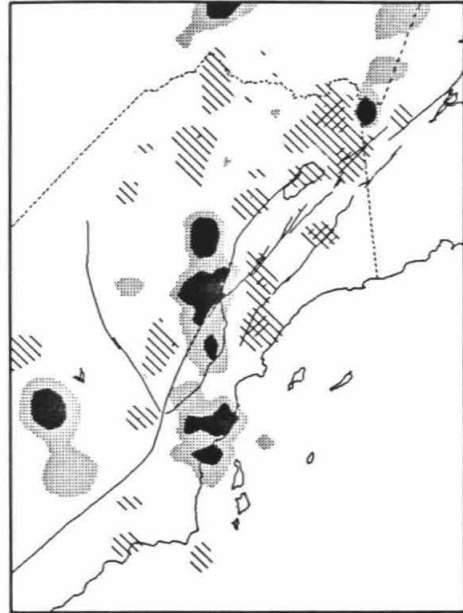
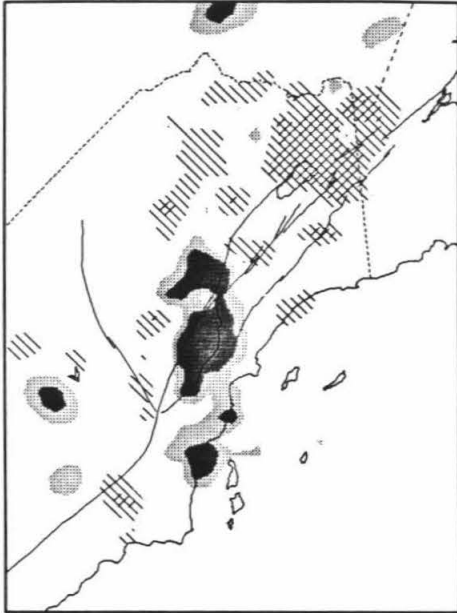


Figure II.14b (continued)



90-120 km

30-60 km

Figure II.14b (continued)

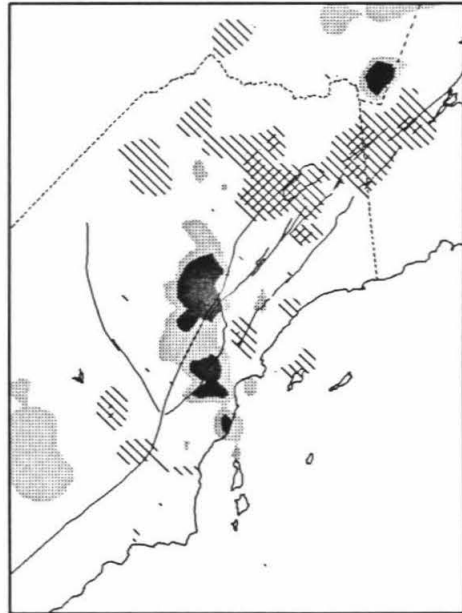
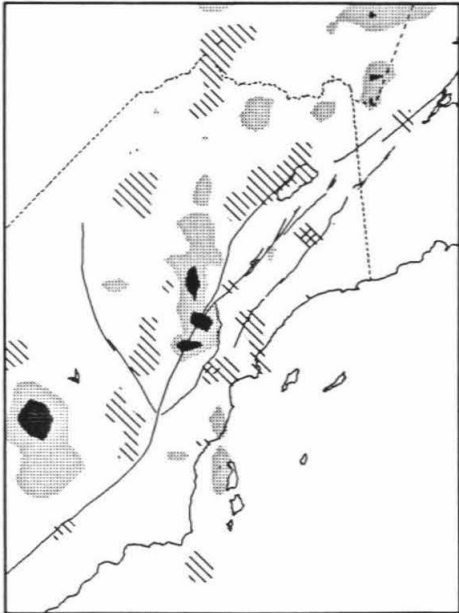
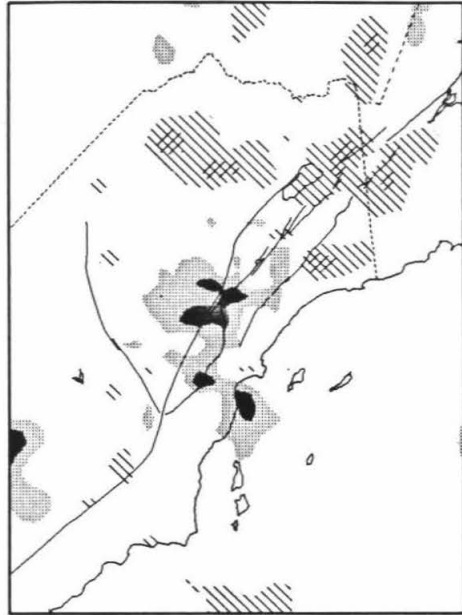
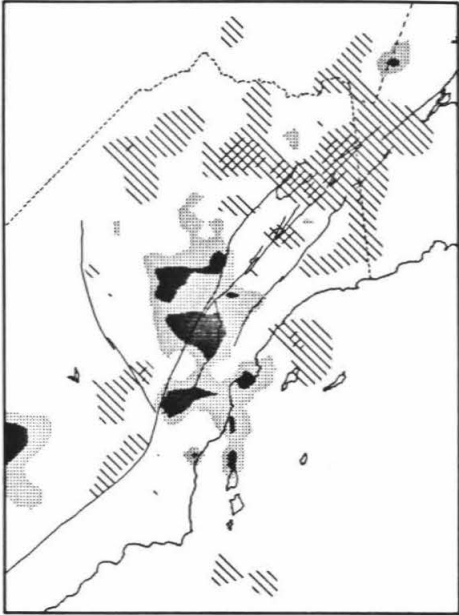


Figure II.14b (continued)

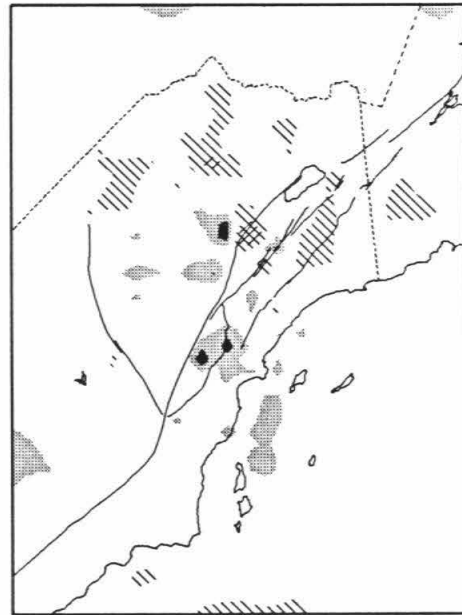
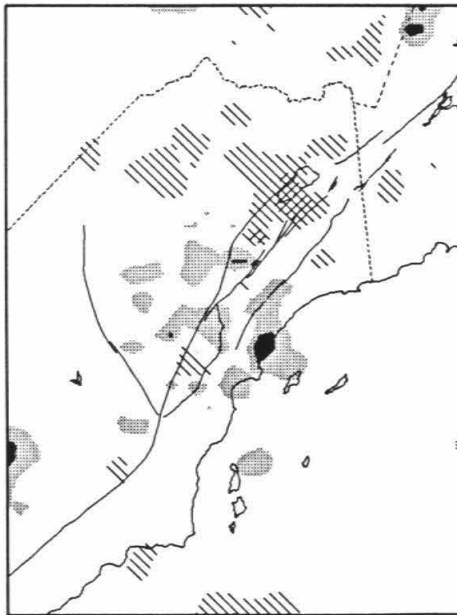
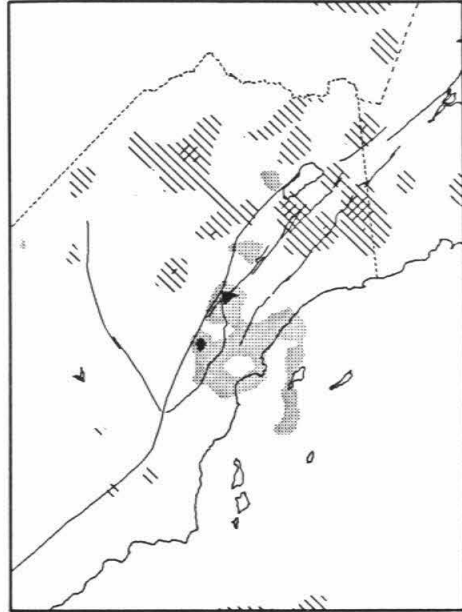
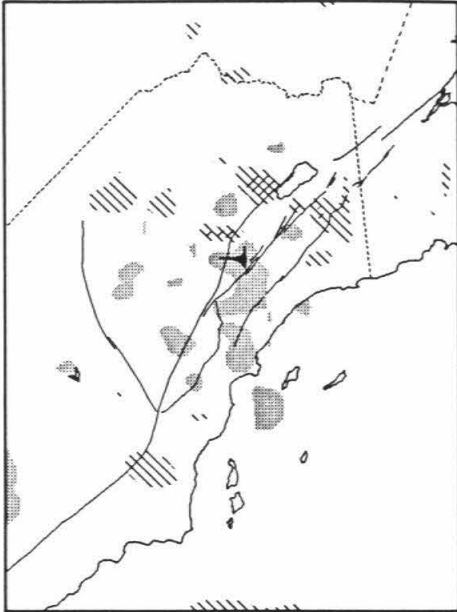


Figure II.14b (continued)

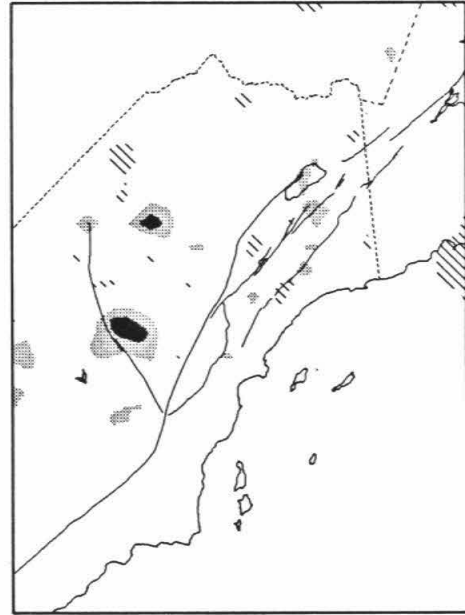
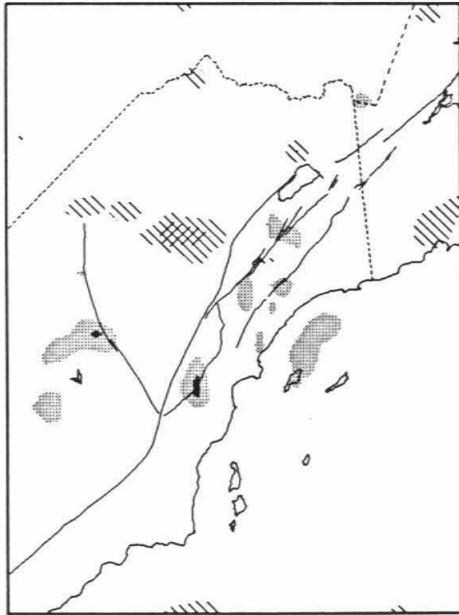
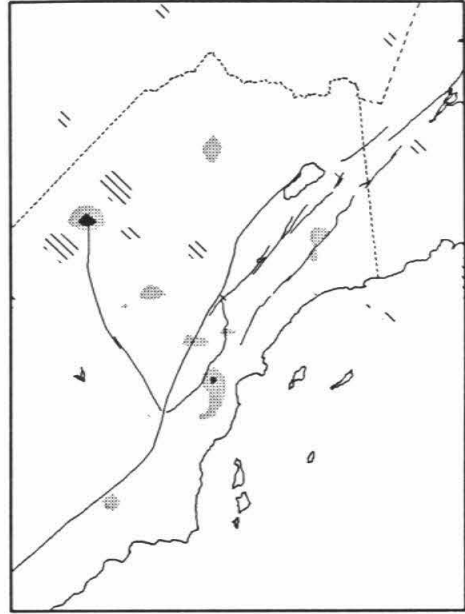
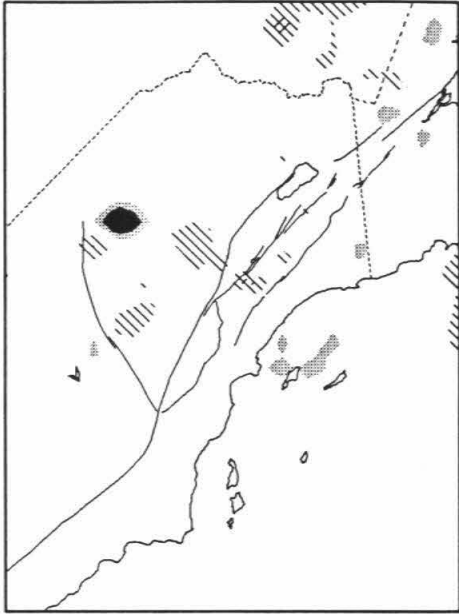


Figure II.14b (continued)

km. The anomalous region is about 3% fast at its fastest, which contrasts with the $\sim 10\%$ fast found for subducted slab beneath Japan (Miyamachi and Moriya, in prep). Comparison of the strong anomaly beneath the Transverse Ranges (Figure II.14) and the hit quality map (Figure II.7) shows that this anomaly is in a well sampled region and resolution should be good. It is satisfying that the Transverse Range anomaly and the hit quality, while being roughly similar in appearance, possess many features that are not in common with each other. The volume beneath about 250 km is rather featureless, and there are no high velocity anomalies observed that may not have been artificially produced. If an anomaly of modest dimensions existed at these depths, especially an anomaly thin in vertical extent, it would be difficult to produce a focused image of this. Intentionally simple synthetic examples have been run to simulate the ability to handle structure similar to that determined beneath southern California. These are shown in Figures II.15-II.17. In particular, Figure II.15 has a thin, wedge-shaped anomaly that has been included beneath the region of the Transverse Ranges, and the inverse of the synthetic delays does very well in reconstructing this structure. This is true even for the location of the bottom of the feature.

Figure II.16 is a reconstruction on a synthetic example that is identical to the structure used in the example for Figure II.15 except that the second layer is without anomaly. The reconstruction shows the influence of the non-anomaly, but also displays well the streaking of the anomaly from above and below into this layer. The strength of this artificial reconstruction compared to the results on the actual data (Figure II.14) suggests that the second layer

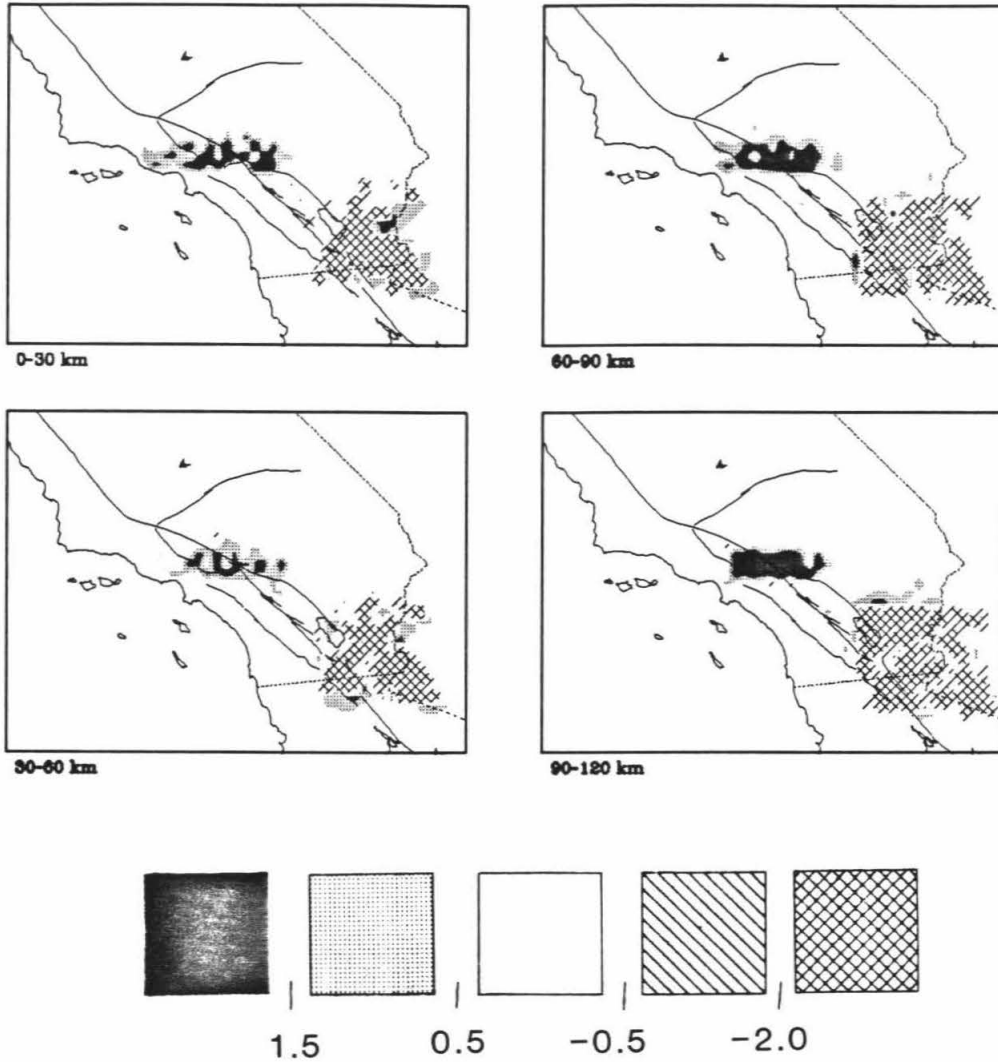


Figure II.15. Inversion of a simple structure designed to simulate the principal features seen in the inversion of the actual delays (Figure II.12). Magnitude of the anomalies are plus two ("Transverse Range" anomaly) and minus three ("Salton Trough" anomaly). The "Transverse Range" anomaly is 60 km wide and extends in depth to the reference line. The "Salton Trough" anomaly is above 90 km. As in the case of the actual delays, binning, deconvolution, and five iterations have been applied. It is seen that both major anomalies are capable of being resolved. The Transverse Range Anomaly is very well resolved and produces little artifact. The Salton Trough anomaly is resolved less accurately, and some deeper anomaly is artificially produced.

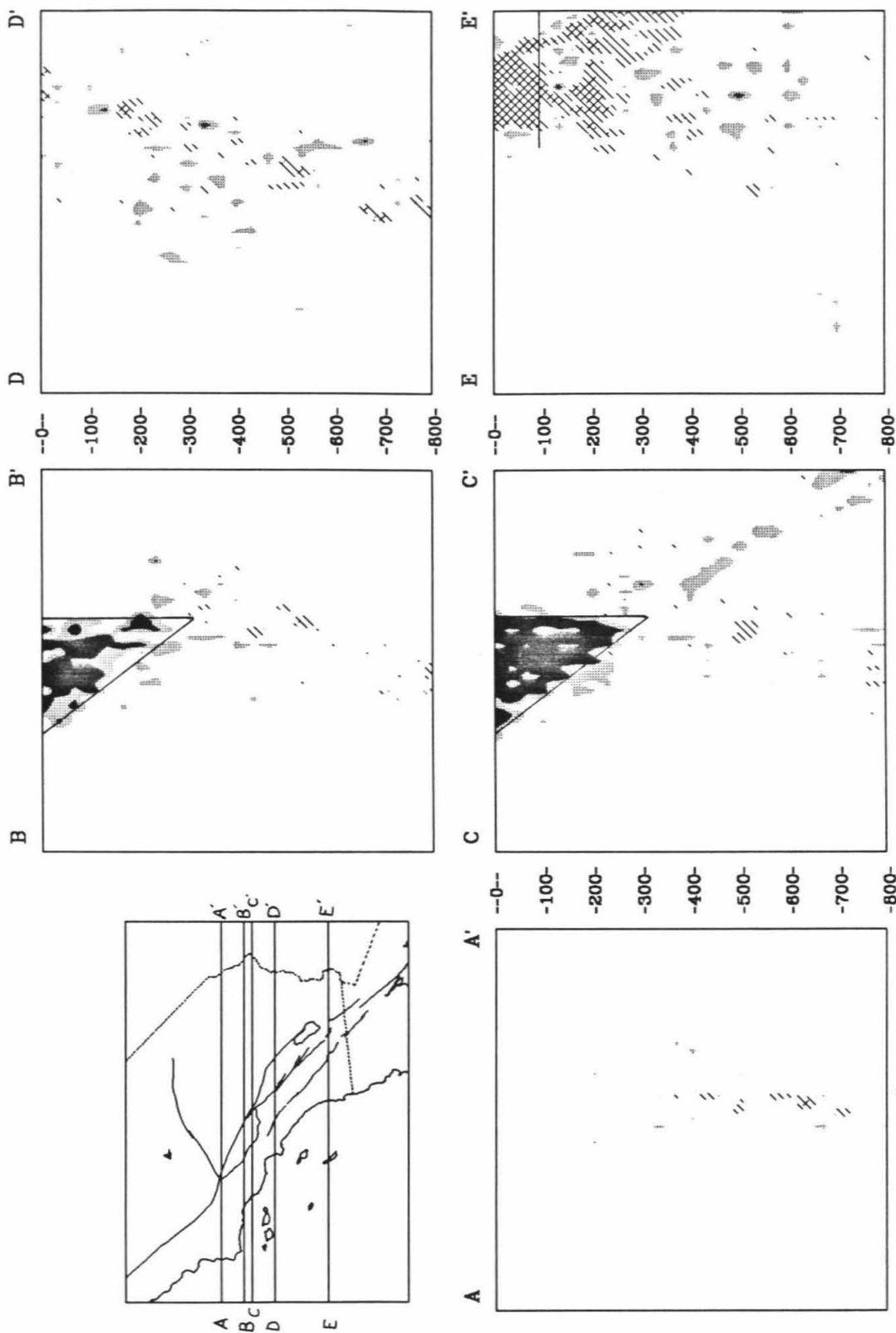


Figure II.15 (continued)

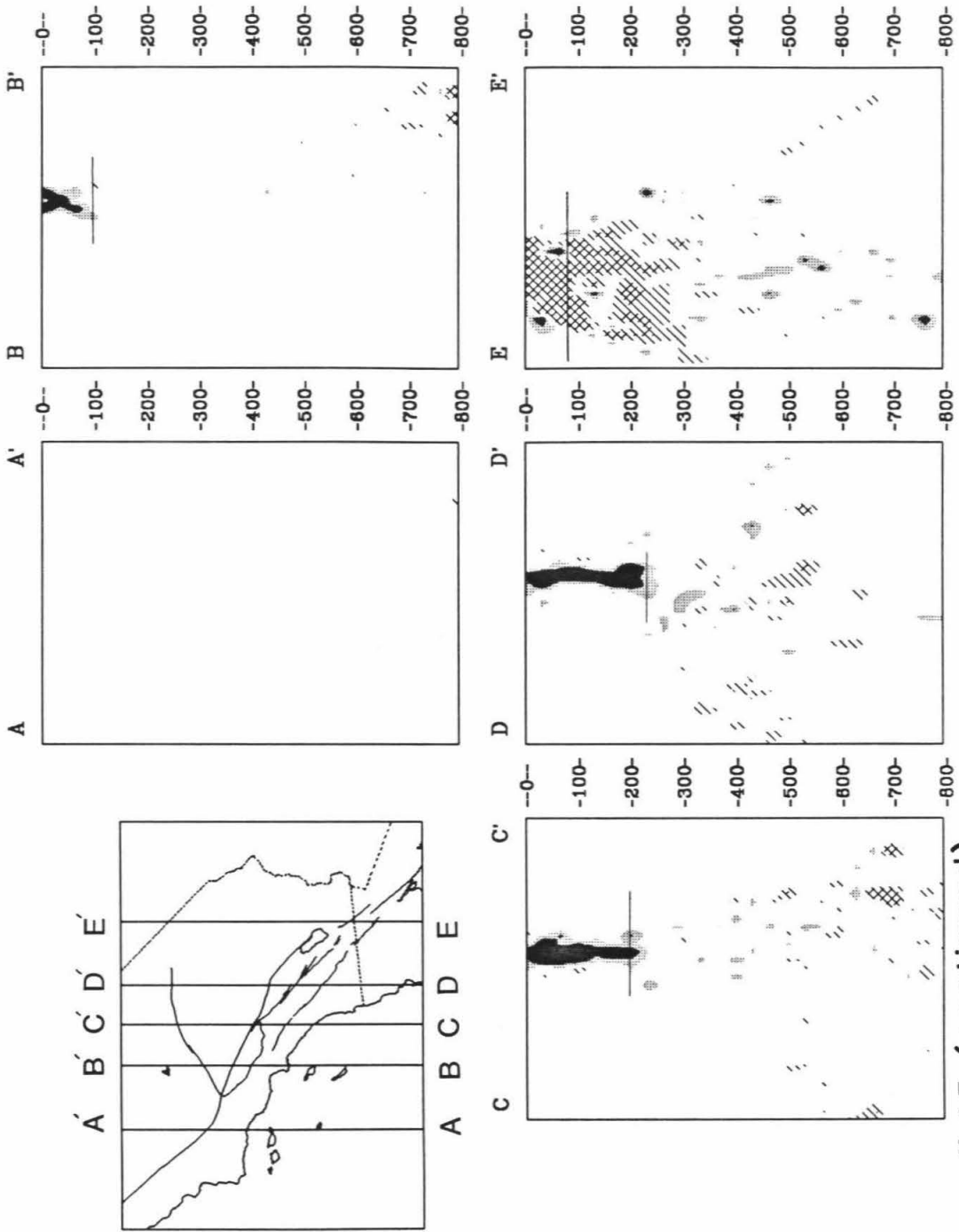


Figure II.15 (continued)

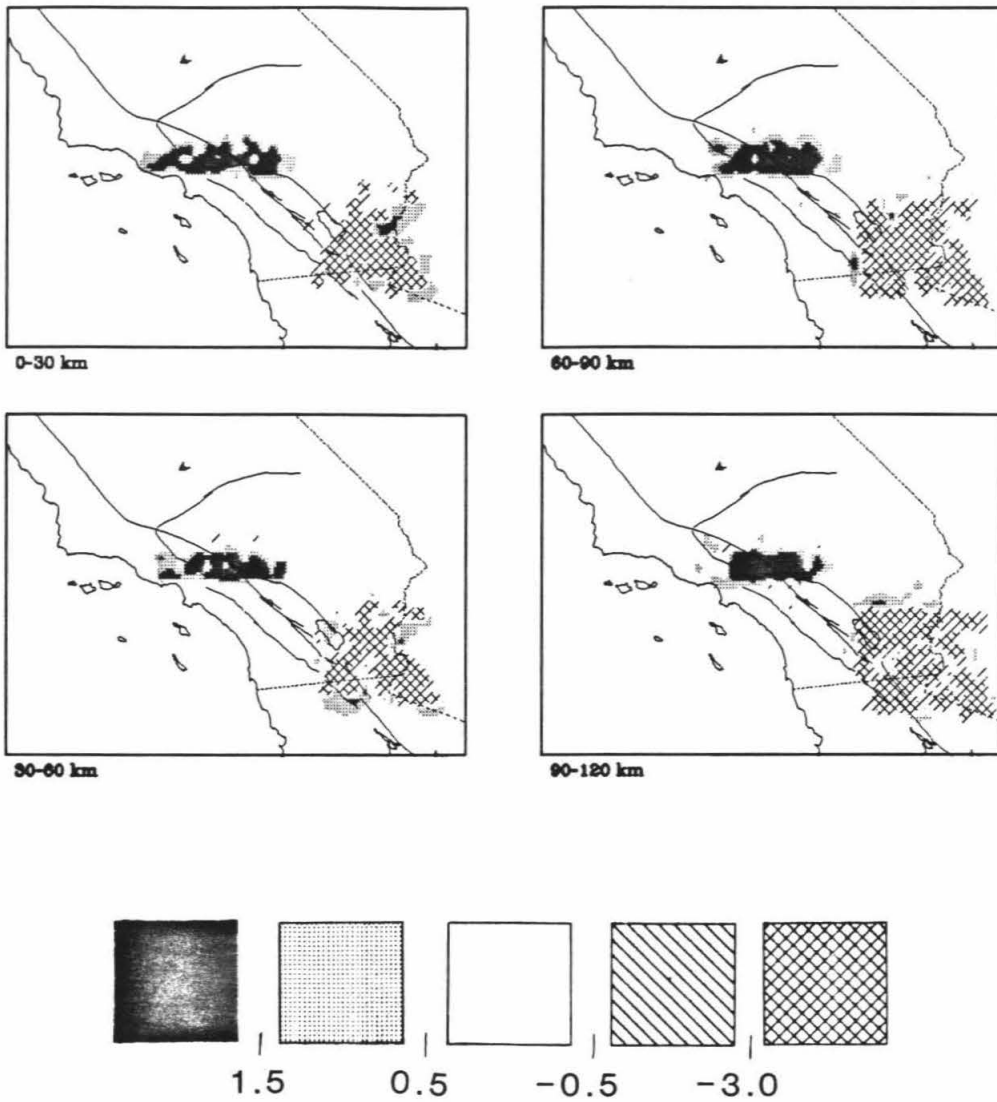


Figure II.16. The same as Figure II.13 except that the original structure has no Transverse Range anomaly in the second layer of blocks. It is seen in the reconstruction that some anomaly is artificially placed in this layer, but that it is markedly smaller in amplitude than in Figure II.13. Also the uppermost layer has been artificially diminished in amplitude as compared to Figure II.13.

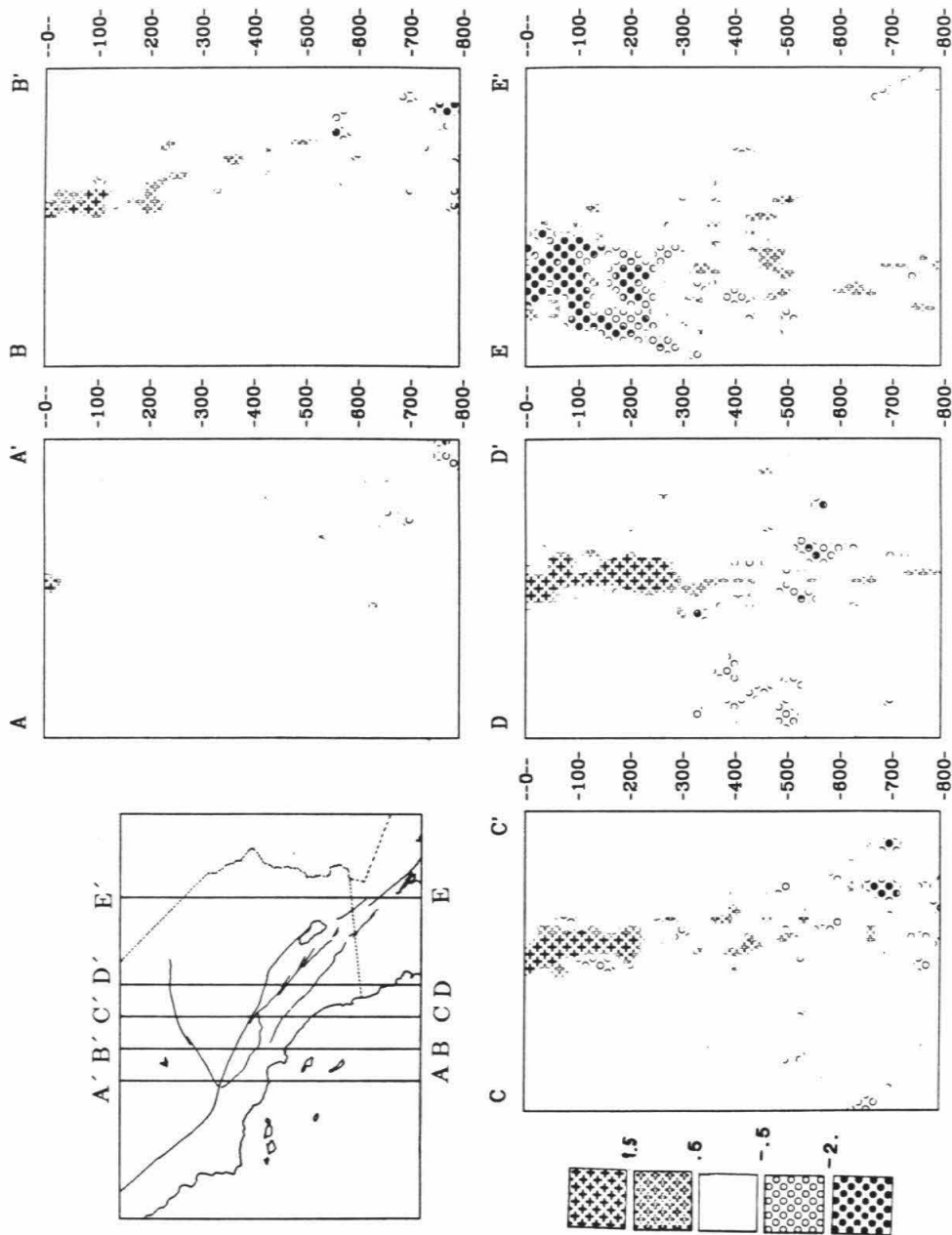


Figure II.17. The same as Figure II.14 except that the surficial Transverse Range anomaly has been moved south two blocks and increased in amplitude by one third. It is seen in the inversion that the surficial Transverse Range anomaly is well reconstructed in its offset position, and that the lack of anomaly in the second layer results in diminished amplitude as compared to the second layer in Figure II.13, where there is no missing anomaly.

of blocks down from the surface (depth range 30-60 km) is, if anything, possibly low in velocity beneath the Transverse Ranges. Figure II.17, like Figure II.16, is a mild variation on Figure II.15. The test structure differs from Figure II.15 only in the position of the Transverse Range anomaly, which has been positioned two blocks (60 km) to the south. The ability of the inverse to reconstruct this detail speaks strongly in favor for the existence and location of the crustal Transverse Range anomaly.

To test if this high velocity region is the result of anisotropic material oriented in a way that allows vertically arriving teleseismic phases to arrive early, two events of $30^{\circ} < \Delta < 35^{\circ}$ were examined. The results of these P delay maps are shown in Figure II.18. Also shown is the antipodal event (Figure II.1) which is presented for comparison. In both cases, a zone of early arrivals corresponding to the high velocity anomaly is seen, despite the low angle of arrival ($< 30^{\circ}$ from horizontal). In fact, the integrated delay associated with the Transverse Range anomaly is about the same as is observed for any other angle of incidence, ruling out the possibility of significant anisotropic contribution to the early P arrivals.

Another large-amplitude, high-velocity anomaly is found in the inversion beneath the southern Sierra Nevada. The ray coverage here is quite poor, especially in its azimuthal completeness, and the indicated inversion should be taken as rather approximate until constrained with more data. Some control on the location of the anomaly is available, however, by carefully looking at the delay times for stations near the area. The station located near Lake Isabella (in the southern Sierra Nevada) is shown in Figure II.2 as station ISA.

This station has more observed variation in delay residual than any of the stations in the Southern California Array. The map of Lake Isabella's delay times is shown in Figure II.19 as a function of ray parameter and azimuth. The indication is that the anomalous region lies somewhere to the NNW of Lake Isabella, and that the anomalous region extends about as far south as station ISA, but not farther. This station delay map by itself gives no indication of the depth to the anomalous region. Figure II.19 shows that station CLC (to the east of Lake Isabella) is not influenced by this anomaly, even for those rays from the NW that are of fairly shallow angle (ray parameter between 5 and 10 deg/sec). The suggestion is that the southern Sierra anomaly does not extend too far to the north of Lake Isabella. Also supporting this statement is the observation that very shallow rays arriving at ISA do not show a strong time advances (The Alaskan event in Figure II.18 is a good example.). Station BMT (to the south of ISA), on the other hand, records a strong negative delay for rays arriving shallowly from the NW (ray parameter between 5 and 10 deg/sec) Figure II.19. Assuming that the same anomaly produced the observed time advances at both stations, the station separation of about 60 km requires the anomaly to be beneath the Moho. However, the difference in arrival angle of the affected rays at ISA and CLC limits the deepest extent of this anomaly to be probably no more than 250 km deep. Notice that, if the inversion has spread the anomaly out over more volume than is in reality the case, the anomalous feature is of even larger magnitude than the 3% fast determined by the inversion.



Figure II.18. Two P-delay maps resulting from two events. Part (a) is the result of an event from Alaska ($\Delta = 30^\circ$ and azimuth as indicated by the arrow), while part (b) is the result of an event from El Salvador ($\Delta = 30^\circ$ and azimuth again indicated by the arrow). Notice that while the pattern shifts in location depending on the direction of the incoming rays, the Transverse Range anomaly leaves a pattern of early arrivals of approximately the same integrated magnitude as the more normally incident ray geometries implying that the anomalous delay pattern associated with the Transverse Ranges is not primarily due to material anisotropy.

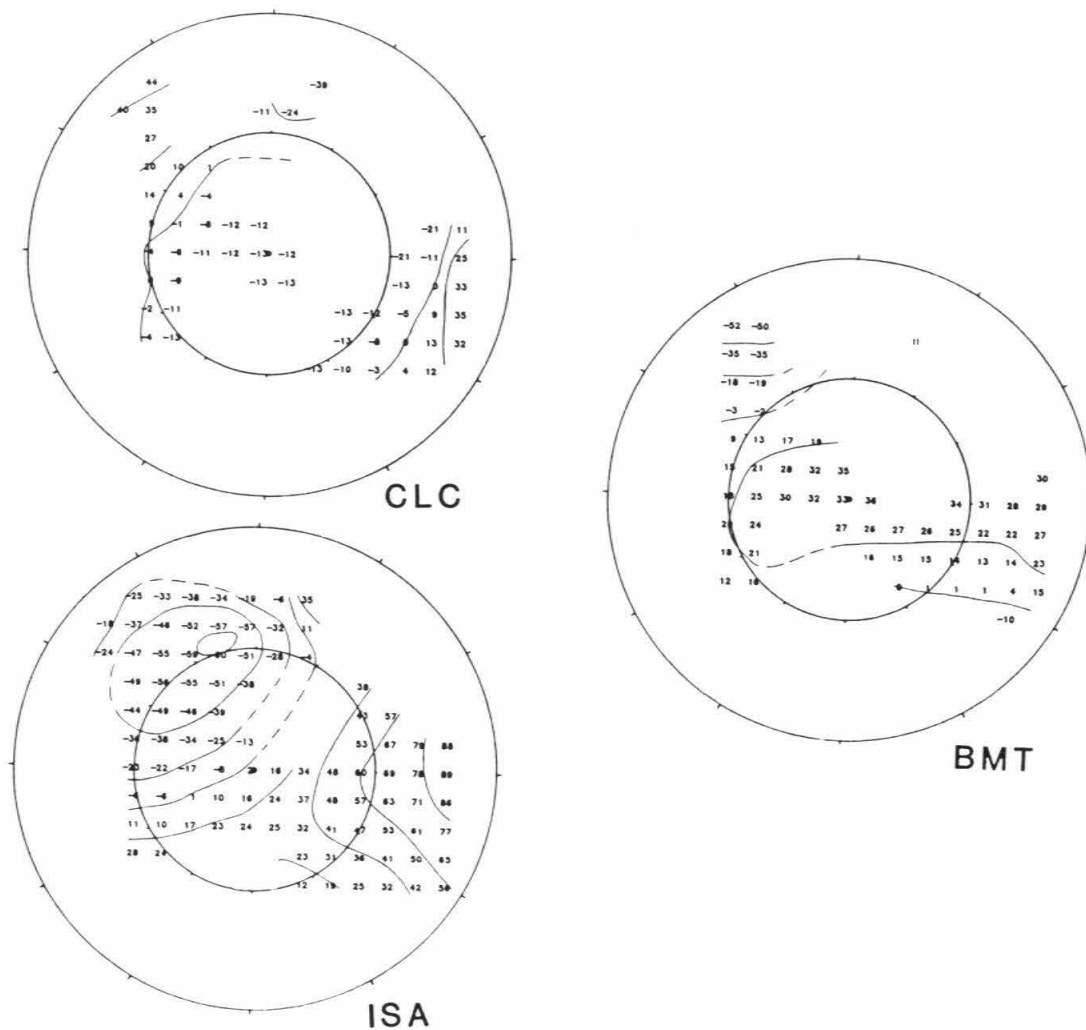


Figure II.19. Displays of the delay time (in hundredths of a second) as a function of ray parameter and azimuth for three particular stations. North is towards the top of the figure and the circles represent 5 sec/deg and 10 sec/deg for the inner and outer circles, respectively. Each number is the average of all measurements falling within the box centered by that number. Part (a) is for station ISA in the southern Sierra Nevada, (b) is for station CLC (which lies to the east of ISA), and station BMT (to the south of ISA) is shown in part (c). Notice that the very early arrivals seen at ISA to the NW are apparently also seen by BMT in the far NW corner, but are not observed at all by BMT.

The region roughly beneath the Salton Trough is the most anomalous volume of slow velocity material observed within the inversion, and in places it attains values more than 4% slow. The presence of slow material here is expected because the rifting in the Gulf of California and the rising of hot mantle from below. It is interesting that in the Salton Trough, which is the northernmost expression of the Gulf of California rifting, only the upper 100 km are markedly slow, though the mantle feature is more regional than the physiographic expression of the rift valley. These results for the Salton Trough can be compared to the seismic velocity models from the south and central gulf, where Walck (1984) found that velocities are slow to a depth of 300 km, with the major region of anomalous material above 250 km. In southern California, the inversion suggests that the volume beneath 100 km has a low amplitude anomaly in the depth range of about 150-250 km. The synthetic examples (Figures II.15-II.17) show that this is probably, at least in part, a consequence of the major anomaly above. In the volume beneath 250 km there is only a hint of a low-velocity region, and because of the small amplitude of the feature it is not possible to say whether this is due to actual slow velocity material or is simply an artifact of the inversion.

Finally, several distinctive features are noted that seem especially worthy of remark. First, the Transverse Range anomaly at about 100 km depth is remarkably similar in outline to the map view of the Transverse Ranges themselves (Figure II.20). This is thought not to be due to erroneously projecting surface or near-surface information down to this depth because any such travel time errors would resolve themselves principally as anomalies within the

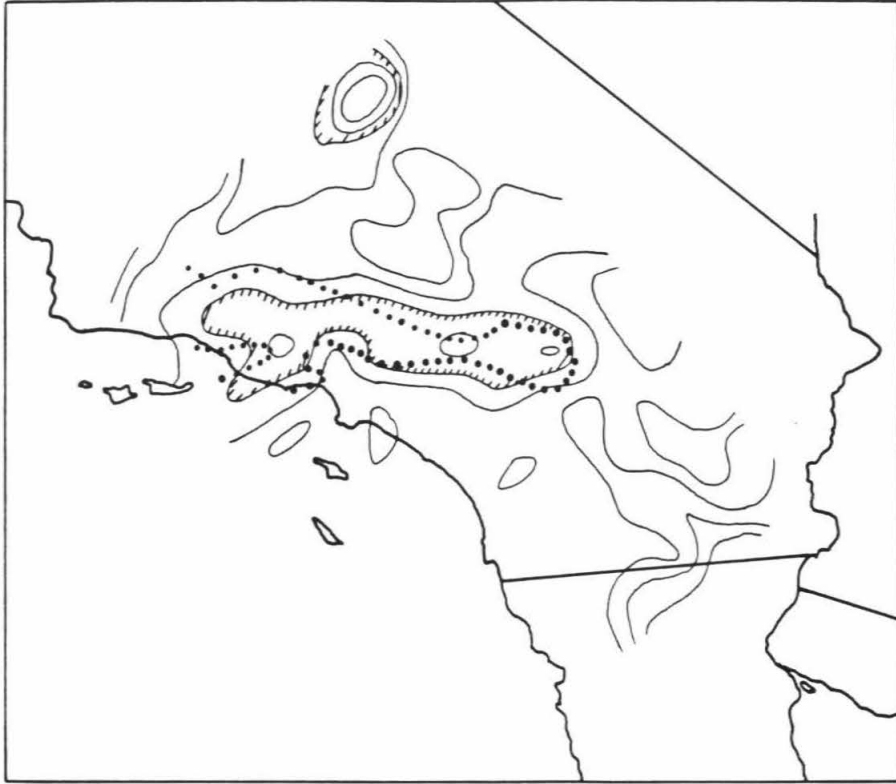


Figure II.20. Similarity of the Transverse Range anomaly at 100 km depth to the physiographically defined Transverse Ranges. The hatched line shows the position of the 3% fast contour at a depth of 100 km and the dotted line indicates the physiographic limit of the Transverse Ranges.

uppermost layer. Another notable observation is that the second layer of blocks (30-60 km in depth) is rather featureless when compared to the layers immediately above and below (see Figures II.16-II.17). In particular, at this depth the Transverse Range anomaly is limited to the Cajon Pass area, and the Salton Trough anomaly is limited to the far SE corner of California. The actual velocities of the material at this depth are difficult to estimate since the very strong anomaly in the horizons above and below will tend to streak into the second layer, artificially altering whatever local anomaly that already exists there. An absence of anomaly, however, can not be artificially produced. It appears that the velocities within this layer are peculiarly less anomalous than the material in the vertically neighboring blocks. Support for this reasoning comes from the test examples. Figure II.16b shows the amount of anomaly that would be placed inaccurately in the second layer of blocks when in fact this layer is anomaly-free. Figure II.15 shows that the reconstruction of a vertical slab has no tendency to artificially diminish the amplitude of the second layer.

The final "special feature" to be discussed is the uppermost layer (i.e., the "crustal" layer, 0-30 km in depth). A problem in interpreting anomalies in this layer arises from the fact that any misapplied station corrections will end up primarily as crustal slowness variations. Two of the station correction terms, the sediment corrections and the Moho corrections, could possibly contribute significant amounts of error to the crustal layer. There are two very strong anomalies, however, that are believed to be of physical origin. These anomalies are found in positions similar to the deeper anomalies; the fast

anomaly is in the vicinity of the Transverse Ranges while the slow anomaly is in the vicinity of the Salton Trough. Hearn (1984) has carefully investigated the crustal layer with the use of P_g arrivals originating from local earthquakes. His results show some similarity to those seen here, but the overall correlation is not strong. There are, potentially, two important reasons for this. First, Hearn's ray paths are wholly within the crustal layer and there is no chance for the structure beneath the crust to contaminate his results. This is not true with the use of teleseismic arrivals. One line of evidence supporting the authenticity of the crustal Transverse Range anomaly is the fact that this feature is centered significantly to the south of the both the physiographic Transverse Ranges and also the associated mantle anomaly (see Figure II.14). In a similar manner, the crustal Salton Trough anomaly is not simply located directly above the deeper anomaly, but rather is more extensive in area (see Figure II.14). Furthermore, Figures II.13 and II.14 suggest that crustal structure is well-resolved in the areas where we find anomalous velocities. The other explanation for the lack of correlation between Hearn's crustal structure and the crustal structure shown here is that the P_g rays used by Hearn (1984) (which have been limited to first arrivals) sample only the upper 7-9 km of the crust while teleseismic rays uniformly sample the entire 30 km thick layer. This suggests that the difference is probably to be accounted for by the difference in the sampling interval between the two ray sets. Assuming this to be true, a direct implication is that there is an anomalous vertical velocity structure within the crust at the two sites where Hearn's and the crustal structure shown here are significantly different, that is, in the Salton Trough and

the Transverse Range regions.

2.8 Discussion

Figure II.14 presents a structure for the region beneath southern California that seems reasonable in view of the delay patterns observed (e.g., Figures II.3 and II.14) and the synthetic test inversions (Figures II.15-II.17). Circumstantial support is lent by the remarkable spatial co-incidence of the major crustal and sub-crustal features. It may be the natural tendency to proceed with confidence in believing that the mantle structure is now well understood, which may in fact be the case. There are, however, reasons for some concern. Problems may exist not so much in what has been inadvertently included in the imaged structure, but rather what may have been omitted. Figures II.11 and II.12 demonstrate that the ability to resolve an anomalous feature depends critically upon the orientation of the feature, while Figure II.13 demonstrates the need for good ray coverage. All of the features described beneath southern California – the Transverse Range and Salton Trough anomalies, the crustal features, and to some extent the “no-anomaly” layer – are features that are capable of being well resolved with the ray set available. The concern is that there are other features beneath southern California for which the information of their existence is contained only in the smaller eigenvalues of the information matrix, and whose reconstructed image is not compact. If such a feature were in a well interrogated region (hit-quality factor greater than .18, Figure II.7), the synthetic examples indicate that only a thin horizontal slab in the presence of other structure would be difficult to detect (as contrasted to

resolved). This is well illustrated in Figure II.11. Figure II.12, on the other hand, demonstrates that an isolated horizontal slab, while poorly focused, is not only detectable, but is of the proper integrated value. (This will be important during dynamic modeling, where it is most important that the net anomaly be accounted for.)

When an anomalous zone lies in a poorly sampled region (hit quality factor less than 18), the ability to reconstruct this anomaly decreases rapidly with diminishing hit quality factor. This is due to the weighting scheme in effect, which has been designed to avoid the production of artificial structure in areas where the signal-to-noise ratio is relatively small. In these regions it is no longer true that the integrated anomaly will be of the proper magnitude. Rather, the reconstruction will be of diminished amplitude.

There are several suggestions in the data that, for one reason or another, some of the structure has not been well imaged. For instance, in Figure II.4 the eastern end of the Transverse Range anomaly is seen to interfinger in a complicated way with late arrivals. This cannot be produced with the reconstruction (Figure II.14). This demonstrates that even in the well sampled regions there is a fair amount detailed structure that is not resolved. Figure II.18b is an extreme example of the influence that structure outside of the inversion space can have on the travel time residuals. The arrivals recorded in the SE corner of the array are very early, which must be due to structure encountered by these rays in the vicinity of the northern Gulf of California.

Kinematic and Dynamic Modeling of Southern California Tectonics

3.1 Introduction

Southern California is a tectonically active region, experiencing continental rifting, transform faulting, and small-scale collision. The forces that drive this activity are only partially understood, and despite a great deal of work even the fundamental aspects of the kinematics are being debated. It is the purpose of this chapter to bring together and discuss the information that pertains to the late Cenozoic geologic history of southern California. The mantle features discussed in Chapter II contribute important new information to this history, and this information should be integrated into the whole story. Because it is difficult to present the subject in a way that weaves all of the important aspects together simultaneously, the discussion has been separated into arbitrary units, each of which comprises one of the following sections. These sections, in order, are:

- A Kinematic Model of the Crust
(the surface at present)
- A Recent History of the San Andreas fault
(the surface through time)
- Constant Viscosity, 3-D Flow Modeling
(present force balances and mantle flow)
- A Model for the late Cenozoic Development of Southern California.

The first two sections address the recent kinematics of southern California. The "present" kinematics are modeled by using late Quaternary slip rates and orientations of the major faults in southern California, and assumes these faults to bound rigid blocks. The primary observation is that little convergence occurs across the San Andreas fault, including the portion in the vicinity of the Transverse Ranges. Combining this with new and recent slip rate data, the following two conclusions are reached: 1) Most of California west of the San Andreas fault is moving parallel to the San Andreas fault in the big bend region, and not parallel to the Pacific Plate motion or to the San Andreas fault north of the big bend. 2) Major near-shore right-lateral faulting with a significant component of convergence is necessary across NW trending faults north and south of the Transverse Ranges.

A review of the literature on the Cenozoic history of the San Andreas fault system is presented next. The slip history of this system is important if the temporal development of the mantle features are to be understood. The recent activity on the San Andreas fault is thought to have begun prior to 10 m.y.B.P., but at a relatively low rate of slip. Since this time the rate has increased substantially, but apparently has acquired a rate of only ~ 35 mm/yr (as compared to the North American-Pacific Plate rate of 56 mm/yr). The rate of 35 mm/yr has probably typified the San Andreas fault for the last 4-5 m.y.

Following this is a discussion of the present-day dynamics, which are modeled by using the seismic image of the mantle (Chapter II) as a map of the density distribution. This image allows for an estimation of the flow field within the mantle, which in turn can be related to tractions at the base of the lithosphere and to stresses and deformations within the lithosphere. The resulting tractions supply forces that

maintain (and locally uplift) the Transverse Ranges.

The final section synthesizes this information and presents a model for the development of southern California over the last 10 m.y. or so. This model proposes that a dynamic mantle has been interactive with the crust.

3.2 The Kinematic Model of the Crust

This section uses new and recent slip rate data for most of the important faults in southern California. The model is a block model of the upper crust and assumes that no deformation occurs within the interior of the blocks. There has been a considerable amount of discussion over the past several years on the manner in which the lower crust is moving with respect to the upper crust. Seismicity suggests that approximately the upper 10 km is acting as a solid unit, and the model developed here is meant to apply to this region. Also, this model is based primarily on late Quaternary slip information, and is therefore a description of what has been occurring very recently in geologic time.

The key to this model is the acceptance of a kinematic situation in which relative motion along the big bend portion of the San Andreas fault is strike slip, and that southern California is therefore not connected to the Pacific Plate. This is a departure from prior kinematic models (e.g., Atwater, 1970; Anderson, 1971; Hill, 1982), but one that must be accepted, it is felt, in light of the data. The more typical approach argues that the geometry of the Pacific-North American Plate boundary results in two anomalous regions: the Salton Trough and the Transverse Ranges. The Transverse Ranges sit in the big bend region and are commonly attributed to compression as the Pacific Plate converges into the North American Plate. In a

similar but opposite manner, the southward stepping San Andreas fault in the Salton Trough necessitates net extension.

Problems with Previous Kinematic Models

The present tectonic regime is usually modeled with western southern California attached to the Pacific Plate and moving about N35W relative to North America (e.g., Atwater, 1970; Anderson, 1971; Hill, 1982; Bird and Rosenstock, 1984). This relative motion is roughly parallel to the sections of the San Andreas fault north and south of the big bend. The Transverse Ranges, which span the big bend region, are commonly attributed to compression in a zone of collision between the Pacific and North American Plates. Several serious problems with this interpretation are discussed below.

1) The net shear strain rate across southern California, determined from recently estimated slip rates on southern California faults, does not add up to the relative Pacific-North American plate velocity (Weldon and Sieh, *in press*; Sieh and Jahns, 1984). By our estimate, one third of the total plate velocity of 56 mm/yr (Minster and Jordan, 1978; 1984) is presently not accounted for by major onshore faults in southern California. Other workers (e.g., Bird and Rosenstock, 1984) have addressed the problem of total slip rate across southern California, and have produced solutions that yield the relative Pacific-North American Plate motion. Recent information on the slip rates of the southern San Andreas fault (Weldon and Sieh, *in press*) and the San Jacinto fault (Sharp, 1981), however, constrains each of these rates to be about 10 mm/yr less than previously thought. These slip rates, and those of the other major faults in southern California that are considered in our model, are shown in

Figure III.2.

2) A mass balance problem exists if southern California is moving with the Pacific Plate because this direction of motion would require a great deal of convergence in the big bend region. A simple calculation for the amount of crust that would have encountered the big bend can be made. The width of the collision zone (normal to the relative plate motions) is about 150 km, and if we assume that the amount of convergence is equal to the offset on the San Andreas fault (about 300 km) and that the crustal thickness is 28 km, a volume of crust greater than one million km^3 must be accounted for. An unusually thin crust or a progressively widening big bend might reduce this volume, but it seems likely that at least one-half million cubic kilometers would have been consumed if this convergence occurred. The dominant contribution to this volume is crustal thickening in the Transverse Range area. Using the depth to Moho estimated by Hearn (1984b) and 28 km as an estimate for the "typical" crustal thickness in southern California, the volume of excess crust is only 140,000 km^3 .

3) There is little geologic support for large-scale Quaternary convergence in the central Transverse Ranges, and the convergence that has been found can be attributed to the local geometry of the fault system (Weldon, 1984a). If California south of the Transverse Ranges were moving with the Pacific Plate, at least 20 mm/yr of convergence would have to occur everywhere across the Transverse Ranges. Most of the convergence across the central Transverse Ranges occurs on the Sierra Madre-Cucamonga fault system (Figure III.1). However, activity here is estimated to be between 1 and 6 mm/yr (Ziony and Yerkes, 1984) and this is the only structure upon which a significant amount of Quaternary shortening has been found. In the eastern

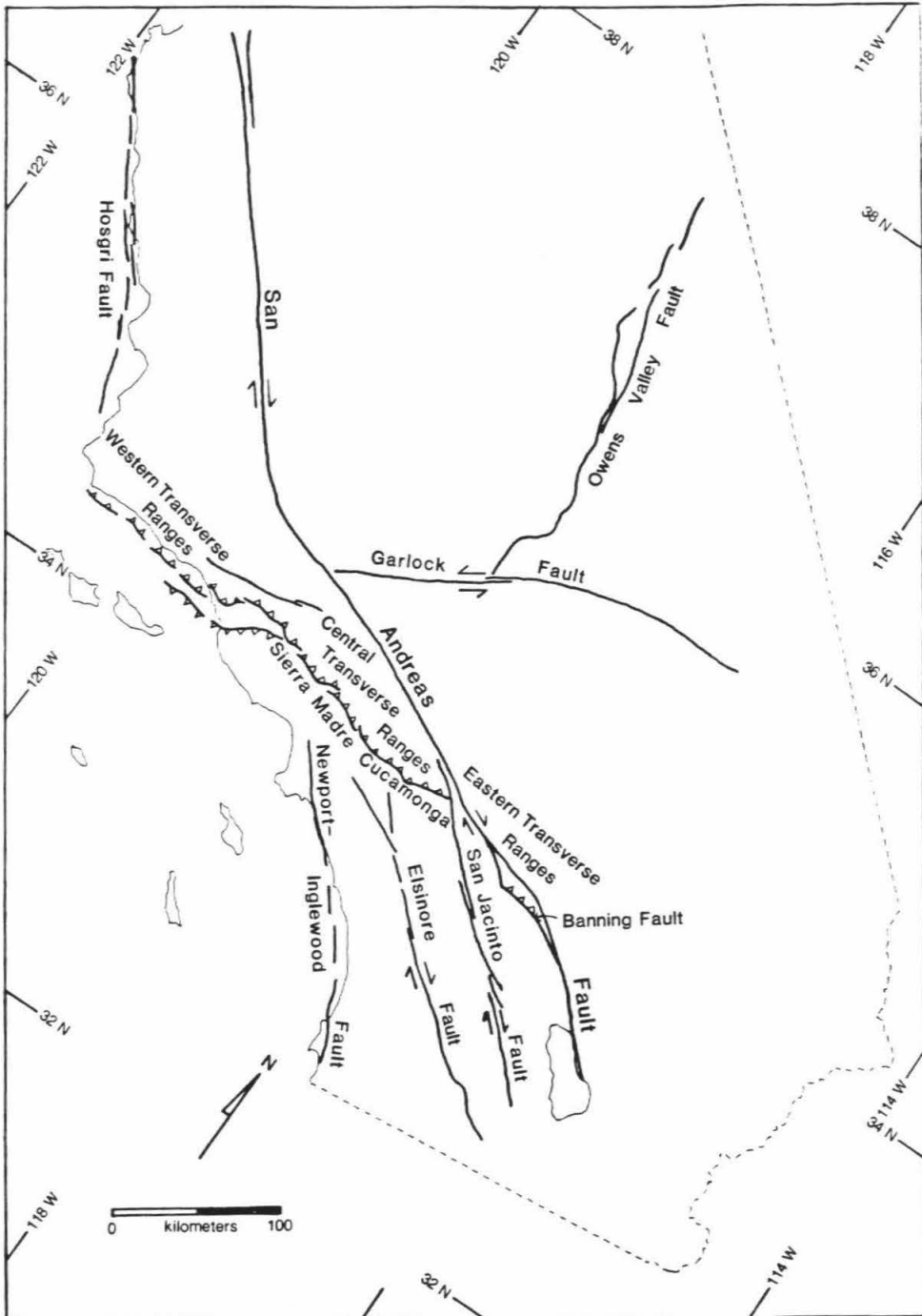


Figure III.1. The principal faults of southern California and the subdivisions of the Transverse Ranges referred to in the text. These faults are assumed to bound essentially rigid blocks which have been modeled as moving in directions consistent with the faults that bound them. The broad deformation with the western Transverse Ranges has been modeled as a simple boundary parallel to the trend of the ranges.

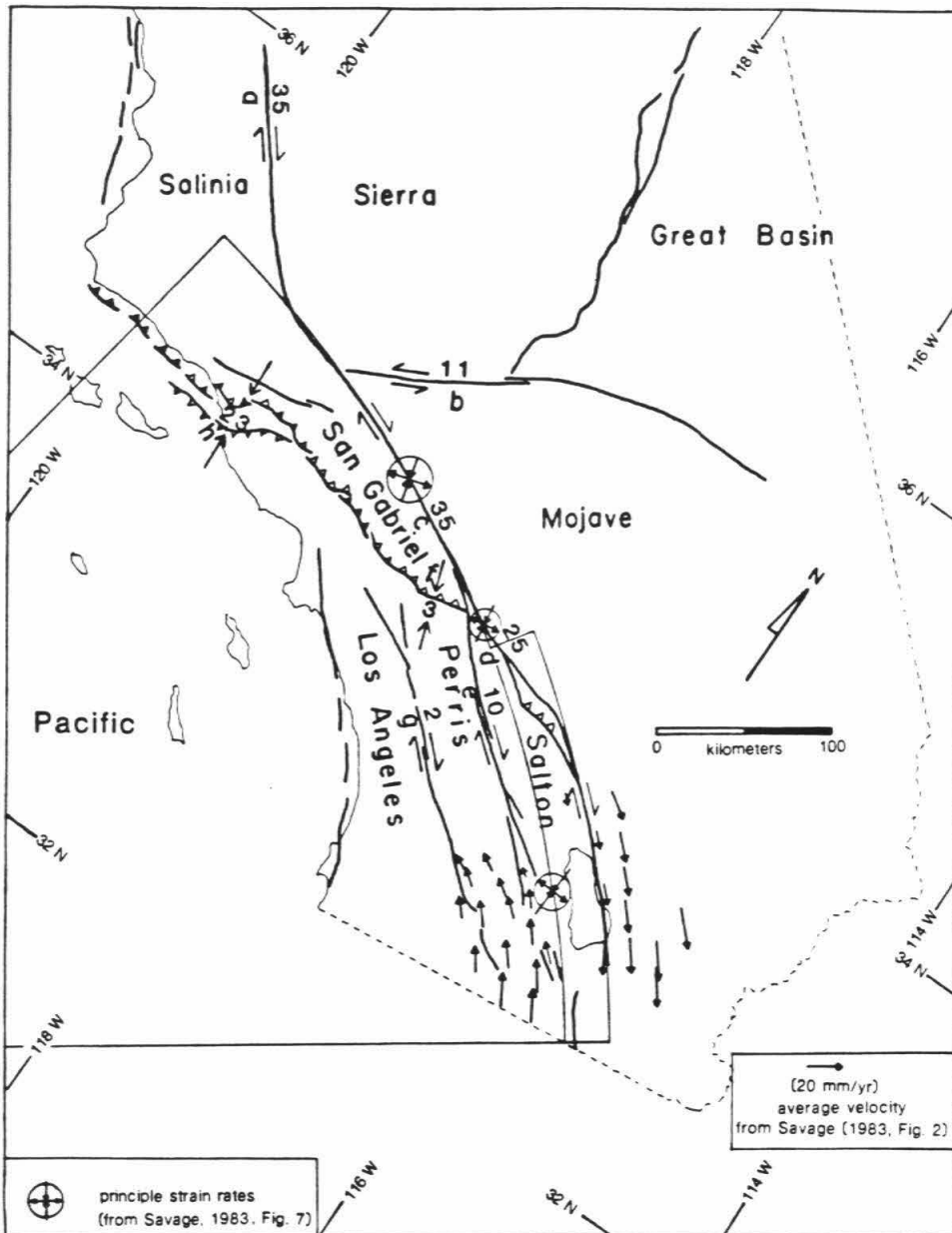


Figure III.2. The major blocks in southern California and the data used to calculate their relative velocities. The arcs have been fit to the trend of the San Andreas fault to determine the direction of motion of southern California south of the fault. Only the crust south of the big bend and east of the Pacific coast is thought to be rotating along the arcs. The principal strain rates from three trilateration networks in southern California and the average velocity field within the Salton network (Savage, 1983) are included to demonstrate the consistency of these data with the curvature of the fault. Slip rates (mm/yr) used in the model are located where the integration paths in Fig. 3 cross the faults. The letters associated with the rates give the sources of the information from which the rates were chosen: a) Sieh and Jahns, 1984; b) Carter, 1980: 1982; c) Weldon, 1984; d) Weldon and Sieh, 1984; e) Sharp, 1981; f) Matti et al, 1982; g) see text; h) Yeats, 1983.

Transverse Ranges considerable convergence may be assigned to the Banning strand of the San Andreas fault (Matti et al., 1984). Between these two regions of thrusting lies a section of the San Andreas fault 50 km in length along which little or no convergence has been documented (Figure III.1). Despite local northeast dips of the San Andreas fault in the area, features offset by the fault may be restored by pure strike slip motion (Weldon, unpublished mapping). In fact, extension locally takes place on faults north (Weldon, 1984a) and south (Matti et al., 1984) of the San Andreas fault in this area. It is impossible to appeal to simple northwest-directed collision between the North American and Pacific Plates to explain the Banning and Cucamonga thrusts without also having major convergence between them.

Other geologic observations constrain the amount of convergence that has occurred across the Sierra Madre-Cucamonga and San Andreas fault systems. The recognition of proximal early Pleistocene and late Pliocene sediments derived from the San Gabriel Mountains, both to the north (Barrows, 1979; Foster, 1980; Weldon, 1984b) and south (Matti and Morton, 1975; Morton and Matti, 1979) of these range bounding faults rules out large amounts of convergence. The detailed match of bedrock terrains, Tertiary deposits, and early Cenozoic structures across the San Andreas fault zone in the Transverse Ranges (e.g., Ehlig, 1981; Ehlig et al., 1975; Crowell, 1981; Silver, 1982; Powell, 1981) argues strongly against "consumption" of significant volumes of material across the San Andreas fault in the central and eastern Transverse Ranges since at least Miocene time.

4) It is difficult to understand how significant motion could occur on the southern San Andreas fault if the portion of southern California south of the big bend is moving in the Pacific Plate direction of Minster and Jordan (1978). The big bend

forms an impediment to the northwestward transport of southern California, producing a situation in which other crustal fractures are more favorably aligned to accommodate the shearing motion (e.g., the San Jacinto and Elsinore faults). Using a finite element method, Kosloff (1978) modeled the southern California crust as elastic blocks separated by relatively weak viscous faults. When driven by a far field shear oriented so as to drive NW directed right-lateral shear, he could not produce an active southern San Andreas fault because the more favorably located faults relieved the stress. This result has lead Kosloff (1978) and Humphreys and Hager (1984) to postulate that the mantle is contributing forces that drive the southern California crust toward the Transverse Ranges. But even including these mantle-derived forces, calculations suggest too little net force to allow for Pacific Plate directed motion (dynamic modeling section below). With the kinematic model suggested here, however, the magnitude of these forces is reduced to a level that can be supplied. A way of accomplishing this is by locally concentrating stresses in the active areas, while relying on an earlier episode of uplift and the strength of the mountains to account for the rest of the ranges.

5) Trilateration strain measurements (Savage, 1983) indicate nearly pure strike-slip motion occurs along the length of the San Andreas fault in southern California. These data indicate that the strain field remains non-convergent and rotates by the amount needed to keep it aligned with the local trend of the San Andreas fault. The principal strain axes across the three southern Californian networks are shown in Figure III.2. The lack of convergence is particularly striking in the central Transverse Ranges where the greatest amount of N-S strain accumulation would be predicted by existing models.

Overall, the evidence does not support Quaternary convergence in the central and eastern Transverse Ranges of large enough magnitude to be consistent with the current models of NW-directed motion of material south of the big bend. Local convergence does occur, but it can be attributed to either abrupt changes in fault trends or junctions between major faults. In fact, serious problems with the geology arise if major regional convergence is assumed during the Quaternary. There are further problems in reconciling the models proposing NW-directed motion and Savage's strain data (Savage, 1983).

Proposed Model

The proposed model has two major new features. First, we suggest that the material between the big bend and the Pacific Coast is moving around the big bend by rotating in a counter-clockwise direction about a pole located approximately 650 km SW of the San Andreas fault in the big bend region. This rotation allows movement along the San Andreas fault to be strike-slip both in the Salton Trough and in the big bend (Figure III.2), in agreement with the strain data of Savage (1983) and the slip rates discussed above. Note that, except for a relatively small step in the trend of the San Andreas fault near the south bend, the San Andreas fault fits remarkably well on a circular arc with its center at the proposed pole position. From the Salton Trough to the north end of the big bend, a distance of 400 km where we believe this rotation occurs, there are no deviations from the arc greater than three km other than the step at the Banning fault. Furthermore, the velocity field presented by Savage (1983) for the trilateration network across the Salton Trough is itself suggestive of rotation about a pole located in approximately the predicted

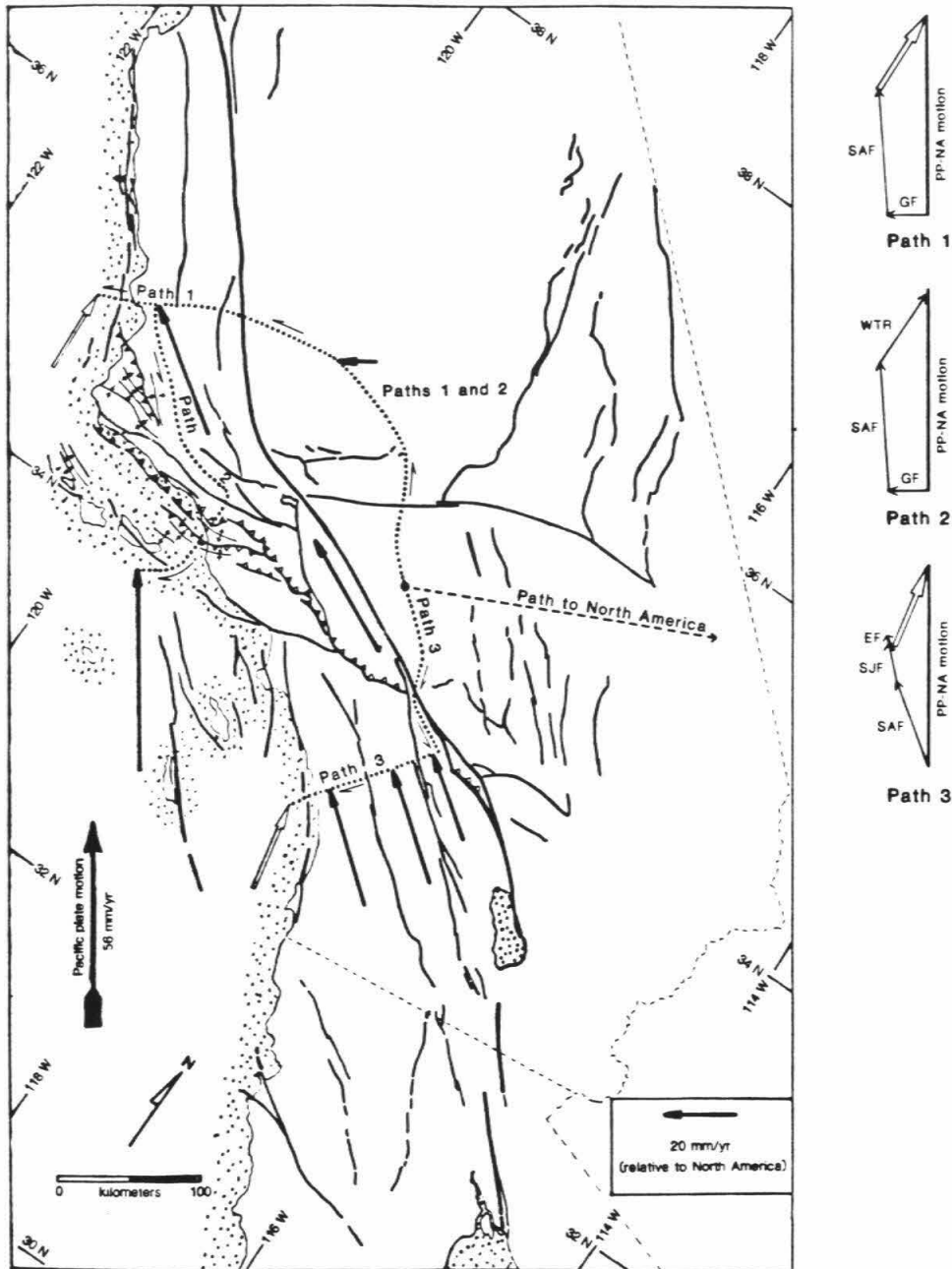


Figure III.3. Integration paths and slip rate vectors for the major blocks in southern California. Solid arrows are velocity vectors relative to North America for points along the path. The corresponding vector diagrams show the construction of these vectors. Because the southern California blocks are rotating about a relatively close pole, the velocity vectors vary across these blocks by a small but significant amount (see text). The corrections are shown in the vector diagrams as vectors with dots instead of arrow heads. The open arrows at the ends of Paths 1, 3, and 4 on the map and the vector diagrams are the discrepancy vectors (the motion needed to bring the velocity up to the relative velocity of the Pacific Plate given by Minster and Jordan, 1978). Only path 2 yields the total plate motion, implying that more than 1/3 of the plate motion is accommodated by structures close to or off the California coastline.

position (Figure III.2). Also, the net velocity acquired across the Imperial Valley net averages 35-40 mm/yr, in general agreement with our kinematic model.

The second feature of our model is that a significant amount of fault activity must take place in southern California west of the Elsinore fault. If the slip is occurring on NW trending faults like the Newport-Inglewood or other offshore faults, about 20 mm/yr of right lateral slip and 5 mm/yr of normal convergence is required. Other authors have proposed relatively large amounts of slip offshore (e.g., Anderson, 1979: ≥ 10 mm/yr) but our model is the first to integrate it into a complete description of the plate boundary.

A convenient way to test the internal consistency of this model is to perform line integrals of the strain rate between points of interest. If this is done between points on the stable North America Plate and the Pacific Plate, the total relative plate motion should be accumulated. This method has been described by Minster and Jordan (1984) and applied to a path across the Great Basin and central California. If all of the motion along any chosen path is considered, the results are independent of the path, and different paths connecting the same end points should yield the same results.

We have considered the four paths shown on Figure III.3. When the path over which the integration is carried out encounters no rotation or distributed deformation of the blocks, the integral reduces to a simple sum of the relative slip rate vectors across each velocity discontinuity, generally a fault. Paths 1 and 2 have been integrated in this manner. Paths 3 and 4, which cross blocks rotating on a relatively small arc, require accounting for continuous motion. For simplicity the overall deformation in the western Transverse Ranges is treated as though it were a single thrust

fault parallel to the trend of the major faults and folds in the area. The effects of errors in the slip rates are discussed separately in the next section.

The paths begin in the Mojave Desert, which we believe is essentially part of the North American Plate. A representative fiducial point is shown on Figure III.3. There are two reasons that lead us to believe that this is true. A path from cratonic North America to the Mojave Desert can be constructed south of the Great Basin that crosses very little significant Quaternary deformation (Figure III.3). Also, there is geologic and paleomagnetic evidence (Weldon et al., 1984; Dokka, 1983) that the Mojave region has not experienced the significant late Cenozoic rotations or deformations that many previous models require. Garfunkel (1974) and Calderone and Butler (1984) have proposed large-scale counter-clockwise rotations, and Luyendyk et al. (1980) and Bird and Rosenstock (1984) have proposed large-scale clockwise rotations within the Mojave Block, accompanied by major shear on the many NW trending faults that exist in the region. However, Dokka (1983) has demonstrated that these faults have not experienced enough total displacement to deform the Mojave significantly. This is in agreement with Diblee's earlier mapping (1961). Geodetic studies in the region give somewhat contradictory results. Sauber and Thacher (1984) have argued for about 5 mm/yr of net strain rate across the NW trending faults in the Mojave region, while King (*in press*) observes no significant strain accumulation over the same area. Furthermore, Weldon et al. (1984) have recently provided convincing paleomagnetic evidence indicating that the SW Mojave has rotated less than 4° since middle Miocene time. We have chosen to regard the Mojave region as being a part of North America. If this assumption is somewhat in error, we feel that the recently acquired data do not allow this error to be of too large a magnitude.

Path 1 begins by crossing the Garlock fault and continues onto the Sierra Nevada block. We assume that the trend of the Garlock fault west of the Owens Valley fault (i.e., west of the Great Basin) indicates the direction of motion of the Sierra Nevada block (S55W) and that the slip rate is 11 mm/yr (the best estimate of Carter, 1980; 1982). There is considerable uncertainty in the slip rate and direction ascribed to the Garlock fault, which will be addressed below. Though uncertainty exists, Carter's estimate provides the best constraint available today. The path continues across the Sierra Nevada block by heading west, and crosses the San Andreas fault. This contributes a vector parallel to the trend of the San Andreas fault (N40W) with a magnitude of 35 mm/yr (Sieh and Jahns, 1984). The result for the relative velocity vector of the Salinia block (relative to North America) is 38 mm/yr directed N58W. This leaves a discrepancy of 23 mm/yr oriented N5W that is needed to bring the net motion up to that of the Pacific Plate. The discrepancy vector is shown in Figure III.3 as an open vector located at the end of path 1. The discrepancy vector is similar to the preferred discrepancy velocity vector of Minster and Jordan (1984), though we find slightly more convergence in the region west of the San Andreas fault as a result of the more southerly drift of the Sierra Nevada block in our model. As noted by Minster and Jordan (1984), much of the discrepancy vector may be taken up on the San Gregorio-Hosgri fault system, and there is geologic support for this. Weber and Lajoie (1977) suggest a rate of 6-13 mm/yr of right-lateral slip for the fault, and Crouch et al. (1984) present evidence for considerable convergence across this and other faults west of the San Andreas fault.

Path 2 follows path 1 across the Garlock and San Andreas faults and then heads south through the western Transverse Ranges to the Continental Borderland. Yeats

(1983) calculated a rate of convergence across the Ventura Basin of 23 mm/yr for the last 200,000 years. More recent unpublished results from this area also give a high, though somewhat lesser rate of convergence (Rockwell, 1983: 17 ± 4 mm/yr). It is not yet known how the rate varies across the province or whether the numbers represent the total convergence across the western Transverse Ranges. We have chosen to use Yeats' published value, and we infer a direction of N5W, normal to the major faults and folds in the area (Figure III.2). Path 2 results in a relative motion (55 mm/yr, N35W), which is indistinguishable from that of the Pacific Plate (as shown in Figure III.3). This suggests that the borderland south of the western Transverse Ranges is moving with the Pacific Plate.

Path 3 crosses the San Andreas fault east of the junction with the San Jacinto fault and enters the Salton block, picking up a velocity of 25 mm/yr (Weldon and Sieh, *in press*) directed N55W, which is parallel to the tangent of the arc fit to the San Andreas fault where path 3 crosses it. From here the path turns SW and heads directly towards the pole of rotation. By heading in this direction the only effect of block rotation is to decrease the magnitude of the velocity vector linearly in such a manner as to attain a value of zero at the pole. The faults encountered along the path are treated as translations that supply velocity vectors that are simply summed to determine a net slip rate for any point along the path. Path 3 crosses the San Jacinto fault, picking up 10 mm/yr (the long term Quaternary slip rate of Sharp, 1981) directed parallel to the fault (N47W), and the San Andreas component decreases by 1.5 mm/yr due to the approach toward the pole of rotation. This results in a velocity vector for the Perris block of 33 mm/yr oriented N52W. Continuing to the SW the Elsinore fault is crossed next, adding about 2 mm/yr

(constraints on this number are discussed in the next section) of right-lateral motion oriented N49W, and passes onto the Los Angeles block. Subtracting an additional 1.5 mm/yr from the San Andreas component of motion for the continued approach towards the pole yields a velocity vector of 33 mm/yr directed N33W. The path is finally brought offshore and another 2 mm/yr is removed from the San Andreas component, yielding a net relative velocity vector of 32 mm/yr pointing N50W. The discrepancy vector at the terminus of path 3 is indicated in Figure III.3 with an open arrow that is 25 mm/yr pointing N11W.

If path 3 were to be continued to the terminus of path 2 a velocity vector would have to be included that nulls the discrepancy vector, implying the existence of a zone of significant dextral shear strain occurring between the Los Angeles block and the end of path 2. Because the north-south compressive deformation in the western Transverse Ranges seems to decrease toward the central Transverse Ranges, the Newport-Inglewood fault and/or other near-shore faults are thought to accommodate most of discrepancy vector 3.

Uncertainties in the Model

The description presented above is our best estimate, based on the data available, of the kinematics of southern California. The data are not well constrained in several critical areas. Possible sources of error include failure to consider strain resulting from smaller structures possessing unknown rates, and inaccurate parameterization of the structures treated. Ideally, uncertainties could be accumulated along the route of integration at the same time that the strain is calculated, so that an uncertainty could be given at any point (relative to the beginning of the path).

However, the nature of the uncertainties make them poorly suited to statistical treatment. The slip rates are the "best estimates" of the workers from their field areas, but the probability distribution of the estimates are often asymmetric and highly non-Gaussian. In lieu of a formal treatment of the error, we discuss probable sources and magnitudes of error and their quantitative effects on the block motions and on the overall kinematic model.

There is considerable uncertainty in both the magnitude and direction of motion of the Sierra Nevada block. Carter's slip rate of 11 mm/yr that we use in deducing the motion of this block is only absolutely constrained between 5 and 30 or more mm/yr (Carter, 1982). However, his best estimate of 11 mm/yr is based on several lines of geologic inference that we consider to be quite good. Also, his rate is for the portion of the Garlock fault east of the Owens Valley fault, while path 1 crosses the fault west of of this fault. The Owens Valley fault probably cannot contribute more than a few mm/yr even in its more active northern segment (Gillespie, 1982). We feel that the inactivity of the southern end of the Owens Valley fault allows us to extend Carter's estimate westward across the fault.

A related problem is that the Garlock fault is quite curved. We have chosen a trend of S55W because this is the trend of the fault in the region where it separates the Mojave block from the Sierra Nevada block, and should therefore best describe the block's local relative motion. Note that choosing this segment of the Garlock fault yields a slip vector orientation that points to the south more than will result from any other part of the Garlock fault. If translation of the Sierra Nevada block occurs in a more westerly direction, the motion of this block would be more in line with that chosen by Minster and Jordan (1984). The effect of increasing the slip rate

on the Garlock fault would be to increase the amount of convergence offshore north of the Transverse Ranges and would be consistent with a component of left-lateral shear occurring in the region of the western Transverse Ranges on E-W trending faults. A small amount of such deformation is known to be occurring there, though in our modeling this has been ignored. However, if the Sierra Nevada block moves westward by rotating about a pole located approximately 200 km to the southeast, as suggested by the curvature of the Garlock fault, the relative velocity vector should be rotated counterclockwise $20-25^{\circ}$ by the time the integration path reaches the San Andreas fault. The possibility of this rotational movement is also suggested by the northward increase in normal fault activity across the Owens Valley fault (Gillespie, 1982), and the presence of increasingly contractile faulting parallel to the Garlock fault west of where our path crosses the Sierra Nevada block (Figure III.3) (Davis and Lague, 1984).

In our model the movement of the Sierra Nevada block is estimated by using information on the Garlock fault. An alternative approach, chosen by Minster and Jordan (1984), is to consider a path that begins on stable North America and arrives at central California by crossing the Great Basin. Though uncertainties in the motions encountered along the path exist in both cases, we feel that there are fewer problems associated with the route we have chosen because of the relatively large degree of uncertainty in the rate and orientation of extension across the Great Basin. Other workers have assumed that some of the motion on the Garlock fault is due to deformation or rotation of the Mojave block relative to North America. We believe that it is entirely due to the opening of the Great Basin. The fact that the Garlock fault does not span the entire southern margin of the Great Basin may be a problem.

We feel, however, that an equally significant problem is produced by appealing to a mobile Mojave block, that is, the apparent absence of deformation on the eastern margin of this block.

Strain along path 2 in the region of the western Transverse Ranges is assumed to be purely convergent normal to the major faults and folds, and ignores the left-lateral faults that, combined, are believed to accommodate less than 2 mm/yr (Clark et al., 1983). The resulting velocity vector for an arbitrary point south of the zone of convergence is very close to the velocity vector for the Pacific Plate (Minster and Jordan, 1978; 1984). This suggests that most of the California borderland west of the end of path 2 (Figure III.3) is indeed part of the Pacific Plate.

Path 3 has the least amount of uncertainty associated with its relative velocity vectors. The slip rates and orientations of all three onshore strike slip faults crossed are fairly well constrained. For the San Andreas fault we use Weldon and Sieh's (*in press*) estimated rate of $24.5 \text{ mm/yr} \pm 3.5 \text{ mm/yr}$ and the orientation tangent to the circular arc shown in Figure III.2 that produces pure strike-slip motion along the San Andreas fault. Sharp (1981) has determined a rate of about 10 mm/yr on the San Jacinto fault, and we have chosen an orientation that on average best describes that fault. Estimates of the slip rate across the Elsinore fault vary from 1 mm/yr (Ziony and Yerkes, 1984) to 7 mm/yr (Kennedy, 1977). New work on the southern Elsinore fault ($\sim 4 \text{ mm/yr}$: Pinault and Rockwell, 1984) may help constrain the slip rate, but at the moment none of the estimates is as well constrained as the other slip rates encountered along path 3. In our model we arbitrarily chose 2 mm/yr to reflect the consensus that the northern Elsinore fault accommodates very little slip. If the lower estimate of 1 mm/yr is valid, it increases the discrepancy vector by a negligible

amount. A rate of 7 mm/yr reduces the discrepancy vector to about 20 mm/yr, a change of only 20%. No reasonable slip rate on the Elsinore fault can change the conclusion that a large fraction of the plate motion must be west of the Los Angeles block.

Another possible source of error in our model is the uncertainty of the pole position about which the blocks are rotating. This source of error must be small because the path covers less than 20% of the distance to the pole and was chosen so that no change occurs in orientation. The uncertainty in the pole position can contribute only a few mm/yr of error to the total. If the Salton Trough is opening with a component normal to the San Andreas fault, as has been suggested by Biehler (pers. comm., 1983), the pole may be farther away from the big bend region. This possible normal component in the Salton Trough, however, is not supported by Savage's (1983) strain data or by the arcuate fit of the San Andreas shown in Figure III.2.

Another route similar to path 3 could be taken to the San Gabriel block across the San Andreas fault NW of the San Jacinto fault and then across the Sierra Madre-Cucamonga fault to the Perris block. This is shown on Figure III.3 as path 4. Crossing the San Andreas fault picks up 35 ± 5 mm/yr (Weldon, 1984b) parallel to the San Andreas fault, N65W. This gives a velocity for the San Gabriel block which is similar to that found for the Salinia block with path 1. This is expected because there are no major active structures recognized between the two blocks. Counter clockwise rotation of the Sierra Nevada block along the curved Garlock fault (as discussed above) will result in Salinia moving with a magnitude and direction even more similar to that of the San Gabriel block. Crossing the Cucamonga fault to the Perris block adds 3 mm/yr (Matti et al., 1982; pers comm, 1984) to the relative velocity

vector and rotates it clockwise about 15° . The resultant Perris block vector (corrected for rotation accumulated by traversing the block to path 3) is virtually identical to that calculated with path 3. Again, the consistency of the results determined with different data sets along different paths tends to support the accuracy of the rates and the kinematic model. Also, because the Los Angeles block is moving parallel to the Perris block, about the same angular discordance remains between the San Gabriel block and the Los Angeles block as exists between the San Gabriel and Perris blocks. The change in orientation of the Sierra Madre-Cucamonga fault zone to the west will affect the relative amounts of convergence and lateral faulting along this boundary. Convergence on the Sierra Madre-Cucamonga fault system is largely responsible for the current uplift of the central Transverse Ranges. In our model this is due to the slightly different direction of motion of the San Gabriel block with respect to those to the south, and not to simple convergence between the Pacific and North American Plates.

Implications

An important feature of our kinematic model is the prediction of a zone of very active deformation offshore. This is a consequence of the discrepancy vectors for paths 1, 3 and 4 and the convergence in the western Transverse Ranges all being nearly the same (vector diagrams, Figure III.3). We propose that the discrepancy vectors for paths 1, 3 and 4 are accommodated on NW trending, predominantly strike-slip faults near the coast, while convergence on E-W thrusts and folds in the western Transverse Ranges accommodate the same motion there. The style of activity varies because the elements differ in orientation. In this "coastal system" the western

Transverse Ranges form a left step between the more NW trending offshore elements. Seismic studies support our model of a switch from predominantly strike-slip motion on northwest trending faults in the borderland to essentially pure convergence in the western Transverse Ranges (e.g., Corbett, 1984). Unfortunately, the length of the seismic record is inadequate to estimate rates of deformation. The diminishing of convergent deformation to the east and west of the western Transverse Ranges places the site of the offshore faulting near the coastline both north and south of the Transverse Ranges. This arrangement of active features defines a coastal system of active boundaries that separate the Pacific Plate to the west from a slice of relatively intact continental material to the east.

In southern California the coastal system is clearly exposed onshore only in the western Transverse Ranges (e.g., the Ventura Basin). Measurements of the rate and direction of convergence across the western Transverse Ranges at various longitudes may provide a direct means of quantifying the location, rate, and style of motion on the NW trending elements of the system that are not exposed onshore. We have calculated that the end of path 2 is moving with the Pacific Plate, but the distribution of activity on the faults within the borderland between the end of path 2 and the Los Angeles block cannot be determined until the distribution of the convergent activity in the Transverse Ranges east of path 2 has been worked out in detail, or until the slip rates of the offshore faults are determined. Another area where constraint on the activity of the coastal system may exist is in Baja California. Allen et al. (1960) report Quaternary deformation on the Agua Blanca fault that indicates up to centimeters per year of activity joining the Gulf of California with the California borderland. Yeats and Haq (1981) also describe active features that trend along the western

length of Baja, suggesting that some of the Pacific-North American plate motion does not enter the Gulf of California.

Another important consideration is the relation between the offshore activity and the value for the Pacific-North American Plate relative motion. We accept the plate motion value determined by Minster and Jordan (1978; 1984) and compare our integrated velocity to theirs. The motion on the NW-trending elements of the coastal system is determined by assigning the difference between the integrated strain and the Pacific-North American Plate motion on these features. We feel justified in doing this because it is consistent with the slip estimates determined by the extension of paths 1, 3 and 4 to the end of path 2, which is a purely internal determination. While the acquisition of the Pacific Plate velocity by the end of path 2 supports the Pacific-North American Plate rates of Minster and Jordan (1978; 1984), we do not intend that this be taken as strong evidence for the accuracy of their value. This is because we have accumulated a certain amount of uncertainty along path 2, and because their rates are based on a 3 m.y. average while ours are late Quaternary estimates. It is not yet known whether our model is valid for the tectonics prior to the late Quaternary. If the actual Pacific-North American Plate rate differs somewhat from the value determined by Minster and Jordan (1978; 1984), an internally consistent model could be produced by only adjusting the model convergence rate in the western Transverse Ranges. The quality of the data from the western Transverse Ranges, however, probably does not allow one to alter the model very much.

We agree with the conclusion of Minster and Jordan (1984) that the convergence across the Pacific-North American plate boundary is due to the westward motion of central California in response to the opening of the Great Basin, and not due to the

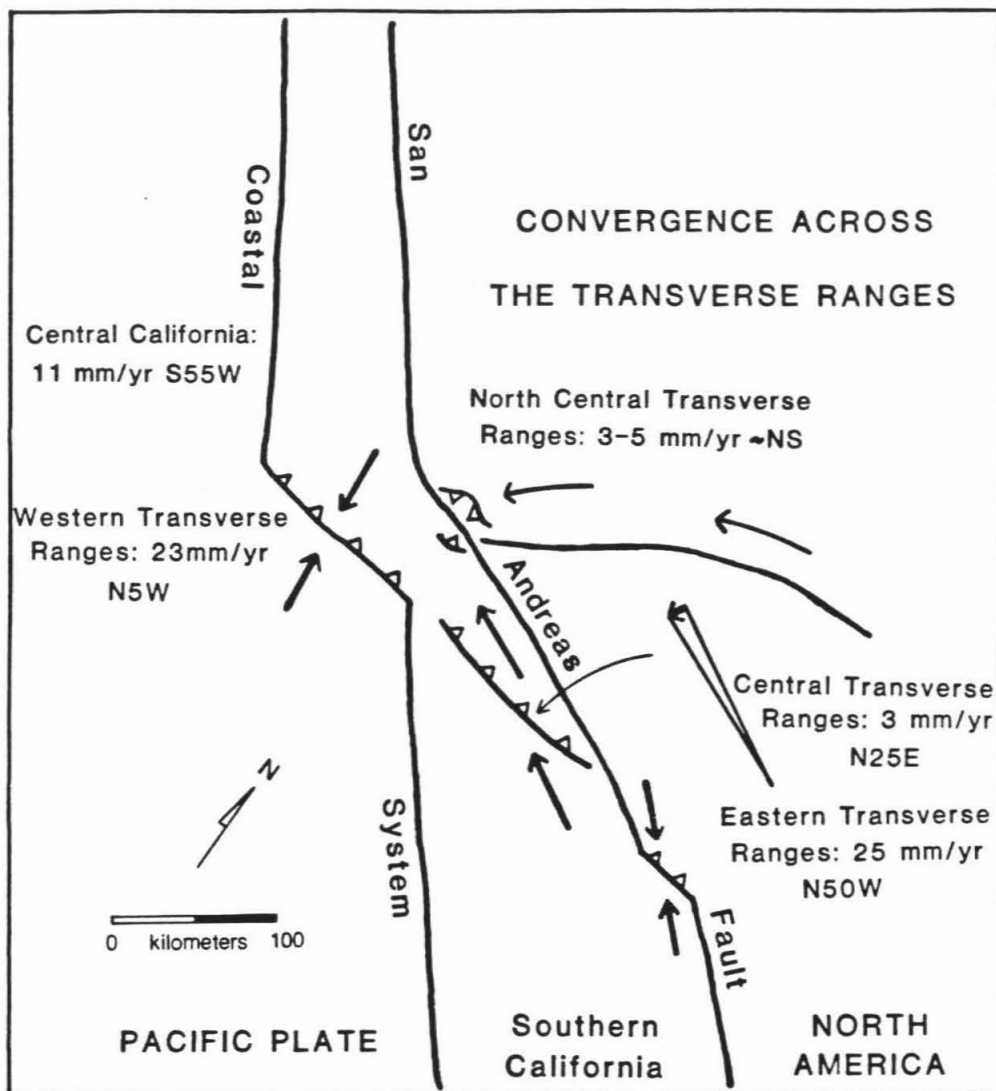


Figure III.4. Schematic representation of the active deformation in the Transverse Ranges. The eastern TR are being uplifted by convergence across a left step in the San Andreas fault in the Banning Pass area, indicating a rate of convergence of 25 mm/yr oriented N50W. The western TR are being shortened by a similar left step in the postulated coastal system at a rate of 23 mm/yr in the direction N5W. The central TR are only experiencing minor rates of convergence due to the direction of motion of the San Gabriel block and southern California. The direction and magnitude of this convergence are very sensitive to the slip rates on the other nearby faults, and are therefore difficult to deduce accurately from the model. Simply determining the difference in motion between the San Gabriel block and the Perris block results in 3 mm/yr directed N25W. If the Sierra block is moving to the west by rotating along the curved portion of the Garlock fault, 3-5 mm/yr of N-S convergence is necessary in the region of the SW corner of the Sierra block. North of the Garlock fault there is about 11 mm/yr of convergence east of the San Andreas fault in a direction that is normal to the local trend of the fault.

QUALITY A EVENTS DEEPER THAN 15 KM, 1977-1981

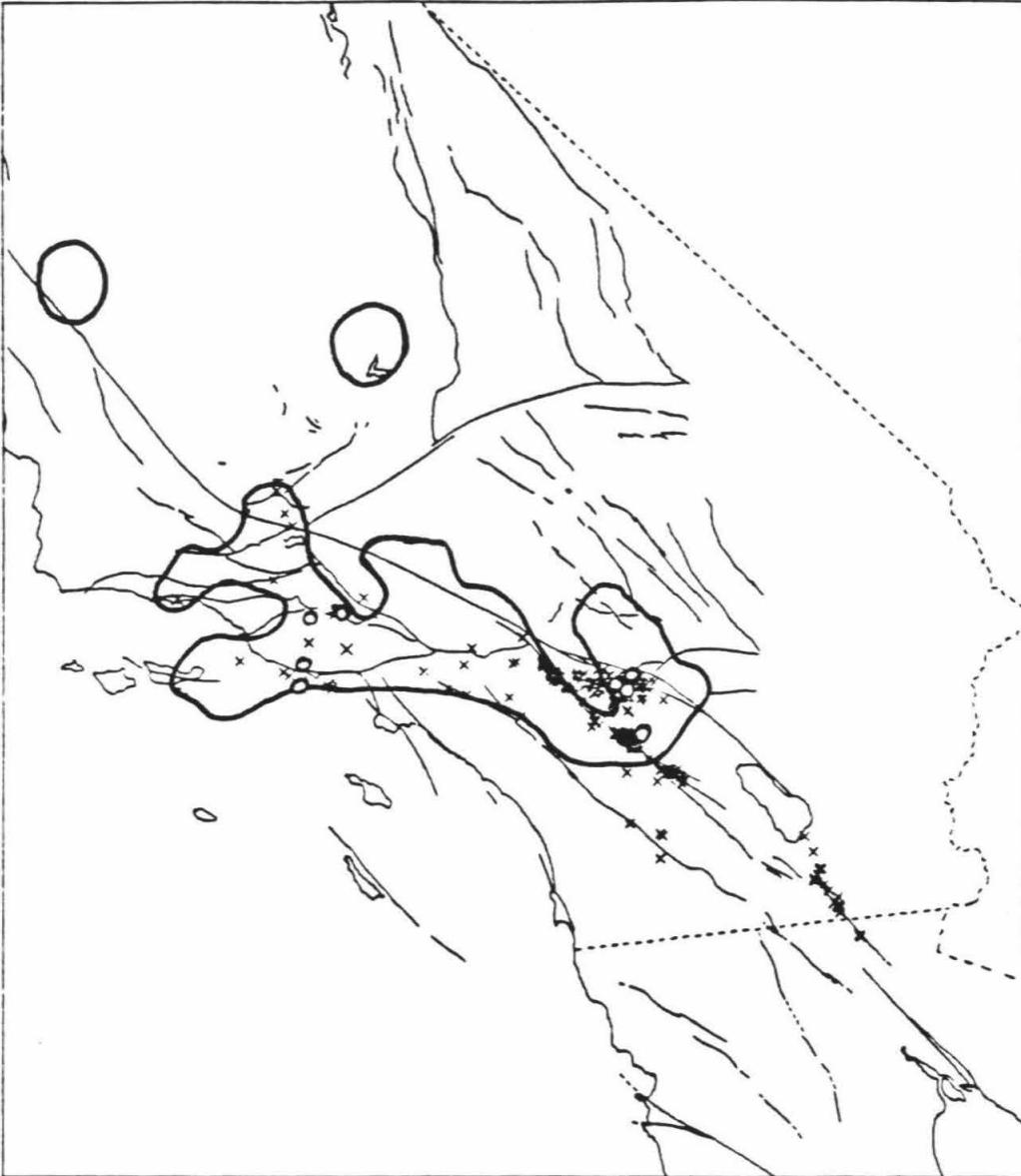


Figure III.5. Location of deep quality A events in southern California between the years 1977-1981 (from Corbett, 1984). The "x" symbols represent events of depth 15-20 km, and the "o" symbols are for events deeper than 20 km. Also shown is the region of the crust having velocities greater than average for southern California crust by at least 3%. There is a strong correlation between deep events and high velocity crust. Also of interest is that the locations where events deeper than 20 km occur are beneath the sites where the kinematic model has exceptionally large rates of convergence.

geometry of the San Andreas system. We feel that the simpler tectonic elements used to infer the motion and rate of the Sierra Nevada block in our model allows for a more constrained estimate than does theirs. Further, if the Sierra Nevada block is rotating west, as suggested by the curvature of the Garlock fault, the convergence in the Transverse Ranges near the junction of the Garlock fault with the San Andreas fault can be explained by the impingement of the SW corner of the Sierra Nevada block into the Salinia-San Gabriel block. We feel that this satisfies the geology (Davis and Lagoe, 1984) better than appealing to the geometry of the San Andreas-Garlock junction.

Finally, our model suggests origins for the tectonic activity in the Transverse Ranges that differ from previous accounts. These ranges have long been taken as evidence that southern California, as part of the Pacific Plate, is colliding with North America in the big bend region. However, our model (Figure III.4) produces uplift in the eastern Transverse Ranges with convergence across a step in the otherwise arcuate and strike-slip southern San Andreas fault. The convergence across this small step is 25 mm/yr oriented N50W. The central Transverse Ranges are being uplifted by the Sierra Madre-Cucamonga fault system. Convergence across this boundary is due to the different directions of motion of the San Gabriel block and the blocks to the south. As shown in Figure III.4, this geometry requires about 3 mm/yr of convergence across this zone. Convergence in the western Transverse Ranges is due to a left step in the "coastal system", and is probably unrelated to the San Andreas fault. Corbett (1984) notes that all well-located earthquakes which occurred deeper than 20 km, and most which occurred deeper than 15 km (from 1971-1981), were either in the Banning Pass area or in the western Transverse Ranges. We explain this as being

due to the existence of cold, brittle material at an unusually great depth as a result of the exceptional degree of convergence occurring within these locations. This is supported by the anomalously high seismic velocity of the deep crust in the same locations (Figure II.14). Figure III.5 shows the location of the deep earthquakes for the years 1971-1981 (from Corbett, 1984) along with the location of the high-velocity crust as indicated by the +3% velocity contour (Figure II.14).

We feel that the major uncertainties in the tectonics of southern California derive themselves from processes external to the region modeled. The opening of the Great Basin appears to control the motion of the Sierra Nevada block, which in turn controls the amount of convergence near and off of the central California coast. It is also felt that the similarity in motion of the Salinia block with that of the San Gabriel block suggests that the extension in the Great Basin (which controls the motion of the Salinia block) is related to the rotation of southern California (which controls the motion of the San Gabriel block). Furthermore, the degree to which the Mojave block is part of North America directly affects the amount of strain required offshore to satisfy the plate boundary conditions. The value chosen for the instantaneous plate velocity affects the estimates of offshore activity in a completely analogous way. In spite of these external uncertainties, it is the internal consistency of the model, which includes the coastal system through the convergence documented in the western Transverse Ranges, that suggests to us that the kinematics of southern California is now reasonably well understood. The single tie across the western Transverse Ranges to the borderland leaves the coastal system as the least certain part of the model, but the agreement of the velocity at the end of path 2 (which crosses the western Transverse Ranges) with the externally derived value for the

velocity of the Pacific Plate (Minster and Jordan, 1978; 1984) lends additional support for the oblique slip nature of the coastal activity. The magnitude of the offshore activity implies that the region between the San Andreas fault and the coastal system may be thought of as a miniplate that is neither part of the North American Plate or the Pacific Plate.

3.3 Late Cenozoic History of the San Andreas fault

The geometry of the San Andreas fault system south of San Francisco is geometrically unusual at two locations: at its southern end, where it terminates via a right step to the Imperial fault; and through the big bend region where the San Andreas fault takes a broad left step. The coincidence of the major sub-lithospheric features (Chapter II) with these peculiar portions of the San Andreas fault (and their associated geomorphic provinces: the Salton Trough and the Transverse Ranges) strongly suggests the existence of a relation between these surficial features and those found at depth. This emphasizes the need to understand the relation between the kinematics of the lithosphere and the underlying mantle. Knowledge of the slip history on the San Andreas fault and of the development of the big bend are fundamental to this. Surprisingly, this history is rather poorly understood. The present kinematics and the observed net displacements of the San Andreas fault are important constraints.

While the timing of the slip along the San Andreas fault is not well-known, it is generally agreed upon that prior to 30 m.y.B.P. the tectonics were dominated not by strike-slip faulting, but rather by subduction off the California coast. This began to change at about 30 m.y.B.P. when the North American Plate started to override the

East Pacific Rise. Atwater (1970), and Dickinson and Snyder (1979) have discussed the transition to transform style tectonics along the North American-Pacific Plate boundary. As the spreading center was overridden, an ever widening offshore strike-slip margin became the plate boundary. Along the strike-slip margin no new oceanic crust was created, and a "window" in the downgoing Farallon Plate opened with its continued subduction (Dickinson and Snyder, 1979).

It has often been stated that the opening of the Gulf of California occurred when the transform plate boundary jumped from its position offshore to the San Andreas fault (Wilson, 1965; Atwater, 1970, Moore and Curray, 1982). Evidence in the mouth of the Gulf, including magnetic anomalies out to anomaly 3 and tectonic disruption of the continental margins, suggest the southern Gulf opened about 4 m.y.B.P. (Larsen et al., 1968) to 5.5 m.y.B.P. (Moore and Curray, 1982), and that since this time the observed ~ 300 km of offset has occurred, as documented in the mouth and along the San Andreas fault system in both central and in southern California.

A review of the literature, however, reveals a more complicated and less certain history. In order to acquire ~ 300 km of offset on the San Andreas fault in conjunction with the opening of the Gulf of California the entire North America-Pacific Plate rate (56 mm/yr, Minster and Jordan, 1978) must have been wholly on the San Andreas fault for the duration of 5.5 m.y. (the earliest estimate for the opening of the Gulf), as suggested by Moore and Curray (1982). If the present 35 mm/yr of slip on the San Andreas fault has been operative for some time there is a need for pre-Gulf of California slip on the San Andreas fault, and in fact the evidence recently accumulating on the late Quaternary slip rates precludes the San Andreas fault from presently

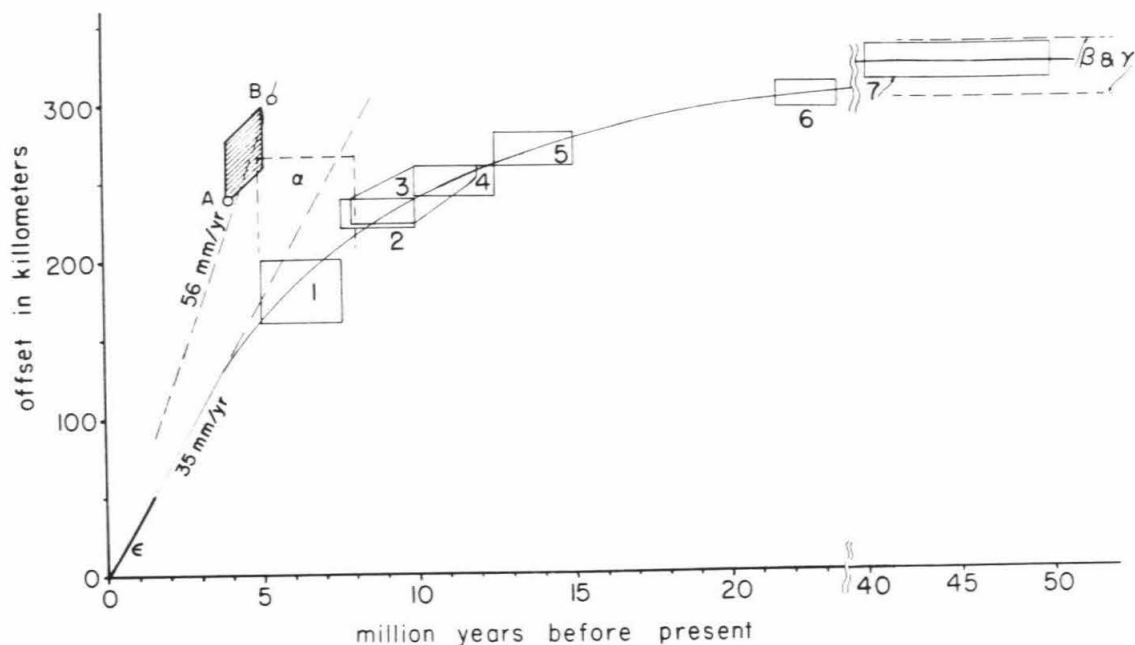


Figure III.6. Offset versus age for the San Andreas fault and the opening of the Gulf of California. The symbols give the region from which the information came and the workers who published the estimate. Arabic numerals are for the northern San Andreas fault, Greek letters for the big bend and southern sections of the San Andreas fault, and capital Roman letters are for the mouth of the Gulf of California.

Arabic numerals:

- 1) Dickinson et al. (1972)
- 2) Dickinson et al. (1972)
- 3) Huffman (1972)
- 4) Dickinson et al. (1972)
- 5) Dickinson et al. (1972)
- 6) Huffman (1972)
- 7) Dickinson et al. (1972)

Greek letters:

- α) Crowell (1981)
- β) Crowell (1981)
- γ) Ehlig (1981)
- ϵ) Weldon (in press)

Roman letters:

- A) Larson (1968)
- B) Moore and Currey (1982)

The San Andreas fault's most recent episode of slip began prior to 15 myBP, while apparently the opening of the Gulf of California has been a more recent occurrence. This situation requires a portion of the relative Pacific Plate rate to be occurring on other features. See text for more discussion.

carrying the total plate rate (as has been discussed in detail above). Furthermore, Weldon and Meisling (in progress) estimate that the San Andreas fault has been slipping at its present ~ 35 mm/yr for at least the last 1.5 m.y. Apparently, some of the San Andreas fault slip occurred prior to the opening of the Gulf.

In trying to understand the earlier slip history, there is a scarcity of high quality data from which to infer a San Andreas fault slip rate, especially south of the big bend. The information on the San Andreas fault found in the literature is shown in Figure III.6. (This figure is similar to one compiled by Atwater and Molnar, 1973.) The solid polygons labeled with Arabic numerals represent data pertaining to the San Andreas fault north of the big bend, while dashed polygons labeled with Greek letters represent data in and to the south of the big bend. Nilsen and Link (1975) give evidence as well as cite work to support the general inactivity of the northern San Andreas fault for at least the 30 m.y. preceding 20 m.y.B.P. Since this time the northern San Andreas fault has experienced about 300 km of slip. Huffman (1972) and Dickinson et al. (1972) present evidence that the San Andreas Fault was active prior to 10 m.y.B.P. Dickinson et al. (1972) discuss evidence for an offset across the San Andreas Fault of about 160-200 km since 5-7.5 m.y.B.P., which implies, roughly, a maximum of only 200 km of slip since the opening of the Gulf of California. These are loosely constrained values, but are rather mutually consistent. The estimates are shown as polygons in order to represent the range of uncertainty suggested by the respective authors (Figure III.6).

In the big bend region the San Gabriel fault (at one time an active branch of the San Andreas fault) appears to have been active prior to the date given for the opening of the Gulf. Crowell (1982) suggests that about 60 km of offset have occurred

here since 14 m.y.B.P. but before 5 m.y.B.P. Ensley and Verosub (1982) present paleomagnetic data that indicate activity had started here by 8.5 m.y.B.P.

South of the big bend, offset of the Pelona-Orocopia Terrains tells of a similar amount of net slip. Crowell (1982) suggests that the San Andreas fault has ~ 270 km of offset, which when combined with the ~ 60 km on the San Gabriel fault implies a total slip of about 330 km. Ehlig et al. (1979), agreeing with ~ 60 km of offset on the San Gabriel fault but preferring only ~ 240 km on the San Andreas fault, estimate a slightly smaller amount of total slip, about 300 km. Structure on which motion from the northern San Andreas fault could have avoided the southern San Andreas fault in the last 10 m.y. is not found, and it is most probable that the northern and southern sections of the San Andreas fault acted together as a single fault, though especially in the big bend this possibly did not occur along the trace that is presently active (Powell, 1981).

The history most compatible with the observations is one of an early, relatively slow but accelerating rate of slip on the San Andreas Fault beginning approximately 15-20 m.y.B.P. This motion appears to have accounted for at least 60 km of slip prior to the opening of the Gulf of California. In the big bend region, about 60 km of the slip appears to have occurred on the San Gabriel fault, and it is possible that additional slip may have occurred along other strands of the paleo-San Andreas fault System (Powell, 1981). The rate of slip probably continued to increase until it reached about 35 mm/yr approximately 4-5 m.y.B.P., a rate which it presently sustains. The final, constant velocity phase seems to be the portion of the history temporally related to the rifting of Baja California documented in the mouth of the Gulf

of California.

There is a fair amount of uncertainty in the above scenario, but it is difficult to tie the opening of the Gulf of California (as it is thought to have occurred) directly to motion on the San Andreas fault. As pointed out by Weldon (pers. comm.), this suggests that the ~ 300 km of offset seen both in the Gulf of California and also along the San Andreas fault must be, to some extent, coincidental.

Regarding the convergence history of the velocity field in the Transverse Range region, the geology supports a few statements of constraint. Ensley and Verosub (1982) argue that convergence in the vicinity of the Ridge Basin was active between 5-8.5 m.y.B.P., and was especially active around 7 m.y.B.P. The preservation of the Sierra Pelona, on the other hand, attests to the lack of regional convergence since the time that this terrain passed the Banning Pass area and entered the big bend. Using the slip history suggested above (Figure III.6), this time would have been about 5 m.y.B.P. Since about 5 m.y.B.P., then, it is thought that the motion in the big bend region has been predominantly non-convergent, though no evidence has been found ruling out the possibility that this non-convergent geometry existed for some time prior to that when the Sierra Pelona encountered the Banning Pass. It is possible that a major episode of uplift occurred in the Transverse Ranges prior to 5 m.y.B.P., but it may also be possible that the uplift of the Transverse Ranges has occurred as a sequence of local uplifts similar to that seen presently occurring north of the Banning Pass area today, and that the especially active ~ 7 m.y.B.P. convergence in the Ridge Basin area was one such local occurrence.

Activity on the Garlock fault is also an important consideration, for motion on this fault results in the widening of the big bend. Presently the Garlock fault plays

the role of an "intra continental transform" (Davis and Burchfiel, 1973) between the active northern Basin and Range and the now quiescent southern Basin and Range. These authors suggest that about 60 km of total slip have occurred on the Garlock fault west of the Sierran front. Zoback et al. (1981) give 10 m.y.B.P. as the initiation of northern Basin and Range extension and the cessation of the southern Basin and Range activity. If the Garlock fault developed out of kinematic necessity related to this activity, it may have begun slipping about 10 m.y.B.P. Based on geologic evidence Carter (1980; 1982) prefers a recent slip rate of about 11 mm/yr. At this rate the 60 km of net slip would have occurred in only about 5 m.y. If the Basin and Range history suggested by Zoback et al. (1981) is correct, this suggests that the Garlock fault has itself experienced an accelerating slip history similar in form to Figure III.6 (though smaller in magnitude).

3.4 Three Dimensional, Constant Viscosity Dynamic Modeling

This section is a natural continuation from the results of the seismically determined P wave velocity structure studied in Chapter II. It is assumed that variations in seismic P wave velocity are positively related to density variations, and that the seismic structure mapped in Chapter II can therefore be used to infer a density structure. In a viscous mantle these density variations will drive flow. It should be expected that the features in the mantle are related to tectonic activity in the crust, and, in fact, that association is striking. The major high-velocity anomaly is situated directly beneath the Transverse Ranges (Figure II.14), and the major low-velocity anomaly lies beneath the general region of the Salton Trough. It is the purpose of this section to investigate this association by constructing simple models of the earth

beneath southern California and comparing the predictions of these models with the observed response of southern California: i.e., the gravity field, the stress field, and the slip history.

Ideally, modeling would be three-dimensional, with rheology that is dependent upon the local environmental parameters. Unfortunately, at present this is beyond our ability to handle. We will therefore determine the 3-D flow field by assuming the mantle to be a constant viscosity half-space. With these assumptions the flow field becomes linear and a Green's function approach may be used.. The mantle is considered to be constrained by a no-slip boundary at the surface of the half-space. With the z-axis in the vertical direction, this surface is the horizontal plane $z=0$. The density distribution that drives the flow is assumed to be related to the P wave velocity by a positive, monotonic expression. When modeling the lithospheric stress, a uniform plate of constant elastic thickness is included to simulate the existence of the lithosphere.

This modeling is designed to include the major features that are thought to be important in the production of the stress and gravity fields. The primary justification for this simple approach is that it is the major effects resulting from the density perturbations that we wish to determine, and that more complicated modeling is both difficult to implement and that the complications are themselves often poorly understood. Intuitively, this modeling is expected to give reasonable results; flow patterns will generally develop with heavy material sinking and light material rising, and the influence of an anomalous region diminishes away from that region. These fundamental qualities are embodied in the simple flow model used. It is realized that the two assumptions about the material properties (constant viscosity half-

space and uniform elastic lithosphere) are unrealistically simple, and in some situations will produce inaccurate results. Viscosity is certain to vary, and these variations relate directly to the nature in which a perturbation at one point will couple to the surrounding region. Also, while the use of a uniform elastic plate in the stress modeling is certainly not representative of the southern California lithosphere, actual lithospheric variations are not expected to vary so rapidly that this assumption does not generate useful results.

The other major assumption, that of the P wave velocity (V_P) to density (ρ) scaling, is a more certainly defined relation. This scaling relation is calculated here with parameters found in Anderson and Bass (1984). Using the relations $dV_P/dT = -5.2 \times 10^{-4} \text{ km/sec } C^0$ (from Figure 1) and $d\rho/dT = -6.2 \times 10^{-5} \text{ gm/cm}^3 C^0$ (from values in Table 1, evaluated at 1200^0C), one finds that $\Delta V_P = -1\%$ corresponds to material that is about 160^0C cooler and 0.30% denser than normal mantle of the same depth.

The probable existence of partial melt beneath the Salton Trough, however, may locally complicate the situation. If there is partial melt beneath the Salton Trough, then the important questions are: what is the amount of partial melt that is implied by the observed velocity structure; and what is the proper V_P^p scaling and thus density of the upper mantle beneath the Salton Trough? Simply applying the above scaling relation to the anomaly beneath the Salton Trough, which in the uppermost 100 km has a general minimum in V_P of about 4%, gives a temperature about 650^0C above the average southern California value. For any reasonable geotherm this temperature is far above the solidus, suggesting the existence of partial melt.

The probable existence of partial melt in this region is supported by the lack of an electrical resistivity basement at any depth, with inferred resistivity values for the crystalline basement rock of between 1-20 Ωm (Humphreys, 1978). This situation is similar to that found by Oldenburg (1981) for the resistivity structure beneath very young ocean (~ 1 ma), where resistivity was found to drop rapidly to 20-30 Ωm at a depth of about 50 km. He interpreted this to be due to 5-10% partial melt. While other conductivity mechanisms may account for a portion of the low resistivity found by Oldenburg, it seems probable that the extremely low magnitude of the resistivity value is due at least in part to partial melt (Roberts, 1983).

Mavko (1980) calculates that a 5% partial melt in a tube geometry will produce a 5% depression in V_P , and that the relation between fraction of partial melt and V_P is nearly linear. This result is for polycrystalline olivine at 20 kbar and 1600 $^{\circ}\text{C}$, though very similar results are obtained for pyroxene, and Mavko argues that the result is not expected to be strongly dependent upon composition. Thus the 4% velocity anomaly beneath the Salton Trough can be explained with a 4% partial melt. However, it is possible that the average temperature beneath southern California within the depth range where the anomalously slow material is observed (i.e., between about 50-100 km) is somewhat below the solidus temperature, and that a portion of the observed velocity anomaly is a result of elevating the temperature of the (solid-state) material beneath the Salton Trough to the solidus. Considering the uncertainties in the knowledge of the average southern California geotherm and the pressure-temperature position of the solidus, a potential range for the temperature difference between the average geotherm and the solidus over the depth range 50-100 km is about 0-160 $^{\circ}\text{C}$. This range in temperature can account for 0-1% variation in V_P ,

suggesting that the amount of partial melt is somewhere between 4–3% for the slowest portions of the Salton Trough anomaly.

The map of seismic velocity (Figure II.14) indicates that the strongly anomalous material is, in lateral extent, considerably broader than the Salton Trough itself. The above arguments suggest that some if not most of this region is partially molten. This possibility of a broad zone of partial melt is supported by electrical measurements made in the region. It has been noticed that the telluric field is strongly polarized in the NW-SE direction within the Imperial Valley at the higher frequencies, that is, for frequencies whose skin depths are shallower than the thickness of the sediment fill (Humphreys, 1978). This is expected because the Salton Trough is a high conductivity channel oriented in the direction of polarization. However, for periods that are large enough to sample significant portions of the basement, the strong polarization gives way to an unpolarized field. The implication is that the conductive basement material is not confined to a channel-like geometry, but is rather broad.

Another data set that should be addressed is the relative frequency content of teleseismic arrivals. If the Salton Trough region is one of partial melt, it might seem natural to expect that the Q is diminished and that the teleseismic arrivals will be locally attenuated. This attenuation is not observed, and in fact the arrivals that traverse the exceptionally low velocity region are relatively enriched in high frequencies (Humphreys, unpublished data). Mavko (1980), however, reasons that the bulk attenuation of a partial melt is not an important factor at frequencies of seismic interest. Thus, while the high Q is not explained, a low Q is not actually expected.

The final question to be addressed regarding partial melt is that of the influence of partial melt on the bulk density of the affected material. Rigden et al. (1984) have

determined that the fluid phase is about 10% less dense than the solid phase for pressures in the range appropriate to the uppermost mantle considered here. Stolper et al. (1980), addressing the density of only the basaltic melt fraction, determine about two-thirds of this value. A partial melt of 4%, which above was associated with a 4% change in V_P , results in a smaller density contrast of about a 0.3-0.4% decrease in the bulk density when using the estimates of Stolper et al. (1981) and Rigden et al. (1984), respectively. In comparison, a 4% change in V_P due to the solid-state thermal expansion is expected to produce a 1.2% decrease in bulk density.

This information can be used to estimate the effect of partial melt beneath the Salton Trough on the body forces expected there. If a temperature of 0-160°C is needed to bring average southern California geotherm to the solidus over the range of depth possessing the anomalously low V_P , a 0-0.3% decrease in density and a 0-1% decrease in V_P is expected. In order to achieve a 4% reduction in V_P , a partial melt of 4-3% is then required, adding a further 0.4-0.3% decrease in density for a net reduction in density of about 0.4-0.6%. (This is using the less extreme density contrast of Rigden et al. (1984), though the estimate of Stolper et al. (1981) may be more applicable to the partial melt situation. The difference between the two estimates, however, is not large. It is seen, then, that the effect of a reasonable amount of partial melt beneath the Salton Trough will reduce the body forces there, for the most anomalous regions encountered, by a factor of 3-1.5.

Modeling proceeds by associating with each block a body force that is the result of its buoyancy. The vector flow field is determined by calculating the flow field resulting from an individual block's body force, and superimposing all of the blocks' flow fields to get a net flow. The superposition of fields is justified because of the

linearity of the problem when viscosity is spatially invariant. The response of a single block is well approximated by the flow resulting from a vertical point force, F (due to the block's excess mass), located at the center of the block. The flow field within a constant viscosity half-space bounded with a no-slip surface is given by (Blake and Chwang, 1974)

$$v_x = \frac{xF}{8\pi\eta} \left[\frac{r_z}{r^3} - \frac{R_z}{R^3} + \frac{2h}{R^3} - \frac{3h(R_z^2 - h^2)}{R^5} \right] \quad \text{(III.1a)}$$

$$v_y = \frac{yF}{8\pi\eta} \left[\frac{r_z}{r^3} - \frac{R_z}{R^3} + \frac{2h}{R^3} - \frac{3h(R_z^2 - h^2)}{R^5} \right] \quad \text{(III.1b)}$$

$$v_z = \frac{F}{8\pi\eta} \left[\frac{1}{r} - \frac{1}{R} + \frac{r_z^2}{r^3} - \frac{R_z^2}{R^3} - \frac{2h}{R^5} (3R_z^2 - R^2)(R_z - h) \right] \quad \text{(III.1c)}$$

where the roles of the variables are indicated in Figure III.7. The shear tractions at the base of the lithosphere are given by $\eta dv_i/dz$, where v_i is the velocity in the i^{th} direction. The normal traction is determined directly from the equation for pressure given by Blake and Chwang (1974). The results are

$$\sigma_{zx} = - \frac{3h^2F}{2\pi} \frac{r_x}{r^5} \quad \text{(III.2a)}$$

$$\sigma_{zy} = - \frac{3h^2F}{2\pi} \frac{r_y}{r^5} \quad \text{(III.2b)}$$

$$\sigma_{zz} = - \frac{3h^2F}{2\pi} \frac{h}{r^5} \quad \text{(III.2c)}$$

where σ_{zi} is the component of stress acting across the z -plane in the i^{th} direction.

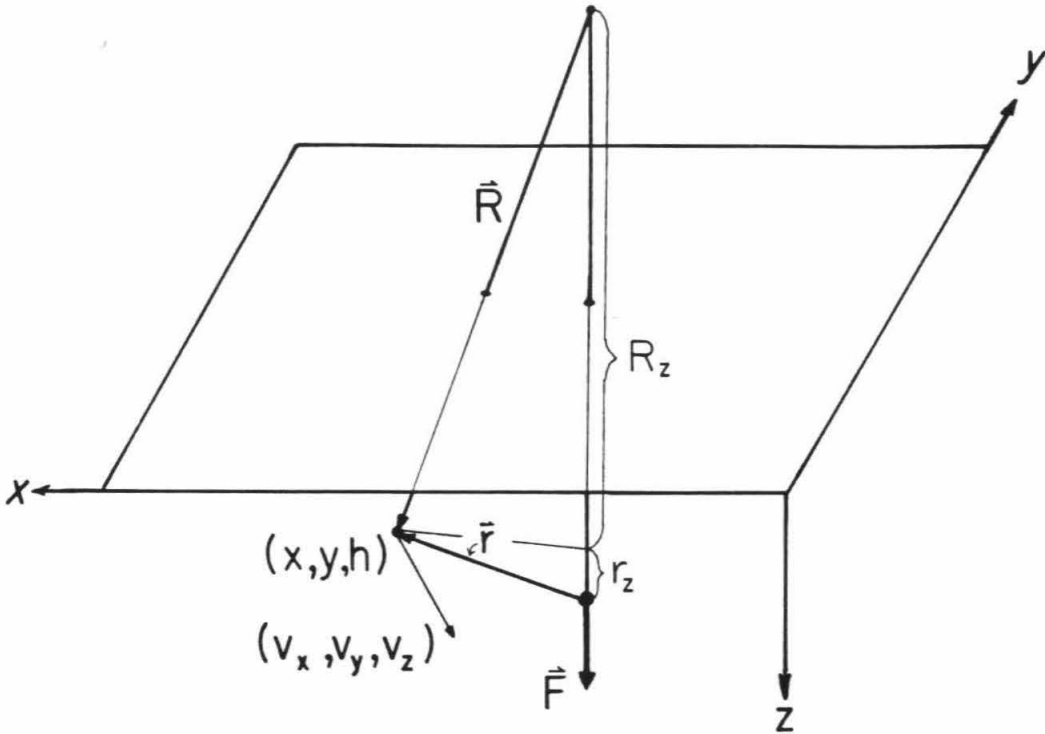


Figure III.7. Geometry of the field and source vectors originating from a point force, F . The origin of a rectangular coordinate system is located in a plane and directly above the point of force, with the plane being defined by $z=0$, and positive z is down. The field point is a distance h away from the plane. The vector locating the field point with respect to the point of force is r , while R is the vector locating the field point with respect to the image of the point of force. The flow field at the field point due to the point force is given by $v = (v_x, v_y, v_z)$.

Tension has been taken to be positive. Notice that the tractions are independent of the viscosity and flow velocity, making knowledge of these unimportant under the assumptions used. The flow field determined by these calculations is shown in Figure III.8, and the basal tractions are shown in Figure III.9.

Stress in the lithosphere is approximated by calculating the stress in a thin elastic plate fixed at infinity and subjected to the basal tractions determined above. The horizontal components of this stress field and the vertical gravity field are determined below. The stress fields are determined with the use of Green's functions for an elastic plate. The effect of this plate is to distribute the individual basal loads spatially, and thus the elastic plate acts as a filter applied to the basal tractions. The stress field for a horizontal point force in the positive x direction is given by (Love, 1952)

$$\sigma_{xx} = \frac{F}{2\pi} \frac{x}{r^2} \left(\frac{2\lambda+3\mu}{\lambda+2\mu} - \frac{2(\lambda+\mu)}{\lambda+2\mu} \frac{y^2}{r^2} \right) \quad \text{(III.3a)}$$

$$\sigma_{yy} = \frac{F}{2\pi} \frac{x}{r^2} \left(\frac{-\mu}{\lambda+2\mu} + \frac{2(\lambda+\mu)}{\lambda+2\mu} \frac{y^2}{r^2} \right) \quad \text{(III.3b)}$$

$$\sigma_{xy} = \frac{F}{2\pi} \frac{y}{r^2} \left(\frac{\mu}{\lambda+2\mu} + \frac{2(\lambda+\mu)}{\lambda+2\mu} \frac{x^2}{r^2} \right) \quad \text{(III.3c)}$$

where r is the horizontal distance from the point of load, and λ and μ are Lamé's constants. A similar expression is found for a force in the y -direction.

Note that gravity, as a measure of isostatic disequilibrium, is used as an indicator of the vertical tractions while the horizontal stress field is used to quantify the horizontal response. In the vertical direction gravity is important since it can be observed. In the horizontal direction we will use the stress components because they are reflected

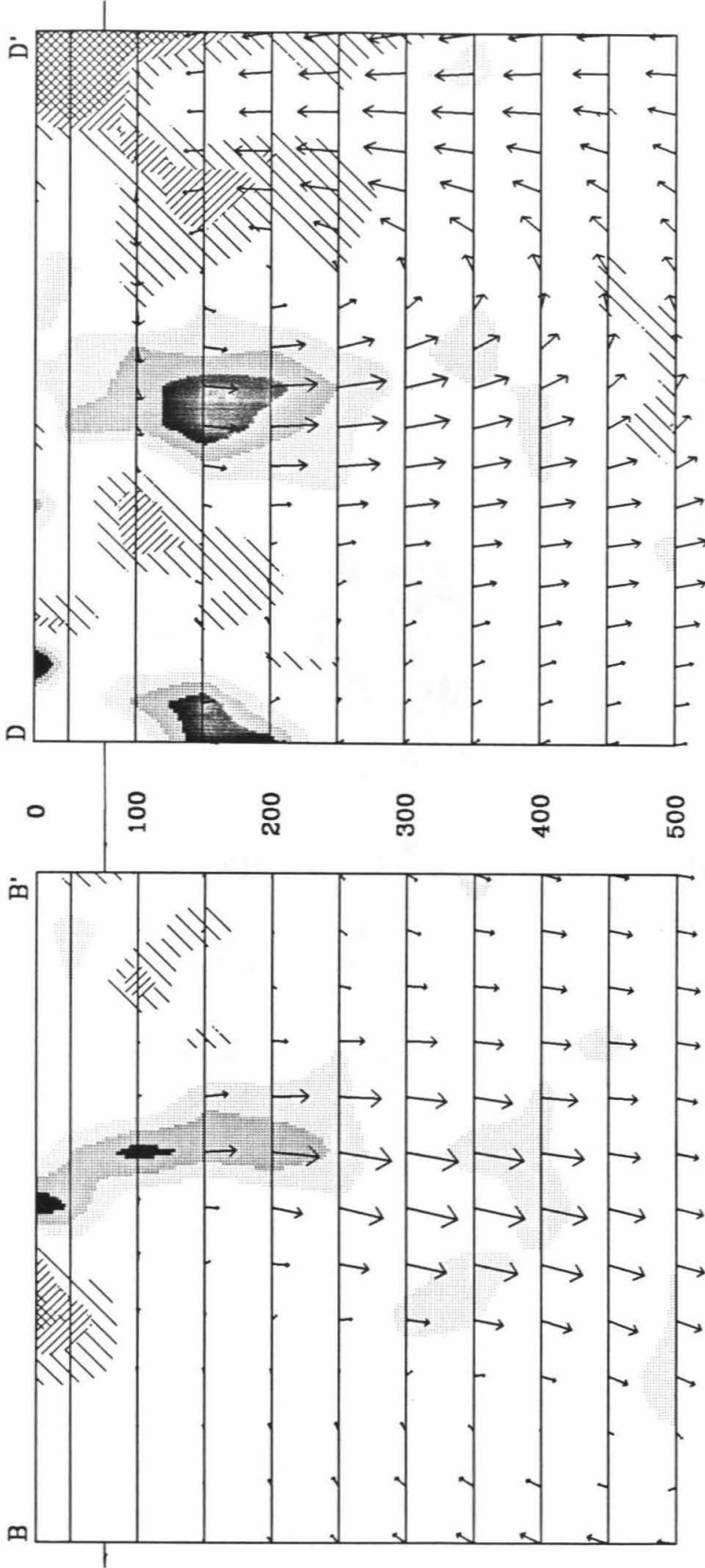


Figure III.8. Flow field resulting from the inferred density distribution beneath the lithosphere, taken here to be between the second and third layers of blocks (i.e., at 80 km). Equations III.1 have been used to calculate this field, where the viscosity has been assumed to be constant and the lithosphere has been assumed to be a surface of no slip. The absolute velocities are arbitrary depending upon the value of viscosity chosen. Cross section D-D' runs NW-SE through the center of both the Transverse Range and the Salton Trough anomalies.

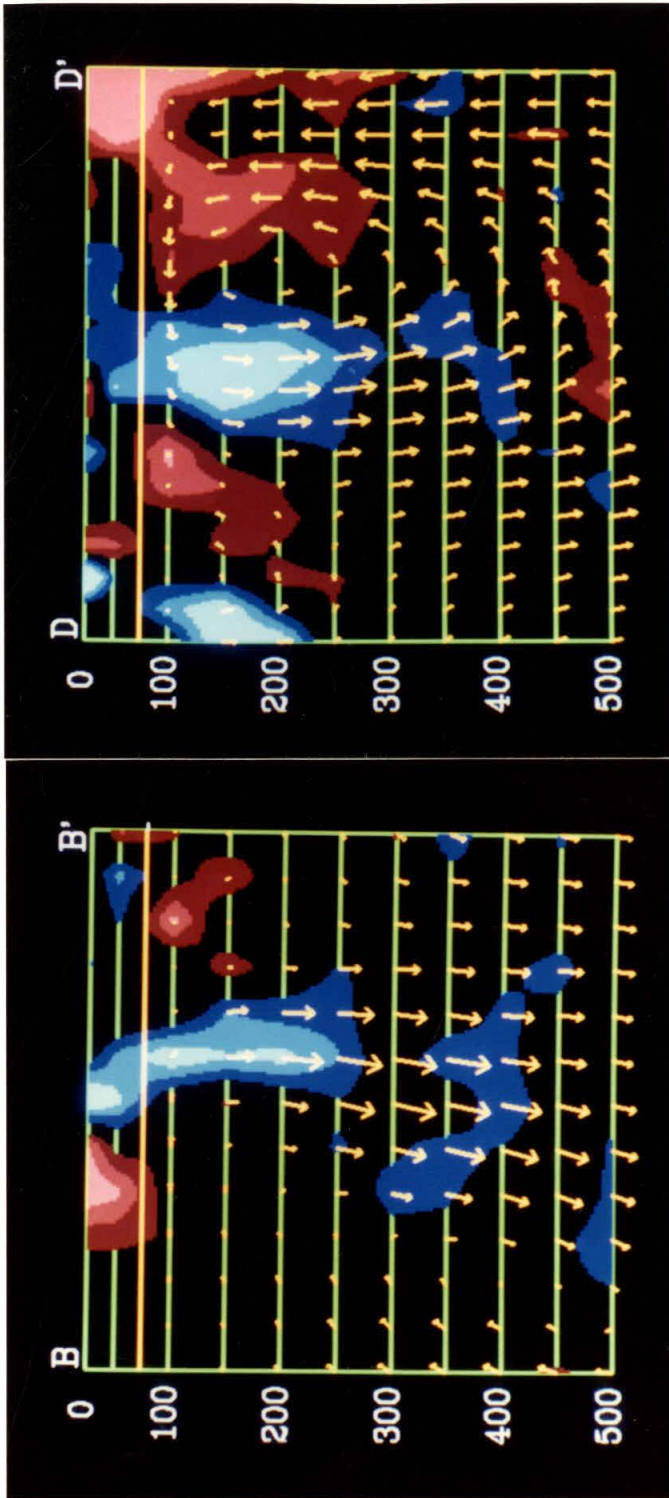


Figure III.8 (continued)

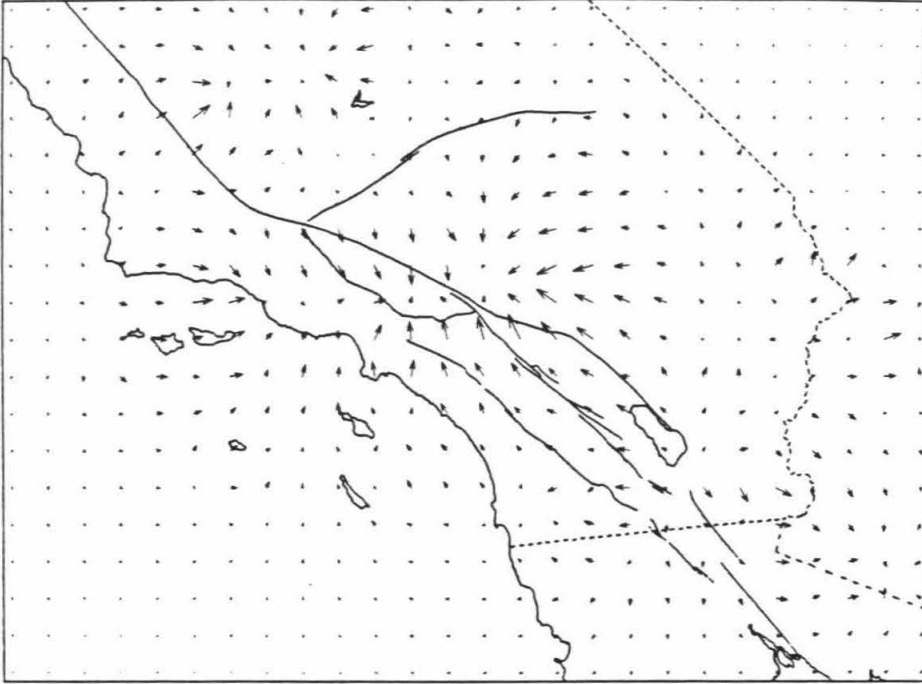


Figure III.9. Tractions at the base of the lithosphere due to the flow field shown in Figure III.8. Equations III.2 are used to determine this field. The scale is 30 bars to one grid unit, and the maximum traction is 28 bars. These values are independent of the viscosity chosen for the underlying half-space.

in the local tectonics.

The horizontal tractions (i.e., equation III.3) have been calculated with a stationary, no-slip boundary for the purpose of determining the tractions at the base of the California lithosphere. This has been done even though it is understood that the lithosphere in southern California is moving at some significant fraction of the mantle flow velocity. This is justified because it is the *contribution* to the lithospheric stress field arising from the mantle flow that is sought, and this contribution is independent of the plate velocity; the tractions due to the mantle flow and due to the plate motion are linearly independent (for a Newtonian rheology) and can be treated separately.

The effects of the horizontal tractions are examined first. Equations III.2 have been used to determine the basal tractions, and these are shown in Figure III.9. These tractions are produced solely through the locally induced flow in the mantle and not due to sources outside of the southern California region. As expected, flow away from the Salton Trough area and towards the Transverse Ranges and southern Sierra Nevada dominate the pattern. The stresses within a 10 km thick plate have been calculated using equation III.3; that is, assuming that the horizontal state of stress does not vary with depth. A thickness of ten kilometers has been chosen because this is the approximate depth to the base of the seismogenic zone, and this is assumed to be the thickness of the portion of the crust that can maintain and elastically transmit stress. In an attempt to display the stress field, Figure III.10 shows the deformation resulting from the application of the calculated stress field to a Laplacian plate that is infinite in extent. Also displayed in Figure III.10 is the decomposition of the stress field into its isotropic and deviatoric components. Clearly seen in these figures is the relatively strong, nearly isotropic compression in the Transverse Ranges

Figure III.10. The response of a Laplacian plate to the basal tractions shown in Figure III.9. Plate has parameters discussed in text, but in particular its thickness is taken as 10 km in an attempt to simulate the elastic portion of the crust (assumed to be given by the seismic zone which averages about this). a) shows the deformation field by displaying the influence on a circle, which deforms into the ellipses shown. An isotropic stress of 90 bars at a point results in a radial change of the reference circle of half its radius. b) displays only the isotropic component of the stress, where a circle of diameter equal to the grid spacing is equal to 90 bars. The maximum isotropic stress calculated is just over 90 bars. c) is a display of the deviatoric portion of the stress. Lines point in the tensile direction and are equal to 45 bars if equal in length to the grid spacing. The maximum deviatoric stress is calculated to be about 35 bars.

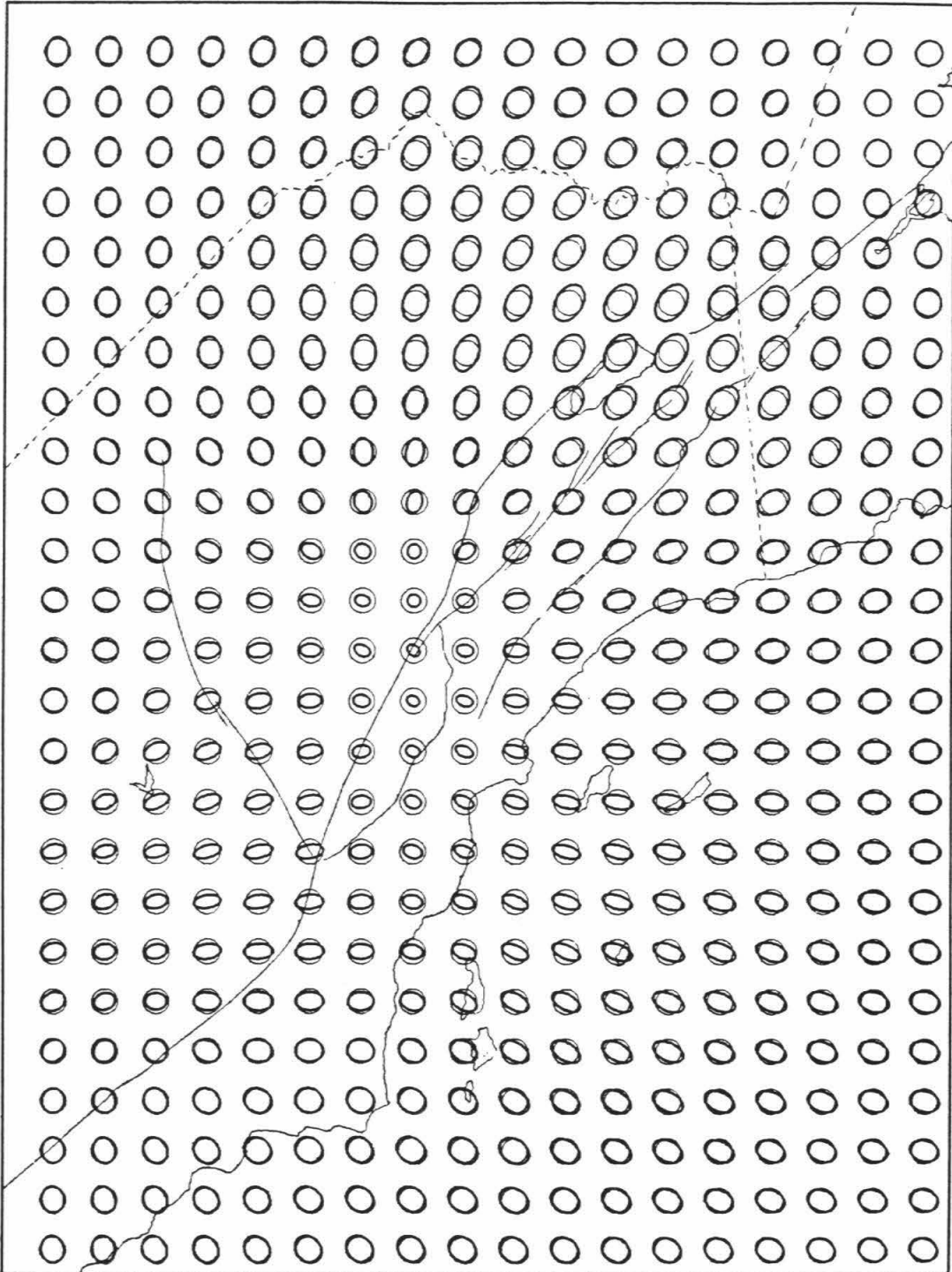


Figure III.10a

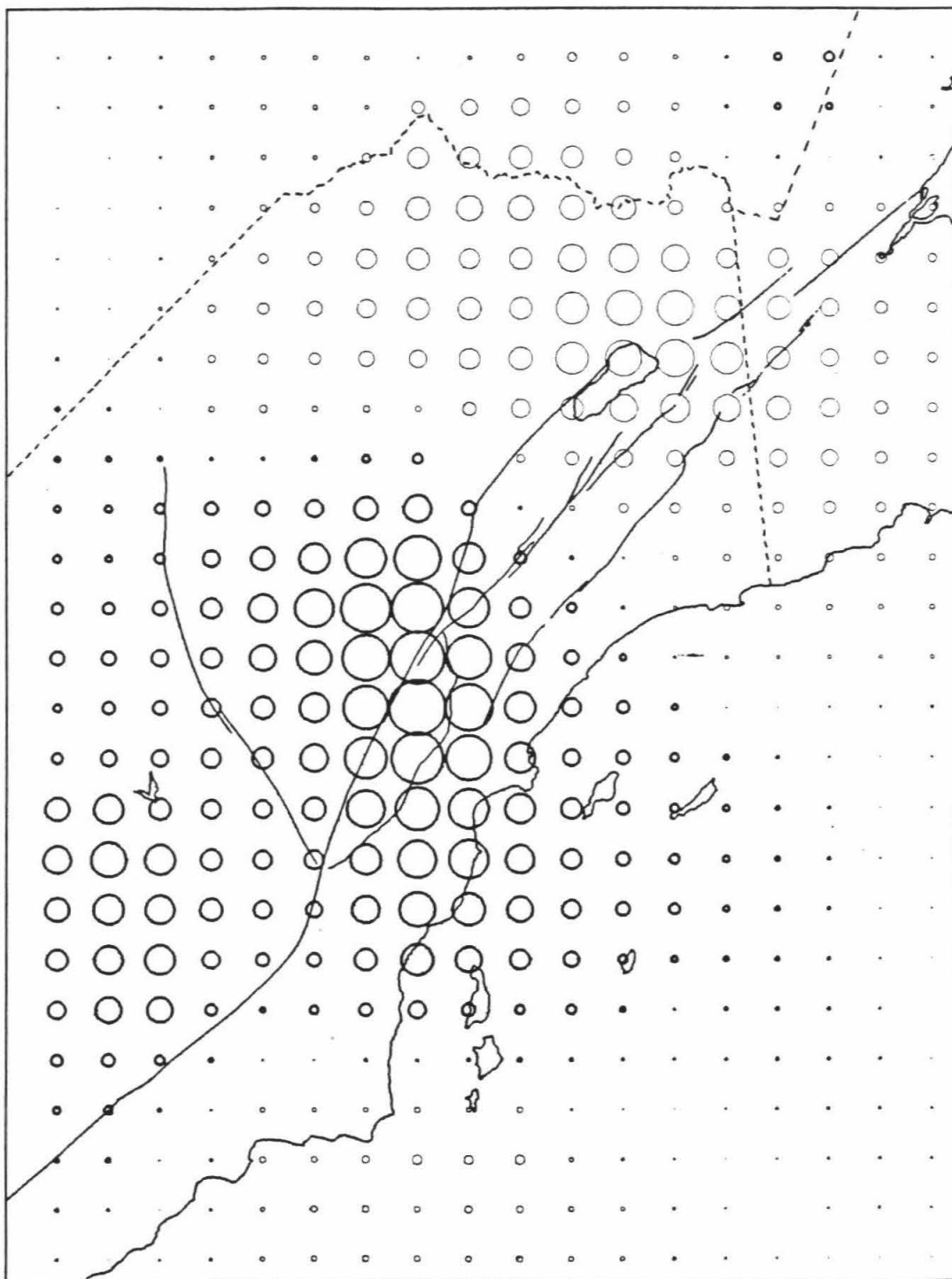


Figure III.10b

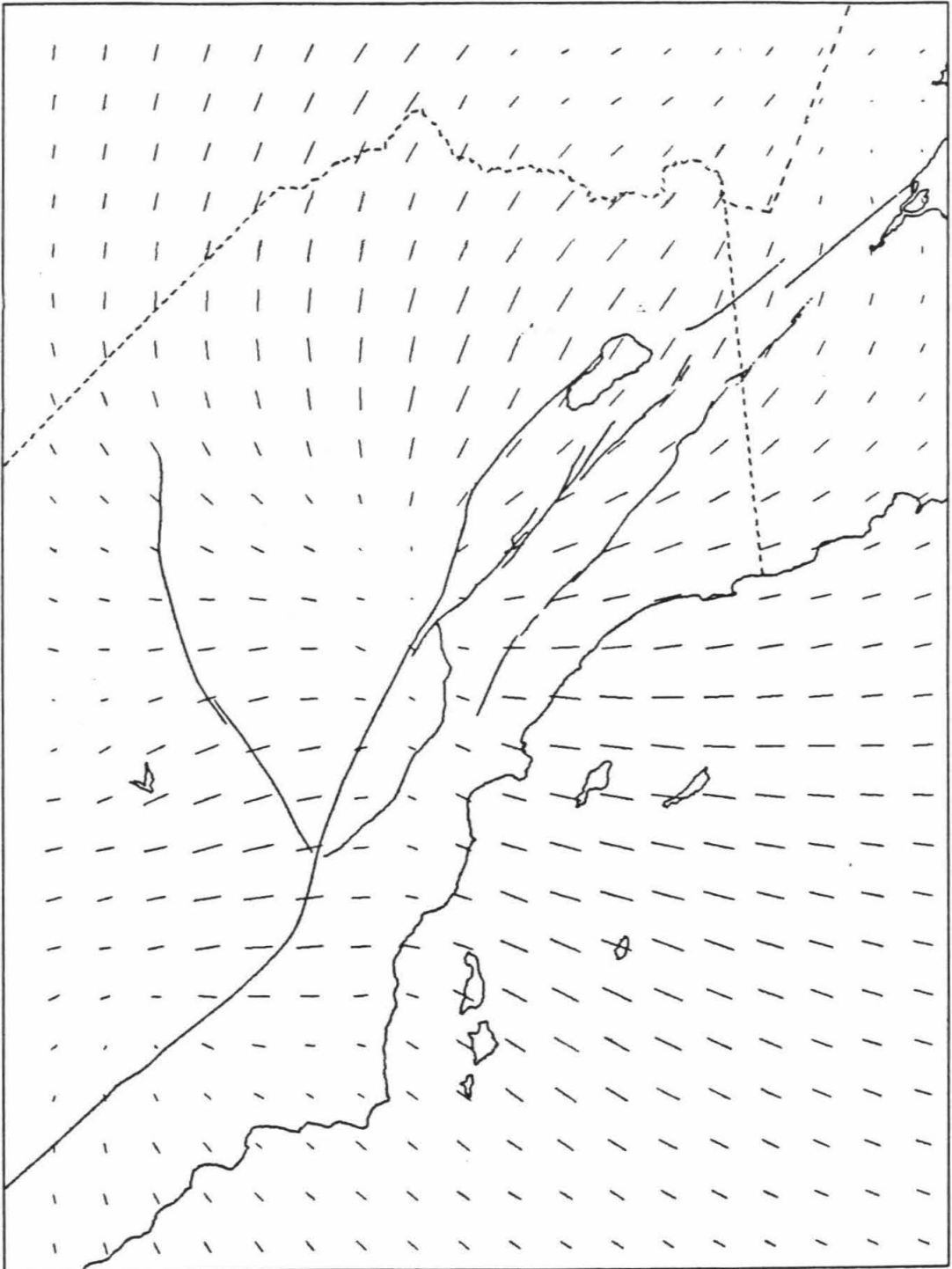


Figure III.10c



Figure III.11. Average topography in southern California. The topography has been averaged in each 50 km^2 , and the contour interval is 400 m. The unshaded zone is centered on zero elevation above sea level. This can also be used as a map of the topographically produced vertical traction across a horizontal plane, σ_{zz} . For this use the contour interval is 100 bars.

region and the NW directed tension in the area of the Salton Trough. This compares favorably with the extensional nature of the Salton Trough and the compressional environment of the Transverse Ranges, and also compares well with the maps of calculated and "observed" crustal thickness, Figures III.14a and III.14b below. The absolute levels of stress, however, are surprisingly low, only about 90 bars. Can these be the actual values of stress in the Transverse Ranges? A simple calculation of the load produced by a kilometer of topography (Figure III.11) results in about 300 bars, or over three times the magnitude of the horizontal compressional stresses just calculated as resulting from the basal tractions. If the ranges were not being uplifted, it could be argued that greater forces in the past uplifted the mountains, and that their intrinsic strength is presently holding them together. But since the ranges are presently being uplifted throughout a good deal of their length this apparent conflict must be resolved.

Two important factors that have been ignored in the elastic plate stress calculations are the effects of faults within the plate and the contribution of stresses originating from outside of the southern California region. The contributions to the stress field from sources external to southern California can conveniently be classified into two groups: basal tractions originating from neighboring regions and far field "plate forces" due to plate motions. In light of the relative plate motion between the North America and Pacific Plates, the possibility that significant shearing forces tending to drive the portion of southern California south of the San Andreas fault towards the NW needs to be addressed. Kosloff (1978) has argued against this on the grounds that the Elsinore and San Jacinto faults provide zones of weakness along which failure should occur if they were loaded in such a fashion. If the strength of

these three faults is comparable, the force applied to the Salton block along the San Jacinto fault is approximately balanced by the drag on the San Andreas fault, and the force needed to maintain the Transverse Ranges is therefore balanced only by the force supplied by the basal tractions. A similar situation exists for the Perris block. Using this argument one can disregard the net forces supplied by the NW trending strike-slip faults.

The problem of not considering basal tractions occurring in adjacent regions may be an important one, especially for the portion of the Salton Trough south of the international border. The Salton Trough, being the northern terminus of the East Pacific Rise, is not thought to be an isolated source of divergent tractions (as indicated in Figure III.9), but rather the northern end of a long zone that has diverging tractions. In actuality, therefore, the SE directed tractions that are shown in Figure III.9 to the SE of the Salton Trough are not expected to be real. Because these SE directed tractions are modeled as acting over the surface of a plate, their contribution will tend to partially cancel and diminish the magnitude of the NW directed tractions seen in the north Salton Trough. The average stress has been calculated for each block in the kinematic model, and in so doing these opposing tractions can be approximately accounted for. This is done by substituting the strongly biased tractions in the southerly portions of the southerly blocks with the values expected to be more typical which are found at a latitude about midway between the Salton Trough and Transverse Range anomalies. Applying this correction and calculating the average stress for each block produces (Figure III.12). The correction applied to the southern blocks results in a force for the Salton block that is about 1.7 times larger than is determined without such a correction, while the factor of increase for the Perris block

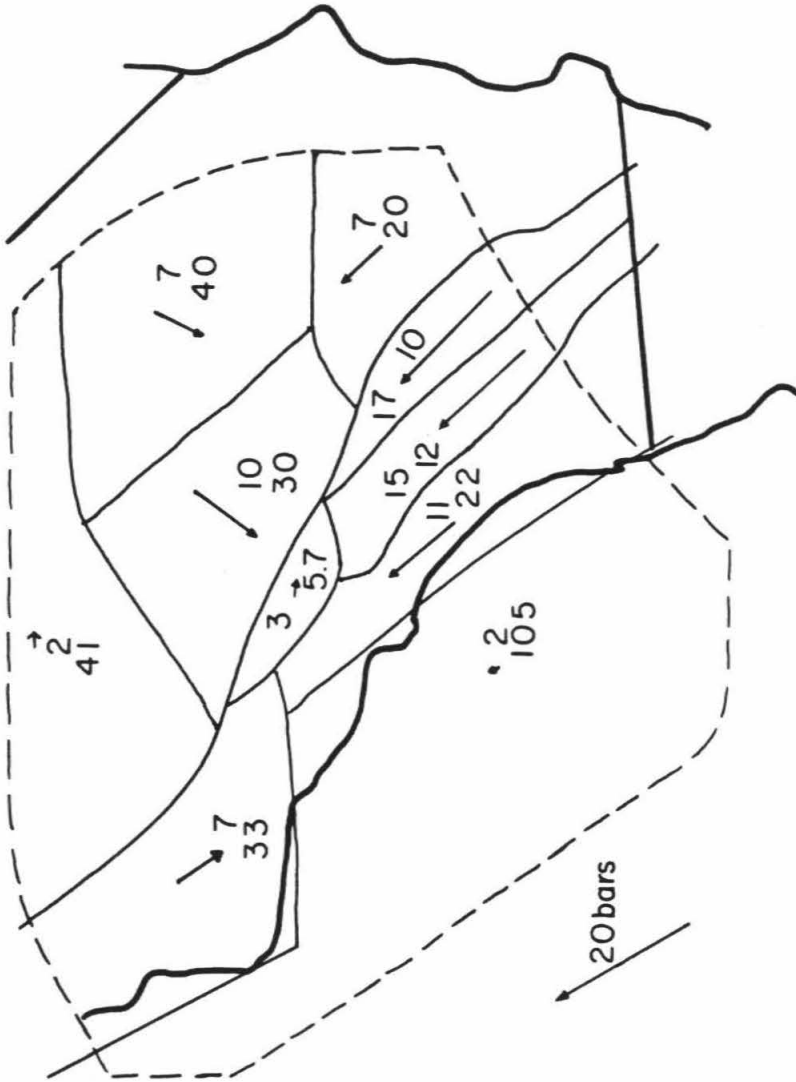


Figure III.12. Average horizontal tractions acting on crustal blocks in southern California. Area inside the dashed line is the only region considered. The magnitude of each vector is given by the top number (bars), and the area of each block is given by the lower number (arbitrary units).

is about 1.5. The influence of Basin and Range spreading may also be important when considering the Mojave blocks, and is probably important to the Sierra Nevada block. These stresses, however, have been ignored because of the lack of information which would allow for a proper consideration. The result is to underestimate the magnitude of the compressive stresses within the Transverse Ranges by an unknown but probably small amount.

Another consideration of importance is the effect of mechanically decoupling blocks from their neighbors. This allows the individual blocks to be more strongly influenced by the local traction field. Using the results shown in Figure III.12, the average N-S directed stress in the Transverse Ranges can be found to be approximately 150 bars, while that in the western Transverse Ranges is about 70 bars. In the central and eastern Transverse Ranges this value is approximately half of the 300 bars needed to maintain the relief, while in the western Transverse Ranges the stress field is adequate to maintain the low relief found there.

For the high Transverse Ranges the calculated stresses are low by a factor of two if they are to be required to maintain the topography. It is possible that the conservative approach taken here has underestimated the stresses by this amount, but an alternative is presented. If uplift is occurring on thrust faults, this wedge-like geometry provides a mechanical advantage for the uplift. Another important consideration is the ability of the fault geometry to locally concentrate the stress field. This has been discussed in the kinematic model as a mechanism for localized uplift of the Transverse Ranges, and it was pointed out that the present sites of active uplift are thought to be localized and associated with geometries that kinematically require convergence. In fact, if the arguments are accepted that basal tractions are required

to maintain the observed kinematics (Kosloff, 1978; kinematic model above), and also that the relatively low levels of stress calculated here are roughly correct, then one is lead to believe that there must be generally low levels of frictional resistance associated with the faults. This is consistent with the heat flow data (Lachenbruch and Sass, 1980) but in conflict with interpretations of the stress measurements of Zoback et al. (1980). Leary (1985), however, suggests that within a crust which is vertically stratified in its strength, simply extrapolating the near surface stress measurements in depth will overestimate the stress at depth. In view of the lack of consensus, the question of the effective stress levels on fault surfaces remains an open one in most workers minds.

So far only the horizontal forces have been examined, and these appear to be generally consistent with the tectonics. The description of the mantle that has been proposed above presents other means by which it can be tested. In particular, we can use the gravitational field and the vertical tractions. The gravity originating from the inferred density distribution in the mantle has been calculated (Figure III.13a). This is compared to the total gravity field which results from the Moho topography (Hearn, 1984b), the sedimentary basins, and the mantle density distribution (Figure III.13b). It is seen immediately that the gravity field due to the mantle source is not a large contributor. The total peak-to-peak calculated Bouguer gravity field is over 200 mgals (Figure III.13b) while the gravity due to the mantle is only about 30 mgals (Figure III.13a). These fields do not allow one to make a strong statement because of their small magnitude. The analysis, however, will be continued in order to examine the expected nature of the various fields. The strategy chosen to display the influence of the various mass inhomogeneities is to calculate the position of the Moho by using

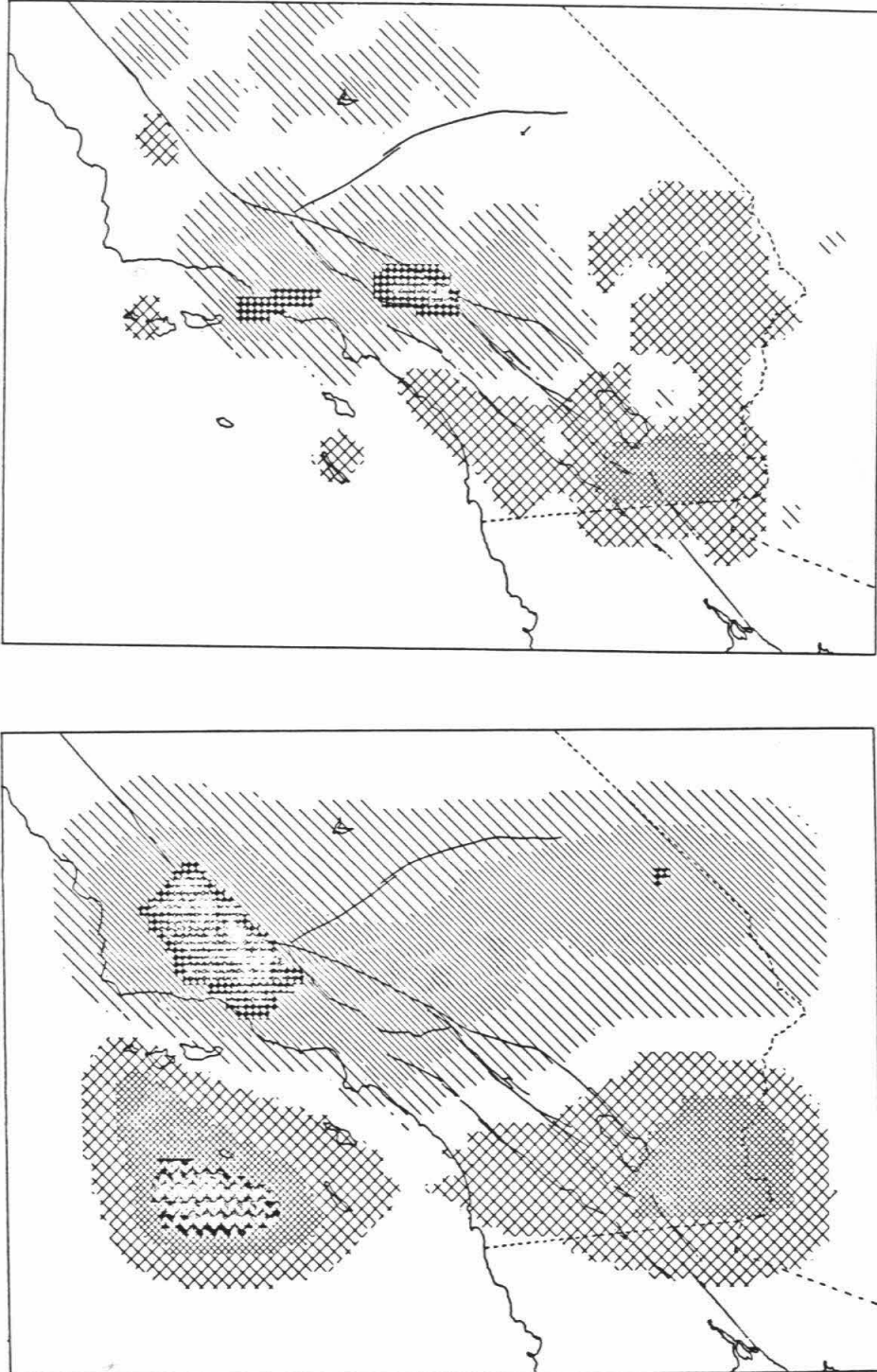
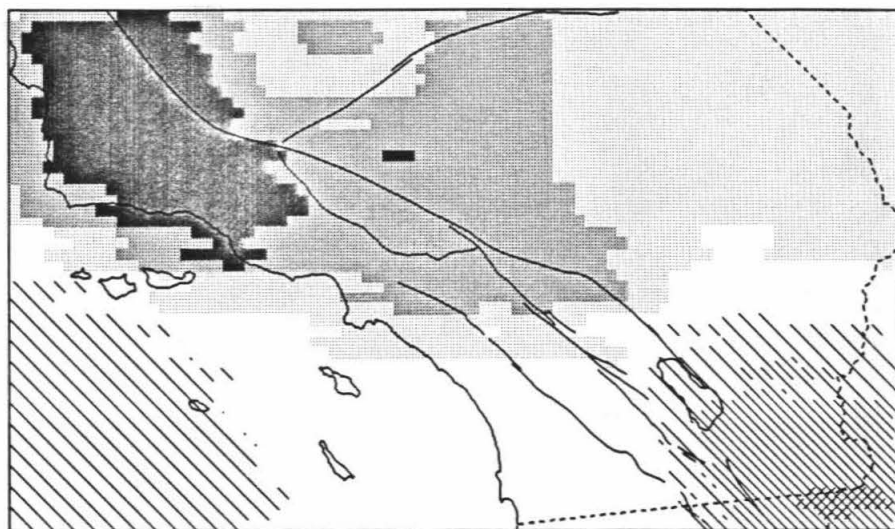


Figure III.13. Calculated Bouguer gravity for southern California. a) is the vertical gravity resulting from just the inferred density variations in the mantle. Contour interval is 5 mgals and the unshaded zone is centered on zero field. Checked pattern is positive. b) is the Bouguer gravity calculated by including the effects of the mantle densities, the Moho topography (Hearn, 1984) with $\Delta\rho=0.5 \text{ gm/cm}^3$, and the sediment fill in the major basins. Contour interval is now 40 mgals, the unshaded zone is centered on zero gravity, and the checked pattern is positive.



a)

Figure III.14. Seismically determined estimation of the position of the Moho (a) (Hearn, 1984b) and calculated variation in the position of Moho (b). Contour level is 2 km, the unshaded region is centered on zero deflection, and the solid pattern represents a downward deflection. a) is the seismically estimated depth to Moho using P_n arrivals (Hearn, 1984b). b) is found by balancing the sum of the vertical tractions due to elevation, sediment load, and the mantle-flow induced traction against the vertical traction due to Moho relief. Three cases are shown for differing density contrasts across the Moho: 0.4, 0.5, and 0.6 gm/cm^3 . The density contrast of 0.5 gm/cm^3 matches the large-scale values the best.

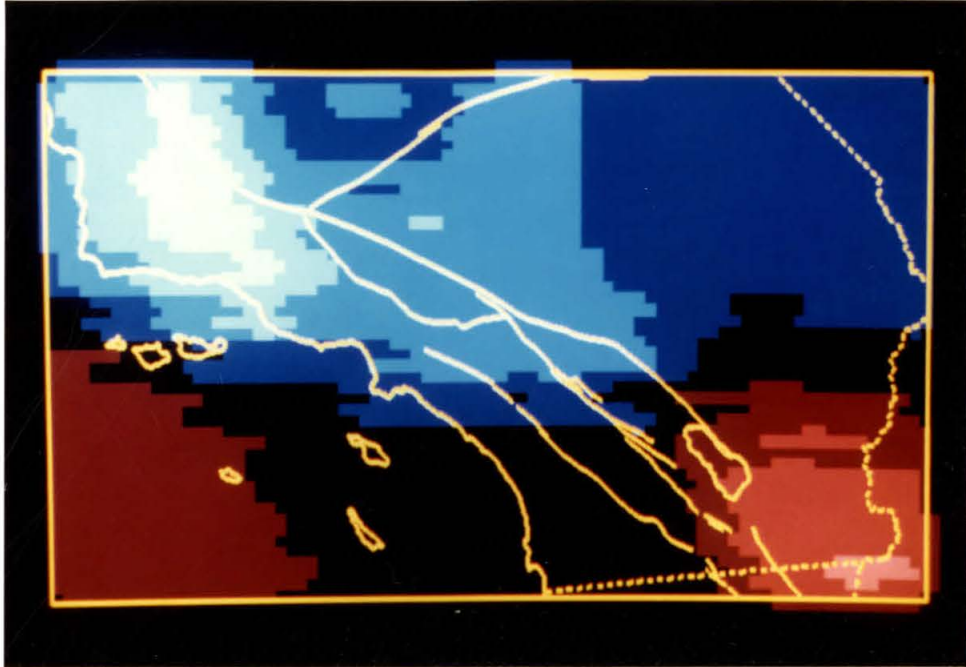


Figure III.14a (continued)

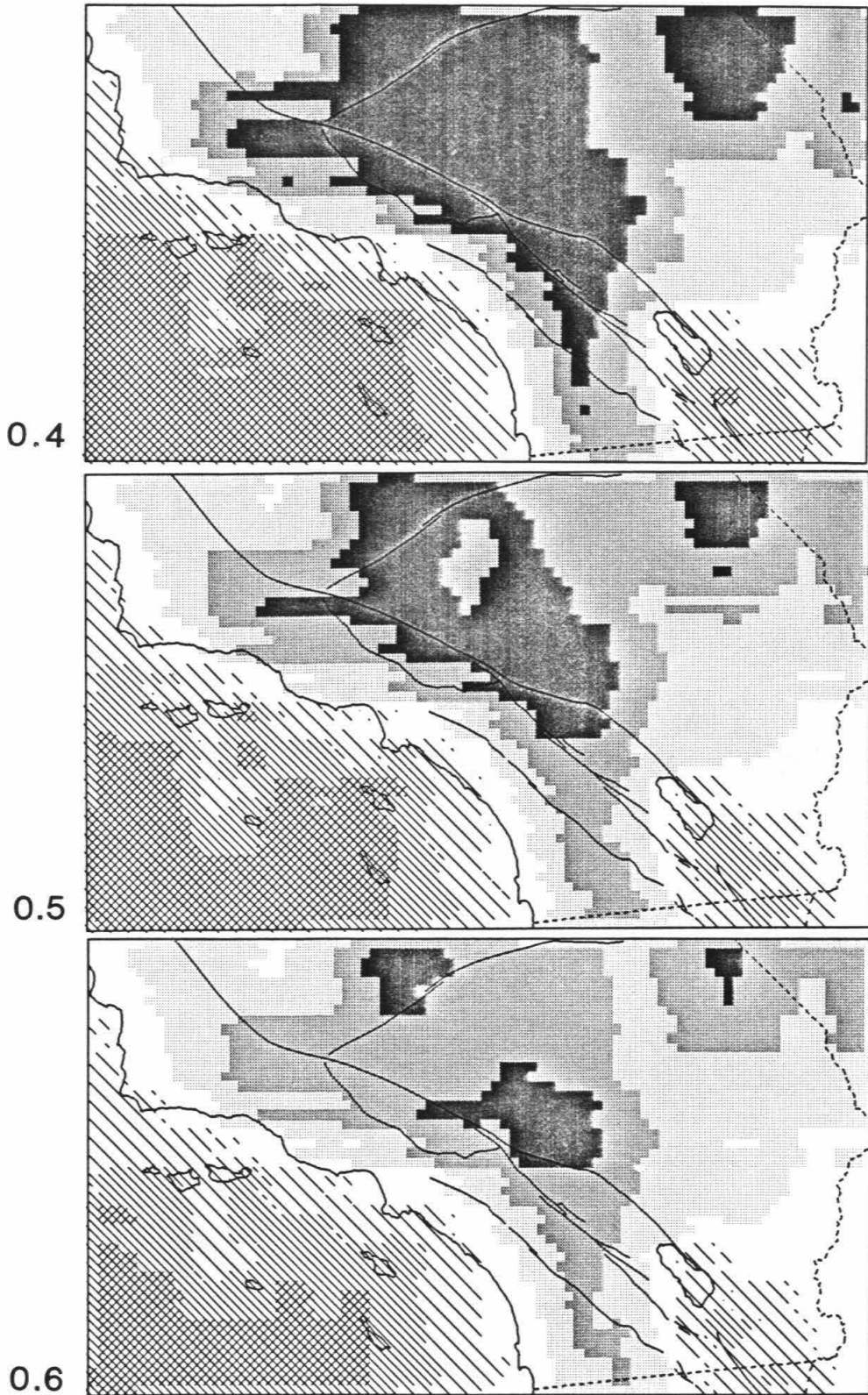


Figure III.14b

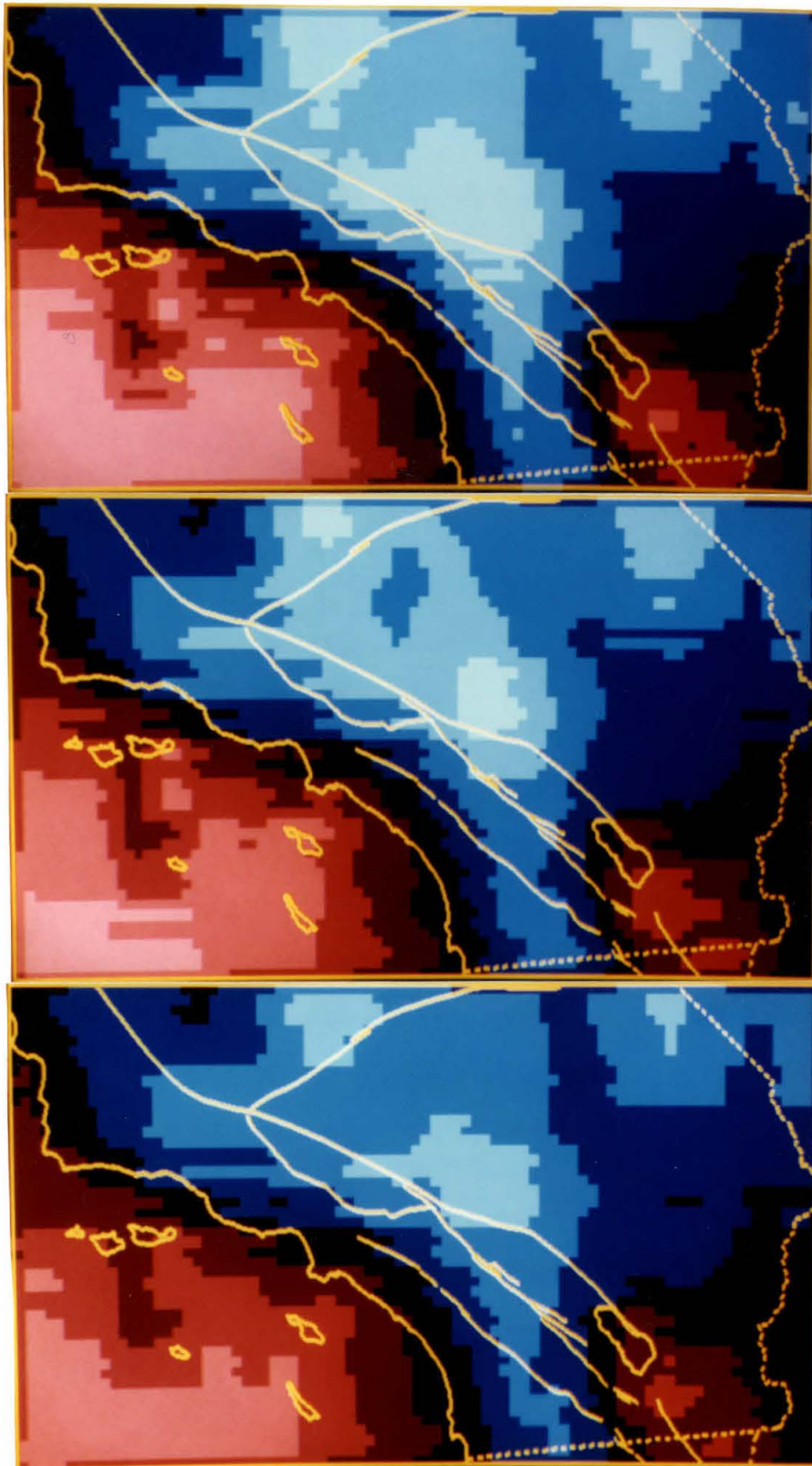


Figure III.14b (continued)

the assumption that Airy compensation applies. The position of the calculated Moho is then compared to its location determined by Hearn (1984b) with the use of P_n time terms. The calculated variation in Moho relief is shown in Figure III.14a for $\Delta\rho$ across the Moho of 0.4, 0.5, and 0.6 gm/cm³. The topography calculated for $\Delta\rho=0.5$ gm/cm³ compares very favorably with Hearn's variations in depth to Moho (Figure III.14b), though there are two significant deviations. These are located in the regions of the Peninsular Ranges and the southern Coast Ranges. An explanation for this is that Hearn's depth to Moho estimation is a direct presentation of the time terms, and while Moho depth is the most important parameter in determining these terms, they are also dependent upon the average slowness of the crust beneath the recording site. Hearn's shallow depth to Moho beneath the Peninsular Ranges may be caused by relatively high-velocity crust there (by about +10%), while the large depth to Moho found beneath the southern Coast Ranges could be due to relatively low-velocity material (by about -10%).

3.5 A Model for the Recent Development of Southern California

In this section a model for the recent development of southern California is presented and discussed. This model includes the observations discussed above and in Chapter II, some of which are quite peculiar. It should go without stating that this model may not be the only explanation for what has been observed, nor may it continue to satisfy future observations. It is also possible that the "observations," most of which are actually interpretations of observations, are not accurate, and the model will be in error accordingly. However, it is felt that the ability of the following model

to explain successfully the diverse set of observations speaks in its favor.

Review of the observations

The major observations discussed above and in Chapter II must be incorporated into any successful model of the development of southern California. Most of these observations are new. The discussion on the San Andreas fault, while not newly synthesized here, has been included because the literature does not presently present a consensus on the topic. Other observations will also be drawn upon as needed. The following is a list of the observations felt to be important.

- The kinematic model of the crust, specifically:

The lack of large amounts of convergence in the central
and eastern Transverse Ranges.

The sites of local convergence exist to the south of the
Transverse Ranges axis (Banning Pass and the frontal faults).

Large rates of convergence are occurring in the western
Transverse Ranges.

Activity on the Garlock fault has resulted in a widening big bend.

The major portion of slip on the northern San Andreas remains
on the San Andreas fault south of the big bend. The Elsinore
Fault is relatively inactive and the San Jacinto fault slightly
less than half as active as the San Andreas fault.

- The shape, magnitude, and position of the major mantle features:

The Transverse Range anomaly.

The Salton Trough anomaly

- The history of the San Andreas fault
 - ~ 50-20 m.y.B.P.: Inactive.
 - ~ 20-5 m.y.B.P.: 70-170 km of offset at a relatively low rate of slip.
 - ~ 5-0 m.y.B.P.: 160-200 km of offset at about 35 mm/yr.
- A high-velocity crust just to the south of the Transverse Ranges axis.
- A similarity in outline of the physiographic Transverse Ranges and the Transverse Range anomaly at a depth of about 100 km.
- The lack of a strong Transverse Range anomaly between 30-60 km.

The development of the Transverse Range anomaly

It is believed that an understanding of the evolution of southern California's surface necessitates the consideration of the upper mantle. That motions in the mantle are expected to contribute an influence has been demonstrated in the previous section on dynamic modeling. That the mantle is active in the surface processes is supported by the maintenance of the big bend (Kosloff, 1978; kinematic model above). And that the mantle has itself been influenced by the surface processes within southern California is recorded in the form of the major mantle features discussed in Chapter II. In particular, the striking Transverse Range anomaly needs to be discussed in terms of the activities occurring in southern California. Yet, at least partially, the information on its development is to be found within the structure of the anomaly itself.

The seismic velocity of the Transverse Range anomaly slightly exceeds +3% when compared to material of the same depth from elsewhere in southern California. With $\Delta V_p = 1\%$ implying $\Delta\rho = 1/3\%$ and $\Delta T = -160^{\circ}\text{C}$ (from the dynamic modeling

section), the Transverse Range anomaly is thought to be more dense than average southern California mantle (of the same depth) by about 1%, and colder by about 500⁰C. Bird and Rosenstock (1984) have suggested that the Transverse Range anomaly is due to the subduction of sub-crustal lithosphere as it converges in the big bend region, and they have proposed a two-sided pattern of subduction to account for the teleseismic P-delays. Their interpretation of the Transverse Range anomaly is supported here by the shape of the anomaly as well as the inferred temperature depression of about 500⁰C.

If this anomaly is indeed produced through the consumption of the lithosphere within the big bend region, the thickness of the thermal lithosphere can be determined. Qualitatively, one can argue that the thickness of the thermal lithosphere is 60-80 km based on the first appearance of the Transverse Range anomaly within the mantle as one descends in depth. This can be seen by examining Figure II.14 (the detailed inversion, layers 2 and 3). No strong Transverse Range anomaly is observed in the layer of depth range 30-60 km. However, in the less detailed inversion (Figure II.14), the Transverse Range anomaly is well developed in the layer of 30-80 km depth. Below 80 km to a depth of about 250 km the anomaly remains constant in thickness and magnitude, implying that the anomalous temperature of this material is of constant ΔT with respect to the horizontally neighboring mantle. This is reasonable because beneath the base of the lithosphere convection controls the thermal state, and the normal temperature gradient is expected to be simply adiabatic. The anomalous tongue should neither mix with the aesthenospheric mantle (due to its relatively high viscosity) nor lose its thermal signature via conduction over the course of only 5-10 million years, and therefore should also increase in temperature in a

simple adiabatic manner.

It can be argued further that the entire thickness of the lithosphere is being consumed in order to produce an anomaly that in its interior is 500°C colder than in its exterior portions. The temperature at the base of the thermal lithosphere is thought to be near 1300°C (e.g., Turcotte and Schubert, 1982). The temperature at the base of the crust is estimated by using the average (non-anomalous) heat flow for southern California of about $75 \text{ mW}/\text{m}^2$ (from a map compiled by Lachenbruch, pers. comm.) and the temperature extrapolations in depth for the western U.S. of Lachenbruch and Sass (1977). At a depth of 30 km the temperature is estimated to be about 800°C at the average southern California value of heat flow. This produces about 500°C change in temperature across the mantle portion of the lithosphere. It is also expected that the entire mantle portion of the lithosphere is involved based on geometrical grounds; if the sub-crustal lithosphere is converging in the big bend region, then it should be consumed in its entirety to make room for the lithosphere just behind it, and there is no obvious impediment to this consumption.

With this model for the kinematics of the sub-crustal lithosphere, its thickness can be calculated. Assumptions made in this calculation are: the crustal portion of the lithosphere averages 30 km in thickness (Hearn, 1984b); the Transverse Range anomaly is 50 km thick and extends to a depth of 250 km (Figure II.14); the angle between the direction of convergence and the axis of the Transverse Range anomaly is 50° (Figure II.14); two-sided convergence is taking place (argued for below); and that 300 km of convergence has taken place (history of the San Andreas fault section above). By maintaining mass balance the thickness of the sub-crustal portion of the lithosphere is determined to be 46 km, implying a whole lithosphere thickness of 76

km. This seems a reasonable, if not well-constrained, estimate.

With the location of the base of the lithosphere estimated, the nature of the consumption process can be discussed. One-sided convergence is simply ruled out because 300 km of convergence are thought to have taken place, yet the Transverse Range anomaly extends in depth only about 180 km from the base of the lithosphere (Figure III.15a and b). Also, the Transverse Range anomaly is symmetrical in cross section implying a symmetrical thermal cross section, while a saw-tooth shaped anomaly would be expected for single-sided consumption (Figure III.15b). Extending this reasoning further, both sides must be passing into the mantle at the same rate or else the symmetrical cross section would not persist through all depths of the Transverse Range anomaly (Figure III.15c). And, the sub-crustal lithosphere is thought to be consumed at the same rate across its entire vertical thickness because the cross section is similar at all depths within the anomaly (Figure III.15c). Finally, it is felt that the consumption process should be referred to as convective downwelling rather than subduction in order to emphasize the fact that the anomalous material is not brittle lithosphere, but rather is material capable of accumulating shear strain without the production of earthquakes. Indeed, this lithosphere has not only turned a sharp corner beneath the Transverse Ranges in an aseismic manner, but potentially has also extended itself by means of pure shear without producing earthquakes. Within the uncertainties of the depth extent of the Transverse Range anomaly, the location of the base of the lithosphere, and the total amount of convergence, it is possible that the Transverse Range anomaly has undergone no pure shear extension. However, using the best estimates for these values, one obtains an estimate of 17% for the extension of the Transverse Range anomaly (from 150 km to 175 km in length) below

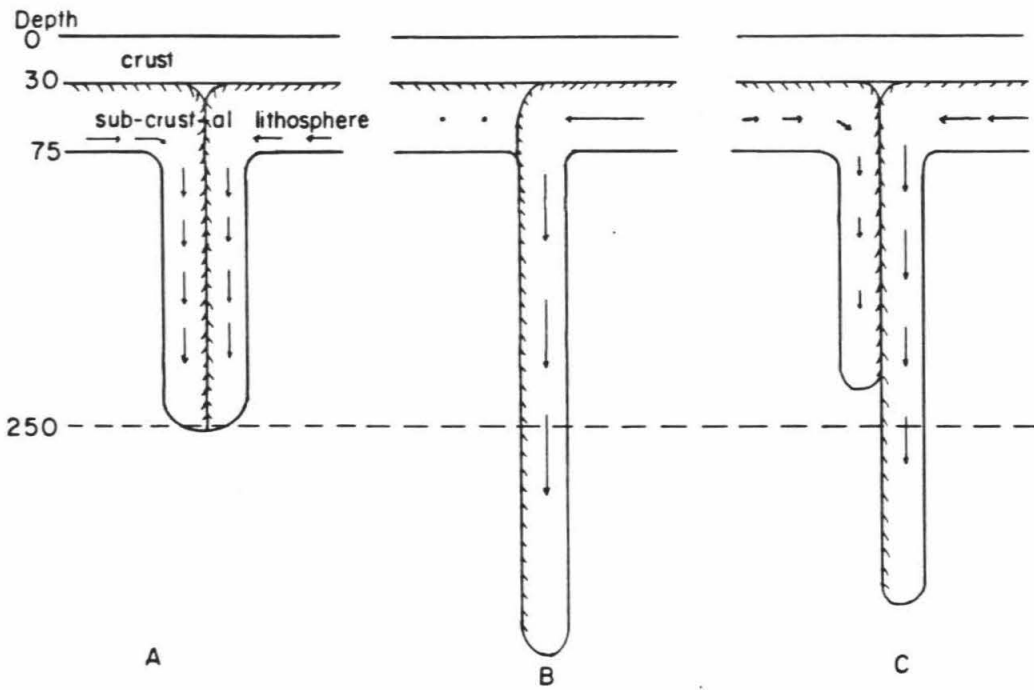


Figure III.15. Possible means by which the sub-crustal lithosphere may be consumed. a) shows the symmetrical situation where both sides converge and sink at the same rate. b) represents single-sided sinking, and c) represents asymmetrical two-sided convergence.

the base of the lithosphere.

The general kinematics of the lithosphere are schematically shown in Figures III.16 and III.17. The Mojave lithosphere is believed to be the most convenient frame of reference with which to view the evolution of the Transverse Range anomaly. This statement is supported by the kinematic model (from prior section), which has the crust south of the big bend rotating counter-clockwise and thus having a diminishing component of San-Andreas-fault-directed convergent velocity as it approaches the big bend. In this manner the crust is avoiding most of the convergence that would be required if its motion were more parallel to the North America-Pacific Plate relative motion. This has presumably occurred because there is no place for the incoming crust to go without expending a great deal of work (such as in elevating the local topography). The sub-crustal lithosphere is expected to be moving approximately in the North America-Pacific Plate direction because there is no impediment to convergent motion, and in fact the sinking of the heavy lithosphere is a source of energy with which work can be accomplished. With the reference frame in the Mojave, the trace of the San Andreas fault in the big bend region is stationary while the California crust south of the big bend generally converges towards the trace of the San Andreas fault within its big bend section. Figure III.17 shows a schematic NE-SW cross section that is perpendicular to the San Andreas fault in the big bend region. The velocity field (relative to the Mojave) is shown on the figure, and within the crust the convergent component of the velocity field diminishes to zero as the San Andreas fault is approached from the south. This is unlike the corresponding portion of the sub-crustal lithosphere, which maintains a constant speed in the plane of the cross section by sinking into the mantle. This different velocity field between the crust and

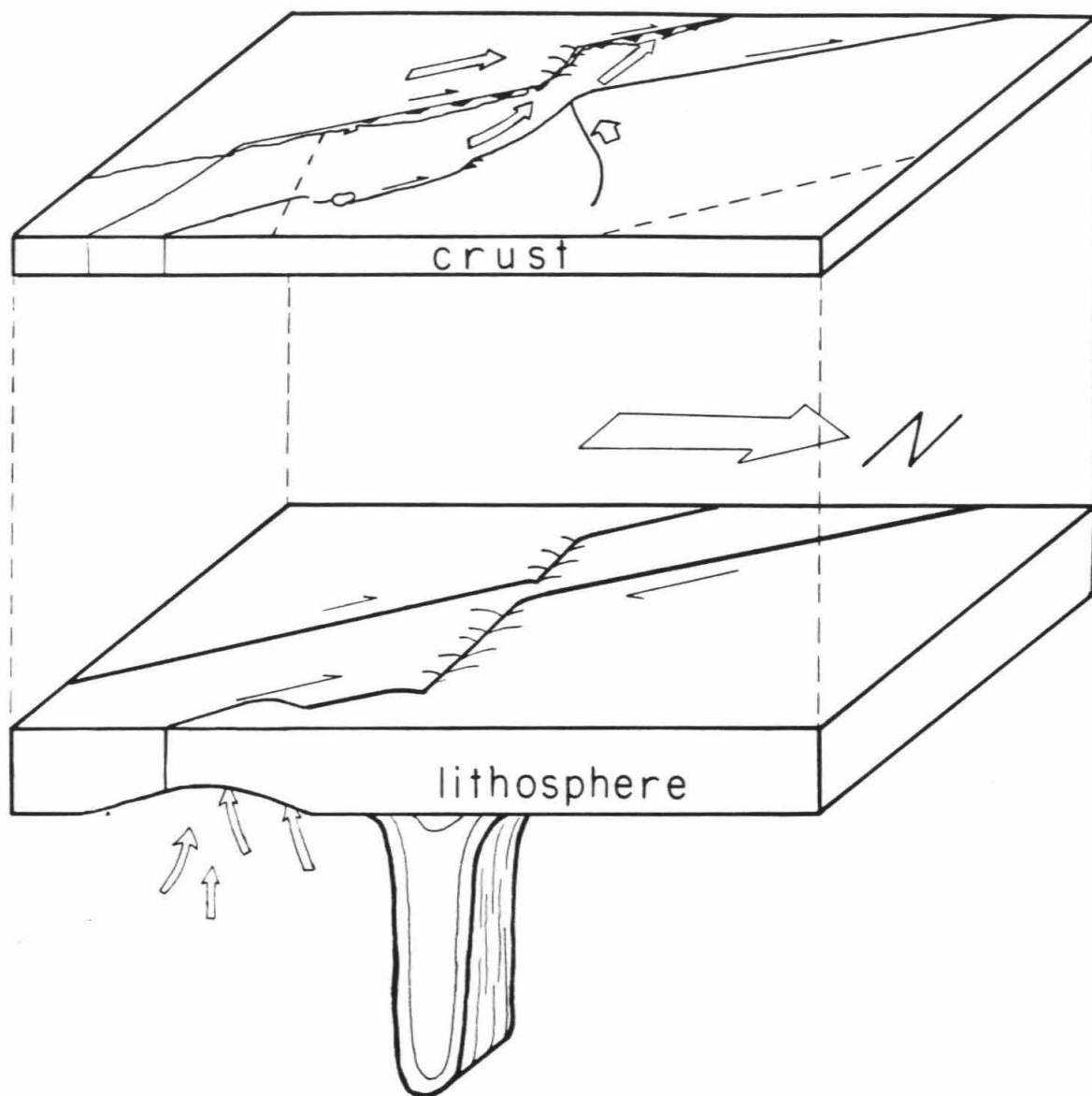


Figure III.16. Simplified model of the lithospheric kinematics for southern California. The crustal kinematics have been described in a previous section, but of importance is the general lack of convergence in the big bend region. The mantle lithosphere does converge in the big bend region and sinks there. Also shown is mantle upwelling and lithospheric divergence in the Salton Trough region.

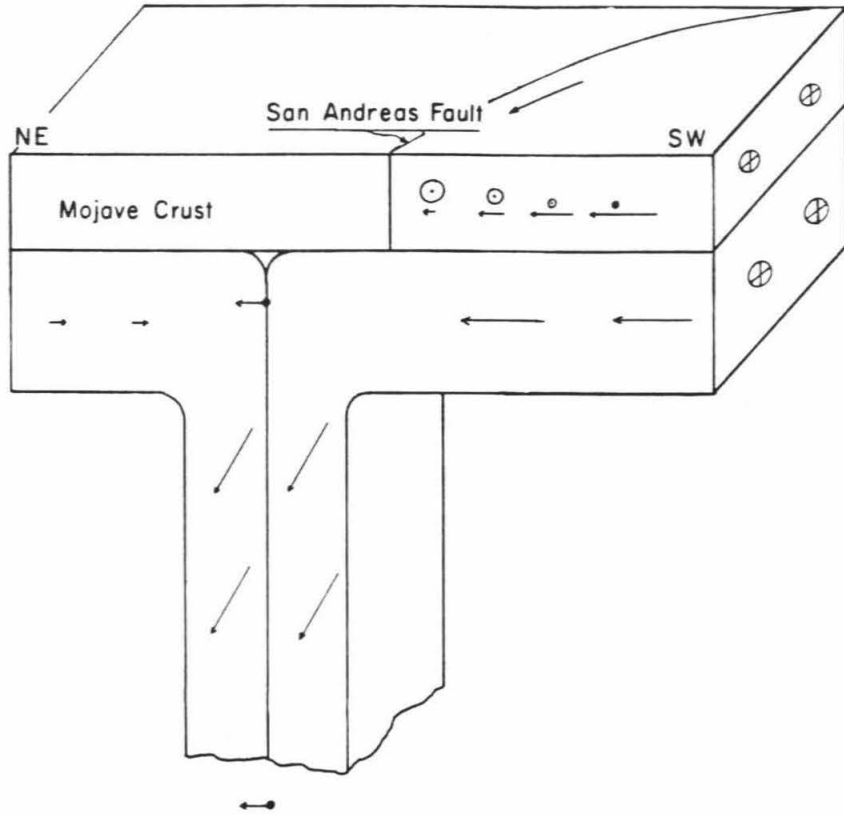


Figure III.17. A NE-SW cross section through the kinematic model that trends normal to the San Andreas fault in the San Bernadino Mountain area. The Mojave crust is the reference frame and is stationary. Southwest of the San Andreas fault southern California is rotating along the trace of the curved San Andreas fault while the mantle lithosphere converges and sinks. This results in differing velocity fields between the two parts of the lithosphere SE of the San Andreas fault, and this disparity increases in magnitude as the big bend is approached. The implication is that a horizontal surface or zone of decoupling must exist between the two. Also noteworthy is the northward migration of the downwelling through time. This results from the small amount of relative motion between the Mojave crust and mantle lithosphere, while the mantle lithosphere south of the zone of convergence is moving towards the Mojave at a relatively high rate.

the mantle implies that a zone of decoupling exists somewhere between the upper crust and the uppermost mantle in the region around and just south of the Transverse Ranges.

With the occurrence of two-sided downwelling the Transverse Range anomaly must be migrating northward with time (relative to the Mojave), as shown in Figure III.17. In the eastern Transverse Ranges this is supported by the location of the Transverse Range anomaly to the north of the San Andreas fault. In the central Transverse Ranges region (vicinity of Cajon Pass), the Transverse Range anomaly lies directly beneath the San Andreas fault. It therefore seems reasonable that in this region the sub-Mojave lithosphere is not stationary but is itself converging into the big bend at a rate similar to the sub-crustal lithosphere from the south. The low-velocity (and presumably high-temperature) region to the north of the central portion of the Transverse Range anomaly (Figure II.14) may be due to local upwelling and infilling as the sub-crustal Mojave lithosphere moves towards the big bend.

A mechanism that is consistent with this discussion is that in the eastern Transverse Ranges, the anomaly has migrated northward due to the strong SE to NW direction of flow produced by the Salton Trough-Transverse Ranges circulation pattern (Figure III.8) south of the big bend. The northward deflection of the eastern Transverse Range anomaly (Figure II.14, BB') may also be due to this local northward drift of the mantle. In the central Transverse Ranges, however, the influence of the Salton Trough upwelling is not as strong, and the normal tendency to produce a stationary site of convergence (relative to the Mojave) is expected. The fact that the locus of convergence within the crust (i.e., thrusting) lies to the south of the central and eastern Transverse Range anomaly axis may attest to the northward migration of

the site of downwelling through time, leaving the frontal thrust system behind in the process. If this locus is used as a marker, migration has been greatest to the east, as is expected in the above model. A similar line of reasoning also supports this: the location of the high-velocity Transverse Range anomaly within the crust lies roughly under the frontal thrust system which is to the south of the mantle Transverse Range anomaly. This is especially pronounced in the east (Figure II.14). This anomaly is thought to represent cold crust which is the result of crustal thickening along the zone of past and present crustal convergence. The deep seismicity, indicating the presence of cold, brittle rock, supports the interpretation of crustal thickening. However, there appears to be no strongly localized root beneath the Transverse Ranges (Hearn, 1984b) as one might expect if crustal thickening had occurred along a fracture system. A possible explanation for this is that only limited amounts of convergence have occurred (10's of km) resulting in average downward displacements of the crust beneath the Transverse Ranges of under ~ 20 km. Because the lower crust is expected to behave in a ductile fashion, allowing it to flow away from the region of convergence, a broad depression may actually be expected as the early expression of a root. If convergence were to continue, the continued downward migration of the cold upper crust would present to the lower crust a stronger material that would be capable of resisting flow and forming an Airy-type root. The net amount of convergence is actually thought to be on the order of 10's of kilometers (evidence cited in the kinematic model), and the broad roots may be used as support for the lack of large amounts of convergence (i.e., about 300 km) in the big bend region.

Finally, the rheology of the mantle Transverse Range anomaly is addressed. The deformation mechanism that is operative here depends upon the temperature,

pressure, and deviatoric stress, and each influence must be considered. Deviatoric stress originates from the vertically directed body forces produced by the density variations within the anomalous regions. Assuming the mantle density to be approximately 3.3 gm/cm^3 , the Transverse Range anomaly to be 1% more dense than normal mantle material (from the dynamic modeling section), and relatively small amounts of shear traction between the sides of the Transverse Range anomaly and the non-anomalous mantle, force balance suggests that $\sigma_{zz} = 0.32 x$ (MPa), where x is the distance up from the bottom of the anomaly in km. The deviatoric stress is half of this value: $\sigma_{\delta} = 0.16 x$ (MPa). At the top of the anomaly ($x = 175$ km) the deviatoric stress attains a value of 28 MPa (280 bars), and the pressure at this depth is about 2300 MPa (23 kbar). The strain within the Transverse Range anomaly is expected to be rate-controlled by its coldest, most viscous portion. Taking this to be about 800°C (from arguments given above) and using the stress field just discussed, Ashby and Verrall (1977) give a strain rates of about 3×10^{-16} per second, or less than 2% strain in 5 m.y. This value is very approximate, but suggests that the Transverse Range anomaly will not deform under its own weight by large amounts over the duration of time in which it is thought to have developed. This does not address the possibility that the Transverse Range anomaly might have been locally extended in the region where it bends sharply and begins to travel vertically (for in this region the deviatoric stresses may be much larger), but only that once this region has been passed, little deformation is expected to occur.

This deformation rate lies in the diffusional creep domain (Ashby and Verrall, 1977), and can be associated with a viscosity $\eta = \sigma / 2\dot{\epsilon} = 5 \times 10^{23}$ poise.

Speculative History

A brief history is now presented and discussed that incorporates the new information available.

The most influential occurrence in the tectonic development of westernmost North America over the past 30 m.y. has been the change in the style of plate margin from a zone subduction to a transform boundary. The range of affected boundary has grown through time, and increasing amounts of the continental margin have been subjected to right lateral shear. As a result of the change in plate margin style the lithospheric basal conditions have undoubtedly been modified as the Farallon Plate subducted and was removed from beneath western North America (Dickinson and Snyder, 1979). Where once low temperatures and east-directed shear tractions prevailed at the base of the lithosphere, the new conditions presented hot, buoyant asthenosphere. Conditions for thermal instability at the base of the lithosphere became greatly enhanced in this new environment (Yuen and Fleitout (1984) have analyzed similar conditions above an ascending plume).

The geologic record argues for much of the shear strain (5-10 m.y.B.P.) along the western boundary of North America to be occurring offshore since only about two thirds of the net slip is observed on shore since about 15 m.y.B.P. (~ 300 km on the San Andreas fault (Crowell, 1981) and about 500 km net displacement (Atwater and Molnar, 1973). Information exists with which the temporal development of the various participating faults can be addressed. The major on shore actor has been the San Andreas fault. Its history of slip is interpreted here to have been slowly and monotonically increasing in rate beginning near or slightly prior to 15 m.y.B.P. and continuing up to about 5 m.y.B.P., at which time the slip rate reached and has since

maintained a rate of 35 mm/yr (Figure III.6). The argument is made above that, the mantle anomaly beneath the central and eastern Transverse Ranges has been produced by convergence in the big bend of the San Andreas fault, and the deepest portions of this anomaly are therefore expected to date back to about 10-15 m.y.B.P., depending on when the bend in the San Andreas fault first became an obstacle to motion.

In a situation geometrically and kinematically similar to the big bend region of the San Andreas fault, convergence is occurring in the western Transverse Ranges through a region that is interpreted to be a left step in a "coastal system" of faults (as discussed in the kinematic model). This zone of lithospheric convergence also has associated with it a mantle anomaly, though here the anomaly extends much less deeply into the mantle indicating that smaller amounts of net convergence have occurred here. Either lesser rates of convergence or a shorter duration of convergent activity can produce this, and both options appear to have contributed: present rates of convergence are smaller (see kinematic model) and the history is thought to be more recent (Yeats, 1983, Rockwell, 1983). Present slip rates assigned to major near- and on-shore faults in the kinematic model account for the relative North America-Pacific Plate motion. If, however, the convergence in the western Transverse Ranges (and by inference the activity along the entire coastal system) was not as rapid in the recent past, there is the need to include offshore slip.

Important questions are when, in what fashion, and why did the locus of shear strain move onto the continent? Several factors probably controlled this evolution. Certainly, the location of the proto-San Andreas fault and the increasing shear load placed on this zone as the width of the transform boundary grew were fundamental.

Also, if the offshore transform boundary had a component of convergence on it, as might be expected due to Basin and Range spreading and the necessity of the westward migration of California, then the transfer of the strike-slip component of motion onto an essentially pure strike-slip fault inland of the zone of convergence appears to be a common occurrence (Fitch, 1972). Two other factors are thought to be important, however. These are the incipient Gulf of California rifting and the probable existence of a major bend in the San Andreas fault (Powell, 1981).

For whatever the reasons, Baja California began to move towards the NW and rift away from mainland Mexico. The kinematic result was the existence of inland right-lateral zone of shear, and this motion was apparently taken up on the San Andreas fault. Basin and Range spreading meanwhile resulted in the westward drift of California north of the Garlock fault (Davis and Burchfiel, 1973) and hence the widening of the big bend. This presents a geometrical difficulty to the slip along the San Andreas fault, and continued slip is thought to have resulted in lithospheric convergence within the big bend region, resulting in forced crustal thickening and mantle downwelling. With the thermally unstable conditions that prevailed at the base of the lithosphere, downwelling beneath the bend in the San Andreas fault and upwelling beneath the Salton Trough (associated with the Gulf of California rifting event) were both energetically favorable developments. The mutual need for proximal sources and sinks of material only enhanced the development, and the convective flow pattern described in the constant viscosity modeling section above was initiated. Basal tractions resulting from this flow field may have been sufficient to continue forcing crustal material into the growing Transverse Ranges. If the San Jacinto and Elsinore faults were stronger (or possibly even non-existent) during this time, some

Pacific Plate directed simple shear can also be supplied by far-field plate forces.

Evidence from the Ridge Basin suggests that convergence was occurring by 8.5 m.y.B.P. and was especially active a million years later (Nilsen and Link, 1975). By about 5.5 m.y.B.P. convergent activity ceased in the Ridge Basin (Nilsen and Link, 1975). In this region, slip was taken up by the San Gabriel fault until it began on the now active, circumventing portion of the San Andreas fault. It is believed that this marks a change from large-scale convergence to nearly non-convergent motion along the southern San Andreas fault. This occurred through abandonment of slip along the trace of the San Gabriel Fault and the development of an arcuate zone of slip, the present San Andreas fault, along which nearly non-convergent slip could occur. It also necessitated a change in the style of motion for the portion of California south of the big bend from Pacific Plate-directed translation to the present rotation about a pole located about 650 km to the SW of the big bend, a motion that displaces the site of convergence to the coastal system. This suggests that the Transverse Ranges ceased their major phase of uplift and began to split along the San Andreas fault forming the present San Bernardino and the San Gabriel Mountains at this time. It is at about this time that the slip rate on the San Andreas fault had acquired its present 35 mm/yr and that the Gulf of California started to open in earnest.

A problem with this simple model is that only 60 km of slip have been observed for the San Gabriel fault, though Figure III.6 suggests possibly about twice this net amount of slip had occurred by about 5.5 m.y.B.P. Two possible solutions to this are: motion on the new section of San Andreas fault had actually begun prior to the termination of activity on the San Gabriel fault; and that the switch in participating faults and style occurred slightly before 5.5 m.y.B.P. These two possibilities are, of

course, not exclusive of each other.

Following this was the transfer of the remaining offshore strike-slip motion onto the coastal system. If this occurred within the last one m.y., as is suggested, the recent convergence in the western Transverse Ranges (Rockwell, 1983; Yeats, 1983), then the observed volume of the mantle anomaly (Figure II.14) suggests that the anomaly either began to develop prior to the occurrence of the rapid crustal convergence seen at the surface, or at a rate well in excess of the rate of convergence seen at the surface. While both of these situations are possible, it also seems wise to allow for the possibility that convergence was active prior to the above mentioned estimates. This may have occurred at a different (but nearby) location and was therefore not addressed by these workers.

It is a curious and not understood observation that this switch in style occurred at about the time when the Murray Fracture zone encountered the big bend.

Finally, a few speculative observations are made. As mentioned in the section on kinematic modeling of southern California's crust, the Garlock fault has a pronounced curvature for most of its length, and where the fault does straighten there are associated thrust faults nearby. The suggestion is that the Sierra Nevada block is rotating counter-clockwise about a pole that happens to lie in the Banning Pass (the eastern end of the big bend). It seems likely that the placement of the Garlock fault is roughly controlled by the location of the narrow neck of the Basin and Range province formed by the westward protruding Colorado Plateau and by the competent mass of the Sierra Nevada. Presently Basin and Range spreading is occurring west of this neck and just south of the Sierras. But it is further suggested that, if Sierra Nevada block rotation is occurring about a pole located near the Banning Pass, that

an initially straight San Andreas fault would begin to bend counter-clockwise north of the pole. Thus the Colorado Plateau may have dictated the positioning of the big bend. Development of a bend in the San Andreas fault, however, requires convergence to the west of the pole (which is, curiously enough, where the Transverse Ranges presently lie). This, in fact, may have been the initial source of convergence in the region if the early San Andreas Fault did not initially inherent a "little bend". In any regard, this situation would have accentuated the convergent activity proceeding here. This high rate of activity could be reduced considerably, however, by allowing for motion on the Garlock fault, a occurrence made all the more likely by the lack of extension in the portion of the Basin and Range east of the Mojave region.

It is also noted briefly that the kinematic motions accommodating the externally imposed motions have further reduced the convergence in the big bend region by concentrating crustal convergence along the offshore region. If the convergent motions are far enough offshore to involve oceanic crust, the amount of energy that would have been spent converging continental crust has been greatly reduced. This hypothesis is not supported by the kinematic model, which attains Pacific Plate velocities in the borderland. But considering the imprecise ability of the kinematic model at prescribing the Pacific Plate motion, the possibility that oceanic subduction is occurring is at least interesting.

In light of the geometrical difficulties presented by a confined zone of spreading (primarily the northern Basin and Range) near a transform boundary (the San Andreas Fault), it seems remarkable that a kinematic solution can (and has) been found that requires little externally supplied energy, indeed, may even be a source of energy.

References

- Aki, K., Christoffersson, A., and Huseby, E.S., 1977, Determination of three-dimensional seismic structure of the lithosphere, *Jour. Geophys. Res.*, 1v. 82, pp. 277-296.
- Allen, C.R., Silver, L.T. and Stehli, F.G., 1960, Agua Blanca fault: a major transverse structure of northern Baja California, Mexico, *Geol. Soc. Am. Bull.*, v.71, pp. 457-482.
- Anderson, D.L., 1971, The San Andreas fault, *Sc. Am.*, v. 225, No. 5, pp. 52-68.
- Anderson, D.L., and Bass, J.D., 1984, Mineralogy and composition of the upper mantle, *Geophys. Res. Lett.*, v. 11, pp. 637-640.
- Anderson, J.G., 1979, Estimating the seismicity from geological structure for seismic-risk studies, *Bull. Seis. Soc. Am.*, v. 69, pp. 135-158.
- Ashby, M.F., and Verrall, R.A., 1977, Micromechanisms of flow and fracture, and their relevance to the rheology of the upper mantle, *Phil. Trans. Royal Soc. London*, v. 288, pp. 59-95.
- Atwater, T., 1970, Implications of plate tectonics for the Cenozoic tectonic evolution of western North America, *Geol. Soc. Am. Bull.* v. 81, pp. 3513-3536.
- Atwater, T. and Molnar, P., 1973, Relative motion of the Pacific and North American Plates deduced from sea-floor spreading in the Atlantic, Indian and South Pacific Oceans, in *Kovach, Robert L. and Nur, Amos, eds., Proceedings Conference on tectonic problems of the San Andreas Fault System*, Stanford University Publications, Ca., pp. 136-148.
- Backus, G., Gilbert, F., 1968, The resolving power of gross earth data, *Geophys. J. R. astr. Soc.*, v. 16, pp. 169-205.
- Barrows, A.G., 1979, Geology and fault activity of the Valyermo segment of the San Andreas fault zone, *Ca. Div. of Mines and Geol.*, Open File Report 79-1 LA, 49 pp.
- Bird, P., and Rosenstock, R.W., 1984, Kinematics of present crust and mantle flow in southern California, *Geol. Soc. Amer. Bull.*, v. 95, pp. 946-957.
- Blake, J.R., and Chwang, A.T., 1974, Fundamental singularities of viscous flow, *Jour. Eng. Math.*, v. 8, pp. 23-29.
- Bracewell, R.N., 1956, Strip integration in radio astronomy, *Aust. Jour. Phys.*, v.9, pp. 198-217.
- Bracewell, R.N., 1965, *The Fourier Transform and its Applications*, p. 253, McGraw-Hill.
- Calderone, G. and Butler, R.F., 1984, Paleomagnetism of Miocene volcanic rocks from southwestern Arizona: Tectonic implications, *Geology*, v. 12, pp. 627-630.
- Carter, B.A., 1980, Quaternary displacement on the Garlock fault, California in *Fife, D.L. and Brown, A.R., eds., Geology and Mineral wealth of the California desert, Dibblee volume: South Coast Geological Society*, Santa Ana, Ca., pp. 457-465.
- Carter, B.A., 1982, Neogene displacement on the Garlock fault, California (abstract), *Am. Geophys. Union Trans., EOS*, v. 63, p. 1124.

- Clark, M.M., Harms, K.K., Lienkaemper, J.J., Harwood, D.S., Lajoie, K.R., Matti, J.C., Perkins, J.A., Rymer, M.J., Sarna-Wojcicki, A.M., Sharp, R.V., Sims, J.D., Tinsley, J.C. III, and Ziony, J.I., 1983, Preliminary slip rate table and map of late Quaternary faults of California, preprint of U. S. Geological Survey Open File Report.
- Corbett, E.J., 1984, Seismicity and crustal structure studies of southern California: Tectonic implications from improved earthquake locations, *Ph.D. Dissertation*, Caltech, 231 pp.
- Comer, R., and Clayton, R., 1985, submitted to *Jour. Geophys. Res.*
- Crouch, J.K., Bachman, S.B., and Shay, J.T., 1984, Post Miocene compressional tectonics along the central California margin, in *Crouch J.K. and Bachman S.B., eds., Tectonics and sedimentation along the California margin: Pacific Section S.E.P.M.*, v. 38, pp. 37-54.
- Crowell, J.C., 1981, An outline of the tectonic history of southeastern California, in *Ernst, W.G., ed., The Geotectonic development of California: Rubey Vol. 1*, Prentice-Hall, N. J., pp. 583-600.
- Crowell, J.C., 1982, The tectonics of Ridge Basin, in *Crowell, J.C. and Link, M.H., eds., Geologic history of Ridge Basin southern California, Pacific Section of Society of Economic Paleontologists and Mineralogists, Ca.*, pp. 25-42.
- Davis, G. A. and Burchfiel, B.C., 1973, Garlock Fault: An intracontinental transform structure, southern California, *Geol. Soc. Am. Bull.*, v. 84, pp. 1407-1422.
- Davis, T. and Lague, M., 1984, Cenozoic structural development on the north-central Transverse Ranges and southern margin of the San Joaquin Valley, *Abs. with Programs, 97th Annual Meeting, Geol. Soc. Am.*, v. 16, p. 484.
- Dickinson, W.R., Cowan, D.S. and Schweickert, W.A., 1972, Test of new global tectonics: Discussion, *Am. Ass. of Petr. Geol. Bull.*, v. 56, pp. 375-384.
- Dickinson, W.R. and Snyder, Walter S., 1979, Geometry of triple junctions related to San Andreas Transform, *Jour. Geophys. Res.*, v. 84, pp. 561-572.
- Dokka, R.K., 1983, Displacements on late Cenozoic strike slip faults of the central Mojave Desert, California, *Geology*, v. 11, pp. 305-308.
- Ehlig, P.L., 1981, Origin and tectonic history of the basement terrane of the San Gabriel Mountains, central Transverse Ranges, in *Ernst, W.G., ed., The geotectonic development of California: Rubey Vol. 1*, Prentice-Hall, N. J., pp. 253-283.
- Ehlig, P.L., Ehlert, K.W., and Crowe, B.M., 1975, Offset of the upper Miocene Caliente and Mint Canyon Formations along the San Gabriel and San Andreas faults, in *Crowell, J.C., ed., San Andreas Fault in southern California: A guide to the San Andreas Fault from Mexico to Carrizo Plain, Ca. Div. of Mines and Geology, Special Report 118*, pp. 83-92.
- Ehlig, P.L., Joseph, S.E., and Ehlert, K.W., 1979, Magnitude and timing of offset on the San Andreas Fault in southern California and its effect on Miocene and Pliocene paleogeography (abstract), in *Armentrout, J.M., Cole, M.R., and Terbest, H., eds., Cenozoic paleogeography of the Western United States, Society of Economic Paleontologists and Mineralogists, Pacific Section, Pacific Coast Paleogeography Symposium*, v. 3, p. 327.

- Ensley, Ross A. and Verosub, Kenneth L., 1982, A magnetostratigraphic study of the sediments of the Ridge Basin, southern California and its tectonic and sedimentologic implications, *Earth and Planet. Sc. Lett.*, v. 59, pp. 192-207.
- Fitch T.J., 1972, Plate convergence, transcurrent faults, and internal deformation adjacent to southeast Asia and the western Pacific, *Jour. Geophys. Res.*, v. 77, pp. 4432-4463.
- Foster, J.H., 1980, Late Cenozoic tectonic evolution of Cajon Valley, southern California, *Ph.D. Dissertation*, U.C. Riverside, 242 pp.
- Garfunkel, Z., 1974, Model for the late Cenozoic tectonic history of the Mojave Desert, California, *Geol. Soc. Am. Bull.*, v. 85, pp. 1931-1944.
- Gilbert, P.F.C., 1972, Iterative methods for three-dimensional reconstructions of an object from projections, *Jour. Theor. Biol.*, v. 36, pp. 105-117.
- Gillespie, A.R., 1982, Quaternary glaciation and tectonism in the southeastern Sierra Nevada, Inyo County, Ca., *Ph.D. Dissertation*, Caltech, 695 pp.
- Hadley, D.M., and Kanamori, H., 1977, Seismic structure of the Transverse Ranges, California, *Geol. Soc. Am. Bull.*, v. 88, pp. 1461-1478.
- Hearn, T. M., 1984, P_n travel times in southern California, *Jour. Geophys. Res.*, v. 89, pp. 1843-1855.
- Hearn, T. M., 1984, Crustal structure in southern California from array data, *Ph.D. Dissertation*, Caltech, 130 pp.
- Herman, G.T., Lent, A., Rowland, S.W., 1973, ART: Mathematics and Applications, *Jour. Theor. Biol.*, v. 42, pp. 1-32.
- Herrin, E., 1968, 1968 seismological tables for P phases, *Bull. Seism. Soc. Am.*, v. 58, pp. 1193-1241.
- Hill, D.P., 1982, Contemporary block tectonics: California and Nevada, *Jour. Geophys. Res.*, v. 87, pp. 5433-5450.
- Huffman, O.F., 1972, Lateral displacement of upper Miocene rocks and Neogene history of offset along the San Andreas fault in central California, *Geol. Soc. Am. Bull.*, v. 83, pp. 2913-2946.
- Humphreys, E., 1980, *Unpublished data*.
- Humphreys, E., 1978, Telluric Sounding and Mapping in the Vicinity of the Salton Sea Geothermal Area, Imperial Valley, California, *Masters Dissertation*, U.C. Riverside, 116 pp.
- Humphreys, E., Clayton, R. W., Hager, B. H., 1984, A tomographic image of mantle structure beneath southern California, *Geophys. Res. Lett.*, v. 11, pp. 625-627.
- Humphreys, E., and Hager, B. H., 1984, Small-scale convection beneath southern California (abstract), *Am. Geophys. Union Trans., EOS*, v. 65, p. 195.

- Jackson, D. D., 1972, Interpretation of Inaccurate, Insufficient and Inconsistent Data, *Geophys. J. R. astr. Soc.*, v. 28, pp. 97-109.
- Kennedy, M.P., 1977, Recency and character of faulting along the Elsinore fault zone in southern Riverside County, California, *Ca. Div. of Mines and Geology*, Special Report 131, 12 pp.
- King, 1985, *Jour. Geophys. Res.*, *in press*.
- Kosloff, D.D., 1978, Numerical models of crustal deformation, *Ph.D. Dissertation*, Caltech, 187 pp.
- Lachenbruch, A., and Sass, J., 1977, Heat flow in the United States and the thermal regime of the crust, in *The Earth's Crust: Its Nature and Physical Properties*, Geophys. Monogr. Ser., v. 20, Heacock, J.G., ed., pp. 626-675.
- Lachenbruch, A., and Sass, J., 1980, Heat flow and energetics of the San Andreas fault zone, *Jour. Geophys. Res.*, v. 85, pp. 6185-6223.
- Lachenbruch, A., 1985, *pers. comm.*
- Larson, R. L., Menard, H. W., and Smith, S. M., 1968, Gulf of California: A result of ocean floor spreading and transform faulting, *Science*, v. 73, pp. 3361-3397.
- Leary, P.C., 1985, Near-surface stress and displacement in a layered elastic crust, *Jour. Geophys. Res.*, pp. 1901-1910.
- Love, A.E.H., 1926, *A treatise on the mathematical theory of elasticity*, Cambridge University Press. 643 pp.
- Luyendyk, B.P., Kamerling, M.J., and Terres, R., 1980, Geometric model for Neogene crustal rotations in southern California, *Geol. Soc. Am. Bull.*, v. 91, pp. 211-217.
- Matti, J.C. and Morton, D.M., 1975, Geologic history of the San Timoteo badlands, southern California, *Abs. with Programs, Cordilleran Section, Geol. Soc. Am.*, v. 7, p. 344.
- Matti, J.C., Tinsley, J.C. Morton, D.M. and McFadden, L.D., 1982, Holocene faulting history as recorded by alluvial stratigraphy within the Cucamonga fault zone: a preliminary view, in *Tinsley, J.C., McFadden, L.D., and Matti, J.C., eds., Late Quaternary pedogenesis and alluvial stratigraphy within the Cucamonga fault zone: Geol. Soc. Am., Cordilleran Section, Field Trip Guide 12*, pp. 21-44.
- Matti, J.C., Morton, D.M., and Cox, B.F., 1984, Geologic framework of the south-central Transverse Ranges, southern California: Distribution and Nomenclature of faults in the San Andreas fault zone and associated fault systems, *preprint*.
- Mavko, Gerald M., 1980, Velocity and attenuation in partially molten rocks, *Jour. Geophys. Res.*, v. 85, pp. 5173-5189.
- Minster, J.B. and Jordan, T.H., 1978, Present-day plate motions, *Jour. Geophys. Res.*, v. 83, pp. 5331-5354.

- Minster, J.B. and Jordan, T.H., 1984, Vector constraints on Quaternary deformation of the western United States east and west of the San Andreas Fault, *preprint*.
- Miyamachi, H., and Moriya, T., 1985, Velocity structure beneath the Hidaka Mountains in Hokkaido, Japan, *preprint*.
- Moore, D. G. and Curray, J. R., 1982, Geologic and tectonic history of the Gulf of California, *Initial Reports of the Deep Sea Drilling Project*, v. 64, pp. 1279-1296.
- Morton, D.M. and Matti, J.C., 1979, Evidence for a vanished post-middle Miocene pre-late Pleistocene alluvial-fan complex in the northern Perris block, southern California, *Abs. with Programs, Cordilleran Section, Geol. Soc. Am.*, v. 11, p. 118.
- Nilsen, Tor H. and Link, Martin H., 1975, Stratigraphy, sedimentology and offset along the San Andreas fault of Eocene to lower Miocene strata of the northern Santa Lucia Range and the San Emigdio Mountains, Coast Ranges, central California, in *Weaver, D.W., Horriday, G.R. and Tipton, A., eds., Paleogene Symposium and selected technical papers, AAPG-SEPM-SEG, Ca.*, pp. 367-400.
- Oldenburg D.W., 1981, Conductivity structure of the oceanic upper mantle beneath the Pacific plate, *Geophys. J. R. astr. Soc.*, v. 65, pp. 359-394.
- Pinault, C.T. and Rockwell, T.K., 1984, Rates and sense of Holocene faulting on the Elsinore fault: Further constraints on the distribution of dextral shear between the Pacific and North American plates, *Abs. with Programs, 97 th Annual Meeting, Geol. Soc. Am.*, v. 16, p. 624.
- Powell, R.E., 1981, Geology of the crystalline basement complex, eastern Transverse Ranges, southern California: Constraints on regional tectonic interpretation, *Ph.D. Dissertation, Caltech*, 441 pp.
- Radon, J., 1917, Über die Bestimmung von Funktionen durch ihre Integralwerte langs gewisser Mannigfaltigkeiten, *Berichte Sachsische Akademie der Wissenschaften. Leipzig, Math.-Phys. Kl.*, v. 69, pp. 262-267.
- Raikes, S. A., 1980, Regional variations in upper mantle structure beneath southern California, *Geophys. J. R. astr. Soc.*, v. 63, pp. 187-216.
- Rigden, Sally M., Ahrens, Thomas J., and Stolper, Edward M., 1984, Densities of liquid silicates at high pressures, *Science*, v. 226, pp. 1071-1074.
- Roberts, R.G., 1983, Electromagnetic evidence for lateral inhomogeneities within the Earth's upper mantle, *Phys. Earth Planet. Int.*, v. 33, pp. 198-212.
- Rockwell, T.K., 1983, Soil chronology, geology and neotectonics of the north-central Ventura basin, California, *Ph.D. Dissertation, U.C. Santa Barbara*, 424 pp.
- Rowland, S.W., 1979, Computer implementation of image reconstruction formulas, in *Image Reconstructions from Projections, G. T. Herman ed.*, Springer-Verlag.
- Sauber, J., and Thacher, W., 1984, Geodetic measurements of deformation in the central Mojave Desert, California (abstract), *Am. Geophys. Union Trans., EOS*, v. 65, p. 993.

- Savage, J.C., 1983, Strain accumulation in western United States, *Ann. Rev. Planet. Sc.*, v. 11, pp. 11-43.
- Sharp, R.V., 1981, Variable rates of late Quaternary strike slip on the San Jacinto fault zone, Southern California, *Jour. Geophys. Res.*, v. 86, pp. 1754-1762.
- Sieh, K.E., and Jahns, R., 1984, Holocene activity of the San Andreas fault at Wallace Creek, California, *Geol. Soc. Am. Bull.*, v. 95, pp. 883-896.
- Silver, L.T., 1982, Evidence and a model for west-directed early to mid-Cenozoic basement overthrusting in southern California, *Abs. with Programs, 78th Annual Meeting, Geol. Soc. Am.*, v. 14, p. 617.
- Stolper, E., Walker, D., Hager, B.H., and Hays, J.F., 1981, Melt segregation from partially molten source regions: The importance of melt density and source region size, *Jour. Geophys. Res.*, v. 86, pp. 6261-6271.
- Turcotte, G.L. and Schubert, G., 1982, *Geodynamics: Applications of continuum physics to geological problems*, John Wiley and Sons, 450 pp.
- Walck, M. C., 1984, Teleseismic array analysis of upper mantle compressional velocity structure, *Ph.D. Dissertation*, Caltech, 233 pp.
- Walck, M. C., and Minster, J. B., 1982, Relative array analysis of upper mantle lateral velocity variations in southern California, *Jour. Geophys. Res.*, v. 87, pp. 1754-1772.
- Weber, G.E. and Lajoie, K.R., 1977, Late Pleistocene and Holocene tectonics of the San Gregorio fault zone between Moss Beach and Point Ano Nuevo, San Mateo County, California, *Abs. with Programs, Cordilleran Section, Geol. Soc. Am.*, v.9, p. 524.
- Weldon, R.J., 1984a, Quaternary deformation due to the junction of the San Andreas and San Jacinto faults, Southern California, *Abs. with Programs, 80th Annual Meeting, Geol. Soc. Am.*, v. 16, p. 689.
- Weldon, R.J., 1984b, Implications of the age and distribution of the late Cenozoic stratigraphy in Cajon Pass, Southern California, in *Hester, R.L. and Hallinger, D.E., eds., San Andreas fault-Cajon Pass to Wrightwood, Pacific Section A.A.P.G.*, guidebook 55, pp. 9-16.
- Weldon, R.J. and Sieh, K.E., 1984, Holocene rate of slip and tentative recurrence interval for large earthquakes on the San Andreas fault in Cajon Pass, Southern California, *Geol. Soc. Am. Bull.*, *in press*.
- Weldon, R.J., Winston, D.S., Kirschvink, J.L. and Burbank, D.W., 1984, Magnetic stratigraphy of the Crowder Formation, Cajon Pass, Southern California, *Abs. with Programs, 80th Annual Meeting, Geol. Soc. Am.*, v. 16, p. 689.
- Weldon, R.J. and Sieh, K.E., 1985, *in press*.
- Weldon, R.J. and Meisling, K., 1985, *in prep*.
- Weldon, R.J., 1985, *pers. comm.*

- Wiggins, R., 1972, The general linear inverse problem: implications of surface waves and free oscillations on earth structure, *Rev. Geophys. Space Phys.*, v. 10, pp. 251-285.
- Wilson, J. T., 1965, A new class of faults and their bearing on continental drift, *Nature*, v. 207, pp. 343-347.
- Yeats, R.S. and Haq, B.U., 1981, Deep-sea drilling off the Californias: Implications of leg 63, *Initial Reports of the Deep Sea Drilling Project* v. 63, pp. 949-961.
- Yeats, R.S., 1983, Large scale Quaternary detachments in Ventura Basin, southern California, *Jour. Geophys. Res.*, v. 88, pp. 569-583.
- Yuen, David A. and Fleitout, Luce, 1985, Thinning of the lithosphere by small-scale convective destabilization, *Nature*, v. 313, pp. 125-128.
- Ziony, J.I. and Yerkes, R.F., 1984, Fault slip-rate estimation for the Los Angeles region: Challenges and opportunities (abstract), *Earthquake Notes, Eastern Section, Seis. Soc. Am.*, v. 55, p. 8.
- Zoback, Mary Lou, Anderson, R.E., and Thompson, G.A., 1981, Cenozoic evolution of the state of stress and style of tectonism of the Basin and Range province of western United States, *Phil. Trans. Royal Soc. London*, v. 300, pp. 407-434.
- Zoback, M.D., Tsukahara, H., and Hickman, S., 1980, Stress measurements at depth in the vicinity of the San Andreas fault: Implications for the magnitude of shear stress at depth, *Jour. Geophys. Res.*, v. 85, pp. 6157-6173.